January 2022

Characterization Of Vertical Growth Of Fractures In Layered Formations

Vibhas Jagdish Pandey

CHARACTERIZATION OF VERTICAL GROWTH OF FRACTURES IN LAYERED FORMATIONS

by

Vibhas J. Pandey

Master of Science, Petroleum Engineering, University of Oklahoma, Norman, Oklahoma, USA. 1998.

Master of Engineering, Turbomachines, Sardar Vallabhbhai National Institute of Technology, Surat, India. 1991.

Bachelor of Engineering, Mechanical Engineering, Sardar Vallabhbhai National Institute of Technology, Surat, India. 1987.

A Dissertation

Submitted to the Graduate Faculty

of the

University of North Dakota

In partial fulfilment of the requirements

for the degree of

Doctor of Philosophy

Grand Forks, North Dakota

August 2022

This thesis submitted by Mr. Vibhas J. Pandey in partial fulfilment of the requirements for the Degree of PhD from The University of North Dakota, has been read by the Faculty Advisory Committee under whom the work has been done and is hereby approved.

_____
Dr. Vamegh Rasouli

_____
Dr. Hui Pu

_____
Dr. Kegang Ling

_____
Dr. Brian Tande

_____

This dissertation is being submitted by the appointed advisory committee as having met all the requirements of the School of Graduate Studies at the University of North Dakota and is hereby approved.

_____
Christopher Nelson
Associate Dean of The Graduate School

_____
Date

PERMISSION

Title: Hydraulic Fracture Height Growth Modeling in Layered Formations

Department: Department of Petroleum Engineering

Degree: Doctor of Philosophy

In presenting this thesis in partial fulfillment of the requirements for a graduate degree from the University of North Dakota, I agree that the library of this University shall make the thesis freely available for inspection. I further agree that permission for extensive copying for scholarly purposes may be granted by the professor who supervised my thesis work or, in his absence, by the chairperson of the department or the Dean of the Graduate School. It is understood that any copying or publication or other use of this thesis or part thereof for financial gain shall not be allowed without my written permission. It is also understood that due recognition shall be given to me and to the University of North Dakota in any scholarly use which may be made of any material in my thesis.

Vibhas Pandey
May 26th, 2022.

Acknowledgements

I would like to thank Dr. Vamegh Rasouli, Department Chair and Continental Resources Distinguished Professor, Department of Petroleum Engineering, University of North Dakota, for his continuous encouragement and support throughout my research work. He was instrumental in providing resources and guidance that made this work possible and gave numerous helpful suggestions to improve the contents of the research work. Thanks, are also due to Dr. Pu, Dr. Ling, and Dr. Tande for their support in making this research work possible.

I would also like to take this opportunity to thank the management of ConocoPhillips Company, Houston, for providing the necessary support in carrying out the research work and for their permission to publish this work.

Special thanks are due to Mr. Jeffrey Spencer, Manager, Global Completions, ConocoPhillips Company, Houston, for the unequivocal support he extended to me during the past several years especially by reviewing and critiquing my technical work and offering valuable advice and suggestions to improve the content of my technical publications. As in many of my previous publications, Mr. Spencer has been instrumental in reviewing this work for its technical content and accuracy.

There are several individuals with whom I have had the fortune to interact with and discuss the various aspects of hydraulic fracturing and by that token they will have contributed to this study in one form or the other; they are too numerous to mention, but I would like to express my gratitude towards them for sharing their knowledge and beliefs with me over the past three decades.

With Thanks,

Vibhas J. Pandey
Engineering Fellow, ConocoPhillips Company.
Houston, TX 77079.
May 26th, 2022.

Dedicated to

My Wife Shilpa and Son Neel,

who were a constant source of inspiration

&

My Parents and In-Laws,

without whose blessings and support this would not have been possible.

Table of Contents

Table of Figures

Publications produced from this research thesis

Following is the list of papers that are associated with this research work:

1. Pandey, V. J. and Rasouli, V., 2021a. Vertical Growth of Hydraulic Fractures in Layered Formations. Presented at The Virtual SPE Hydraulic Fracturing Technology Conference, The Woodlands, TX, USA, 4–6 May. SPE-204155-MS. http://dx.doi.org/10.2118/204155-MS.
2. Pandey, V.J. and Rasouli, V., 2021b. Fracture Height Growth Prediction Using Fluid Velocity Based Apparent Fracture Toughness Model. *Rock Mech. Rock Eng. J*. May 2021. **54:** 4059-4078. https://doi.org/10.1007/s00603-021-02489-w
3. Pandey, V.J. and Rasouli, V., 2021c. A semi-analytical model for estimation of hydraulic fracture height growth calibrated with field data. *J. Pet. Sci. and Eng*. **202**, July 2021, 108503. https://doi.org/10.1016/j.petrol.2021.108503.
4. Pandey, V. J., 2021. Pressure Interpretation in Acid Fracturing Treatments. *SPE Prod. & Oper*. **37** (02): 346–361. SPE-205990-PA. http://dx.doi.org/10.2118/205990-PA.
5. Pandey, V.J. and Rasouli, V., 2022a. Estimating Fracture Containment in Layered Formations Using 3D Fracture Growth Assumptions. Presented in the SPE Hydraulic Fracturing Technology Conference and Exhibition, The Woodlands, Texas, USA, 3-5 February. SPE-209151-MS. doi: https://doi.org/10.2118/209151-MS.
6. Pandey, V.J. and Rasouli, V., 2022. Development of a Fracture Width Induced Net Stress Model to Predict Constraints to Fracture Height Growth. 110429. *J. of Pet. Sci. & Eng.* **213**. June 2022, 110429. https://doi.org/10.1016/j.petrol.2022.110429.

ABSTRACT

Hydraulic fracturing treatments are routinely pumped in oil and gas wells worldwide to enhance production and manage the economic recovery of hydrocarbon reserves. The uplift in the production after a fracture stimulation job depends on several parameters, of which optimal coverage of the payzone by the treatment is one of the more important ones. The vertical growth of hydraulic fractures thus is a topic of great interest amongst researchers because of its ability to influence the outcome of a stimulation treatment.

The modeling and prediction of fracture height, especially in layered formations, is a challenging task given the associated complexities often observed when setting up the mathematical model. The models developed for a case where the fracture is confined to the payzone layer surrounded by barriers in a simple 3-layer case, serves as a starting point for developing more complex models that can account for stress and mechanical property changes in layered or laminated reservoir with contrasting properties. In this study, the solution to such complex and rigorous mathematical problems were obtained by developing a simulation model which adopted a semi-analytical approach during the computational process.

Apart from strength and mechanical attributes of the formation rocks, it is also important to account for the fracturing treatment parameters such as the injection rates and fracturing fluid rheology in fracture height estimation process because of the influence they wield. To accurately determine the fracture evolution during the treatment, the newly developed height growth model was extended to enable history matching of the treatment data. To validate this model, it was applied to several field cases worldwide, covering a variety of completions including treatment on shallow coal bed methane wells, low permeability sandstone reservoirs, foamed fluid treatments, offshore frac packs, and high-rate fracturing treatments typically pumped in unconventional reservoirs. The fracture dimensions predicted by the model reasonably matched the field observations and also led to additional model-enhancements.

The findings from the research were published in various journals and shared with audiences worldwide via presentations in SPE conferences. Whilst the prediction of fracture height will continue to attract and engage researchers worldwide, it is hoped that this work will make significant contributions to the existing literature and assist those who wish to continue exploring further in this arena.

CHAPTER 1

Hydraulic Fracturing and Fracture Dimensions

1.1. Introduction

Hydraulic fracturing is a popular and well known well stimulation technique routinely employed to accelerate the hydrocarbon production and improve the overall recovery from subterranean reservoirs. The process involves injecting fluids in the downhole formations at pressures that far exceed the failure pressures of the rock formation, thus initiating and propagating a fracture which is then held open by pumping solid materials termed as proppants. The presence of proppant prevents the walls of the hydraulically created fracture to close completely even after the high injection pressures are released at end of the treatment. The fracture, now purposely held open by proppant, acts as a conductive pathway that eases the flow of formation fluids into the wellbore and results in increased hydrocarbon production.

Since its inception after first such treatment was pumped in 1949 (Montgomery and Smith 2010) the technique continued to evolve in the decades that followed. Over the time, various fracturing methods appeared to gain popularity only to be replaced by another approach as the benefits from one versus the other were evaluated. Economic benefits from a fracturing treatment over an untreated well has always been the cornerstone of fracturing design philosophy and the exclusive driver behind the advancement in technology.

With the advent of hydraulic fracturing, it is possible to economically exploit hydrocarbon reserves from not only the conventional low permeability sandstones (trap rock) reservoirs but also from ultralow permeability rocks such as shales that form most of the source rocks. An optimally designed hydraulic fracturing treatment results in increased surface contact area of the hydrocarbon bearing rock with the wellbore and thus leads to accelerated hydrocarbon recovery. This understanding which is adapted from Darcy's equation (Darcy 1856) for pressure drop in porous media, is shown in Eq. (1.1) which relates the production from a well to surface area available for inflow of reservoir fluids.

$$q \approx \frac{\Delta P}{\Delta x}\frac{kh}{\mu}\left(\frac{A}{h}\right) \quad \text{.....(1.1)}$$

where, q is the flow rate, k is the effective permeability to fluid, h is the pay-zone height and, μ is the viscosity of the produced fluid. The fluid flow rate into the wellbore will increase with the application of larger pressure drawdown (ΔP) over unit length Δx, and with increase area A available for flow, as is the case after the treatment. Since the post-treatment well production is several folds higher than that from an unstimulated well in most cases, the treatments are overall economic to pump and is the primary reason for the popularity of this technique.

1.2. Fracture Dimensions

A hydraulic fracture is typically represented as an entity with planar features that are described with dimensions such as fracture height (h_f), fracture half-length (X_f) assuming a bi-wing fracture emanating from the injection point and, fracture width, which may vary from a maximum value at the wellbore (w_w) to an average value ($\bar{w}$) across the fracture length. In most cases, the fracture geometrical attributes are sufficient in describing the fracture advancement during the treatment and even for most mathematical calculations related to fracture modeling and production forecast from a hydraulically fractured well. A simple fracture geometry simulated using one of the commercially available fracture simulators is shown in **Fig. 1.1** where the fracture half-length and height are illustrated. The track on the left shows the modeled formation stresses and the contour on the right reflects the distribution of the proppant inside the fracture.

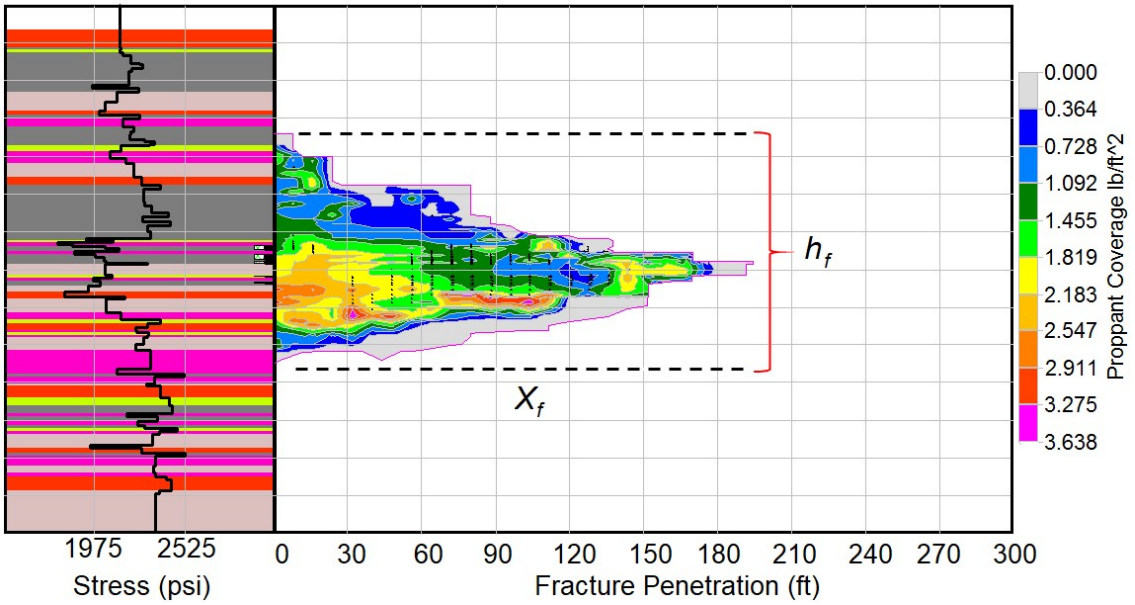

Fig. 1.1: Fracture dimensions of a planar fracture. (Pandey and Cramer, 2019)

1.2.1. Influence of Fracture Dimensions on Well Production

The influence of hydraulic fractures in improving well performance has been thoroughly researched and well documented in the literature. The presence of fracture dominates the early time production and continues to the pseudo-steady state flow regime where the effects of drainage boundary are starting to be felt at the wellbore (Raghavan and Hadinoto 1978). Equations (1.2) and (1.3) show the flow potential in this state.

$$p_{wD} = 2\pi t_{DA} + \ln\left(\frac{x_e}{X_f}\right) + \frac{1}{2}\ln\left(\frac{2.25}{C_A}\right) \quad \text{.....(1.2)}$$

where,

$$t_{DA} = \frac{0.0002639\,kt}{\phi\mu c_t A}\ ;A\ = 4x_e y_e \quad \text{.....(1.3)}$$

Here, p_{wD} and t_{DA} are dimensionless pressure and time respectively, x_e and y_e are half-lengths of reservoir dimensions, C_A is the geometric shape factor (Dietz 1965), k is the permeability of the reservoir, t is the time in hours, μ is the viscosity in cP, c_t is the total compressibility in psi^{-1} and A is in ft^2. The production rates from a fractured well and its unstimulated counterpart may eventually converge, but the benefits from fracturing the well will have already been obtained by this time.

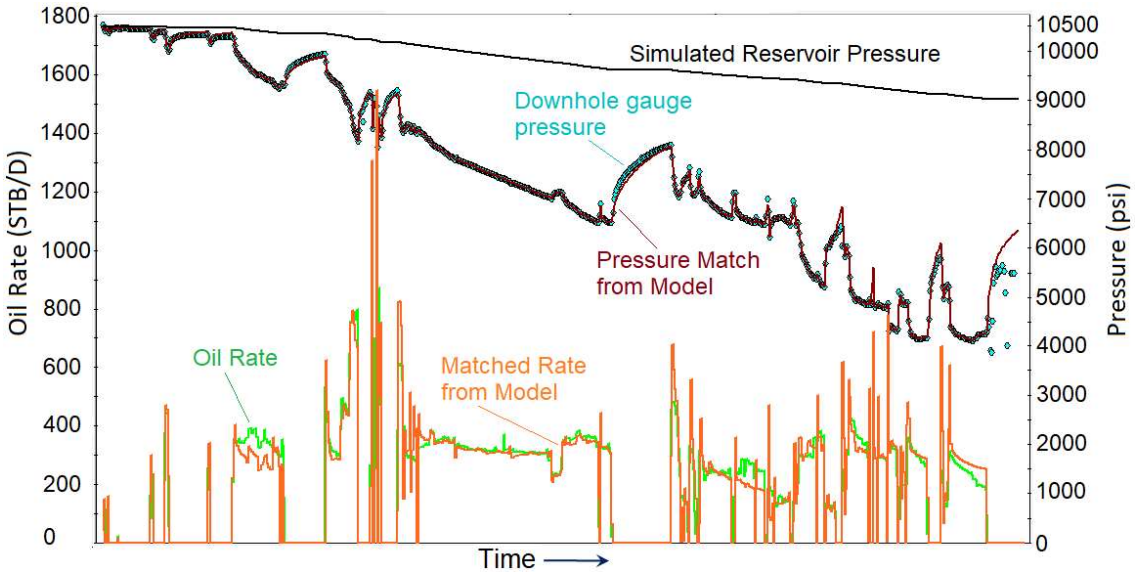

Fig. 1.2: Production History match of an example case. X_f = 280 ft, h_f = 100 ft.

To maximize the production using hydraulic fracturing treatment, it is important that both, the fracture half-length and fracture height, are allowed to grow to the optimal dimensions. Though both propped and unpropped fractures may contribute to production (Warpinski 2010; Sharma and Manchanda 2015; Britt et al. 2006) based on separate mechanisms, inadequate vertical coverage of the pay section can negatively affect the well performance. As presented in Eq. (1.1), the flow rate is directly proportional to the thickness of the payzone (h) and hence a conductive fracture must completely cover the payzone. To illustrate this effect an example is shown in **Fig. 1.2** where the production model for a multi-stage hydraulically fractured shale formation with ultra-low permeability of 0.023 nd is first calibrated with history match of production data and then used for forecasting production for various fracture heights. It may be noted that though the payzone thickness is nearly 200 ft (60.96 m), only 50% of it was accessed during the stimulation process. The treatment pressure history-matched fracture half-length that was calibrated with the help of microseismic (MS) survey data, was determined to be nearly 280 ft (85.3 m). The plot of cumulative production versus production time shown in **Fig. 1.3** was generated with the help of numerical simulator and clearly indicates the possible uplift in production if the effective fracture heights are increased till the entire payzone is sufficiently covered. The "Base Case" refers to the fracture height obtained from history match of the treatment and calibrated with MS data.

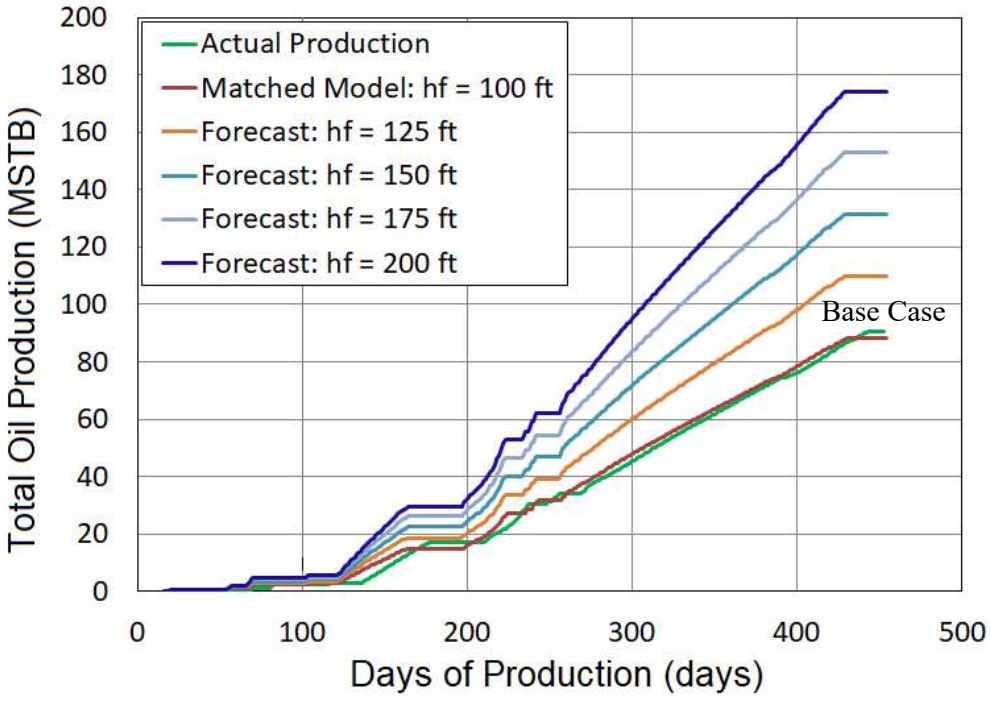

Fig. 1.3: Sensitivity analysis of expected production with increasing fracture height.

1.2.2. Influence of Fracture Height on Well Planning

The extent of height growth or a lack thereof can also be a deciding factor when making decisions related to the placement of horizonal wellbores in thicker payzones with variable stresses. The hypothetical scenario of well placement strategy commonly encountered in the real world is shown in **Fig. 1.4**. The influence of stresses on controlling hydraulic fracture vertical growth is well known (Warpinski and Smith 1989) and presence of any high-stress layer as shown, can limit the vertical growth. For the fracture to grow past such high-stress layers, higher fracture pressures may be required which depends on pumping parameters and other factors. If a horizontal wellbore (Well A) is drilled in the lower section of the payzone highlighted by yellow color, the individual fractures may not cover the entire payzone if there is a lack of ample pressure energy and result in a partially stimulate pay. Likewise, in the presence of strong stress barriers, the downward fracture growth will be limited if the lateral is landed in upper section (Well B) of the pay. Both these scenarios can result in sub-optimal production and may call of either a stacked-pay type completions that cover the entire pay or use of other technologies such as multi-lateral well completions.

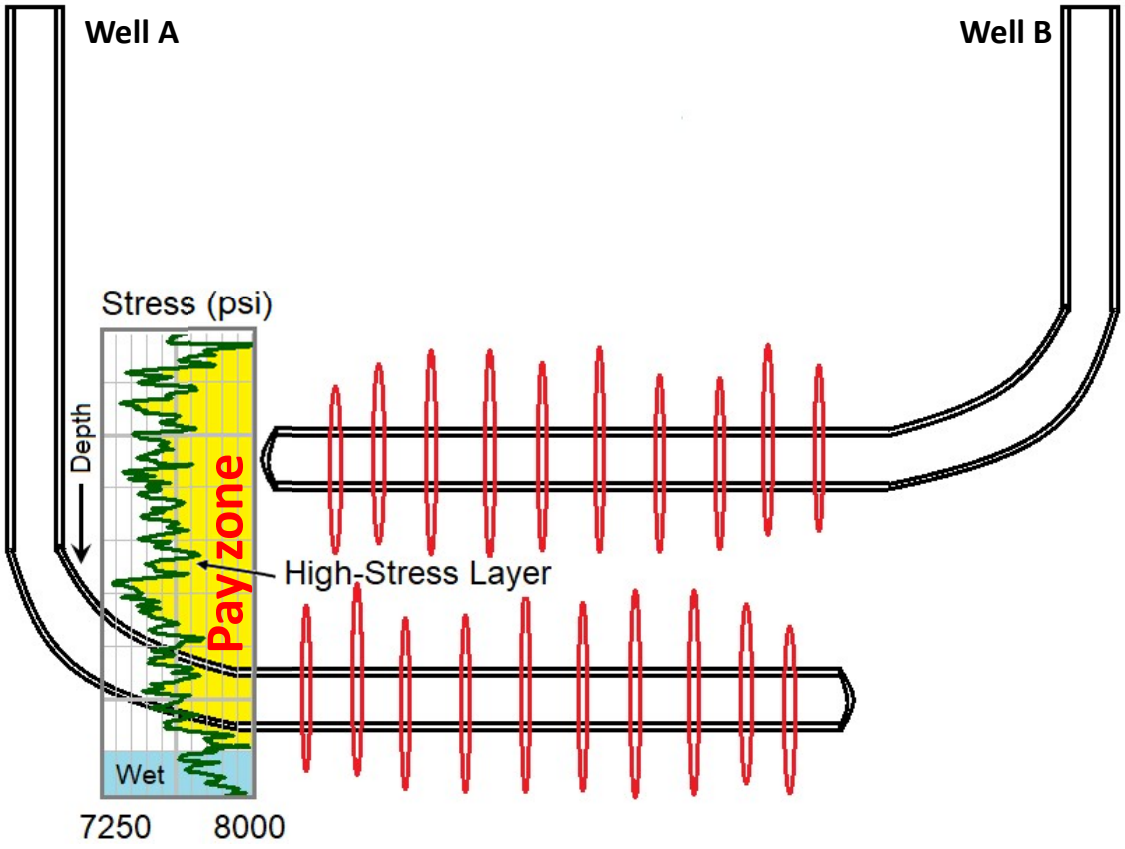

Fig. 1.4: Well planning and placement strategy when considering fracture vertical growth.

1.3. Fracture Height Measurements

The vertical growth of hydraulic fracture is an important parameter that is critical to the success of hydraulic fractures and hence attempts to measure this parameter in the field are common. Measurement of major fracture dimensions be it half-length or height, is not an exact science and is often inferred even if direct measurement techniques such as microseismic survey mapping, radioactive tracer survey, temperature logs, pre and post formation stress measurements, and other such techniques are used. The data published by several researchers show a large variation in fracture heights measured in the field ranging from few tens of a feet to more than a thousand feet in some cases.

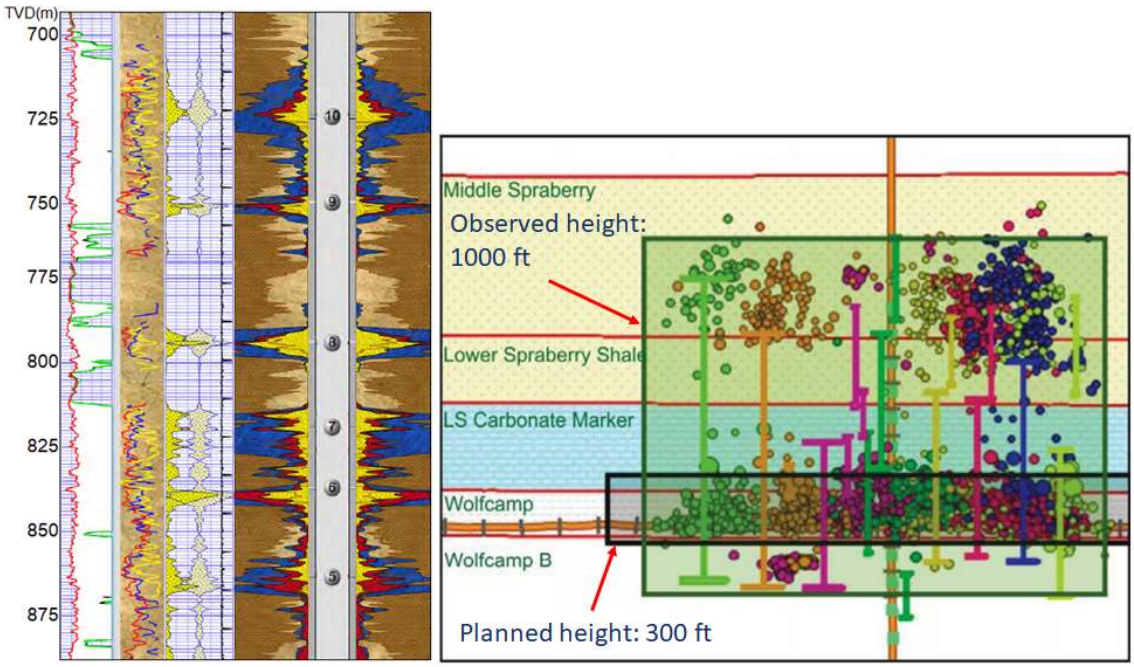

Fig. 1.5: Fracture height measurements. Pandey, et al. (2015) and Stegent, et al. (2019).

The results from a radioactive tracer survey conducted on shallow wells completed to exploit coal bed methane from Walloons coals measures of Surat Basin, eastern Australia (Pandey and Flottmann 2015) are shown on the left section of **Fig. 1.5**. The well was fracture stimulated in multiple stages to place the fractures across the coal seams using specialized techniques to contain the fracture height growth to productive coal seams only. The average fracture height was less than 20 m (65.6 ft) in each stage. In a contrast, fracture heights of up to 1,000 ft (304.8 m) were observed when microseismic survey was conducted while fracture stimulating a well in Wolfcamp B formation in Permian basin as reported by Stegnet et al. (2019). Fracture

heights inferred during fracture stimulation on several treatments pumped in major US shale plays of Barnett, Woodford, Marcellus and Eagleford shales were reported by Fisher and Warpinski in 2012 and show variations that are characteristic to respective plays.

1.4. Fracture Height Estimation

The estimation of fracture dimensions prior to pumping the actual treatment is pivotal to the modeling efforts involved in hydraulic fracturing treatment design. The performance from a fracturing treatment can be maximized if the treatment results in a desired geometry, i.e., where the effective fracture half-length reaches the designed value and the conductive fracture adequately covers but remains bound within the payzone. To accomplish this goal, the height growth is often modeled based on various numerical schemes that account for various critical parameters such as stress distribution in the formation, rock mechanical properties and injection fluid properties. The accuracy of prediction however depends on the workings of the model, and it is not uncommon to see variation in outcomes from various simulators and an overall mismatch of predicted and observed data. This shortcoming often results in unfavorable treatment outcomes which negatively effects the well performance.

The underlying theory and assumptions of modeling fracture height growth of a planar fracture is discussed in detail in the text that follows. A full-fledged semi-analytical model capable of predicting fracture height growth in layered formations was developed during the study and its details are presented in Chapter 3. The model generates a map of fracture vertical growth with respect to fracture net pressure and predicts fracture location and height as the treatment evolves.

Continuing the study, a model to carryout out pressure history match of fracturing treatment using fracture height versus net pressure mapping was also developed; this numerical model accounts for all critical pumping parameters such as injection rates, fluid rheology, fracturing fluid leakoff and the relationship between fracture growth and fracture net pressure to predict fracture height growth, fracture half-length and width. The results from this simulator were compared with those from commercially available simulator and with field observed fracture dimensions. The model was also extended to acid fracturing cases to determine etched fracture parameters such as length, height, and width.

The various outcomes indicate an interesting behavior of fracture height growth history that were corroborated by field observations and have helped in optimizing fracture stimulation designs.

1.5. Nomenclature

A = drainage area, $M^0L^2t^0$, ft^2 (m^2)

c_t = total compressibility, $M^{-1}L^1t^2$, psi^{-1} (Pa^{-1})

C_A = geometric shape factor, dimensionless

h = height of the payzone, $M^0L^1t^0$, ft (m)

k = reservoir permeability, $M^0L^2t^0$, md (m^2)

p_{WD} = dimensionless pressure, dimensionless

ΔP = drawdown pressure, $M^1L^{-1}t^{-2}$, psi (Pa)

t = time, hours

t_{DA} = dimensionless time, dimensionless

x_e = half-length of reservoir dimension, $M^0L^1t^0$, ft (m)

x_f = fracture half-length, $M^0L^1t^0$, ft (m)

Δx = distance, $M^0L^1t^0$, ft (m)

y_e = half-length of reservoir dimension, $M^0L^1t^0$, ft (m)

ϕ = porosity, fraction

μ = fluid viscosity, $M^1L^{-1}t^{-1}$, cP (Pa.s)

CHAPTER 2

Fracture Height in Multilayered Stress Models

2.1. Crack Propagation and Fracture Toughness

The pioneering work done by Griffith and Taylor in 1921 and Griffith in 1924 on crack growth in low tensile strength brittle materials laid the foundation to the theory of linear elastic fracture mechanics (LEFM) which became the cornerstone of modern-day fracture mechanics. The theory states that the onset of crack propagation occurs when the strain energy release rate (G_e) is twice the value of fracture specific surface energy, G_f because two new surfaces are created. G_f (J/m^2) is a material property that quantifies the energy required to create a fracture of unit area from an unloaded state and bears similar units as surface tension of a fluid. Irwin (1957) showed that after proper substitution, fracture specific surface energy for one surface can be related to the fracture toughness, K_{IC}:

$$G_f = \frac{K_{IC}^2}{E'} \quad \text{.....(2.1)}$$

in which the modified elasticity is $E' = E/(1-\nu^2)$ for plane strain and $E' = E$ for plane stress assumptions. K_{Ic} is considered a material property for a perfectly elastic medium as shown by Thiercelin (1987) and its typical values for various materials in literature (Warpinski and Smith 1989). It can be likened to resistance to fracture propagation and can also be calculated from fracture tip pressures or vice versa; fracture tip pressure may be assumed as the value of fracture pressure itself at the start of the treatment where fracture tip pressures dominate the propagation mode. As noted by Gulrajani and Nolte (2000), because of its dependence on fracture geometry, the effective or apparent fracture toughness values are not considered a material property and require a correction prior to use. In general, the fracture tip pressure-based value of fracture toughness is higher by one order magnitude than typically assumed or laboratory derived values of fracture toughness for various rock types as shown by Shlyapobersky (1985).

The work of Barenblatt (1962) on crack tip behavior, is equally noteworthy as it facilitated the assumption and use of smoothly closing fracture tip by one of the two-dimensional fracture models of constant height.

2.2. Stress Intensity Factors

Based on the work of Muskhelishvili (1953a, 1953b), Rice (1968) defined complex stress function in plane elasticity to generate solutions for *n* number of cracks along the same axis.

He also noted that all crack tip stress fields exhibit an inverse square root singularity. For the case of a single finite crack of length $2a$, the solutions were compared with the stress fields around the crack tips obtained by Irwin (1960), resulting in stress intensity factors at the tip of the fractures for three distinct singular stress fields for opening (mode I), sliding (mode II) and shear (mode III; anti-plane) sliding cases, while introducing stress intensity factor K_I which in a way represents the strength of singularity. For a mode I fracture in the presence of uniform stress field σ, stress intensity factor can be given as follows:

$$K_I = \sigma\sqrt{\pi a} \quad \text{.....(2.2)}$$

In a more specific configuration, of crack extending from $-a$ to $+a$ along the distance ξ along the crack, having internal pressure changes given by function $p(\xi)$, the stress intensity factor K_I for mode I fracture is given as:

$$K_I = \frac{1}{\sqrt{\pi a}} \int_{+a}^{-a} p(\xi) \frac{\sqrt{a+\xi}}{\sqrt{a-\xi}} d\xi \quad \text{.....(2.3)}$$

The above relationship has proved extremely useful in development of height growth models.

For the fracture to propagate, the value of stress intensity factor should exceed a critical value termed as *fracture toughness* and denoted by K_{Ic}. The relation between the net pressure in the fracture which is the difference between the fracture pressure that keeps the fracture open and the externally acting insitu stress tending to close it, and the fracture toughness, can be obtained by simply substituting stress σ in Eq. (2.2) with $(P_f - \sigma_3)$ as shown below:

$$K_{Ic} = \left(P_f - \sigma_3\right)\sqrt{\pi a} \quad \text{.....(2.4)}$$

where, P_f is fracture pressure, and σ_3 is minimum in-situ stress. Now that the behavior of crack formation in infinite or semi-infinite, brittle and/or elastic rock-type materials was established, the postulations were extended to multiple formation layers or interfaces.

2.3. Fracture Height Calculations

The basis of fracture height calculation is already established in Eq. (2.3) where the solution can be obtained by solving the integral across the length of the crack $2a$. The relationship shows a clear dependence of fracture growth on net pressure across the crack where a ununiformly pressurized crack is assumed; Eq. (2.4) shows net pressure on right hand side under parenthesis.

2.3.1. Vertical Stress Calculation

For an isotropic medium in tectonically relaxed environment the insitu stress can be calculated as a function of depth using the following relation (Detournay and Cheng 1993) that is a simple

extension of Hooke's stress-strain relationship (Hooke 1678) where the horizontal strains are constrained and only the vertical deformation is permitted, with the introduction of Poisson's ratio (Poisson 1829):

$$\sigma_h = \frac{\nu}{1-\nu}\left(\sigma_v - \alpha P_p\right) + \alpha P_p \quad \text{.....(2.5)}$$

where, α is Biot's poroelastic constant (Biot 1941, 1956), σ_h is the in-situ stress in horizontal direction assuming isotropic stresses, ν is Poisson's ratio, σ_v is overburden stress, and P_p is the pore pressure. In presence of tectonics, (Thiercelin and Plumb 1994) proposed the following relation to determine insitu stress where the strains ε_h & ε_H in the minimum and maximum principal stress directions respectively, are added to the calculation along with plane strain modulus described by $E/(1-\nu^2)$.

$$\sigma_h = \frac{\nu}{1-\nu}\left(\sigma_v - \alpha P_p\right) + \alpha P_p + \epsilon_h \frac{E}{(1-\nu^2)} + \epsilon_H \frac{\nu E}{(1-\nu^2)} \quad \text{.....(2.6)}$$

Formation stresses generated using downhole logs or other data help in defining stress model which can be converted to a layered data model that averages stresses across various lithologies along with creating a description of rock mechanical properties such as elastic modulus, Poisson's ratio, and fracture toughness.

2.3.2. Stress Intensity Factors at Fracture Tips

The mode I stress intensity factor at the two crack tips can be given by following relations (Anderson, 2005) that are nearly similar to Eq. (2.3) above:

$$K_{I(x=2a)} = \frac{1}{\sqrt{\pi a}} \int_0^{2a} p(x) \sqrt{\frac{x}{2a-x}}\, dx \quad \text{.....(2.7)}$$

$$K_{I(x=0)} = \frac{1}{\sqrt{\pi a}} \int_0^{2a} p(x) \sqrt{\frac{2a-x}{x}}\, dx \quad \text{.....(2.8)}$$

The setup described in these equations relates to a crack extending from 0 to $2a$ and acted upon with non-uniform crack-face traction $p(x)$ which acts normally to the plane of crack when the body is still uncracked as shown in **Fig. 2.1** (adapted from Anderson 2005). This scenario represents the variation in insitu stress profile that may be calculated along the wellbore depth using Equations (2.5) or (2.6) above.

A slow advancing or a quasi-static fracture which is nearly in equilibrium with the layers that it has already penetrated will have vertical dimension that can be estimated by simple force balance between the net stresses in the layers of various thicknesses where the fracture resides and the strength of the layers that the fracture has intersected. The term $x/(2a-x)$ or its

reciprocal, in Eq. (2.7) and (2.8) respectively represents the ratio of sectional lengths from one end of the crack to the location of interest along the crack length. The ratio will take the form that is dependent on how integral is set. For example, if the crack tip locations are located at $-a$ and a, the ratio will take the form $(a+x)/(a-x)$ and $(a-x)/(a+x)$ for upper and lower stress intensity factors, respectively.

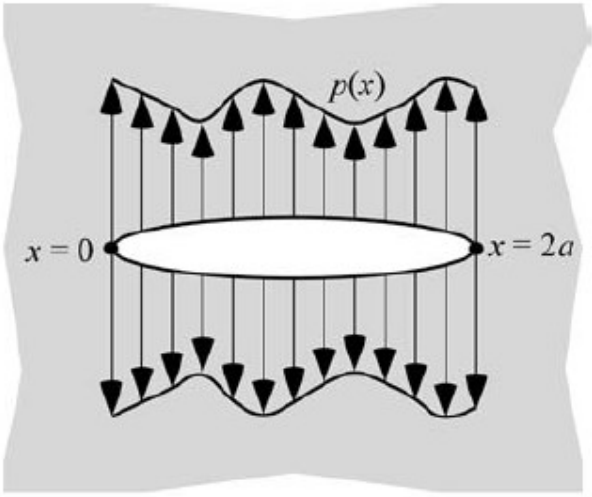

Fig. 2.1: Arbitrary traction on crack surfaces (*Adapted from* Anderson 2005).

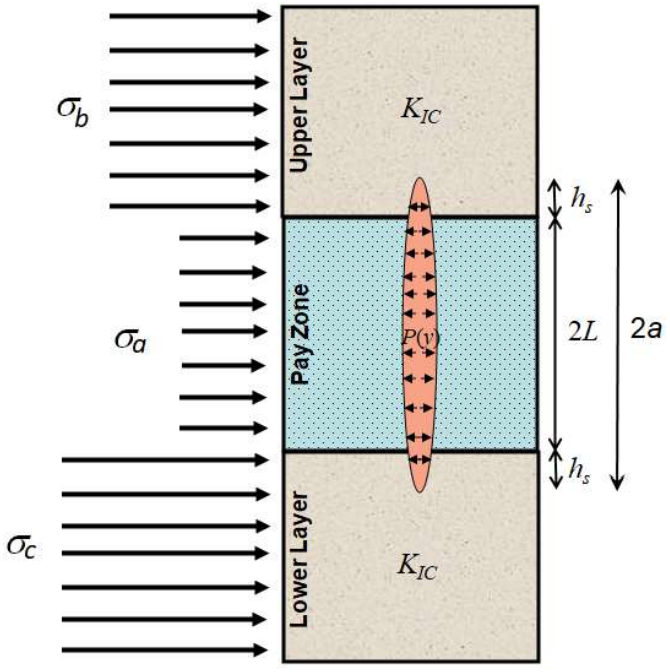

Fig. 2.2: 3-layered stress model showing payzone bound by high-stress members.

2.3.3. Height growth in 3-layered stress model

A three-layered model consisting of payzone or targeted zone in the middle and upper and layers forming stress barriers, is shown in **Fig. 2.2**. The thickness of the middle zone is given by $2L$ and the fracture half-height is depicted as a. The pressurized fracture with pressure distribution $p(y)$ in the vertical direction has penetrated both the barriers by a distance of h_s. The upper and lower layers have a fracture toughness value of K_{Ic} whereas, σ_a, σ_b and σ_c denote the insitu stresses of payzone, upper and lower layers, respectively. For such a configuration, Simonson et al. (1978) utilized the superposition principle to solve for stress intensity factor by following the Rice (1968) and Erdogan (1962) approach. The stress intensity factor at the tip of the crack is given by:

$$K_I = \frac{1}{\sqrt{\pi l}} \int_{-l}^{+l} p(y) \sqrt{\frac{l+y}{l-y}}\, dy \quad \text{.....(2.9)}$$

where $p(y)$ is crack pressure in vertical direction. The solution to the above integral for the case where upper and lower layers have identical strengths is shown as:

$$K_I = (\sigma_b - \sigma_a)\sqrt{\frac{l}{\pi}}\left\{2\sin^{-1}\left(\frac{L}{l}\right)\right\} + (p - \sigma_b)\sqrt{\pi l} \quad \text{.....(2.10)}$$

The excess pressure required to advance the crack length can be determined from Eq, (2.10). For an asymmetric case, the stress intensity factors at the top and bottom tips of the fractures are shown by the following expression.

$$K_I^{m,n} = \frac{\sqrt{\pi l}}{2} p_s \pm \frac{1}{\sqrt{\pi l}}(\sigma_c - \sigma_b)\sqrt{l^2 - L^2} + \sqrt{\frac{l}{\pi}} \sin^{-1}\left(\frac{L}{l}\right)(\sigma_c + \sigma_b - 2\sigma_a) \quad \text{.....(2.11)}$$

where, $p_s = 2p - \sigma_b - \sigma_c$, m and n denote the top and bottom fracture tips, respectively with the corresponding ± sign for mathematical operation.

Fracture half-height and location can now be obtained by adding and subtracting individual equations for top and bottom stress intensity factors and by substituting K_I with known values of fracture toughness (K_{Ic}). The use of K_{Ic} is valid because it is known that the crack advancement takes place only when stress intensity factor reaches the critical value K_{Ic} of the material. It is inherently assumed in this solution method, also known as the equilibrium-height solution, that the contributions of the pressure differences at any one tip position does not influence the stress intensity factor at the other tip. These solutions are shown in Appendix A.

2.3.4. Literature Review: Height Growth in Multilayered Stress Models

2.3.4.1. Method 1

The stress distribution in most formations is too complex to be represented by a simple 3 layered setup and hence recognizing the need, the solution was extended to incorporate multiple layers by using the principle of superposition. Tada et al. in 1973 presented one such model for fracture half-height *a* which is shown below.

$$K_I^{m,n} = \frac{1}{\sqrt{\pi a}} \int_{-a}^{a} \Delta p(x, y_o + y') \sqrt{\frac{2a \pm 2y'}{2a \mp 2y'}} dy' \quad \text{.....(2.12)}$$

Here, *m* and *n* represent top and bottom tips of the fractures respectively, Δp is the pressure distribution at a given cross section held constant at a horizontal distance *x* from fracture, *y'* is vertical distance measured from center of the fracture, and y_o is half the difference in distance that the fracture extends in both directions from the pay zone. For a fracture with slow vertical growth in comparison to horizontal extension, the pressure-drop of the fluid traversing vertically to the fracture-tips can be neglected and thus, Δp assumes the value of net pressure.

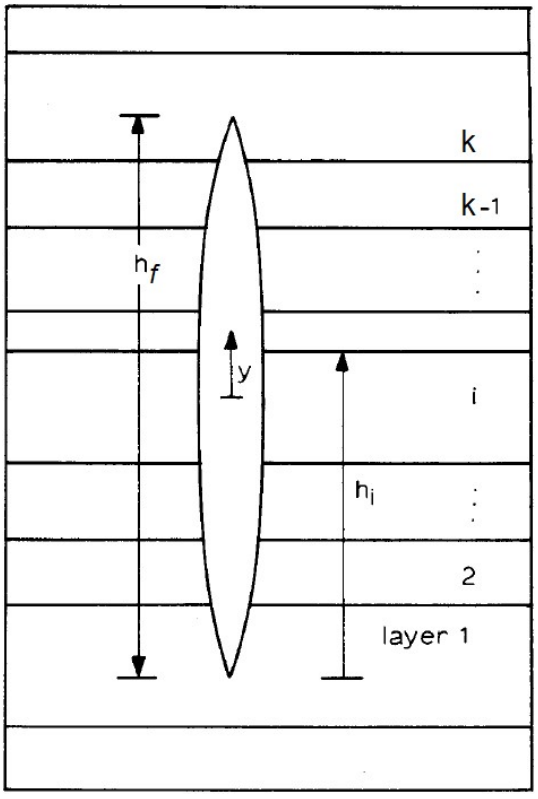

Fig. 2.3: Multilayered Model – Method 2 & 4. (*Adapted from* Fung et al. 1987)

2.3.4.2. Method 2

In 1987, Fung et al. introduced an equilibrium-height model which has been frequently quoted in industry for its application to asymmetric multi-layer cases obtained after solving the following integral:

$$F_{\sigma 1,2} = \sqrt{\frac{2}{\pi h_f}} \int_{-h_f/2}^{h_f/2} [p - \sigma(y)] \sqrt{\frac{1 \mp y}{1 \pm y}}\, dy \quad \text{.....(2.13)}$$

where, $F_{\sigma 1,2}$ represents the stress intensity factor for lower and upper fracture tips respectively, p is the pressure in the fracture, and h_f is the fracture height. $\sigma(y)$ is stress distribution in vertical direction, y. The solution is obtained by integrating over the various layers starting from bottom tip of the fracture to top of the fracture and results in the following form, after applying minor correction from original publication to ensure dimensional accuracy.

$$F_{\sigma c} = \sqrt{\frac{h_f}{2\pi}} \left\{ p_k \pi + \sum_{i=1}^{k} (\sigma_{i+1} - \sigma_i) \times \left[2 \sin^{-1} \sqrt{\frac{h_i}{h_f}} - (-1)^c \sqrt{1 - \left(\frac{2h_i - h_f}{h_f} \right)^2} \right] \right\} \quad \text{.....(2.14)}$$

where c assumes the value of 1 or 2 for lower and upper tips respectively, h_f is total fracture height, and h_i is the elevation from bottom tip of the fracture to the top of the i^{th} stress-layer, counting from bottom upwards as shown in **Fig. 2.3**. The count of k is the upper-most layer bearing a stress of σ_k, where the upper tip of the fracture resides and $p_k = p - \sigma_k$. To solve the integration for each segment of layer thickness while moving up, the location of the top of any given layer i, is denoted as h_i-a where a is the half height $h_f/2$ in Eq. (2.14).

2.3.4.3. Method 3

The solution to finding fracture location for a given height was also proposed by Warpinski and Smith (1989) where the problem was solved for both, the upper and lower half of the fracture with the help of a specific geometry coefficient b_2 by applying the superposition principle on the basic relation presented in Eq. (2.3). The solution resulted in two non-linear equations that can be solved iteratively to obtain fracture location for input height for a given layered stress distribution and fracture toughness scenario, and the corresponding fracture pressures. These are presented below after rectifying a few minor errors in the original format of the equations.

$$\frac{\sqrt{\pi a}(K_{Icn} - K_{Icm})}{2} = \sum_{i=2,2}^{m} S_i \sqrt{a^2 - b_i^2} - \sum_{j=3,2}^{n} S_j \sqrt{a^2 - b_j^2} \quad \text{.....(2.15)}$$

$$\frac{\sqrt{\pi}(K_{Icm} + K_{Icn})}{2\sqrt{a}} = S_o \frac{\pi}{2} + \sum_{i=2,2}^{m} S_i \sin^{-1}\left(\frac{b_i}{a}\right) + \sum_{j=3,2}^{n} S_j \sin^{-1}\left(\frac{b_j}{a}\right) \quad \text{.....(2.16)}$$

Here, K_{Icn} and K_{Icm} denote the fracture toughness of the layers where bottom and top tips of the fracture reside respectively, a is fracture half-height, and b_i and b_j represent geometry coefficients for upper and lower layers from the center of the fracture, respectively. The fracture initiation layer is apportioned into b_2 (upper section) and b_3 (lower section) as shown in **Fig. 2.4** and is useful in obtaining the solution by employing iterative methods such as Newton Raphson that seeks the value of b_2 that will satisfy Eq. (2.15). Also, $S_i = \sigma_i - \sigma_{i-2}$ for $i>2$, $S_j = \sigma_j - \sigma_{j-2}$ for $j>3$, and $i = 2,2$ (or j=3,2) implies that i (or j) is incremented by a value of 2 because the upper half layers are denoted by even numbers and bottom half layers are denoted odd numbers. In Eq. (2.14) , $S_o = p_s - \sigma_{top} - \sigma_{bot}$, p_s is treatment pressure above the closure stress (or net pressure) and σ_{top} and σ_{bot} represents stresses in top and bottom layers where the tip of the fracture resides. Additional details are provided in the original publication (Warpinski and Smith 1989).

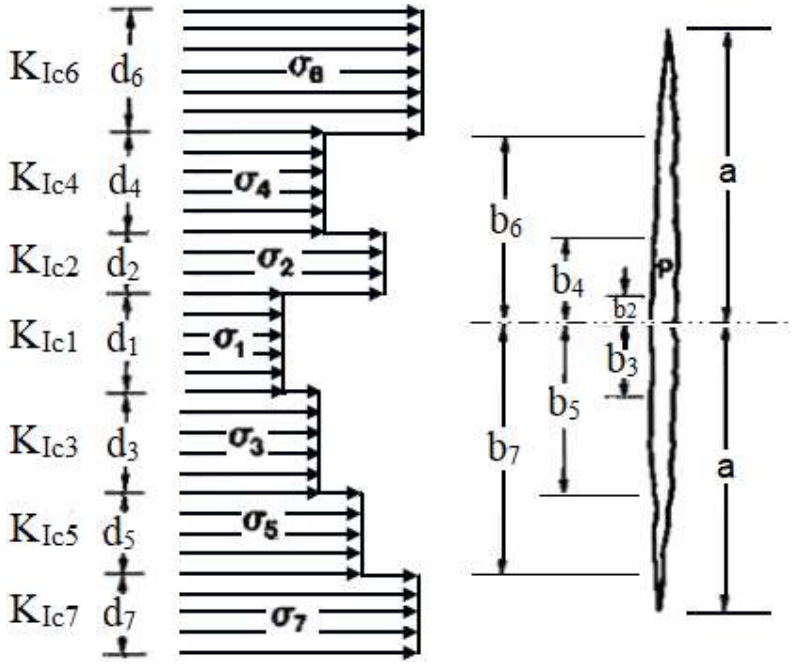

Fig. 2.4: Multilayered Model – Method 2 & 3. (*Adapted from* Warpinski and Smith 1989)

2.3.4.4. Method 4

Another solution to Eq. (2.9) was proposed by Mack et al. in 1992 by following a similar approach as the one adopted by Fung et al. (1987) where the integration was carried out from bottom tip upwards. The effect of gravity was also included in effective pressure calculations. The pressure p of Eq. (2.9) can be expressed as a sum of pressures at the center of the

perforations p_{cp} and the hydrostatic pressure difference between the center of the perforation h_{cp}, and at a given elevation z from bottom tip of the fracture. Thus, Eq (2.17) is then obtained after substituting for p as, $p = p_{cp} + \rho_f g(h_{cp} - z)$ in base Eq. (2.9) along with "a" for fracture half-height and presented as follows:

$$K_I^{bot,top} = \frac{1}{\sqrt{\pi a}} \int_{-a}^{a} \left[p_{cp} + \rho_f g(h_{cp} - z) - \sigma(z)\right] \sqrt{\frac{a \mp z}{a \pm z}}\, dz \quad \text{.....(2.17)}$$

where, $K_I^{bot,top}$ is the stress intensity factor for bottom and top fracture tips and defined in the equation with the help of mathematical operator $\mp$, ρ_f is the fluid density and g is the acceleration due to gravity. To solve for various parts of the integral that cover the fracture from half-height -a to a while intersecting k number of stress layers, z is taken as a-h_i to reach the final expression. The solution of Eq. (2.17) is presented below and resembles the solutions obtained by Fung et al. (1987).

$$K_I^{bot,top} = \sqrt{\frac{\pi h}{2}} \left[p_{cp} - \sigma_k + \rho_f g \left\{h_{cp} - \frac{\delta h}{4}\right\}\right] + \sqrt{\frac{2}{\pi h}} \sum_{i=1}^{k-1} (\sigma_{i+1} - \sigma_i) \left[\frac{h}{2} \cos^{-1}\left(\frac{h-2h_i}{h}\right) \pm \sqrt{h_i(h-h_i)}\right] \quad \text{.....(2.18)}$$

In this equation, δ is 1 for bottom layers and 3 for top layers. The derivation of Eq. (2.18) is shown in Appendix B.

The pressure term can be eliminated if the equations are arranged to find the difference of stress intensity factors. This will result in the following non-linear expression that can be solved using iterative methods to determine fracture location if the fracture height (or half-height) is assumed:

$$K_I^{bot} - K_I^{top} = \sqrt{\frac{2}{\pi h}} \left\{\sum_{i=1}^{k-1} (\sigma_{i+1} - \sigma_i) \left[\frac{h}{2} \cos^{-1}\left(\frac{h-2h_i}{h}\right) + \sqrt{h_i(h-h_i)}\right] - \sum_{i=1}^{k-1} (\sigma_{i+1} - \sigma_i) \left[\frac{h}{2} \cos^{-1}\left(\frac{h-2h_i}{h}\right) - \sqrt{h_i(h-h_i)}\right]\right\} + \sqrt{\frac{\pi h}{2}} \rho_f g \frac{h}{2} \quad \text{.....(2.19)}$$

Fracture pressure can now be determined explicitly after adding both the stress intensity factors and solving for fracture pressure at the center of perforations p_{cp} and including the contribution from hydrostatic pressure as shown by the following equation.

$$p_{cp} = \sigma_k - \rho_f g\left(h_{cp} - \frac{h}{2}\right) + \sqrt{\frac{2}{\pi h}}\frac{K_I^{bot} + K_I^{top}}{2} - \frac{1}{\pi h}\left\{\sum_{i=1}^{k-1}(\sigma_{i+1} - \sigma_i)\left[\frac{h}{2}\cos^{-1}\left(\frac{h-2h_i}{h}\right) + \sqrt{h_i(h-h_i)}\right] + \sum_{i=1}^{k-1}(\sigma_{i+1} - \sigma_i)\left[\frac{h}{2}\cos^{-1}\left(\frac{h-2h_i}{h}\right) - \sqrt{h_i(h-h_i)}\right]\right\} \quad \text{.....(2.20)}$$

With all the inputs now available, the fracture width in the vertical direction $w(y)$ in each layer can be estimated by the following relation:

$$w(y) = \frac{4}{E'}\left\{p_{cp} + \rho_f g\left(h_{cp} - y\right) - \sigma_k\right\}\sqrt{y(h-y)} + \frac{4}{\pi E'}\sum_{i=1}^{k-1}(\sigma_{i+1} - \sigma_i)\left[(h_i - y)\cosh^{-1}\left(\frac{y}{|y-h_i|}\frac{h-2h_i}{h} + \frac{h_i}{|y-h_i|}\right) + \sqrt{y(h-y)}\cos^{-1}\left(\frac{h-2h_i}{h}\right)\right] \quad \text{.(2.21)}$$

where y is the elevation measured from perforation depth and, E' is the plane strain modulus. The calculations in the model proposed by Mack et al. (1992) are based on elevations measured from the bottom tip of the fracture, and hence, it is not necessary to continuously identify the layer where the center of the fracture resides which makes the solution process simple.

Modifications to the height growth model have been proposed in several recent studies including those by Weng et al. (2011), Cohen et al. (2015), Liu and Valkó (2018) and Xu et al. (2019) addressing the fracture vertical growth computation. The effects of layered stress contrast, elastic modulus contrast and, sliding and slipping interfaces on fracture height containment have been discussed in these papers at length and a few modeling-based solutions are offered to assist in better prediction. Equilibrium-height models assume uniform pressure distribution in the fracture and do not account for possible variations in the predicted outcomes due to non-uniform pressures. The fluid-flow induced pressure distribution in the fracture was incorporated in the modeling process for the case where the base model was not able to match the predicted outcome with field-measured fracture height.

2.4. Nomenclature

a = radius of crack, crack half-length, fracture half-height, $M^0L^1t^0$, ft (m)

b_2 = specific geometry factor, $M^0L^1t^0$, ft (m)

b_i, b_j = geometry coefficients, upper and lower layers from mid-frac depth, $M^1L^1t^0$, ft (m)

c = number, Eq. (2.14)

E = Young's modulus, $M^1L^{-1}t^{-2}$, psi (Pa)

E' = plane strain modulus, $M^1L^{-1}t^{-2}$, psi (Pa)

$F_{\sigma 1,2}$ = stress intensity factors for bottom and top layers, $M^1L^{-0.5}t^{-2}$, psi-in.$^{0.5}$ (Pa.m$^{0.5}$)

$F_{\sigma c}$ = stress intensity factors - bottom & top layers, $M^1L^{-0.5}t^{-2}$, psi-in.$^{0.5}$ (Pa.m$^{0.5}$)

g = acceleration due to gravity, $M^0L^1t^{-2}$, ft/s^2 (m/s^2)

G_f = fracture specific surface energy, $M^1L^0t^{-2}$, J/m^2

h = fracture height, $M^1L^1t^0$, ft (m)

h_{cp} = elevation from the bottom tip of the fracture to center of perforations, $M^1L^1t^0$, ft (m)

h_f = fracture height, $M^1L^1t^0$, ft (m)

h_i = elevation of i^{th} layer top from bottom tip of the fracture, $M^1L^1t^0$, ft (m)

h_s = fracture penetration in surrounding layers (Fig. 2.2) $M^1L^1t^0$, ft (m)

$i,j,$ = count, unitless

k = number of layers, number

K_I = stress intensity factor, $M^1L^{-0.5}t^{-2}$, psi-in.$^{0.5}$ (Pa.m$^{0.5}$)

K_{Icn} = stress intensity factor – bottom tip of fracture, $M^1L^{-0.5}t^{-2}$, psi-in.$^{0.5}$ (Pa.m$^{0.5}$)

K_{Icm} = stress intensity factor – top tip of fracture, $M^1L^{-0.5}t^{-2}$, psi-in.$^{0.5}$ (Pa.m$^{0.5}$)

$K_I^{top,bot}$ = stress intensity factor for top and bottom layers, $M^1L^{-0.5}t^{-2}$, psi-in.$^{0.5}$ (Pa.m$^{0.5}$)

K_{Ic} = critical stress intensity factor, $M^1L^{-0.5}t^{-2}$, psi-in.$^{0.5}$ (Pa.m$^{0.5}$)

l = fracture half-height, $M^0L^1t^0$, ft (m)

L = half of payzone thickness, $M^0L^1t^0$, ft (m)

m = top tip of the fracture, unitless

n = bottom tip of the fracture, unitless

p = pressure in the fracture, $M^1L^{-1}t^{-2}$, psi (Pa)

p_{cp} = pressure at the center of the perforations, $M^1L^{-1}t^{-2}$, psi (Pa)

p_s = stress/pressure difference, $M^1L^{-1}t^{-2}$, psi (Pa)

$p(x)$ = crack face traction (Fig.2.1), $M^1L^{-1}t^{-2}$, psi (Pa)

$p(y)$ = pressure in the crack in vertical direction, $M^1L^{-1}t^{-2}$, psi (Pa)

$p(\xi)$ = pressure in the crack in vertical direction, $M^1L^{-1}t^{-2}$, psi (Pa)

P_f = fracture pressure, $M^1L^{-1}t^{-2}$, psi (Pa)

P_p = pore pressure, $M^1L^{-1}t^{-2}$, psi (Pa)

Si, Sj, S_o = various stresses, Eq. (2.16) and Eq. (14), $M^1L^{-1}t^{-2}$, psi (Pa)

$w(y)$ = width in vertical direction y, $M^0L^1t^0$, in. (mm)

x = any distance value in horizontal x-axis, $M^0L^1t^0$, ft (m)

y = elevation in vertical distance, $M^0L^1t^0$, in. (m)

y' = vertical distance measured from center of the fracture, $M^0L^1t^0$, in. (m)

y_o = half-difference in distance of fracture extension from fracture ends, $M^0L^1t^0$, in. (m)

z = elevation in vertical distance from bottom tip/center of the fracture, $M^0L^1t^0$, in. (m)

α = Biot's constant, dimensionless

δ = coefficient, unitless

Δp = pressure distribution in Eq. (2.12), $M^1L^{-1}t^{-2}$, psi (Pa)

ϵ_h = strain in minimum principal horizontal stress direction, dimensionless

ϵ_H = strain in maximum principal horizontal stress direction, dimensionless

ν = Poisson's ratio, unitless

μ = fluid viscosity, $M^1L^{-1}t^{-1}$, cP (Pa.s)

ρ, ρ_f = fluid density, $M^1L^{-3}t^0$, lbm/gal (kg/m^3)

σ = stress in crack or fracture, $M^1L^{-1}t^{-2}$, psi (Pa)

σ_h = maximum principal stress in horizontal direction, $M^1L^{-1}t^{-2}$, psi (Pa)

σ_i, σ_j = stress in i^{th} and j^{th} layers, $M^1L^{-1}t^{-2}$, psi (Pa)

σ_k = stress in the n^{th} or uppermost layer, $M^1L^{-1}t^{-2}$, psi (Pa)

σ_v = vertical principal stress, $M^1L^{-1}t^{-2}$, psi (Pa)

σ_a = stress in payzone (Fig. 2.2), $M^1L^{-1}t^{-2}$, psi (Pa)

σ_b = stress in barriers or stress in upper barrier alone (Fig. 2.2), $M^1L^{-1}t^{-2}$, psi (Pa)

σ_{bot} = stress in the bottom layer where fracture bottom tip resides, $M^1L^{-1}t^{-2}$, psi (Pa)

σ_c = stress in lower barrier (Fig. 2.2), $M^1L^{-1}t^{-2}$, psi (Pa)

σ_{top} = stress in the top layer where fracture bottom tip resides, $M^1L^{-1}t^{-2}$, psi (Pa)

$\sigma(y)$ = stresses distribution in vertical y-direction, $M^1L^{-1}t^{-2}$, psi (Pa)

σ_3 = minimum insitu principal stress in horizonal direction, $M^1L^{-1}t^{-2}$, psi (Pa)

ξ = distance along the crack, $M^0L^1t^0$, ft (m)

CHAPTER 3

Modeling Fracture Growth in Multi-Layer Setup

3.1. Modeling Approach

The various methods discussed in Chapter 2 allow for estimation of fracture growth in layered formations. One of the primary assumptions is the slow advancement of the fracture to allow the fracture tips to equilibrate to the stress environment that surrounds the fracture but pressures at one tip not to influence the other tip. Furthermore, this solution is primarily a "solid mechanics" solution because it does not account for the fluid flow induced pressure drop inside the fracture by assuming a uniform pressure distribution. The modeling approach adopted in this research study is summarized in the following steps:

1. Develop the basic solid mechanics solutions method:
    a. to handle up to 100 layers of stress and mechanical property data,
    b. to solve using both fixed and floating fracture location.
2. Calibrate the model output with the data available in the literature.
3. Predict fracture height growth for various cases and compare with field measurements.
4. Incorporate the effects of fluid flow inside the fracture using superposition principle.
5. Extend the model to allow pressure history matching of treatment injection data and forecast fracture height growth pattern during the treatment.
6. Extend model to account for other non-ideal behavior such as abrupt height growth truncation and others.

The steps are discussed in detail in the following text and in various chapters that follow.

3.2. Developing Preliminary Height Growth Model

During the initial phase of research, the solutions provided in Equations (2.14), (2.15), (2.16) and (2.19) were programmed separately as calculation "modes" and individually applied to reach the solution to a 7-layered stress model shared by Warpinski and Smith (1989). The simulator engine was ultimately reprogrammed to adopt a solution approach that introduced speed and accuracy to the process.

The model was programmed in Microsoft Excel^{TM} VBA using array, strings, and variant tables to allow speedy calculations for up to 100 layers of input data consisting of layer depths, thicknesses, stresses, fracture toughness, Poisson's ratio, modulus, and fluid leakoff. The

program is written in a manner that number of layers is not a limitation. The calculations can be carried out using any of the following routines:

a. increment the fracture bottom tip location to determine corresponding fracture height,
b. input a known fracture height and find fracture location (fracture location not fixed),
c. accept or ignore "alternate" solutions where taller fractures could be obtained even with lower net pressures, and
d. assume a given net pressure and run a nested loop to obtain fracture location and height using either modes (a) or (b). This is a more rigorous case but is useful when fluid flow related modifications to the calculations must be carried out.

The solution to the non-linear equations described in Equations (2.14), (2.15), (2.16) and (2.19) were obtained by determining the roots of the equation by employing iterative solutions such as bisection method which is guaranteed to find a root if it exits and Newton-Raphson method which is several folds faster than bisection method. A combination of these methods was also used wherever applicable.

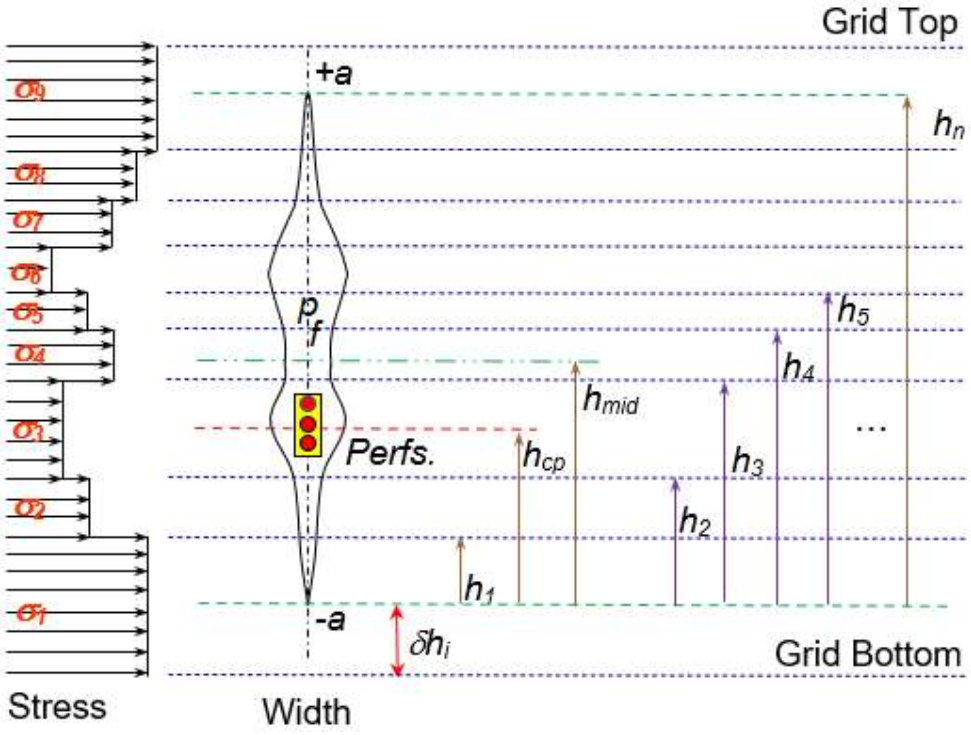

Fig. 3.1: Superposition solution for height growth problem in multiple layers.

To speed up the calculations it is necessary to (a) make a good initial guess and, (b) define boundary conditions to prevent endless iterative loops. To enable this, the calculation is initiated by first assuming a fracture height h_f, greater than the perforated interval, and assign

a lower and upper bound to the distance by which its center can move with respect to the layer from which the fracture initiates. The fracture is then "moved" across the layers with stress and fracture toughness inputs until Equations (2.14) or (2.19) are satisfied or until the solver reaches a certain pre-decided number of iterations. The calculation is then moved to the next incremented fracture height. The tip location h_i shown in **Fig. 3.1** is thus dynamic and its value is obtained by solving for δh_i which is the depth difference between the grid bottom and bottom tip of the fracture. This special feature introduced in the modeling phase enables close guess of the root and helps in quicker convergence. One may note that the middle of the fracture denoted by h_{mid} is different than the middle of perforation distance h_{cp}, measured from bottom tip of the fracture. The pressure values are obtained from Eq. (2.20). The height increments are decided at the start of the program and are generally set to 0.5 to 1 ft (0.15 to 0.31 m); there is no limit to the increment value so long as it is greater than zero. On average, for a 100-layer input model, the simulation for 200 values of height can be carried out in less than a minute.

The routines discussed above describe the assumptions and processes to calculate fracture vertical growth in formations with variable rock properties along the depth. With addition of lithological layer data in the model, the calculation complexity increases, but the relative ease with which additional constraints can be introduced to the solution scheme makes the semi-analytical fracture height growth model an attractive choice. The model presented in this study follows a similar methodology and introduces constraints based on field measurements of fracture height. The codes used for programming the subroutine are show in Appendix D.

3.3. Benchmarking Model Outputs with Literature Data

The base benchmarking model selected in the study was from the one presented by Warpinski and Smith (1989). The model comprises of 7 layers of non-uniform stresses but the facture toughness of all the layers was set to 1,000 psi.in0.5 (3,806.5 kPa.m$^{0.5}$). The stress data are presented in Fig. 3.2. The fracture initiation layer is in the middle and the distance of zero on the left vertical axis denotes the perforation depth. The middle layer is 50 ft (15.24 m) thick, the bottom most layer is 75 ft (22.9 m) thick, whereas the remainder of the layers are 25 ft (7.62 m) thick. The plot shows treating or net pressures in the x-axis. With the increase in net pressure, not only the fracture height appears to increase but its location also changes. The stress member with 1,500 psi (10.34 MPa) just above the pay zone acts a strong barrier initially and prevents upward growth of the fracture thus driving it down. However, as the net pressures exceed 200 psi (1.38 MPa), barrier strength is overcome, and fracture shows an upward growth

as well. The center of the fracture stays within the payzone but moves about indicating that hydraulic fracture may not be always centered around the perforation.

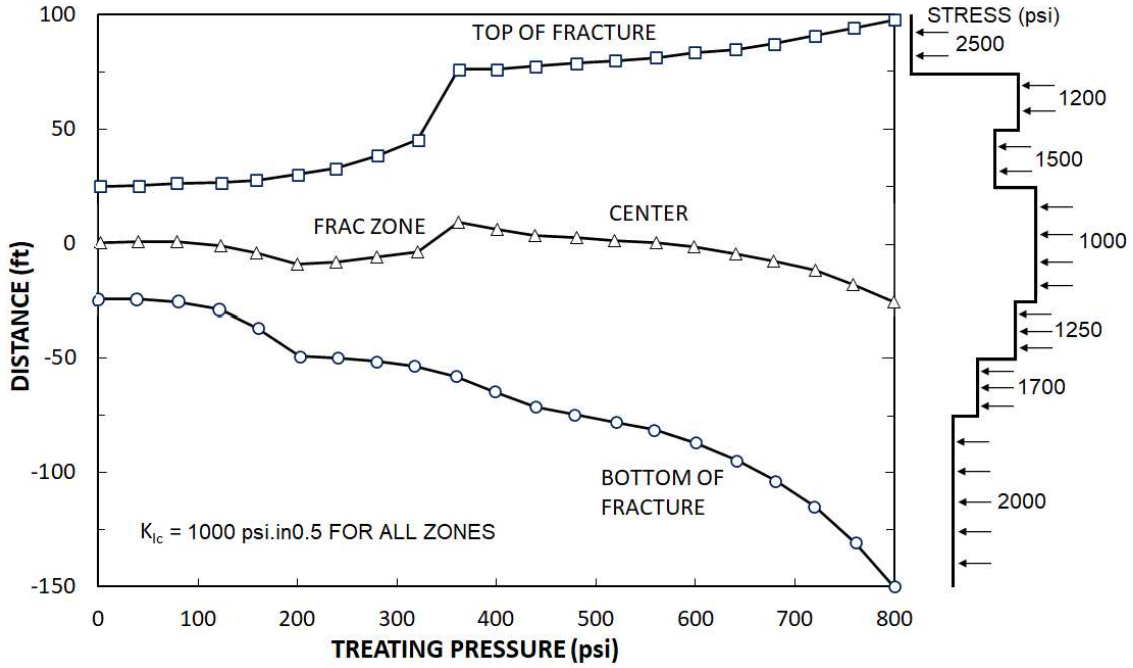

Fig. 3.2: Multilayered height growth model example (Warpinski and Smith 1989).

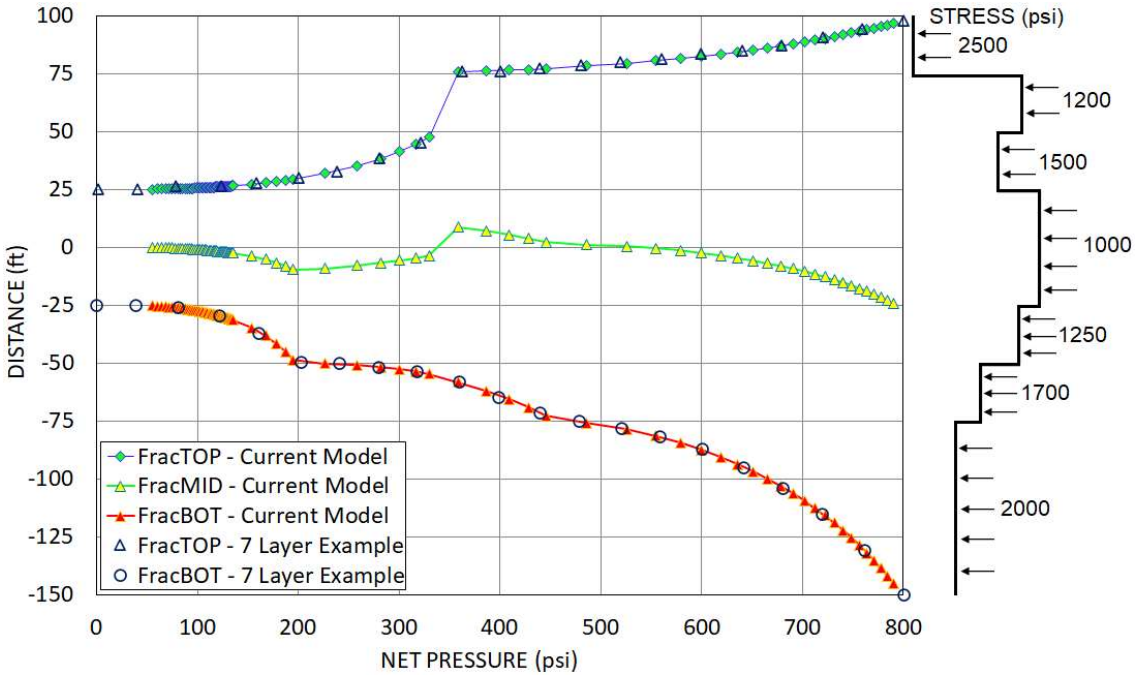

Fig. 3.3: Data points reproduced by current model in the model calibration process.

The location of the top and bottom of the fracture tips can be read from the left y-axis representing the distance of the point from the fracture initiation point denoted by zero. This

distance versus net pressure mapping is extremely beneficial in forecasting fracture pressures and is also useful in carrying out pressure history match of treatment data as will be seen in later in Chapter 5.

The results reproduced by the current height growth simulation model is shown in **Fig. 3.3**. In this case the mode "b" setup of simulation, mentioned in section 3.2 above, where the fracture tip location is not fixed but is determined for an input fracture height, was employed. As can be seen from the closeness of output data points represented as "FracTOP" and "FracBOT" in the plot, the height increments used were very small.

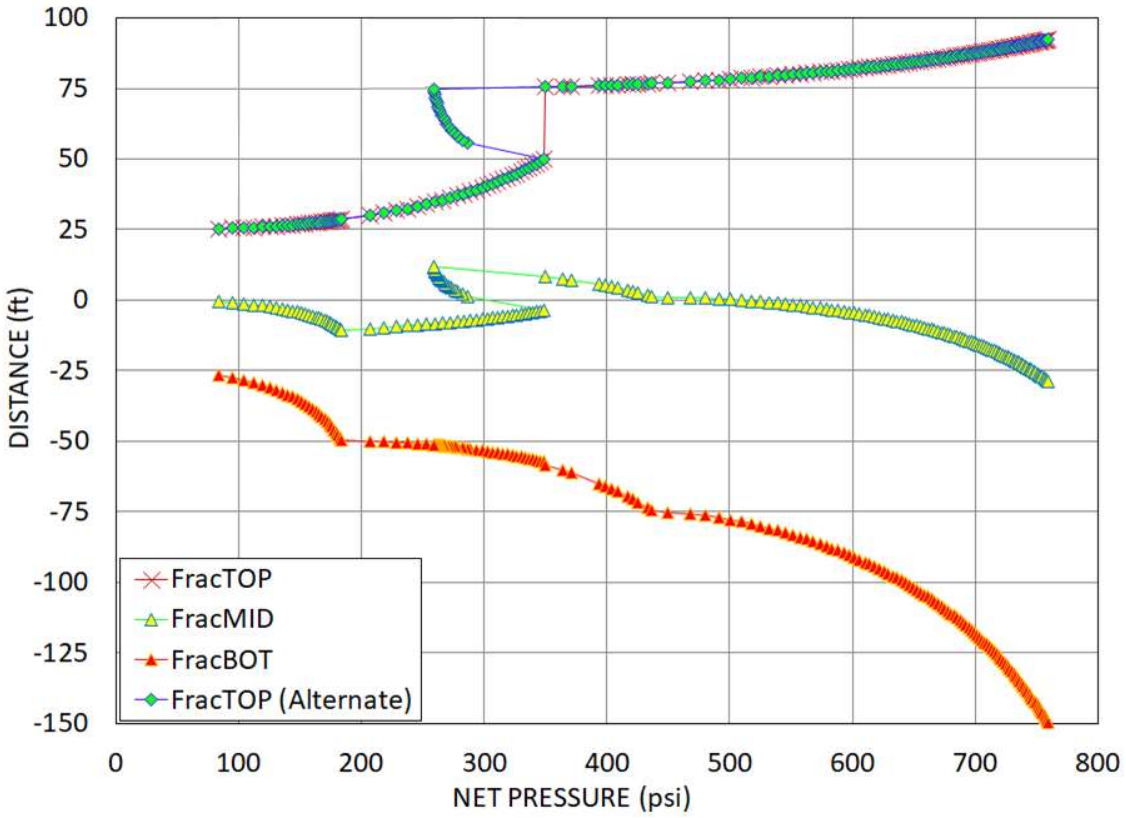

Fig. 3.4: Alternate solution for fracture top location once the height reaches 50 ft.

An alternate solution quoted under item "c" of modeling steps above (section 3.2) is shown in **Fig. 3.4**. This scenario is possible once the fracture top fracture grows past 50 ft (15.2 m) and crosses the stress barrier of 1,500 psi (10.3 MPa) just above the pay zone. From this point onwards, for a brief period, further height growth is possible even with lower net pressures because the stress layer where the upper tip of the fracture resides σ_k, in Eq. (2.20) used in obtaining fracture pressure, reduces from 1,500 psi (10.34 MPa) to 1,200 psi (8.30 MPa) as shown in Fig. 3.4. With the remainder of the component on right of σ_k either remaining constant or increasing with increasing height, the overall effect is a reduced value of p_{cp}. The effect

shown in Fig. 3.4 by the "FracToP (Alternate)" curve, is thus a real-world possibility and not just a mathematical artifact. However, keeping the fracture open at the injection-point is necessary to continue the fracturing operations, which could be challenging because of loss of net pressure (and subsequent loss of fracture width) as the fracture migrates to lower stressed zones. Note that eventually with increase in net pressure and fracture vertical growth, the solutions from both the methods merge. The mode of alternate solution was adopted in majority of the case histories studied because it supports the general notion and fact that it is relatively easy to propagate larger fractures (Daneshy 1978) which would be the case here with increasing fracture heights and half-lengths.

Using this procedure, both solutions shown for the example above can be obtained. The net pressures differ slightly because of inclusion of hydrostatic effects in this solution method, but the overall values are comparable. The programming codes for height growth prediction simulator developed in Excel VBA.

3.4. Model Application: Horizontal Well Landing

This example case pertains to the hypothetical case of landing a horizontal well in a laminated formation as a close analog to the scenario mentioned in section 1.2.2. The formation is characterized by non-uniform stress distribution which are obtained from downhole logs. The 7-layer model is now extended to a 100-layer of data input model with thickness varying form stress and mechanical property model. The average values of inputs for the real-world case study are shown in table below.

Number of layers in the stress model	100
Payzone Stress	5,050 psi (34.82 MPa)
Average Stress	5,475 psi (37.75 MPa)
Fracture initiation layer thickness	2.3 ft (0.70 m)
Average layer thickness	2.7 ft (0.83 m)
Average Young's Modulus	2.33×10^6 psi (16.1 GPa)
Average Poisson's Ratio	0.23
Average Fracture Toughness	3,064 psi.in$^{0.5}$ (3,367.0 kPa/min$^{0.5}$)
Payzone True Vertical Depths (TVD)	8,240 to 8,380 ft (140 ft thick)

TABLE 3.1: Formation properties used as input in the horizontal well landing example.

The simulation was carried out for fracture heights ranging from 5 ft to 220 ft (1.52 to 67.1 m) in 1 ft (0.31 m) intervals. Solutions were obtained for 178 values of height inputs with the maximum height for which a solution could be obtained being the one where both the fracture tips stayed within the top and bottom grid of the layered model defined (see Fig. 3.1). In most cases, a higher fracture height was associated with increased net pressure, but with alternate solutions being part of the solving process, it was observed that in early time when fracture height was still evolving, even a lower net pressure could result in taller fractures. However, with the increase in fracture height, this effect diminishes, and fracture growth occurs proportionately with net pressure increase. These effects are seen in distance versus net pressure plot of **Fig. 3.5** where the horizontal wellbore was landed just above the high stress middle layer member at 8,320 ft shown in the right plot.

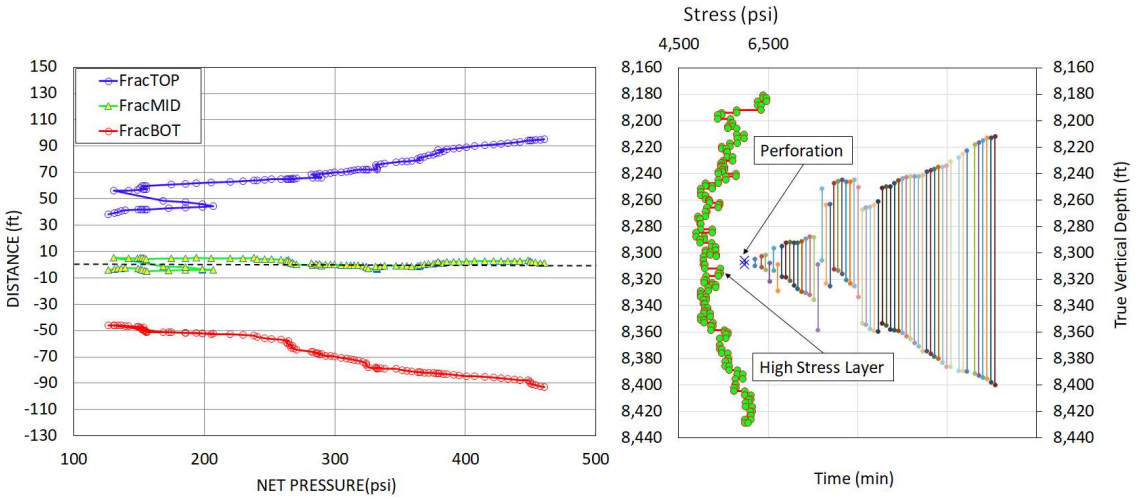

Fig. 3.5: Fracture location plot for horizontal well landed above middle stress layer.

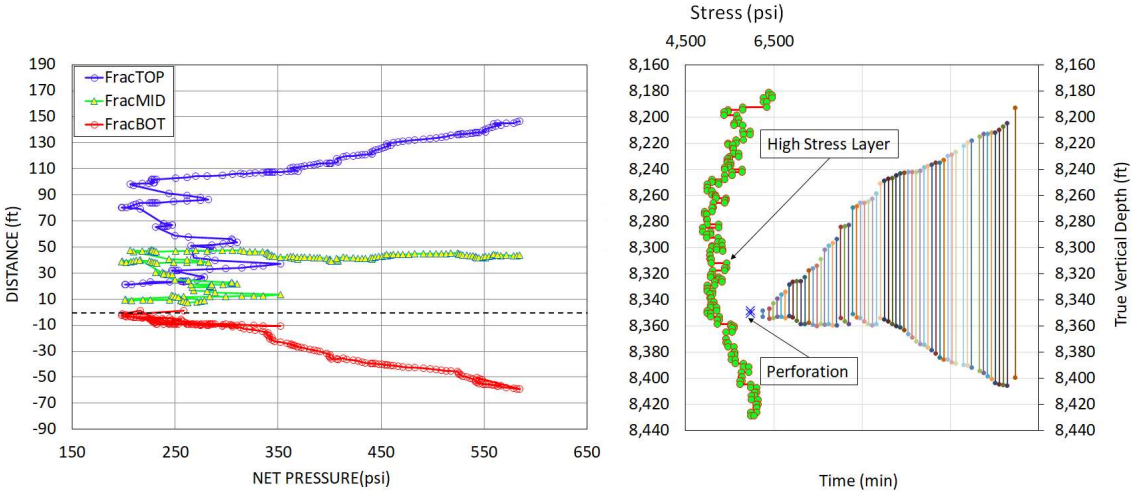

Fig. 3.6: Fracture location plot for horizontal well landed below the middle stress layer.

The input fracture heights for which the results could be obtained are shown as vertical bars on the right plot, with each bar representing a fracture height. The depths in this plot are aligned with the distances in the left plot with the perforations (or depth of the lateral) corresponding to the 0 distance (denoted by dashed line). For sake of clarity early time data is not shown in left plot as it reflects several alternate solutions. In this setup, the fractures will tend to grow upwards first and unless high net pressures are generated, will not grow down to adequately cover lower pay.

The scenario shown in **Fig. 3.6** represents the case where the lateral section of the horizontal well was drilled in lower section below the high stress member which was also the more productive region of the pay. Also, for oil well, with assistance from gravity, better drainage could be expected. From hydraulic fracturing viewpoint, this case is more favorable because the fracture tends to cover the lower section of the pay even with lower net pressures. Even if the net pressures were to increase during the treatment, they will assist in covering the entire pay vertically and hence will be most beneficial from production standpoint.

The model outputs for this case study clearly illustrates that the fracture height growth potential and net pressure requirements will vary with the location of fracture initiation point specially for cases where there are significant changes in the stress profiles and mechanical property values. The model derived height growth mapping for given net pressure is thus a helpful tool in planning the placement of perforations or in case of horizontal wells, its positioning in the payzone to derive maximum benefit from fracture stimulation.

CHAPTER 4

Height Growth Model Applied to Field Cases

4.1. Fracture Growth Measurements in Field – Vertical Wells

The vertical growth of a hydraulic fracture during a treatment is often measured with the help of techniques such as tracing the treatment with radioactive (RA) material where specific small half-life isotopes of Antimony, Scandium and Iridium are introduced in the fracturing fluid during the treatment. After the treatment is pumped and wellbore is cleaned up, a gamma ray tool is run in the well to identify the presence of RA tracers which provides an estimate of fracture height in vertical wells as shown in Fig. 1.5 (left figure). For multi-stage treatments in vertical wells, it is customary to alternate between these isotopes to help in identifying fracture growth in individual stages, whereas for single stage treatments or when there is sufficient distance separating subsequent stages in a multi-stage treatment, the three isotopes maybe injected in the pad, and various proppant stages.

Microseismic (MS) measurements are yet another method to estimate fracture dimensions and offers an insight into fracture height growth, both in vertical and horizontal wellbores. Other less common methods to estimate fracture height growth especially in vertical wells are use of temperature logging and post-treatment sonic logs to survey changes in compressional and shear wave transit times to determine fracture height.

4.2. Case Study Selection and Modeling Steps

The objective of the case study was to compare the model outputs with the observed data and examine the accuracy of predictions. For this purpose, examples from various hydraulic fracturing case studies were selected as test cases. The examples were selected from past studies (Pandey and Agreda 2014, Kirk-Burnnand et al. 2015, Pandey and Flottmann 2015) and presented in detail in Pandey and Rasouli (2021a, 2021c). The cases discussed were found suitable because of the relatively lower treatment injection rates that satisfies the condition of gradual fracture advancement, and the low-permeability environment which helps in limiting the leak-off velocity. The common features amongst these cases are listed below:

i. vertical well treatments where multiple zones that were treated,
ii. availability of dipole sonic log data which enabled generating vertical stress profile,
iii. RA tagged treatments for fracture height measurement,
iv. availability of bottomhole pressure (BHP) data in most cases,

v. fracture initiation from single cluster, (pinpoint injection) and,
vi. low rate and low viscosity treatments to contain the fracture height growth by minimizing the net pressure (NP).

The following list highlights the various steps adopted during fracture height growth modeling and analysis:

1. Prepare a preliminary stress and mechanical properties model using downhole log data.
2. Calibrate the layered stress model by history matching the treatment.
3. Using the model, generate distance versus NP map for the calibrated stress model.
4. Based on the mapping, obtain the fracture height for the observed net pressure.
5. Compare the fracture height with field traced fracture height from RA tracer survey.

4.3. Case Studies

4.3.1. Vertical Well: Shallow Sandstone – Case 1

This example is taken from the data published by Pandey and Agreda (2014) that summarizes the successes of low rate and low viscosity fracture stimulations executed on several shallow wells completed in the San Miguel formation in the Sacatosa field in south Texas with an objective to minimizing the horizontal or "pancake" fractures by controlling the net pressures. The low injection rate design and execution assisted in limiting the net pressures which resulted in gradual fracture advancement, making these wells ideal candidates for the current study.

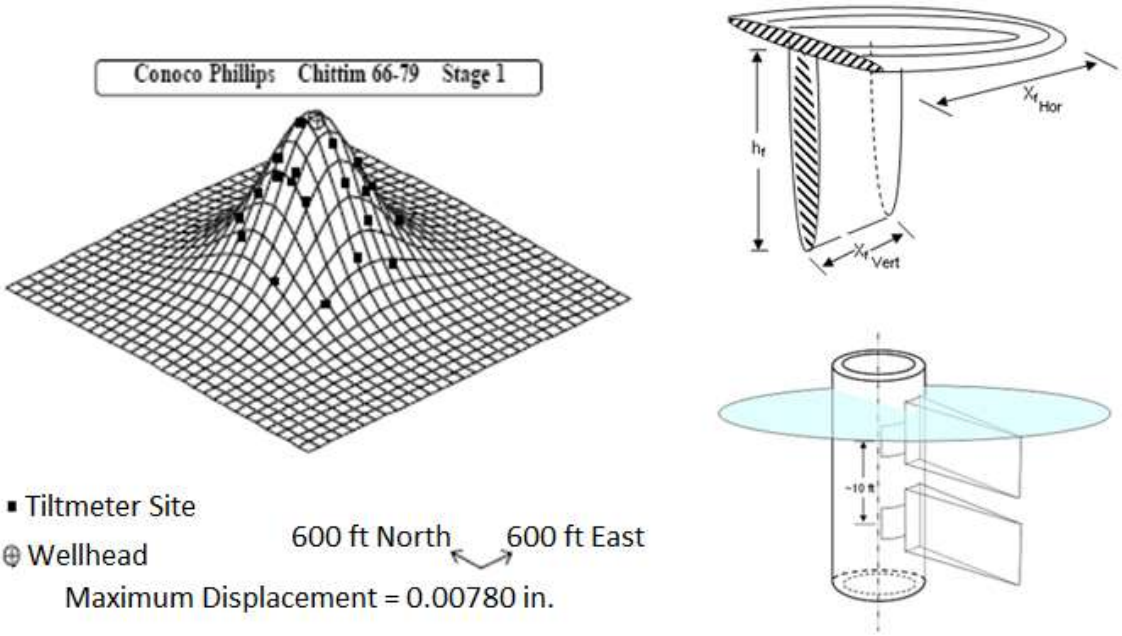

Fig. 4.1: Horizontal fracture component from tiltmeter. Conceptual sketch on right.

The typical fracture gradient of pay sands range from 0.85 to 0.92 psi/ft (19.23 to 20.8 kPa/m) for average depths of 1,600 ft (487.7 m) and hence if the net pressure in the fracture were to exceed 220 psi (1.52 MPa), fracture rotation in horizontal plane is possible because effective injection pressures can overcome the overburden. This was also evinced by tiltmeter survey carried in the field as shown in **Fig. 4.1** (Pandey and Agreda 2014). The model description and other layer properties are listed in Table 4.2 below.

Number of layers in the stress model	67
Payzone Stress	1,467.0 psi (10.11 MPa)
Average Stress	1,626.7 psi (11.56 MPa)
Fracture initiation layer thickness	3.1 ft (0.95 m)
Average layer thickness	2.4 ft (0.73 m)
Average Young's Modulus	1.33×10^6 psi (9.2 GPa)
Average Poisson's Ratio	0.28
Average Fracture Toughness	1,288 psi.in$^{0.5}$ (4,902.8 kPa.m$^{0.5}$)
Payzone True Vertical Depths (TVD)	1,593 to 1,609 ft (16 ft thick)

TABLE 4.1: Formation properties used as input in Case 1.

The main treatment comprising of low concentration cross-linked gel of 12.0 lbm/Mgal (1.44 kg/m^3) loading, was pumped down the 4 ½ in. casing × 1 ¾ Coiled Tubing (CT) annulus, at a maximum of 8.0 bbl/min (0.021 m^3/s), after the CT was used to jet-cut holes in the casing. The jetting ports of CT allowed for constant monitoring of the bottomhole treating pressures (BHP). The injection test analysis indicated a high fluid efficiency of 60% for a closure pressure of 1,500 psi (10.3 MPa) resulting in a fracture gradient of 0.935 psi/ft (21.2 kPa/m).

The treatment plot of **Fig. 4.2** shows measured and matched bottomhole pressure (BHPInj) and BHP_Match respectively. The formation face pressure (FFP) and net pressure (NP) shown in Fig. 4.2 were generated from the treatment data using technique discussed in Pandey et al. (2020) and calculated bottomhole injection pressure was history matched to calibrate the stress model. The net pressure gradually increases to 200 psi (1.38 MPa) at the end of the pad indicating the much-desired extension and preventing fracture from rotating to horizontal plane. However, the increase of injection rate to 8.0 bbl/min with onset of proppant in the formation and subsequent increase of net pressure more than 220 psi could lead to this condition. This is also supported by the "flat" net pressure response seen from 25 to 27 minutes if injection history. Due to the apparent pad dehydration owing to possible presence of horizontal component (Daneshy 2003), the tip screen out (TSO) set in, and the treatment was

terminated early. The equilibrium height model will not apply under these circumstances for late time data. It is generally assumed that with the occurrence of TSO the fracture dimensions including height may not change much unless the barriers are extremely weak and rock has moderate strength (Smith 1985, Smith et al. 1987, Smith et al. 1996).

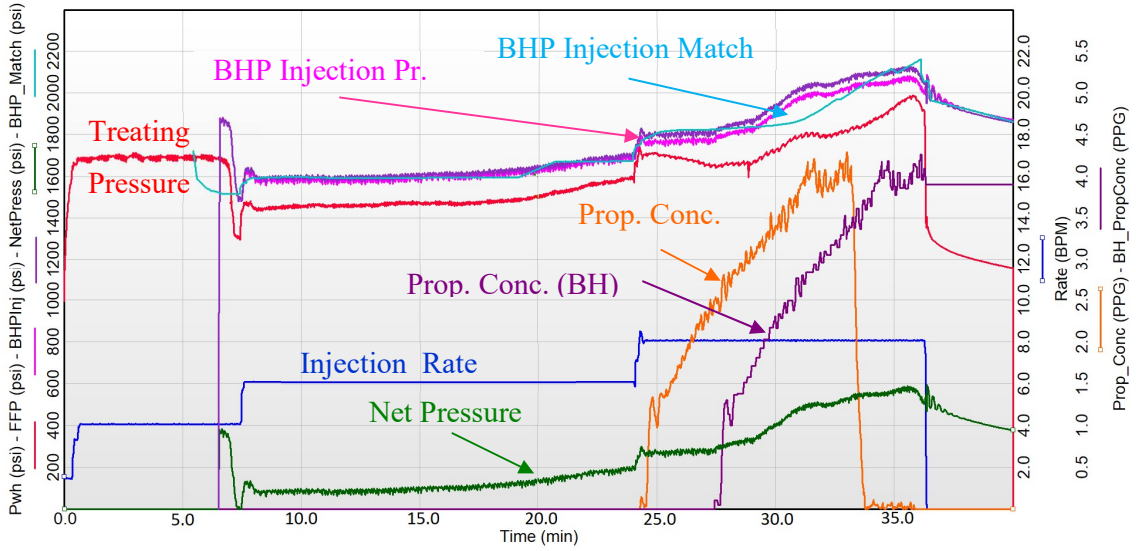

Fig. 4.2: Fracture stimulation treatment plot for Case 1.

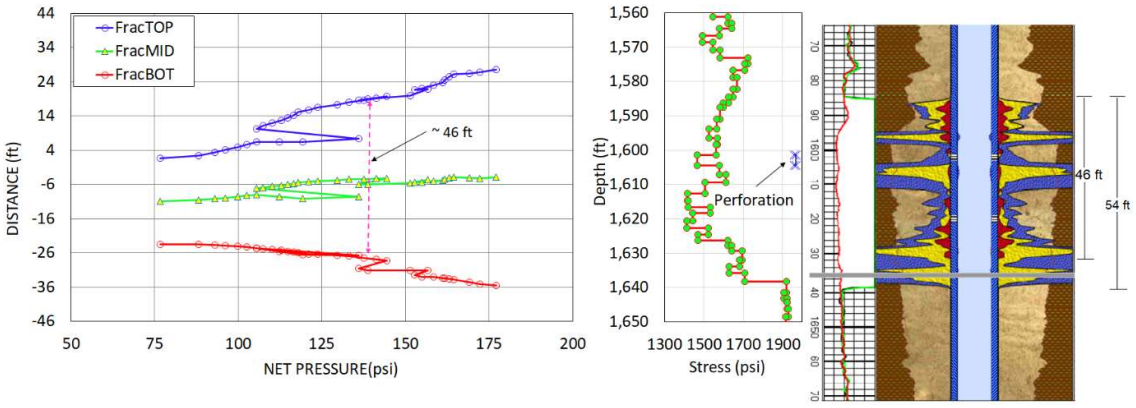

Fig. 4.3: Height growth vs. NP match and comparison with RA tracer survey data in field.

The treatment was traced with single RA tracer iridium, shown by red shades in extreme right track of **Fig. 4.2** to differentiate the signature from previous stage that was traced using antimony and scandium which are represented by blue and yellow shades, respectively. This color scheme applies to all cases presented henceforth. The depths from 1,584 to 1,638 ft (482.8 to 499.3 m) show presence of tracers for nearly 54 ft (16.5 m), though the 2nd stage being discussed shows around 46 ft (14.0 m) of vertical growth based on the iridium traces (red color).

The distance versus net pressure plot in **Fig. 4.3** (far left) shows the model-calculated top and bottom tips of the vertical fracture as the net pressure increases. The dashed vertical purple line shows the fracture height of nearly 46 ft (14.0 m) corresponding to the net pressure of 140 psi that was generated during the pad stage in the treatment. The center of this plot which is represented by "0" in the y-axis, coincides with the perforation depth shown in the middle plot of depth versus stress, to give a perspective on fracture growth with respect to stress profile. Additional details regarding the case history are presented in Pandey and Rasouli (2021c).

4.3.2. Vertical Well: Shallow Sandstone – Case 2

In this vertical well completion, a 4 ½ in. (114.3 mm) casing was set at 1,700 ft (518.2 m) and perforated in San Miguel C sand, with the middle of the perforations at a depth of 1,600 ft (487.7 m). The treatment was injected down 2 ⅞ in. (73.1 mm) tubing using a 12.0 lbm/Mgal (1.44 kg/m^3) borate crosslinked fluid. In the first stage of the treatment, a total of 9,500 lbm (4.31 t) of US mesh-size 16/30 resin-coated sand was pumped at 6.0 bbl/min (0.016 m^3/s) with a maximum concentration of 5 lbm/gal (600.0 kg/m^3).

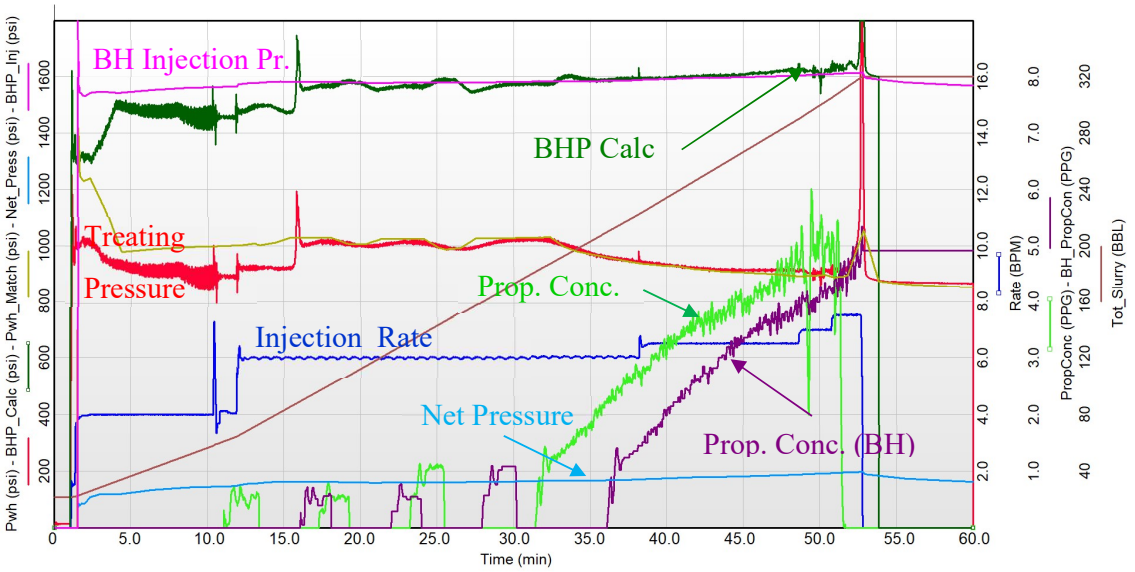

Fig. 4.4: Fracture stimulation treatment plot for Case 2.

The treatment plot presented in **Fig. 4.4** shows that to cure near-wellbore restrictions identified in the pre-job injection tests, 500 gal (1.9 m^3) of 15% HCl by wt. and sand slugs of small concentrations were introduced. The fracture closure was picked at 1, 380 psi (7.8 MPa), or 0.862 psi/ft (19.5 kPa/m), which implied an operating window of 220 psi (1.52 MPa) for an overburden gradient of 1.0 psi/ft (22.62 kPa/m) before pancake fractures could potentially form. The treatment pressure match indicates a maximum net pressure gain (matched) of 165

psi (1.14 MPa) in the pad, and an overall gain of nearly 200 psi (1.38 MPa) for the entire treatment. Formation and model properties are shown in **Table 4.2** below.

Number of layers in the stress model	60
Payzone Stress	1,375.0 psi (9.48 MPa)
Average Stress	1,519.0 psi (10.47 MPa)
Fracture initiation layer thickness	4.1 ft (1.25 m)
Average layer thickness	3.15 ft (0.96 m)
Average Young's Modulus	1.86×10^6 psi (12.82 GPa)
Average Poisson's Ratio	0.28
Average Fracture Toughness	1,308 psi.in$^{0.5}$ (4,979.0 kPa.m$^{0.5}$)
Payzone True Vertical Depths (TVD)	1,584 to 1,600 ft (16 ft thick)

TABLE 4.2: Formation properties used as input in Case 2.

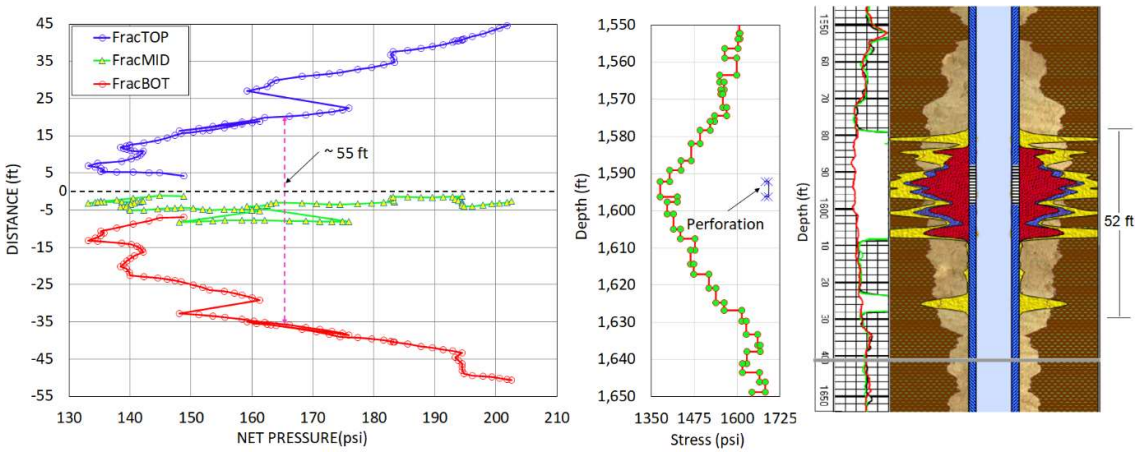

Fig. 4.5: Fracture height growth measurements and modeling for Case 2.

The results of height growth model analysis are presented in **Fig. 4.5**. The distance versus net pressure plot indicates that an overall height growth of nearly 55 ft (16.76 m) is possible if a net pressure of 165 psi is available, as highlighted by dashed purple line. This prediction is nearly 6% more than the actual height growth of 52 ft (15.85 m) observed in the field, shown by the RA tracer log in the extreme right of Fig. 4.5. All three RA tracer types were pumped in the treatment. Though majority of RA tracer activity is confined to the depths of 1,578 to 1,610 ft (481 to 490.73 m), the scandium pumped in the pad is also seen at the deeper depth of 1,625 ft (495.3 m). The fracture may have grown deeper as supported by the model, but most of the proppant stages were confined to shallower depth due to low injection rates.

4.3.3. Vertical Well: Shallow Sandstone – Case 3

The third case history details the fracture stimulation of shallow well completed in San Miguel sands (Pandey and Agreda, 2014), where the treatment was injected down 4 ½ in. (114.3 mm) casing set at 1,618 ft (493.2 m) with perforations at 1,435 ft (437.4 m). The treatment consisted of 20,000 lbm (9.1 t) of US-mesh-size 20/40 Ottawa sand pumped at a maximum concentration of 5.0 lbm/gal at 12.0 bbl/min (0.032 m^3/s) with a 30 lbm/Mgal (3.6 kg/m^3) linear gel of 23 cP (0.0023 Pa.s) viscosity at ambient conditions. A closure pressure of 1,290 psi (8.38 MPa) was obtained from the pressure decline analysis which equates to a fracture gradient of 0.90 psi/ft (20.4 kPa/m). This implies that if the net pressures increase beyond 220 psi (1.52 MPa), the during the treatment, the fracture pressures will exceed overburden and may cause the fracture to rotate in the horizontal plane.

The gradual increase of net pressure in the treatment data plot presented in **Fig. 4.6** shows that the fracture remains confined and continues to extend till the end of the pad. The threshold net pressure of 220 psi is exceeded at nearly 23 min into the treatment. The increase in injection rate, primarily to ensure good proppant transport, especially with low viscosity linear gel as the fracturing fluid, may have contributed to that.

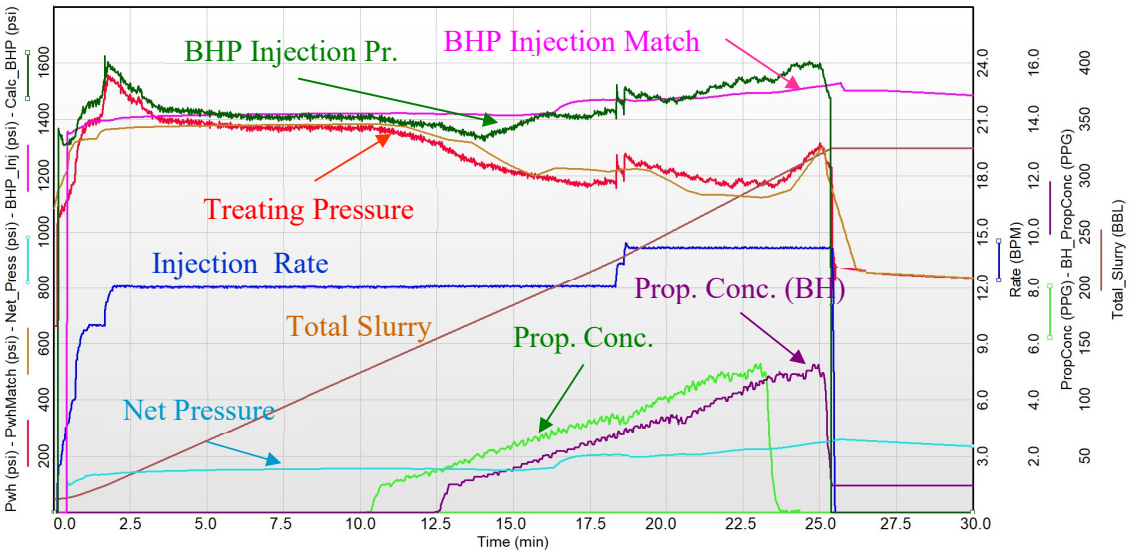

Fig. 4.6: Fracture stimulation treatment plot for Case 3.

A maximum net pressure of 155 psi (1.10 MPa) is obtained in the pad, though the gain in net pressure at the end of the treatment is nearly 275 psi (1.89 MPa). The end-of-job fracture pressure is around 1,490 psi (10.3 MPa) which results in a final fracture gradient of nearly 1.04 psi/ft (23.5 kPa/m). During the treatment, all 3 RA tracer isotopes were pumped to trace pad

and proppant stages. These are shown in the rightmost track of Fig. **4.7** where an overall fracture height of 18 ft (5.48 m) was measured based on gamma ray responses from 1,426 to 1,444 ft (434.6 to 440.1 m). Below is the summary for stress and formation property data used in the model.

Number of layers in the stress model	64
Payzone Stress	1,252.8 psi (8.64 MPa)
Average Stress	1,382.2 psi (9.53 MPa)
Fracture initiation layer thickness	4.1 ft (1.25 m)
Average layer thickness	4.2 ft (1.28 m)
Average Young's Modulus	1.46×10^6 psi (10.0 GPa)
Average Poisson's Ratio	0.28
Average Fracture Toughness	1,867 psi.in$^{0.5}$ (7,106.7 kPa.m$^{0.5}$)
Payzone True Vertical Depths (TVD)	1,428 to 1,440 ft (12 ft thick)

TABLE 4.3: Formation properties used as input in Case 3.

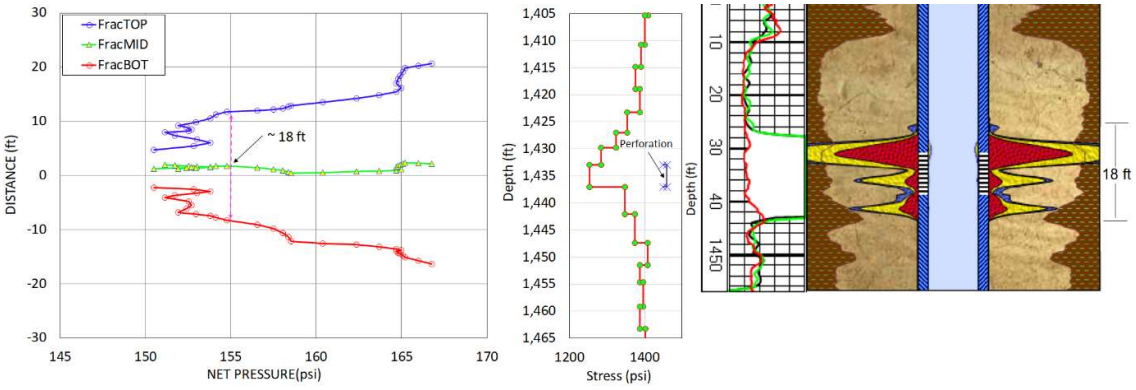

Fig. 4.7: Fracture height measurement modeled evolution with net pressure for Case 3.

The stress profile in the middle track of Fig. 4.7 shows low stresses pay interval surrounded by various non-pay lithological layers with increasing stress which is near identical to a classic textbook case used during the model calibration process (Chapter 3). With such a stress distribution, the fracture will not only remain contained but also the middle of the fracture will hover around the middle perforation depth as can be seen in the distance versus net pressure plot on the left. For stress setups that similar to these, the fractures will continue to increase as more net pressure is added into the system. However, in real world, if the effective fracture pressure exceeds overburden, additional fracture components in horizontal plane may form and

prevent further vertical growth as is the case here where even though net pressure of 275 psi was generated in the treatment, the height was restricted to 18 ft as depicted by RA tracer data. In their paper, Pandey and Agreda (2014) explain the presence of calcium rich quartz streaks where material property changes are prominent and could be the potential sites where the horizonal component of the fractures could originate. The fracture location plot also shows that a height growth of nearly 18 ft corresponds to a net pressure of 155 psi which aligns well with the data from RA tracer logs for this well. The conditions that favor the horizontal fracture component are discussed in Ch. 7 in details.

4.3.4. Vertical Well: Coal Bed Methane – Case 4

The height growth model application was extended to estimate fracture height in shallow coal bed methane gas wells that were drilled and completed in low permeability Walloon coal measures in Surat basin, eastern Australia. Given the low rate and viscosity techniques applied when stimulating selective coal seams, the data was found suitable for the study (Pandey and Rasouli 2021a) because it satisfies the slow fracture advancement rates while ignoring fracturing fluid leakoff. The evolution of treatment designs is documented by Pandey and Flottmann (2015) and Kirk-Burnnand et. al. (2015) with additional details on these Jurrasic age sequences that were formed as a part of an extensive intra-continental sag basin (Cook and Draper 2013).

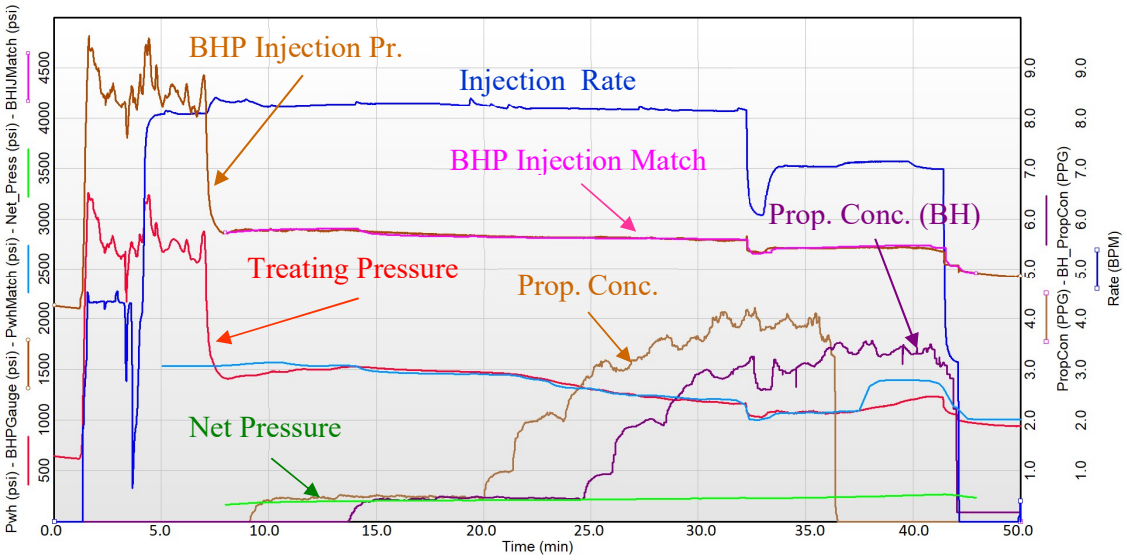

Fig. 4.8: Treatment plot of fracture stimulation in Walloons coal measures for Case 4.

The next two cases relate to a well where fracturing treatments were pumped in low permeability coals using a Coiled Tubing (CT)-conveyed pinpoint fracturing method. The

perforations were first jet-cut with 100-mesh sand pumped down a 1⅜ in. (34.93 mm) CT, whereas the main treatment was injected down the annulus of the CT and 5-½ in. (139.7 mm) casing. In the first stage of the treatment that is being discussed, the targeted interval was a thin coal seam at a depth of 3,268 ft (996.1 m), and most of the treatment was pumped at a low rate of 8.0 bbl/min (0.021 m^3/s) using low viscosity fluids of 15 to 20 lbm/Mgal [1.8 to 2.4 kg/m^3] crosslinked gels, with a maximum proppant concentration of 4.0 PPA (479.3 kg/m^3). The treatment plot is shown in **Fig. 4.8**. The downhole pressures were recorded during the treatment and used to calibrate the stress model generated with the help of dipole sonic data. The model data and average formation properties are shown below:

Number of layers in the stress model	99
Payzone Stress	2,225.0 psi (15.3 MPa)
Average Stress	2,398 psi (15.53 MPa)
Fracture initiation layer thickness	1.31 ft (1.25 m)
Average layer thickness	2.62 ft (0.80 m)
Average Young's Modulus (pay)	3.43×10^5 psi (2.36 GPa)
Average Poisson's Ratio (pay)	0.31
Average Fracture Toughness	1,402 $psi.in^{0.5}$ (5,336.7 $kPa.m^{0.5}$)
Payzone True Vertical Depths (TVD)	3,265 to 3,275 ft (10 ft thick)

TABLE 4.4: Formation properties used as input in Case 4.

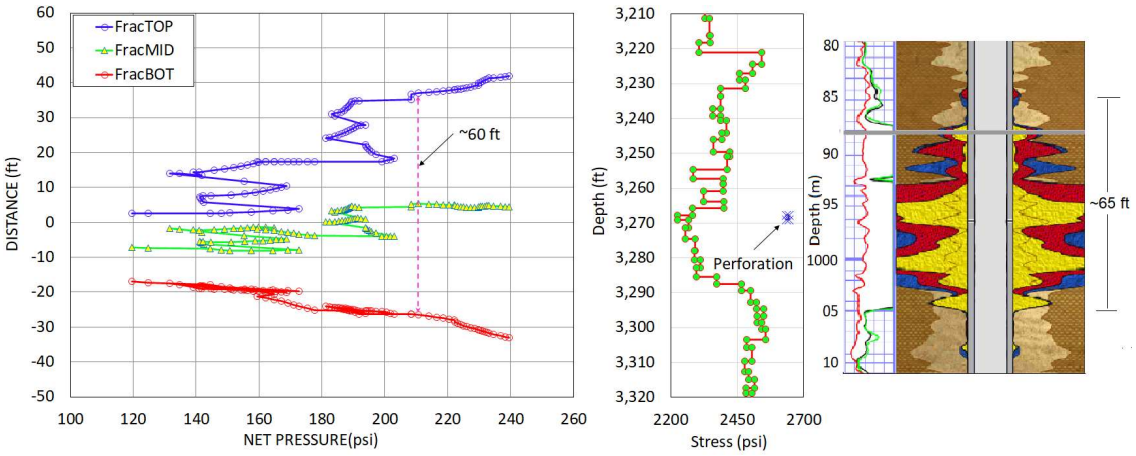

Fig. 4.9: Fracture height measurement modeled evolution with net pressure for Case 4.

The net pressure in the pad increases from 165 to 210 psi (1.14 to 1.45 MPa) which corresponds to a maximum fracture height of 60 ft (18.3 m) and reasonably agrees with the fracture height

of 65 ft (~19.8 m) interpreted from RA tracer survey and shown in the extreme right track of **Fig. 4.9**. In the presence of low-stressed members below the perforations, the fracture may grow downward initially, but as it approaches the high-stress regions around 3,295 ft (1,004.3 m) the growth direction may reverse. As noted, with the net pressure enough to overcome the barrier strength of stresses around the depth of 3,250 ft (990.6 m), the fracture yet again changes its growth pattern and tends to grow in upward direction which is supported by traces of RA material as high as 985 m (3,231.6 ft) measured depth.

4.3.5. Vertical Well: Coalbed Methane – Case 5

This case study was also taken from the same well as the previous one but targeting much shallower coal seam in the multistage completion with Coiled Tubing. The perforations were jet-cut with the help of CT at the depth of 2,663.8 ft (811.9 m). The treatment was pumped at 8.0 bbl/min (0.021 m^3/s) down the annulus of casing and CT as in previous case using low viscosity fluids of 20 lbm/Mgal [2.4 kg/m^3] crosslinked gel, with a maximum proppant concentration of 8.0 PPA (958.6 kg/m^3). A total of 37,000 lbm (16.78 t) were pumped in the treatment successfully. The treatment plot shown in **Fig. 4.10** shows both surface and bottomhole treating pressures and the net pressure generated during the treatment. The specialized low-rate and low-viscosity pinpoint fracturing method helped in limiting the net pressure gain to 220 psi (1.52 MPa) during the treatment. The downhole pressures were recorded during the treatment and used to calibrate the stress model generated with the help of dipole sonic data. The model data and average formation properties are shown below:

Number of layers in the stress model	98
Payzone Stress	1,833.4 psi (12.64 MPa)
Average Stress	1,994.4 psi (13.75 MPa)
Fracture initiation layer thickness	2.30 ft (0.70 m)
Average layer thickness	1.66 ft (0.51 m)
Average Young's Modulus (pay)	3.43×10^5 psi (2.36 GPa)
Average Poisson's Ratio (pay)	0.31
Average Fracture Toughness	1,614 $psi.in^{0.5}$ (6,143.7 $kPa.m^{0.5}$)
Payzone True Vertical Depths (TVD)	2,660 to 2,670 ft (10 ft thick)

TABLE 4.5: Formation properties used as input in Case 5.

The layered stress and mechanical property data was input in the model to generate fracture height growth pattern for the shallow stage and compare the forecasted output with the field

observed data. The distance versus net pressure plot in **Fig. 4.11** predicts a fracture height growth of nearly 70 ft (21.34 m) for a net pressure of 220 psi. This prediction matches closely with the fracture height measurements from RA Tracer shown in the extreme right track. In this case, the downward growth is more prominent as the net pressure exceed 180 psi (1.24 MPa) a condition that is reached within the first few minutes into the treatment as shown in Fig. 4.10.

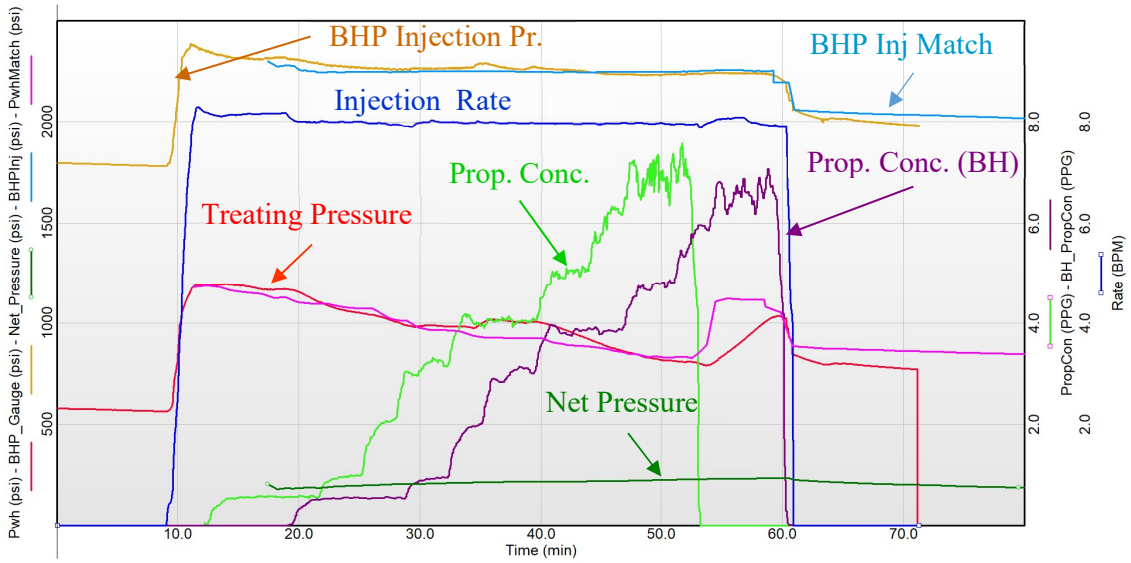

Fig. 4.10: Treatment plot of fracture stimulation in Walloons coal measures for Case 5.

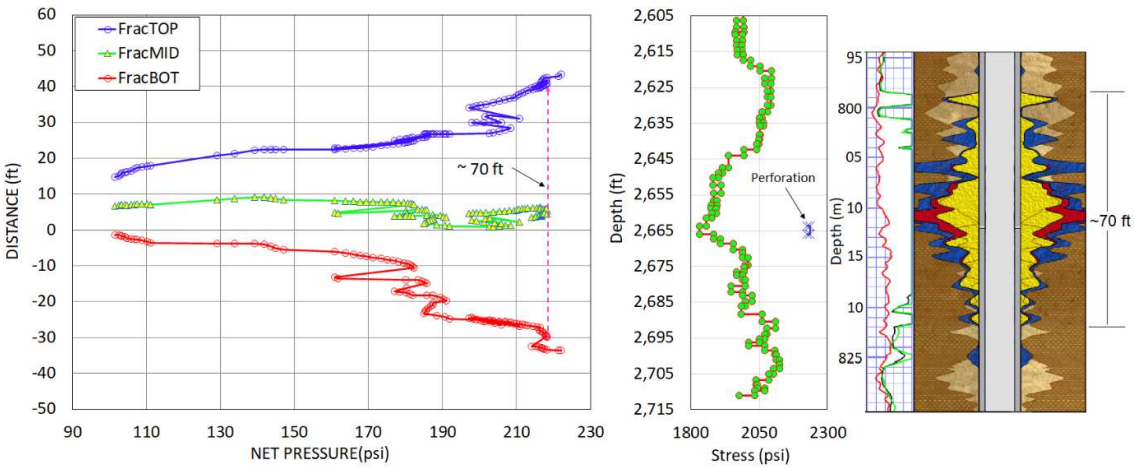

Fig. 4.11: Fracture height measurement modeled evolution with net pressure for Case 5.

4.3.6. Deviated Well: Offshore Frac-Pack – Case 6

The use of the newly developed fracture height growth prediction model was also extended to offshore frac and pack example cited in Haddad et al. (2012), which is also elaborated in

Pandey and Cramer (2019). The job was designed as a TSO treatment for Wilcox 1 and 2 sands, in Cascade/Chinook field, with the former shown here as case history. The average permeability of Wilcox 1 was observed to be 25 md whereas Wilcox 2 was slightly lower at 10 md, though both are reasonably high to result in appreciable fluid loss during pumping. In principle the presence of high leak-off velocities violates the basic assumption of equilibrium model, but nevertheless an attempt was made to predict the fracture growth in this unique case and compare with the fracture heights determined from RA survey conducted after the treatment. The treatment was placed at 30 bbl/min (0.08 m3/s). The TSO design called for a maximum proppant concentration of 10.0 lbm/gal (1,198.3 kg/m^3) but only up to 8.6 lbm/gal was placed in the formation before taking the returns at the surface and inducing an annulus pack.

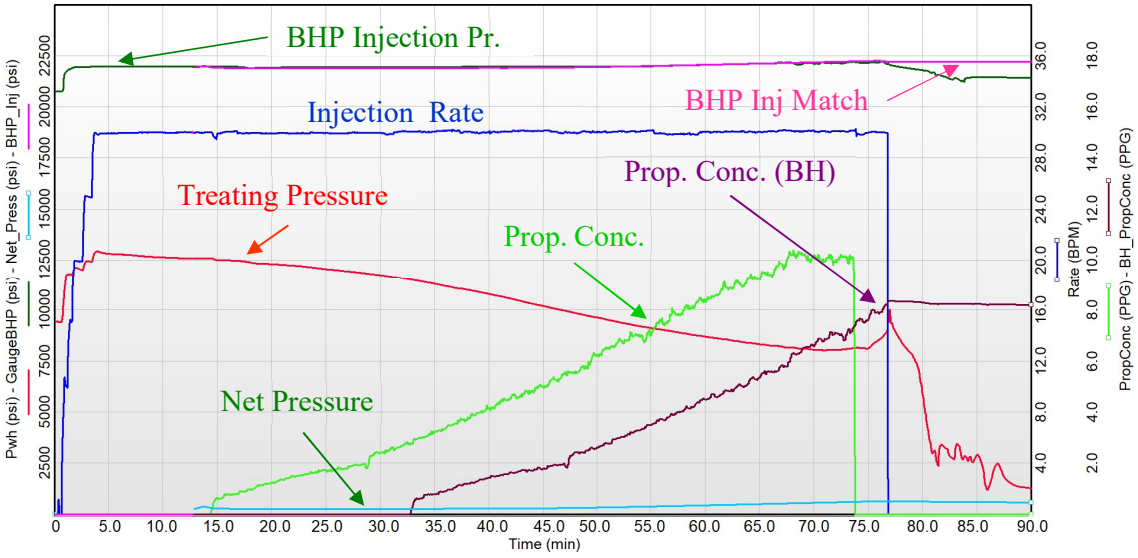

Fig. 4.12: Frac and pack Tip Screen Out treatment pumped in Willcox Sand 1.

The history match of treatment data shown in **Fig. 4.12** shows a nominal net pressure build up during the treatment with a near constant value of 255 psi (1.76 MPa) during the early stage of the treatment, despite a small pad indicating low strength and high permeable rock, where the tip effects may dominate fracture propagation. The range of Young's Modulus was reported to be 2.0 to 3.0 × 10^6 psi (13.8 to 20.7 × 10^4 MPa) which is a moderate value, and the fracture toughness was assumed to be a constant value of 2,000 psi.in$^{0.5}$ (7,613.0 kPa.m$^{0.5}$) for all the layers. The stress and mechanical property data was input in the predictive model and the plot of distance versus net pressure was generated to predict fracture height growth. The plot shown in **Fig. 4.13** depicts a gradual vertical growth with the increase of net pressure and with 255

psi, a fracture height of nearly 200 ft (61.0 m) is possible. The RA tracer survey plot at the far right reported a similar fracture height growth.

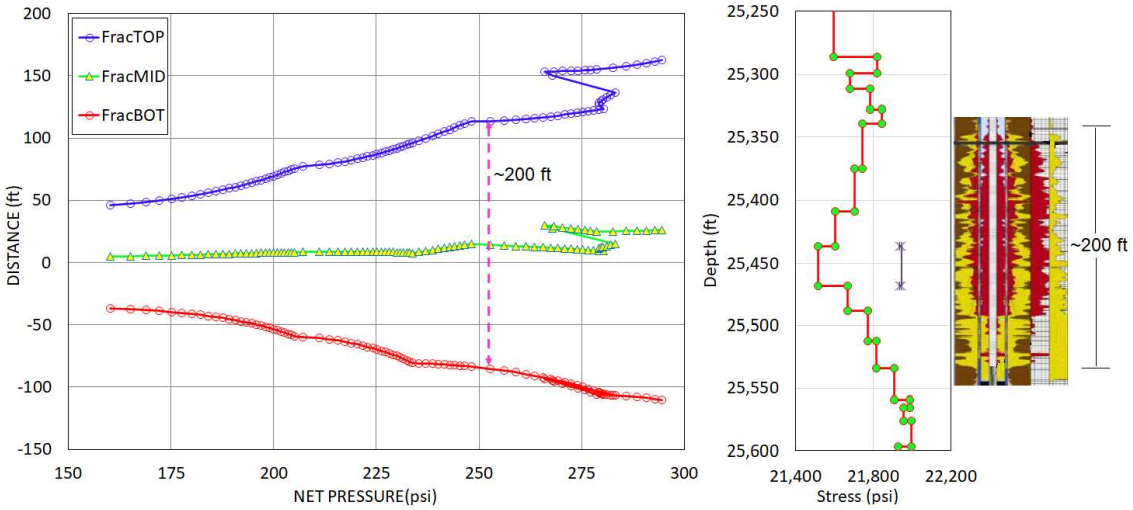

Fig. 4.13: Fracture height measurement modeled evolution with net pressure for Case 6.

Though the height growth observed in the field for the frac and pack case conforms well with the predictions from the newly developed model, the conditions do not align with the requirements set for the candidate selection because (a) the candidate well is slightly deviated, (b) treatment was pumped at higher rate, (c) high fluid losses and finite leak-off velocity were expected, and (d) assumption of linear elastic fracture mechanics (LEFM) may not fully apply to soft rock fracturing which is generally the case for most frac-packs. Despite these, since the model follows a rigorous and sound calculation approach, the predictions will match in most cases if the injection flux, which is the ratio of injection rate to generated fracture height is small and by virtue of that allows fracture vertical growth at slow enough pace to allow adequate equilibrium.

4.4. Model Modification to Account for Non-Uniform Fracture Pressure

The model was successfully tested in several field cases that employed low rate and low viscosity type treatment schedules that did not principally violate the basis on which the model was developed because of slow pace of fracture advancement. Most of the treatments were pumped with fracturing fluids that aided in maintaining low net pressures by not imparting excessive slurry frictional pressures in the slot-like fracture. Though, the solid mechanics-based fracture height prediction were found to be adequate in these examples, there were some exceptions where the model predicted fracture heights were lower than those observed in the

field. With the formation and stress properties being nearly the same, these mismatches were attributed to higher slurry friction in the fracture, which did not align with the assumption of uniform pressure inside the fracture.

4.4.1. Non-uniform Fracture Pressure Profile

In the cases where the flow of the injected fluid in the fracture generates higher frictional pressures such as when using the foamed fluid, a non-uniformity in fracture pressure profile can be expected. The non-uniform pressure distribution can follow either linear, quadratic or a power law behavior and can influence the outcome of the model – in related studies (Rummel and Winter 1982; Nolte 1979), it is recommended to assume power law or quadratic behavior of pressure distribution to solve this problem mathematically. The details of the non-uniform pressure behavior are presented in Pandey and Rasouli (2021a, 2021c) and are mainly highlighted here to acknowledge their influence. The fracture pressures during the pumping phase can be represented as either a simple quadratic form of $p_{cp}[1 - \beta(z/a)^2]$, where p_{cp} is the pressure at the center of the perforations, z/a is the ratio of elevation to fracture half-height and β is the calibration constant. A more accurate fit to the projected pressure in the fracture can be shown with a quadratic form $p_{cp}[1 - c_2(z/a)^2 + c_3(z/a)]$, where c_2 and c_3 are calibration coefficients. The value of p_{cp} is the cumulative of individual pressure drops across various widths in given layers from the upper tip to the center of perforations and can be equated to net pressure from fluid mechanics solution.

The pressure term in Eq. (2.17) can be modified to account for quadratic pressure behavior in the fracture resulting from frictional flow of slurries in the fracture and is presented below for stress intensity factors at the top and bottom of the fracture as follows:

$$K_I^{bot,top} = \frac{1}{\sqrt{\pi a}} \int_{-a}^{a} \left[p_{cp} \left\{ 1 - \beta \left(\frac{z}{a} \right)^2 \right\} + \rho_f g \left(h_{cp} - z \right) - \sigma(z) \right] \sqrt{\frac{a \mp z}{a \pm z}}\, dz \quad (4.1)$$

For the sake of simplification, it is assumed that (a) both the sections of fracture will exhibit uniform quadratic pressure behavior, and (b) there is no fluid leak-off. For a vertically asymmetric fracture from the perforation depth, the integral can be expanded as follows:

$$K_I^{bot,top} = \frac{1}{\sqrt{\pi a}} \left\{ \int_{-a}^{a} \left[p_{cp} + \rho_f g h_{cp} - \sigma(z) \right] \sqrt{\frac{a \mp z}{a \pm z}}\, dz - \int_{-a}^{a} \rho_f g z \sqrt{\frac{a \mp z}{a \pm z}}\, dz - \right.$$

$$\left. p_{cp} \left[\int_{-a}^{a} \beta \left(\frac{z}{a} \right)^2 \sqrt{\frac{a \mp z}{a \pm z}}\, dz \right] \right\} \quad (4.2)$$

If the last term on the right is denoted by I, its integration for both upper and lower stress intensity factors lead to the following form after simplification:

$$I^{bot} = \frac{\beta p_{cp}}{\sqrt{\pi a}}\left[\frac{a}{2}\sin^{-1}\left(\frac{z}{a}\right) + \frac{\sqrt{a^2-z^2}}{6a^2}(4a^2 - 3az + 2z^2)\right] \quad \text{.....(4.3)}$$

$$I^{top} = \frac{\beta p_{cp}}{\sqrt{\pi a}}\left[\frac{a}{2}\sin^{-1}\left(\frac{z}{a}\right) - \frac{\sqrt{a^2-z^2}}{6a^2}(4a^2 + 3az + 2z^2)\right] \quad \text{.....(4.4)}$$

Further simplification during the subtraction process leads to a residual term of only $\pi a/2$ where $a = h/2$ is fracture half-height, since the right side of both integrals vanish as the term under square root reduces to zero on evaluation for z. This mathematical manipulation also allows the elimination of pressure term p_{cp} which is convenient when performing iterations to solve for fracture height. To obtain pressure, an additional geometric calibration term $(\beta\pi h/2)$ is introduced in the denominator as shown below:

$$p_{cp} = \left\{\pi h\left[\sigma_k - \rho_f g\left(h_{cp} - \frac{h}{2}\right)\right] + \sqrt{\frac{\pi h}{2}}\left(K_I^{bot} + K_I^{top}\right) - \sum_{i=1}^{k-1}(\sigma_{i+1} - \sigma_i)\left[\frac{h}{2}\cos^{-1}\left(\frac{h-2h_i}{h}\right) + \sqrt{h_i(h-h_i)}\right] - \sum_{i=1}^{k-1}(\sigma_{i+1} - \sigma_i)\left[\frac{h}{2}\cos^{-1}\left(\frac{h-2h_i}{h}\right) - \sqrt{h_i(h-h_i)}\right]\right\} \div \left(\pi h - \beta\frac{\pi h}{2}\right) \quad \text{.....(4.5)}$$

If it is assumed that just as the fracture height exceeds the *entire* pay height where the perforations are located, the p_{cp} is nearly the same as the stress value in the pay, the calibration constant β can be determined easily. Further, in this case $h_{cp} \approx h/2$ and $h_i = h$. This assumption will result in the elimination of $\rho_f g h$ term and the term $\cos^{-1}$ term will result in a value of $\pi h/2$; β can now be determined conveniently. The overall effect of including the pressure distribution in the calculations results in a requirement of higher net pressure values to attain the same fracture height.

4.4.2. Vertical Well: Coalbed Methane – Case 7

The non-uniform pressure distribution mode was invoked in some of the cases where the base model was unable to generate the distance versus net pressure plot accurately that led to underestimation of fracture height. The example presented here is detailed in Pandey and Rasouli (2021a, 2021c) and pertains to a shallow coal bed methane completion at a depth of 3,250 ft (990.6 m) and fracture stimulated with nitrogen assisted 70-quality foamed treatment. The treatment was injected down the annulus of 1 ¾ in CT and 4 ½ inch casing where the perforations were jet-cut with the help of CT. During the treatment, an injection rate of 0.25 bbl/min (2.38 m^3/h) was maintained in the CT to prevent influx of fracturing slurry. The treatment was designed and successfully placed at the designed injection rate of 8.0 bbl/min (0.021 m^3/s) and maximum bottomhole proppant concentration of 4.0 PPA (479.3 kg/m^3).

The treatment plot containing pressure history match data is shown in **Fig. 4.14**. Because of a foamed treatment, the surface proppant concentration is higher than effective bottomhole proppant concentration. An average net pressure of 210 psi (1.45 MPa) is obtained from the match. Following the workflow adopted, the stress and mechanical property data from the match were used to generate fracture height and width profiles. The corresponding pressure drop profile in the fracture for a 20 lbm/Mgal (2.40 kg/m^3) 70 quality nitrogen foamed fluid with *n'* of 0.71 and *K'* of 0.00563 lbf-s^n/ft^2 (0.0723 Pa.s) was calculated in the final step.

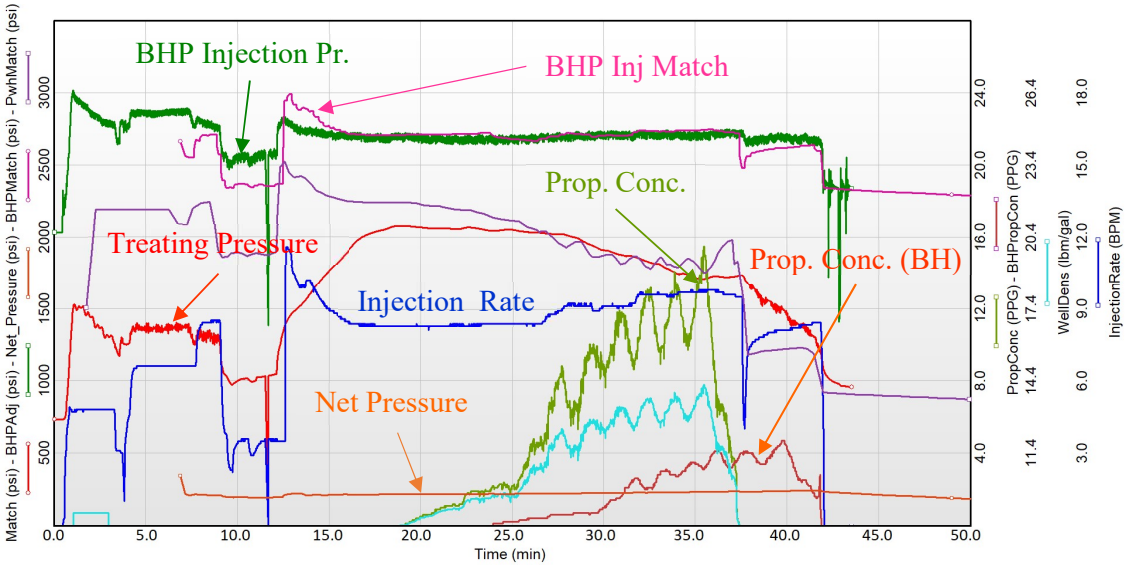

Fig. 4.14: Treatment plot of foamed job pumped in CBM well detailed in Case 7.

.

The modified model was able to incorporate the calibration variable. For case 7 a match was obtained with β = 0.1325 which was within 5% of the initial guess obtained with help of procedure mentioned above. The distance versus net pressure plot is shown in Fig. 4.15 below and indicates that for a net pressure of 210 psi, a fracture height of nearly 65 ft (19.81 m) may be obtained for the layered stress distribution shown in the middle track. The results from the RA tracer survey shows similar results. The value of β less than unity will tend to increase the calculated fracture pressure; the movement of foamed fluid inside the fracture at the designed injection rates can result in higher than normally expected fracture pressure especially for smaller width fractures associated with foamed fluids (because of lower viscosity). The larger pressure drop can also result in fluid diversion into regions where higher fracture widths will be generated for smaller rock moduli in an absence of significant stress contrast amongst various layers (which is the case here). This action leads to a downward fracture growth as projected by fracture height plot and observed in the tracer survey to the right, in Fig. 4.15.

The layered mechanical properties are show in Table 4.7 below.

Number of layers in the stress model	99
Payzone Stress	2,135.8 psi (14.74 MPa)
Average Stress	2,249.3 psi (15.51 MPa)
Fracture initiation layer thickness	1.64 ft (0.50 m)
Average layer thickness	1.97 ft (0.60 m)
Average Young's Modulus (pay)	5.87×10^5 psi (4.1 GPa)
Average Poisson's Ratio (pay)	0.31
Average Fracture Toughness	1,614 psi.in$^{0.5}$ (6,143.7 kPa.m$^{0.5}$)
Payzone True Vertical Depths (TVD)	3,138 to 3,148 ft (10 ft thick)

TABLE 4.7: Formation properties used as input in Case 7.

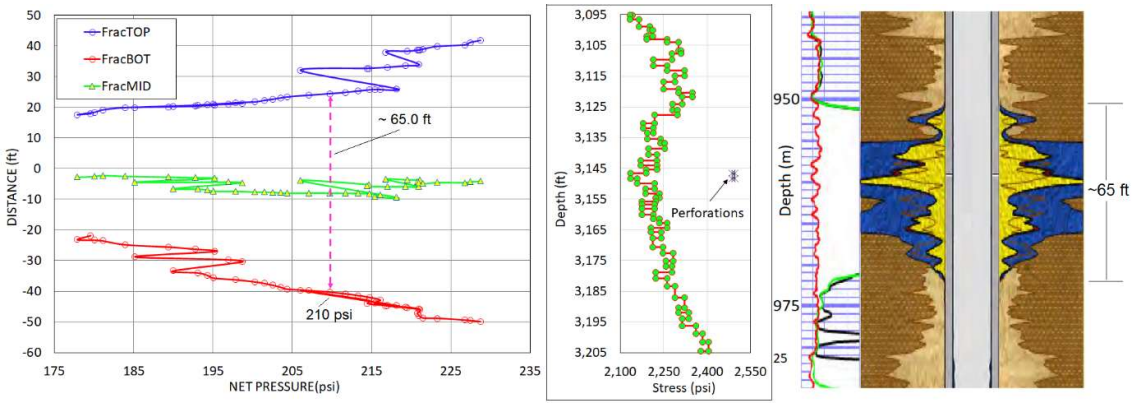

Fig. 4.15: Fracture height estimation after model modification for Case 7.

This case was also solved using the alternate approach where the pressure distribution in the fracture was represented by the pressure format $p_{cp}[1 - c_1(z/a)^2 + c_2(z/a)]$ but results in a residual term of $p_{cp}.c_3.\sqrt{\pi h/2}$ when carrying out the procedure of $K_{Ibot} - K_{Itop}$ to eliminate the pressure term p_{cp}. As mentioned earlier, this cannot be readily solved using the procedure adopted so far. The expression is shown below.

$$K_I^{bot} - K_I^{top} = \sqrt{\frac{2}{\pi h}}\left\{\sum_{i=1}^{k-1}(\sigma_{i+1} - \sigma_i)\left[\frac{h}{2}\cos^{-1}\left(\frac{h-2h_i}{h}\right) + \sqrt{h_i(h-h_i)}\right] - \sum_{i=1}^{k-1}(\sigma_{i+1} - \sigma_i)\left[\frac{h}{2}\cos^{-1}\left(\frac{h-2h_i}{h}\right) - \sqrt{h_i(h-h_i)}\right]\right\} + \sqrt{\frac{\pi h}{2}}\rho_f g\frac{h}{2} - \sqrt{\frac{\pi h}{2}}p_{cp}c_3 \quad \text{.....(4.6)}$$

The solution for fracture height using Eq. (4.6) requires the use of a "nested" loop approach where for a given p_{cp}, the fracture location is determined for a fracture of assumed height. The value of p_{cp} is then incremented in the outward loop, and the inward loop calculates the corresponding location for the new fracture. The term c_3 requires calibration because of uncertainty in pressure distribution, although its initial value may be predicted using relevant expressions such as the one developed by Rummel and Winter (1982). The solution obtained by this procedure is also detailed in Pandey and Rasouli (2021a, 2021c). The table below compares the predicted and observed fractured heights after fracture stimulation treatment.

Case History	Net Pressure (psi)	Fracture Height (ft)		Height Diff. (ft)	% Difference
		From Model	From RA Tracer		
Case 1	140(0.97 MPa)	46 (14.0 m)	46 (14.0 m)	0	0
Case 2	165 (1.14 MPa)	55 (16.76 m)	52 (15.85 m)	+3 (0.91 m)	6.0%
Case 3	155 (1.10 MPa)	18 (5.5 m)	18 (5.5 m)	0	0
Case 4	210 (1.45 MPa)	60 (18.3 m)	65 (19.81 m)	-5 (1.52 m)	-7.6%
Case 5	220 (1.52 MPa)	70 (21.34 m)	70 (21.34 m)	0	0
Case 6	255 (1.76 MPa)	200 (61.0 m)	200 (61.0 m)	0	0
Case 7	210 (1.45 MPa)	65 (18.21 m)	65 (18.21 m)	0	0

TABLE 4.9: Summary of modeled and observed fracture height in the field.

The modification of the model to account for the pressure drop in the fracture due to fluid movement appears to account for the difference in observed and predicted values. The problem of estimating fracture vertical growth, however, is a complex one and there may be other mechanisms by which the growth is either accelerated or impeded. With net pressure being the main driver, the crack advancement in the vertical direction will largely depend on how it balances against the stresses and fracture toughness of various layers that tend to counteract the propagation force.

4.5. Nomenclature

a = radius of crack, crack half-length, fracture half-height, $M^0L^1t^0$, ft (m)

c_1, c_2, c_3 = coefficients, dimensionless

g = acceleration due to gravity, $M^0L^1t^{-2}$, ft/s^2 (m/s^2)

h = fracture height, $M^1L^1t^0$, ft (m)

h_{cp} = elevation from the bottom tip of the fracture to center of perforations, $M^1L^1t^0$, ft (m)

h_i = elevation of i^{th} layer top from bottom tip of the fracture, $M^1L^1t^0$, ft (m)

$I^{top,bot}$ = Integration for upper and lower stress intensity factors, Eq. (4.3) & (4.4)

i = count, unitless

k = number of layers, number

$K_I^{top,bot}$ = stress intensity factor for top and bottom layers, $M^1L^{-0.5}t^{-2}$, psi-in.$^{0.5}$ (Pa.m$^{0.5}$)

p_{cp} = pressure at the center of the perforations, $M^1L^{-1}t^{-2}$, psi (Pa)

z = elevation in vertical distance from bottom tip/center of the fracture, $M^0L^1t^0$, in. (m)

β = calibration constant, Eq. (4.1), unitless

ρ = fluid density, $M^1L^{-3}t^0$, lbm/gal (kg/m^3)

σ_i, σ_j = stress in i^{th} and j^{th} layers, $M^1L^{-1}t^{-2}$, psi (Pa)

σ_k = stress in the n^{th} or uppermost layer, $M^1L^{-1}t^{-2}$, psi (Pa)

Chapter 5

Developing Velocity Based Toughness Model

5.1. Stress Intensity Factor

For linear, homogenous, and isotropic elastic materials, if the strain in one of the directions, e.g., along the wellbore, is neglected then the condition leads to a plane strain assumption which is both acceptable and practical as it greatly simplifies the solution to several fracture mechanics related problems. If u_1 and u_2 are the displacements in directions of a cartesian coordinate system of x_1 and x_2, then they can be defined as $u_1 = u_1(x_1, x_2)$ and $u_1 = u_1(x_1, x_2)$. As per Airy (Saad 2005), the stress function $\Phi(x,y)$ maybe used to define the normal stresses in x and y directions (σ_{xx} and σ_{yy}, respectively), and shear stress (τ_{xy}), for a two-dimensional continuous elastic medium as shown by Rice (1968).

$$\sigma_{xx} = \frac{\partial^2 \Phi}{\partial y^2};\ \sigma_{yy} = \frac{\partial^2 \Phi}{\partial x^2}\ ;\ \tau_{xy} = \frac{\partial^2 \Phi}{\partial x \partial y} \qquad \text{.....(5.1)}$$

For the equilibrium and compatibility conditions to be satisfied automatically for plane stress conditions, the function Φ must have the property of $\nabla^2\nabla^2\Phi = 0$. On the other hand, the relation of stress intensity factor which represents the strength of singularity of the stress field that exists near the crack tip, can be obtained by compact calculations offered by Westergaard (1939). It was shown that a limited class of problems can be resolved by introduction of a complex stress function Z(z) such that $z = x + iy$, where $i = \sqrt{-1}$ is the imaginary portion of the function. The Westergaard function can be related to Airy stress function as follows, where Re denotes the real part of the function and Im is the imaginary part:

$$\Phi = \mathrm{Re}\bar{\bar{Z}} + y\ \mathrm{Im}\bar{Z} \qquad \text{.....(5.2)}$$

Here, $\bar{Z} = d\bar{\bar{Z}}/dZ$ and $Z = d\bar{Z}/dZ$ are integrals with respect to z. To apply the Westergaard solution to above problem, the normal stress components σ_{xx} and σ_{yy} in Eq. (5.1) can be equated to ReZ – y ImZ' and ReZ + y ImZ' respectively, for a case of identical stress values on a crack plane of vertical displacement $y = 0$ and crack of length $2a$ along x axis. This will result in the following expressions:

$$\sigma_{xx} = \sigma_{yy} = \mathrm{ReZ} = \frac{\sigma x}{\sqrt{x^2 - a^2}};\ \text{for}\ Z(z) = \frac{\sigma z}{\sqrt{z^2 - a^2}} \qquad \text{.....(5.3)}$$

where, for distance $-a < x < a$, Z is imaginary. The square-root term in the denominator can be replaced by $2x^*$ if $x^* = x - a$ and with $x^* << a$, whereby this assumption implies $x = \sqrt{a}$. The inverse square root singularity of stresses as a function distance away from crack tip is

seen here. From Eq. (5.3), the stresses on the crack plane, at angle $\theta = 0$, are given by the following:

$$\sigma_{\theta\theta} = \sigma_{xx} = \sigma_{yy} = \frac{K_I}{\sqrt{2\pi x^*}} \quad \text{.....(5.4)}$$

where K_I is the stress intensity factor or the strength of singularity. Further simplification of Eq. (5.3) and (5.4) leads to yet another important relation for a determining stress intensity factor (Irwin 1960) for mode-I fracture in the presence of uniform stress field σ:

$$K_I = \sigma\sqrt{\pi a}, \quad \text{.....(5.5)}$$

where a is the radius of the crack or fracture half-height or, half-length for other applications. For the fracture to propagate, the stress intensity factor should exceed a critical value also termed as *fracture toughness* and is denoted by K_{Ic}. Fracture toughness can be related to net pressure by replacing the stress term σ in the above equation with net pressure ($P_f - \sigma_3$) as shown below:

$$\left(P_f - \sigma_3\right) = \frac{K_{Ic}}{\sqrt{\pi a}}, \quad \text{.....(5.6)}$$

where, P_f is the fracture pressure, and σ_3 is the minimum in-situ stress in horizontal direction. This relation is useful in calibration of layered stress and mechanical property model. Additional explanations to above derivations are given in Pandey and Rasouli (2021b). It may be noted that because of the stress field around the fracture tip, even if the influence of fracture toughness is ignored, the singularity does not vanish because of effects from coupled fluid flow and leakoff. SCR Geomechanics Group (1993), and Lenoach (1994, 1995) show that for power law fluids the hydraulic fracture singularity depends on power law index n, as it assumes a form of $n/(n+2)$ for impermeable rocks and up to $3n/(4 + 4n)$ for permeable rocks. Thus, even for cases where fracture toughness is notionally ineffective, the singularity of stresses persists because of the relationship the fluid flow shares with elastic formation properties.

5.2. Obtaining Fracture Toughness from Tip Velocity

Based on the work carried out by Desroches et al. (1994) and Lenoach (1994) that used the potential function $\phi(z)$ described above, the crack opening can be obtained by the following expression:

$$w(x) = \frac{4A}{E'\alpha} \sin(\alpha\pi) x^{\alpha} \quad \text{.....(5.7)}$$

where, x is the distance from the crack tip along axis of the crack, $w(x)$ denotes near-tip crack opening, A and α are the amplitudes and exponent respectively, that must be determined to

obtain the solution, and *E'* is the plane strain modulus. The pressure on the fracture faces obtained from the same potential function was given as:

$$p(x) = \sigma_o - A\cos([1-\alpha]\pi)x^{\alpha-1} \quad \text{.....(5.8)}$$

where, σ_o is the far-field compressive state acting perpendicular to the fracture plane. Equations (5.7) and (5.8) define the width and pressures at near-tip region for a semi-infinite problem, respectively. For a non-uniformly pressurized crack, the pressure gradient in the crack assumes the following form after finding the derivative of Eq. (5.8):

$$\frac{d\Delta P}{dx} = \frac{(1-\alpha)}{x^{\alpha-2}} A\cos([1-\alpha]\pi) \quad \text{.....(5.9)}$$

To introduce lubrication in the above equation which would assist in further simplification, the left-hand side can be replaced by equation for flow in elliptical geometry. This expression as proposed by Nolte (1991) is shown below:

$$\frac{d\Delta P}{dx} = \frac{Rv^n}{(n+2)w^{n+1}} \quad \text{.....(5.10)}$$

where,

$$R = \frac{2K(2m)^m(n+2)}{[(4/\pi)^m\phi(n)]^n}; m = \frac{2n+1}{n}; \phi^n(n) \cong 1 - 0.41n^{0.61} \quad \text{.....(5.11)}$$

In Eq. (5.10), the left-hand term denotes the pressure drop in the fracture over a distance *x* measured from the tip of the fracture, *ΔP* is the net pressure itself (fracture pressure minus closure stress), *w* is the average cross-sectional width, and *v* is the average cross-sectional velocity. The term *R*, shown in Eq. (5.11) is composed of power law fluid components *K* which denotes consistency index, and *n*, which represents flow behavior index, along with $\phi(n)$ that is the m^{th} moment of the dimensionless width over the fracture cross-section which can be shown as the function of flow behavior index.

If right hand terms of Equations (5.9) and (5.10) are equated and the value of *R* is substituted in Eq. (5.10), the following form is obtained after rearranging the terms for fluid velocity which closely approximates the fracture tip velocity after assuming a near impermeable linearly elastic solid where the body forces are neglected.

$$v = \left(\frac{4}{\pi}\right)^m \left(\frac{n}{2n+1}\right)\phi(n)\left[\frac{(1-\alpha)A\cos[(1-\alpha)\pi]}{Kx^{2-\alpha}}\right]^{\frac{1}{n}}\left[\frac{2A\sin(\alpha\pi)x^{\alpha}}{E'\alpha}\right]^{1+\frac{1}{n}} \quad \text{.....(5.12)}$$

The right-side term is independent of distance since uniform velocity is assumed. The value of exponent α is obtained as a function of *n* as, $\alpha(n) = 2/(2+n)$. As suggested by Lenoach (1995), using inversion process, the value of amplitude *A* can be obtained explicitly. The

amplitude A can also be deconvoluted by studying a similar relationship shown for Newtonian fluid with n=1, by Dontstov and Peirce (2015) after ignoring the constant, as follows:

$$d = \frac{\Delta K_{Ic}^6}{\mu^2 E'^4 V^2} \quad \text{.....(5.13)}$$

where d is the characteristic length of the problem, ΔK_{Ic} is apparent fracture toughness, μ is the viscosity, E' is plane strain modulus and V is the vertical velocity of the horizontal fracture fronts at the top or bottom of the blade-like fracture. Using dimensionality and similitude, the amplitude A in Eq. (5.12) is numerically equivalent to apparent fracture toughness ΔK_{Ic}, with the characteristic length x assuming a 1/6th power for Newtonian fluids, the same as d in Eq. (5.13), when expressed in terms of fracture toughness. This important relationship was used in the newly developed model to define fracture toughness directly as a function of vertical velocity, thus eliminating the need to input values in the model that may be possibly incorrect.

The apparent fracture toughness (ΔK_{Ic}) can now be expressed in terms of fracturing fluid, formation properties and pumping parameters as follows:

$$\Delta K_{Ic} = \left\{ v \left(\frac{\pi}{4}\right)^m \left(\frac{2n+1}{n}\right) \frac{1}{\phi(n)} \right\}^{\frac{n}{n+2}} \left[\frac{K x^{2-\alpha}}{(1-\alpha)\cos[(1-\alpha)\pi]}\right]^{\frac{1}{n+2}} \left[\frac{E'\alpha}{2\sin(\alpha\pi) x^{\alpha-0.25}}\right]^{\frac{n+1}{n+2}} \text{...(5.14)}$$

For Newtonian fluids where, n = 1, the following proportionality is obtained which agrees with Eq. (5.13):

$$\Delta K_{Ic} \propto v^{1/3} \mu^{1/3} E'^{2/3} x^{1/6} \quad \text{.....(5.15)}$$

The dependence of ΔK_{Ic} on fracture tip (or fluid) velocity and fluid viscosity is the same and proportional to ⅓rd power. In an analog comparison, the net pressure also shows the same power of dependence (¼th for Newtonian fluids) on injection rates and fluid viscosity in two-dimensional fracturing models. In case of power law fluids, the dependence is that by n/(n+2) under fluid flow conditions.

The characteristic length ξ (or same as x in Eq. 5.14) in the tip region of the fracture can be expressed in terms of flow behavior index n as follows:

$$\xi = L \left(\frac{\pi(2-n)}{2\sqrt{2}(2+n)}\right)^{\frac{n}{(2+n)}} \quad \text{.....(5.16)}$$

where, L is crack half-length. As an example, for a fracture half-height of 50 ft (15.24 m) and fluid behavior index of 0.71, ξ is obtained as 2.14 ft (0.65 m) which is nearly 1/23rd of the fracture height and is also the typically calculated ratio. For Newtonian fluids (n = 1), this ratio is nearly 1/30. This estimate, though considerably larger than the fluid-lag region obtained by other methods such as Barenblatt (1962), serves an important input as it replaces the "x" in Eq.

(5.14) and still represents the near crack-tip region. Furthermore, the simulations by SCR Geomechanics Group (1993) show that the size of the fluid lag region adjusts to meet the fracture propagation criteria. For a specific scaling or characteristic length defined as $L_h = V(K/E')^{1/n}$ by the above researchers, the following relationship for fracture width at near-tip region was presented which accounts for the elastic response of rock to the fluid pressure:

$$w = \xi^{2/(2+n)} L_h^{n/(2+n)} \left[\left(\frac{2n+1}{n} \right)^n \frac{(2+n)^2}{n} \frac{\sin(\alpha\pi)}{\cos[(1-\alpha)\pi]} - c_2(n) \left(\frac{\xi}{L} \right)^{(2+3n)/(4+2n)} \right] \quad \text{.....(5.17)}$$

where value of $c_2(n)$ is nearly 3.17 for Newtonian fluids or around $\sqrt{32/\pi}$. For Newtonian fluids this constant is around $2^{1/3} \times 3^{5/6}$. This solution thus provides a term that dominates the crack-tip region requiring smaller energy to propagate than what is required to pump the fluid into the crack.

It is known from solid-mechanics solutions that the fracture toughness and fracture net pressure share a direct relationship though connected with the square root of the ratio of fracture half-heights which is depicted in Equations (2.20) and (5.6). If the closely stacked fracture heights obtained from height-to-net pressure mapping, are nearly the same, the proportionality is ultimately rendered to that of the ratio between fluid velocities. This *ansatz* is used in pressure scaling during simulation and described in the section below.

5.3. Fracture Tip Pressures

The net pressure in the fracture can be determined with the help of Eq. (5.10) by making appropriate substitution of fracture width and inserting the fracture compliance term if the fracture responds elastically to the internal pressure (Nolte 1979, 1991). The pressure is then given as product of fracture width and local fracture stiffness *S*, which is the inverse of fracture compliance, c_F whose local value is given as:

$$c_F = \frac{\pi}{2} \frac{\beta_p}{E'} h_f = \frac{1}{S} \quad \text{.....(5.18)}$$

where, h_f is the fracture height, β_p is the ratio of average net pressure to the net pressure at the wellbore while pumping, and *E'* is the plane strain modulus. β_p is obtained as a function of power law index *n* as $(2n+2)/(3n+3+a_v)$ where, a_v ranges from 0 to 2 depending on viscosity degradation assumed (Nolte 1979). Eq. (5.10) can now be expressed in the terms of fracture tip pressure (p_o), at follows:

$$\Delta p(x) = [p_0^e + (R v_w^n x)/c_F^{n+1}]^{1/e};\ v_w = q_w/h_f w_w \quad \text{.....(5.19)}$$

where, $\Delta p(x)$ is the pressure at any point *x* in the fracture measured from the tip, $e = n+2$, and v_w is the fluid velocity obtained from volumetric flow rate per wing, q_w. Furthermore, h_f is the

fracture height and w_w is the width of the fracture at the wellbore. The fluid pressure from the viscous flow alone p_F, can be determined if the pressure at the tip of the fracture ($x = x_f$, where x_f is fracture half-length) p_o, is assumed to be nearly zero.

$$p_F = \left[\left(R v_w^n x_f\right)/c_F^{n+1}\right]^{1/e} \quad \text{.....(5.20)}$$

With proper substitutions and rearrangement of terms, the fracture net pressure Δp_f can be linked with a dimensionless ratio p_T that captures the tip effects and pumping parameters for power law fluids in a very useful equation for fracture history match modeling used in the model development. This is shown below:

$$\Delta p_f = \left(\frac{R q_w^n x_f}{h_f^n c_F^{2n+1} p_T}\right)^{1/(2n+2)} ;\ p_T = 1/[1 + (p_o/p_F)^e] \quad \text{.....(5.21)}$$

where volumetric flow rate q_w replaces fluid velocity with the inclusion of fracture height h_f in the equality. The simultaneous solution of fracture half-length and vertical height is challenging and hence must be solved using iterative techniques. For this purpose, if a tip velocity-calibrated apparent fracture toughness model is used to generate the fracture height versus net pressure relation for the given stress setup, then the calibration of such a model can be carried out with the help of p_T. With further algebraic manipulation of Eq. (5.19) to Eq. (5.21), it can be shown that for a dimensionless fracture length variable ξ' such that $\xi' = x/x_f$, where x is the measurement from the tip of the fracture to the wellbore, the net pressure distribution along the fracture can be expressed as follows:

$$\Delta p(\xi') = p_F[(1/p_T - 1) + \xi']^{1/e} \quad \text{.....(5.22)}$$

where $e = n+2$ for power law fluids. Once the value of p_T is obtained from iterative solution above, then the fracture width at wellbore can be determined from the following relation, expressed in known notations. It may be noted that wellbore width is also the product of local fracture compliance and net pressure given as $w_w = c_F \Delta p_f$.

$$w_w = \left[\frac{4K(2m)^n(n+2)q_w^n x_f}{E' h^{n-1} \phi^n p_T}\right]^{1/(2n+2)} \quad \text{.....(5.23)}$$

5.4. Fracture Propagation Modeling

Following the successful development of height growth model and its calibration with field data that is covered in Ch. 1 to 4, in the next step of model development, additional features were added to facilitate net pressure history matching aimed at studying the early time fracture height evolution and fracture tips effects. Key fracture dimensions such as width and half-length were also obtained as a function of time from the actual pumping data. To eliminate the

uncertainty in the inputs of fracture toughness, the velocity-based fracture toughness calculations developed in study and expressed by Eq. (5.14) was also included in the solution scheme.

5.4.1. Fracturing Fluid Rheology and Efficiency

The rheology of the power fluids traditionally used in hydraulic fracturing is sensitive to shear and must be accounted for as the fluid moves in the narrow fracture width. The shear rate ($\dot{\gamma}$) can be obtained as follows, if the tip-velocity and fracture width are available:

$$\dot{\gamma} = \frac{8v}{D_h\left(\frac{2n}{2n+1}\right)} \quad \text{.....(5.24)}$$

where v is the fluid velocity and D_h is the hydraulic diameter which is taken as twice the fracture width in this case. Power law indices n and K inputs can be updated continuously with fracture growth with the changes in fluid shear and corresponding viscosities, and in the static mode when the fracture toughness mapping is being generated for a given fixed injection rate or assumed tip velocity.

The fracturing fluid efficiency η, which is an indicator of how much of the pumped fluid is spent in creating and propagating a fracture versus the amount lost to the formation, plays an important role in determining net pressure which is the main driver behind the vertical growth of the fracture. This parameter must be duly accounted for in net pressure calculations. Elbel (1993) presented an expression for fluid efficiency that is independent of injection and depends on net pressure and fluid parameters such as fluid leak-off and spurt loss. A much simpler time-dependent relation that accounts for fluid leakoff (C_L) and average fracture width ($\overline{w}$) can also be used to calculate fluid efficiency and is given below:

$$\eta = \frac{1}{1+2C_L\sqrt{t_p}/\overline{w}} \quad \text{.....(5.25)}$$

The average fracture width can be easily calculated if wellbore widths are known. The efficiency is then used as an input to compute "reduced time" as described by Nolte (1991).

When developing the codes for calculating fracture height, width, and half-length it was assumed that with the introduction of elemental volume of fluid into the fracture, the net pressure will develop with the interaction of three primary actions which are : (a) insitu stresses of the payzone and surroundings, (b) resistance offered to fracture advancement by fracture toughness and (c) fluid parameters such as leakoff and viscosity. The extent of fracture growth will depend on net pressure magnitude. The influence from any other external stress source, e.g., stress interference amongst various fractures, etc. is not currently included in the model.

With the continued injection, the net pressure is expected to increase if the fluids exhibit reasonable efficiency. The net pressure will continuously test the stress barriers and play a role in fracture height estimation based on the fracture height versus net pressure mapping generated for given stress distribution along formation depth. Since the influence of tip effects is unknown at this time, it is calibrated to match the reduced-time derived net pressures with those obtained from apparent fracture toughness calculations.

The net pressure at the wellbore for the given time step was obtained as follows:

$$\Delta p_f = \frac{1}{c_F}\left[\frac{Rc_F}{\beta_p p_T}\left(\frac{q_w}{h}\right)^{n+1}\right]^{1/(2n+3)} (t^*)^{1/(2n+3)} \quad \text{.....(5.26)}$$

Similarly, fracture half-length was calculated using the following equation:

$$x_f = \frac{1}{\beta_p}\left[\frac{\beta_p p_T}{Rc_F}\left(\frac{q_w}{h}\right)^{n+2}\right]^{1/(2n+3)} (t^*)^{(2n+2)/(2n+3)} \quad \text{.....(5.27)}$$

Fracture width at the wellbore as function of time was estimated with the help of following:

$$w_w = \frac{4}{\pi}\left[\frac{Rc_F}{\beta_p p_T}\left(\frac{q_w}{h}\right)^{n+1}\right]^{1/(2n+3)} (t^*)^{1/(2n+3)} \quad \text{.....(5.28)}$$

In all the above equations, Eq. (5.26) to (5.28), $t^* = \eta t_e$ is the reduced time that depreciates the exposure time to account for fluid efficiency, with t_e being the actual exposure time of the given fluid on a given formation layer. The set of equation presented above are sufficient to develop a fracture growth model that can predict fracture growth in field cases.

5.5. Extensions to Model – History Match Simulator

The previous height-growth prediction model was extended (Pandey and Rasouli 2021b) to incorporate the post stimulation analysis features to conduct in depth study on how the fracture height evolves during a stimulation treatment. The fracture height versus net pressure height provides an insight into how the fracture height could potentially evolve, but instead of hypothetical net pressures if actual net pressures are input with respect to time, a clearer fracture growth pattern will emerge. The model development workflow is summarized as follows:

Step 1. Generate apparent fracture toughness matrix for the layered model to assist in creating fracture height growth versus net pressure mapping instead of using generic values,

Step 2. Simulate time-dependent fracture pressure using actual injection rate and fluid properties while applying corrections to the tip-velocity calculation dynamically, and

Step 3. Obtain the fracture height growth history and other relevant output.

5.5.1. Step 1: Generate Fracture Toughness Matrix

To carry out the first step, processed downhole logs that contain depth, stress, elastic modulus, and Poisson's ratio are used as input in a layered format. The input data must also contain petrophysical data such as porosity, permeability, formation compressibility and others to enable help in preliminary estimates of fluid leakoff. It is however not mandatory to input fracture toughness at this point.

With all the necessary information available, the effective (or apparent) fracture toughness is obtained using Eq. (5.14) where the value of characteristic length x is replaced by ξ whose solution is presented in Eq. (5.16). The apparent fracture toughness (hereon only mentioned as "fracture toughness") array is calculated for every fracture location and height combination and it is expected to change as the fluid velocity changes with the change in flux (q/h) and fracture width. The fluid velocity v which is assumed at the start of calculations (generally 0.5 to 1.5 ft/s), and the flux is recalculated as the new fracture heights are added to the solution set. The corresponding widths in crack-tip region are obtained from Eq. (5.17). The fracture toughness array for each height solution is retained to assist in solution process later.

5.5.2. Step 2 and Step 3: History match to obtain fracture height

The workflow of the second and third steps are listed below:

1. From treatment data, construct a BH pump schedule with rate and fluid property data.
2. For every time step (a) compute effective shear rate using Eq. (5.24); parameters V and D_h are determined using iterative process, and (b) update fluid viscosity for shear rate.
3. To start the calculation process, (a) set the fracture height equal to that of pay zone and calculate the net pressure using Eq. (5.21), using corresponding injection rate and fluid rheology parameters, local fracture compliance from Eq. (5.18), and fracture half-length from Eq. (5.27), and (b) use this net pressure to update the fracture height from distance versus net pressure mapping such as shown in Fig. 3.2 after applying fluid-velocity based correction to net pressure.
4. The net pressure from the Eq. (5.21) and the velocity-corrected net pressure are not expected to match, hence use , p_T in Eq. (5.21) as the calibrating parameter to converge their values. Update n, K' and $\dot{\gamma}$ after every time step.
5. With most inputs now known, calculate net pressures using Eq. (5.26). Note that there may be small differences in results if Eq. (5.21) which accounts for time dependence with the help of fracture half-length, is used instead. Obtain injection rate q and time

t_e from pump schedule, fracture height and compliance from initial net pressure/height/compliance mapping, R from current value of n, and the fluid behavior dependent variable, β_p using the relation described in the text above.

6. Calculate fracture half-length from Eq. (5.27) and wellbore width from Eq. (5.28).
7. Calculate average fracture width from wellbore fracture width and update the fluid efficiency of Eq. (5.25). The effective leak-of C_L is a height averaged leakoff of all the layers now exposed to the latest value of fracture height and t_p is the total injection time till the time step under consideration.

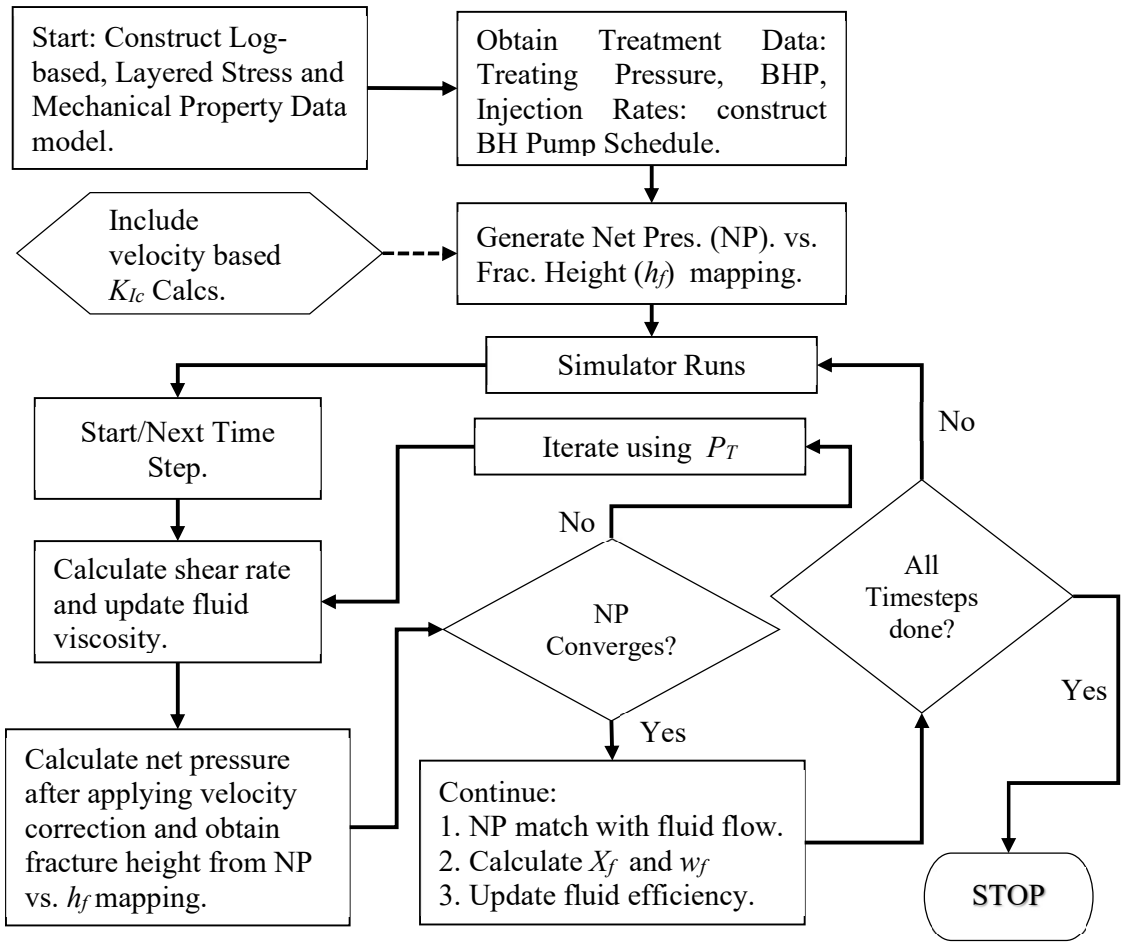

Fig. 5.1: Flow chart showing the workflow of pressure history match calculations.

The flow chart in **Fig. 5.1** illustrates the various steps of history matching modeling process and workflow adopted in the study. The calculations account for fluid leakoff and hence the efficiency in two principal ways. The first method employs inclusions of layered leakoff properties by effective book-keeping of all the layers the fracture has touched and its

corresponding length in those layers, whereas the second approach uses a height-averaged leakoff coefficient as an approximation. The calculations did not reveal a significant difference between the two approaches since the effect of leakoffs are proportional to square root of time. For smaller duration of injection i.e., periods less than 2 to 3 hours, the latter approach was found to be effective and computationally efficient.

To ensure a smooth outcome from the iterative process at every time step (i.e., uniformly increasing/decreasing/constant fracture pressures), the initial guess of p_T was taken as the same value for which a solution was obtained in the previous time step. However, when using this technique, the solution must run ample loops for the error to be rendered to near zero values to prevent cumulative errors in the successive solution. Average error in model output was 1×10^{-6} % and computation time for 30 min of per second data (~1600 rows) is around 5 seconds. It was noted that extremely large values of leakoff (e.g., > 0.1 ft/min$^{0.5}$) can cause instability in calculations which is also observed in many commercial software.

5.6. Case Studies

The pressure history simulator was tested on several case studies, a few of which are presented here. Additional details can be found in Pandey and Rasouli (2021b).

5.6.1. Vertical Well: Low Pressured Sandstone Completion – Case 1

The primary reasons for selecting this case study were (a) presence of dead string that allowed constant monitoring of bottomhole injection pressures, and (b) the injection rates were increased gradually at the start of the treatment that aided in estimating evolution of fracture height growth from onset of the treatment. Below are the model properties and inputs.

Number of layers in the stress model	44
Payzone Stress	3,848.5 psi (26.5 MPa)
Average Stress	4,203.0 psi (29.0 MPa)
Fracture initiation layer thickness	5.3 ft (1.62 m)
Average layer thickness	6.76 ft (2.1 m)
Average Young's Modulus (pay)	2.4×10^6 psi (16.5 GPa)
Average Poisson's Ratio (pay)	0.29
Average Fracture Toughness	1,300 psi.in$^{0.5}$ (4,948.5 kPa.m$^{0.5}$)
Payzone True Vertical Depths (TVD)	5,545 to 5,555.4 ft (10 ft thick)

TABLE 5.1: Formation properties used as input in Case 1.

The well was completed with 4 ½ in. (114.3 mm) casing set at 5,750 ft (1,752.6 m) with a 1.9 in. (48.2 mm) velocity string hung packer-less above the perforation depth of 5,540 ft (1,688.6 m). The treatment was pumped at 22.0 bbl/min (0.058 m^3/s)down the annulus of casing and tubing string thus providing a dead string for BHP measurements; the displacement volume to the top of the perforations was around 70.5 bbl (11.21 m^3). The fracture gradient was calculated as 0.71 psi/ft (16.15 kPa/m). Initial wellbore fluid was circulated out and displaced with 2% by wt. solution of potassium chloride (KCl). A diagnostic injection test was then performed with 30 lbm/Mgal (3.6 kg/m^3) linear gel that was flushed to the perforation depth with a linear gel of identical loading.

The cross-linked fluid rheology was reported in the field as *n* of 0.4 and viscosity of 320 cP (0.32 Pa.s) at 100 s^{-1}, which results in consistency index (*K*) of 0.1059 lbf-$s^{0.4}$/ft^2 (5.1 Pa.$s^{0.4}$). This data, along with actual pump schedule was input in a regular fracture simulator to generate the match, mostly to ensure that the stress model was reasonable. The leakoff calibrated from pressure match was nearly 0.00168 ft/$min^{0.5}$. The result from the match is shown in **Fig. 5.2**. The BH injection and net pressure matches are shown by the curves "BHP_Match" and "NetPr". The formation face pressure (FFP) is same as the fracture inlet pressure and is used in determining net-pressure.

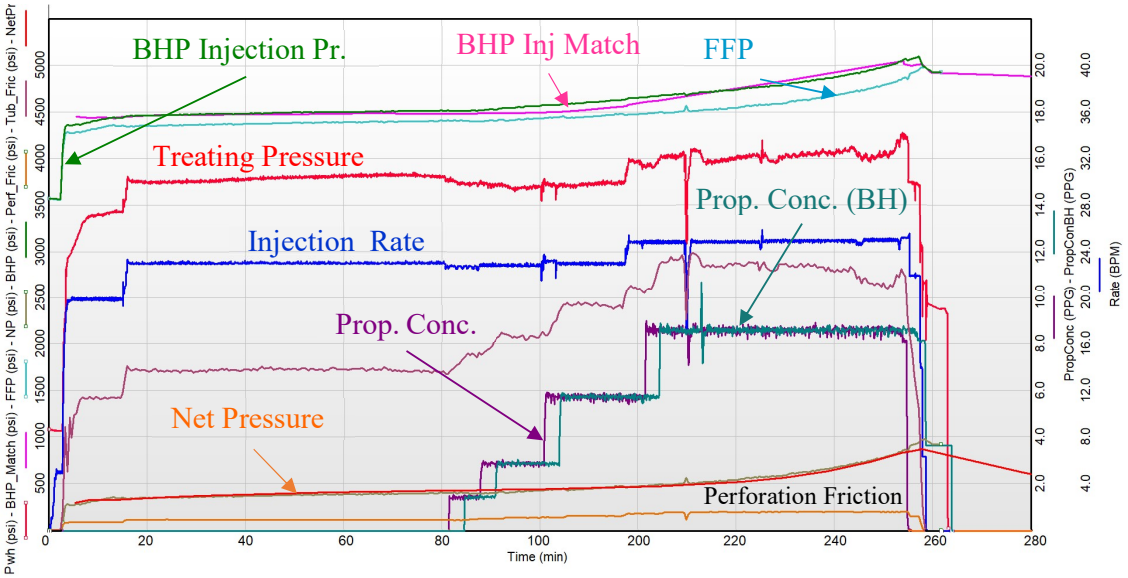

Fig. 5.2: Pressure, injection rate and proppant concentration plot for treatment of Case 1.

To generate the fracture height versus net pressure mapping, the layered fracture toughness was set to zero value in absence of pertinent data but expected fracture tip velocity was set to values ranging from 0.29 to 1.0 ft/s (0.09 to 0.31 m/s). The resultant plot is shown in **Fig. 5.3**,

where the upper and bottom tip of the fractures are shown as the distance from the center of the fracture. The fracture heights were generated in 1.0 ft (0.31 m) interval and when plotted against depth, appear to show nearly uniform distribution in both the upper and lower section, with the center of the fracture staying close to the injection point. The maximum fracture height possible for the given stress profile is 215 ft (65.5 m) for a net pressure of nearly 455 psi (3.13 MPa). Fracture compliance for corresponding fracture height and location pair were calculated with the help of Eq. (5.18), for use in the next step.

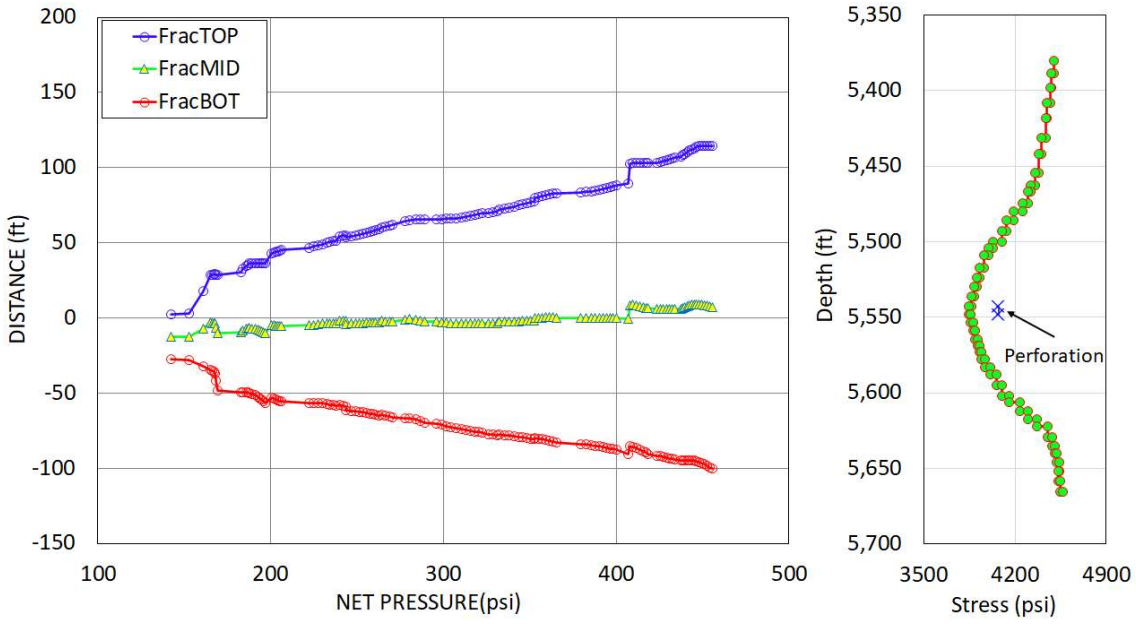

Fig. 5.3: Fracture height and location versus net pressure plot for Case 1.

The simulated fracture height values for fracture toughness values of 0 and 1000 psi.in$^{0.5}$ (1099.0 kPa.m$^{0.5}$) were also generated for comparison purposes and are shown in **Fig. 5.4**. The fracture height based on the fracture toughness based on velocity model is also presented. The fracture growth pattern for uniform fracture toughness cases is identical with the only difference being the pressure offset which represents the strength of singularity for the given case. The curve (green) obtained for the final fracture height, using velocity-based fracture toughness method, bears a similar profile also but leans towards the values obtained for K_{IC} = 1000 psi.in$^{0.5}$. The curves also demonstrate that with an increase in fracture toughness (from L to R), more net pressure is required to attain the same height. Finally, the fracture height versus net pressure relationship observed from the actual simulation is shown by yellow triangles which indicate good agreement with modeled values and also falling in the reasonable fracture toughness range of 0 to 1,000 psi.in$^{0.5}$.

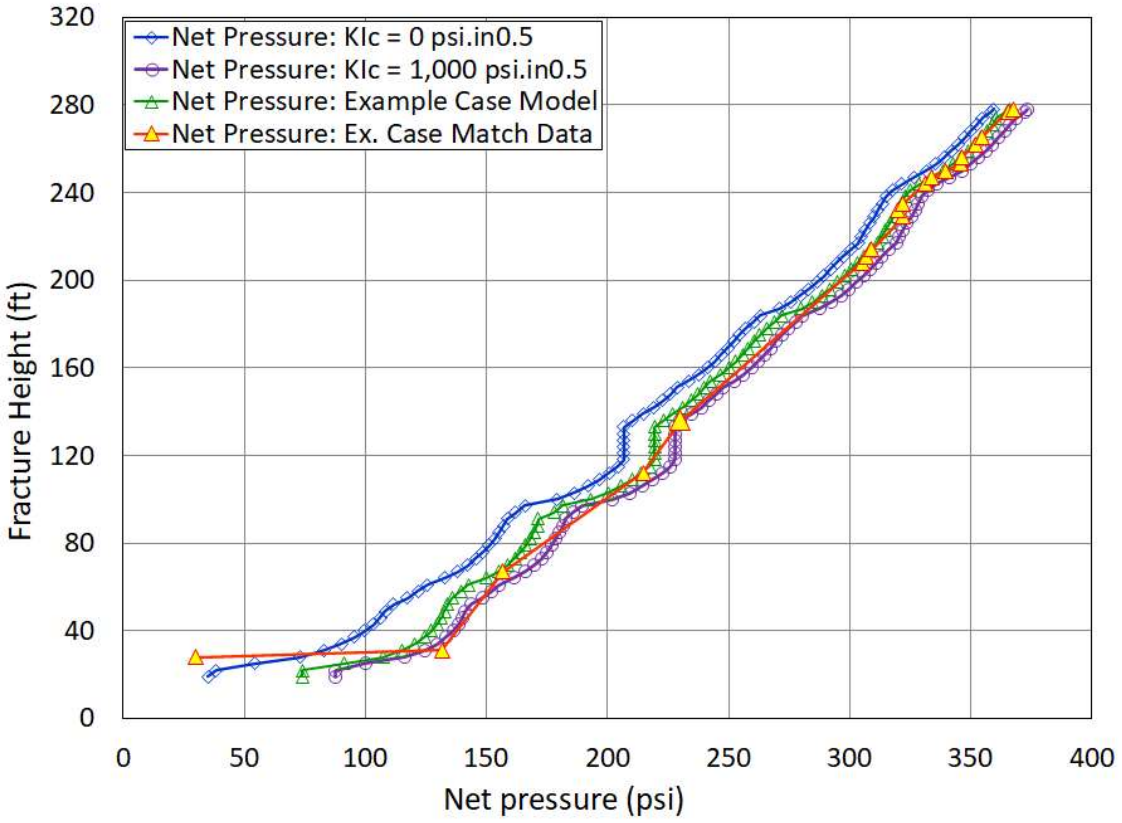

Fig. 5.4: Fracture height vs. Net pressure curves for various fracture toughness values.

5.6.1.1.Pressure History Simulation

The history-matched net pressure data obtained from the newly developed simulator is shown in **Fig. 5.5**. The main objective here was to study the fracture height growth evolution in the early time since the early time data is generally not handled very accurately by most commercial simulators. The pressure data shows a reasonable match of simulated net pressure with the observed values. Since the model is not programmed to account for changes in net pressure in presence of proppants in the fracture, the simulation was run till the point where the proppant enters the fracture.

With the rapid increase in injection rates, the fracture attains a height of 125 ft (38.1 m) in 3.6 minutes of the treatment even with a low viscosity (1.0 cP) wellbore fluid. With continued injection and eventual switching to cross-linked fluid, the fracture height gradually increases to 165 ft (50.3 m) as the net pressures increase to 365 psi (2.52 MPa) after 16 minutes into the treatment. Since the net pressure is continuously increasing, the simulated fracture height will also show an increase in accordance with the relationship shown in Fig. 5.3 ultimately reaching nearly 198 ft (60.4 m) prior to the proppant onset in the formation. The fracture half-length increases proportionately and extends to nearly 515 ft (157.0 m).

5.6.1.2. Comparison of Model Output with Commercial Simulator

The results from the simulator developed in the study were compared with those obtained for identical inputs, from some of the commercially available numerical fracture simulators that employ a pseudo-3D or fully 3D solution scheme. This exercise was conducted to ensure that the results predicted by the semi-analytical simulator were within the reasonable range of the ones output by typical numerical simulators. One such comparison is shown in Fig. 5.5 for one of those simulators where the P3D simulator outputs are shown by dashed curves that connect the discrete data points described in the legend.

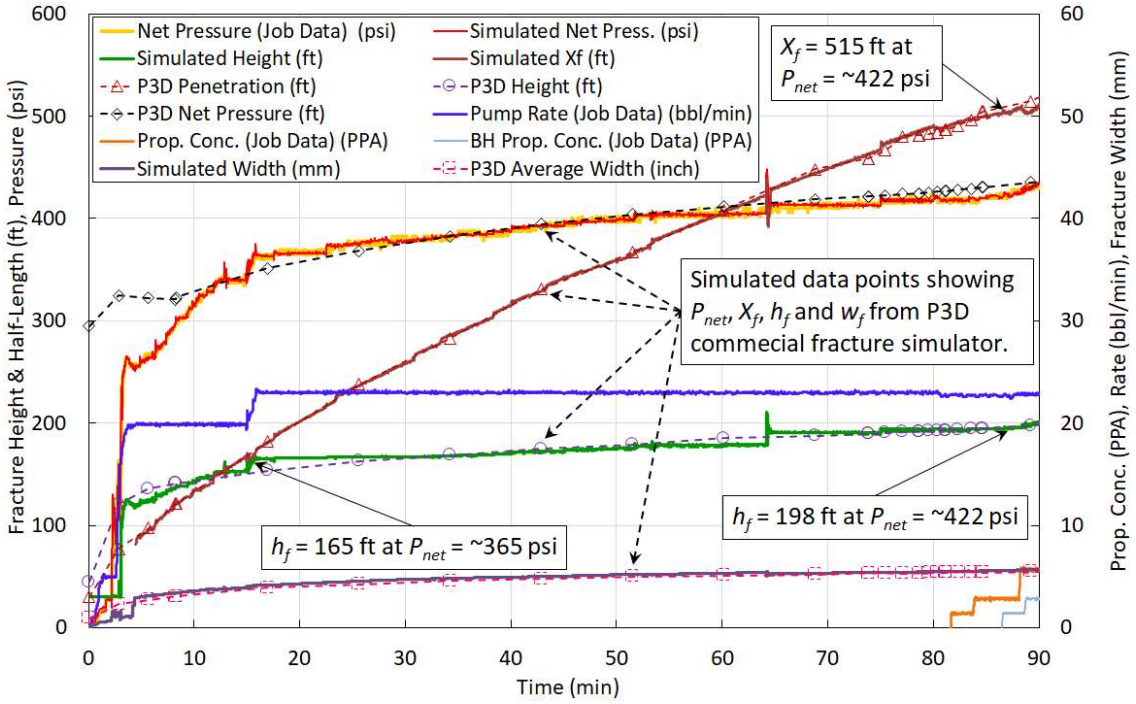

Fig. 5.5: Net pressure history match showing fracture height evolution for Case 1.

The data points from simulator outputs were obtained after history matching the bottomhole injection pressure and net pressure by this simulator and shown in Fig. 5.2 for net pressure (P_{net}), fracture half-length (X_f), fracture height (h_f), and fracture width (w_f). Whilst the commercial simulator matches most of the recorded net pressure accurately, the match in the initial period (<10 min) is not exact. Contrary to this, the output from the newly developed simulator offers a more accurate and systemic representation of how the net pressure and the corresponding fracture height may have evolved given the small initial injection rates. Apart from initial mismatch where the current model outputs details fracture evolution patterns, the simulator is also able to successfully replicate the evolution of P_{net}, X_f, h_f, and w_f simulated by the numerical P3D simulator.

Some of the key observations made during the pressure history matching are listed below:

1) Longer fracture half-lengths are simulated if low viscosity fluids are used.
2) Low viscosity fluid has negative effect on the fluid efficiency due to higher leakoff.
3) With increase in viscosity, X_f tends to increase at a slower pace but the h_f may increase if P_{net} has not reached the maximum value defined in the h_f versus P_{net} mapping.
4) The fluid behavior index affects the incremental changes in fracture parameters.

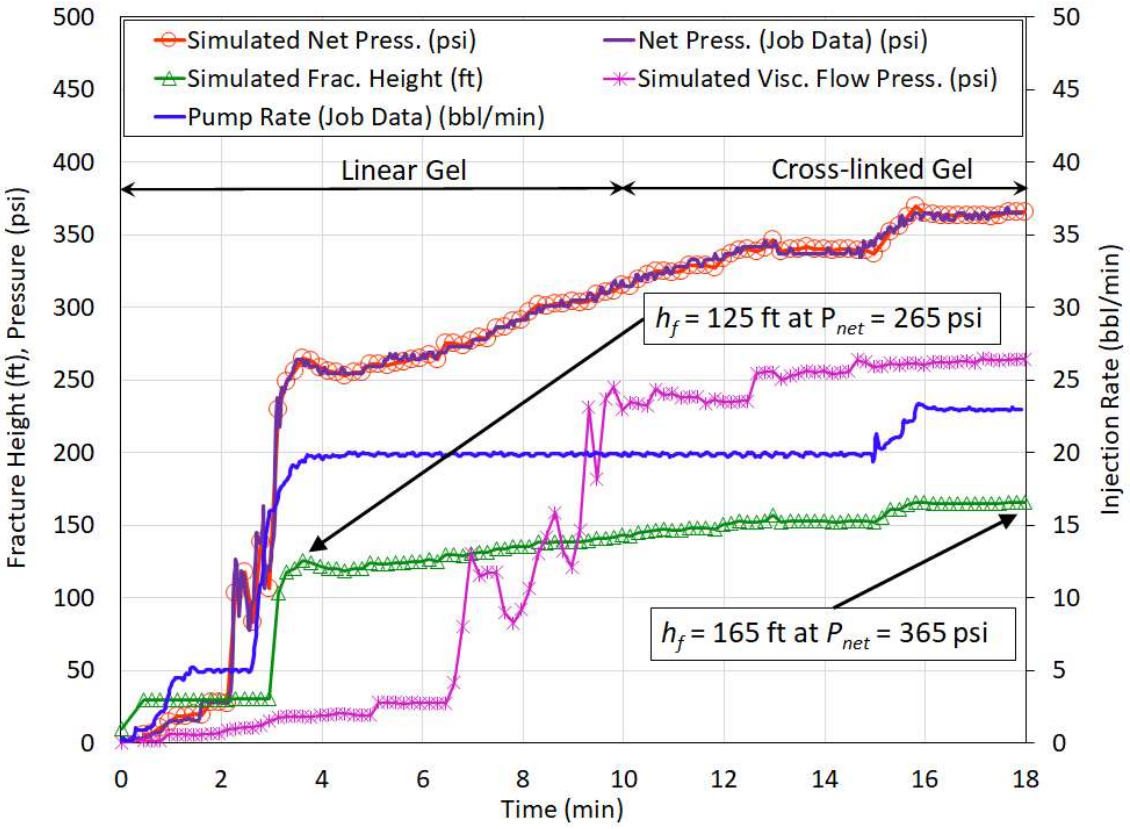

Fig. 5.6: Early time fracture height evolution for Case 1 from the new simulator.

5.6.1.3.Fracture Height Growth Development

The very early (< 1.0 min) part of the net pressure match is obtained using the simulator developed in the study, with higher-than-average fluid leakoff values as would be expected. The simulation shows that the fracture height was relatively contained in the first 2 minutes of injection where low viscosity near-Newtonian type wellbore fluid is entering the fracture. With the increase in injection rates however, the net pressure generation is quick, and this accelerates the fracture vertical growth. With nearly 3.6 min into the treatment and with injection of nearly 20 bbl (3.2 m^3) of wellbore fluid injected in the formation, a fracture height of nearly 125 ft (38.1 m) is simulated, for a corresponding net pressure of 265 psi (1.83 MPa) as shown in **Fig.**

5.6. The red hollow-circles representing the matched net-pressure, show a good agreement between observed (solid purple curve) and simulated values. Based on the simulation, it may be noted that *nearly 65% of the total fracture height growth occurs within the first few minutes of the treatment*. The increase in injection rate and a corresponding increase in net pressure around 15 min in the treatment with the fracture height that is now nearly constrained, the continued increase of net pressure reflects viscous fluid movement inside the fracture, especially after 10.0 min when the cross-linked viscous fluid enters the formation. As the fluid rheology stabilizes around 13.0 min, even a rate increase to 23.0 bbl/min (0.061 m^3/s) does not result in appreciable net pressure increase.

5.6.1.4.Fracture Half-Length Evolution

The time-dependent fracture half-length is calculated with the help of Eq. (5.27) and compared with the height-weighted average of fracture extension in all the layers; the calculations in the latter case include fluid losses to various layers for corresponding exposure times. With increasing injection rates, the fracture half-length should also increase because of its direct dependence on flux $(q/h)^{(n+2)/(2n+3)}$ and elapsed time at $t^{(2n+2)/(2n+3)}$, provided the fluid leakoff is limited or under control. This behavior is seen once the fracture height "stabilizes" around 165 ft (50.3 m) and the injection takes place at near constant rate of 23.0 bbl/min (0.061 m^3/s). During the pressure history matching process, it was realized that it is important to account for early -time data and preferably perform the initial simulation steps at smaller time interval to characterize the fracture development because the fracture can grow rapidly at the start of the treatment.

5.6.1.5.*Fracture Tip Effects*

The influence of tip pressure on overall fracture pressures can be obtained with the help of variable p_T described in Eq. (5.21). Due to the uncertain nature of this variable, it was also used as calibrating parameter because unless a negligible pressure (p_o) at the fracture tip ($x = 0$ at x_f) is assumed, its value cannot be obtained explicitly. Results from various simulations clearly showed that once the fracture vertical growth occurs in initial period, the value of p_T diminishes considerably implying a fracture propagation that was dominated by viscous pressure and not so much by the tip effects. This behavior is also seen in the viscous pressure curve (represents flow pressure near tip region only and hence is less than total net pressure) of Fig. 5.6, that is affected by change in injection rates, especially in the early part of the treatment. With constant injection rates and fluid properties, its influence is near constant, especially after 3.5 min in the treatment.

The viscous pressures are yet to influence the pressure behavior at the very beginning of the treatment in most cases, and here is where the fracture tip effects dominate the fracture extension. Eventually as the viscous non-Newtonian type fluid enters the fracture, the contribution of viscous-flow related pressures to net pressure generation far exceeds the now diminishing solid mechanics-based tip pressure values. The plot in **Fig. 5.7** is generated using Eq. (5.22) after accounting for β_p, for various dimensionless length ratios along the fracture, where ξ' =1 is at the fracture inlet and $\xi = 0$, is at the tip of the fracture. The various curves show the presence of stress singularity and even near-zero tip pressures at a characteristic distance that is short of the actual fracture-tip in cases where $p_T > 1.0$. As the value of p_T reduces, the pressure at the tip of the fracture is no longer zero but has some finite value represented by the local viscous pressure p_F itself. This is reflected by the curves "PT= 0.984 and Pnet = 14.5 psi" and "PT= 0.891 and Pnet = 15.3 psi"in Fig. 5.7 where the gap between viscous pressure front and the fracture tip appears to close completely.

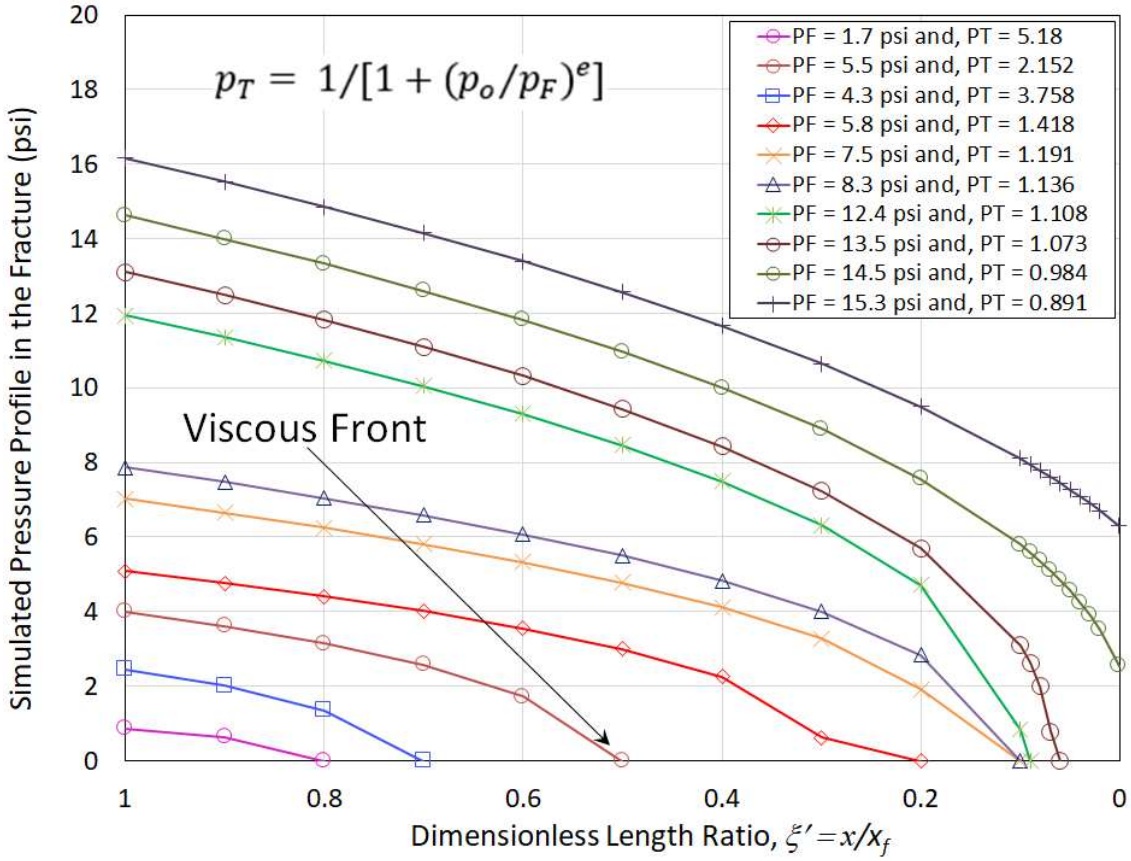

Fig. 5.7: Movement of viscous pressure front with respect to the fracture tip for Case 1.

5.6.2. Vertical Well: Low Pressured Sandstone Completion – Case 2

This field case study pertains to a 30-quality liquid CO_2 assisted treatment pumped down the annulus of a 4 ½ in. (114.3 mm) casing and a velocity string, with the latter to serve as dead-string during the treatment and helpful in obtaining BHP. The pay, primarily a low permeability (<0.1 md) sandstone, was located at a depth of 6,320 ft (1,926.3 m) having an average Young's Modulus of 3.88×10^6 psi (26.75 GPa) and a Poisson's ratio of 0.27. The YM was determined from calibration injection test. An average fracture gradient of 0.69 psi/ft (15.61 kPa/m) was obtained from decline analysis. The leakoff estimated from pressure decline and history match was a low value of 0.000154 ft/min$^{0.5}$ which explains the near-constant pressure value after shut-in at 20 minutes in **Fig. 5.8**. The various data curves have similar descriptors as Fig. 5.2.

Number of layers in the stress model	39
Payzone Stress	4,326.4 psi (29.83 MPa)
Average Stress	4,718.1 psi (32.53 MPa)
Fracture initiation layer thickness	10.0 ft (3.08 m)
Average layer thickness	20.41 ft (6.22 m)
Average Young's Modulus (pay)	3.08×10^6 psi (21.1 GPa)
Average Poisson's Ratio (pay)	0.30
Average Fracture Toughness	4,500 psi.in$^{0.5}$ (17,129.0 kPa.m$^{0.5}$)
Payzone True Vertical Depths (TVD)	6,295 to 6,305 ft (10 ft thick)

TABLE 5.2: Formation properties used as input in Case 2.

Following the step-by-step procedure established, the model was populated with layered data and a fracture tip distance versus net pressure plot was developed based on velocity-based layered fracture toughness values. The average toughness value was nearly 4,500 psi.in$^{0.5}$ (17,129.0 kPa.m$^{0.5}$) for average velocity of 1.5 ft/s of fluid n' of 0.39 and viscosity of 350 cP at average shear rate of 70 s^{-1}. The plot shown in **Fig. 5.9** shows the expected fracture growth profile with fractures potentially reaching a height of nearly 288 ft (87.8 m) for a net pressure of 610 psi (4.21 MPa). The is a tendency of fracture to have more downward growth once the barrier strength of higher stress layer from 6,450 to 6,490 ft (1,966.0 to 1,978.2 m) is overcome.

The treatment history match of net pressure with the current model results in a net pressure gain of 400 psi (2.76 MPa) after 12 min of injection as show in **Fig. 5.10** where the simulated fracture height is nearly 165 ft (50.3 m). The initial wellbore 2% KCl brine is displaced by a

delayed zirconate cross-linked foam-assisted fluid that enters the perforations around 8 min where a change in net pressure slope is also seen. Simulated fracture height reaches nearly 143 ft (43.6 m) in the first minute of injection given the low leakoff formation which supports rapid net pressure build up.

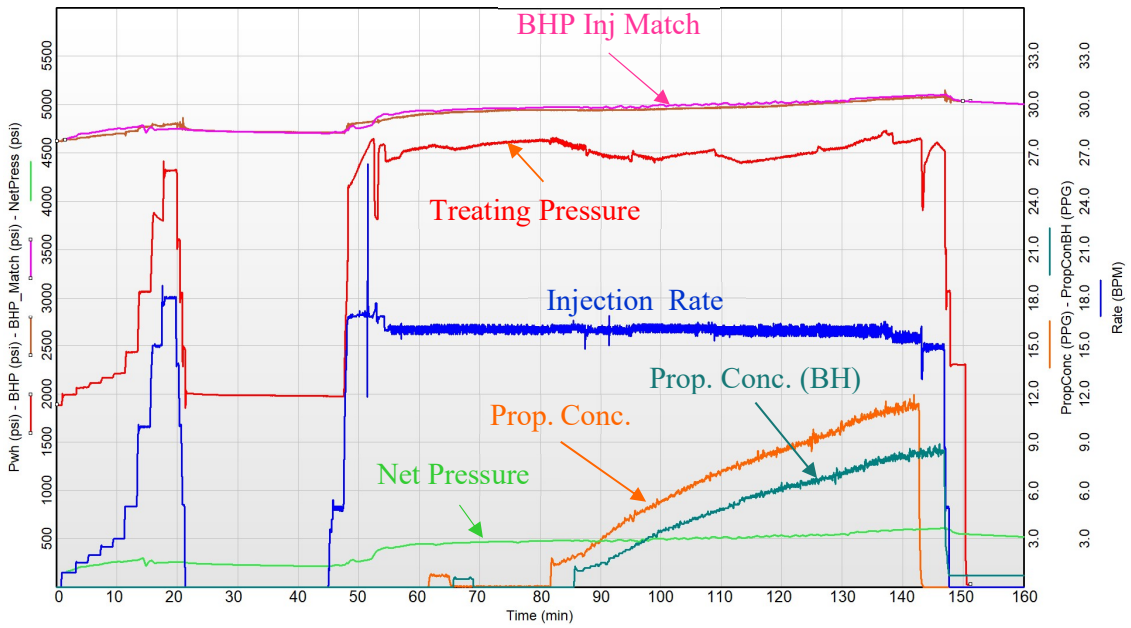

Fig. 5.8: Pressure, injection rate and proppant concentration plot for treatment of Case 2.

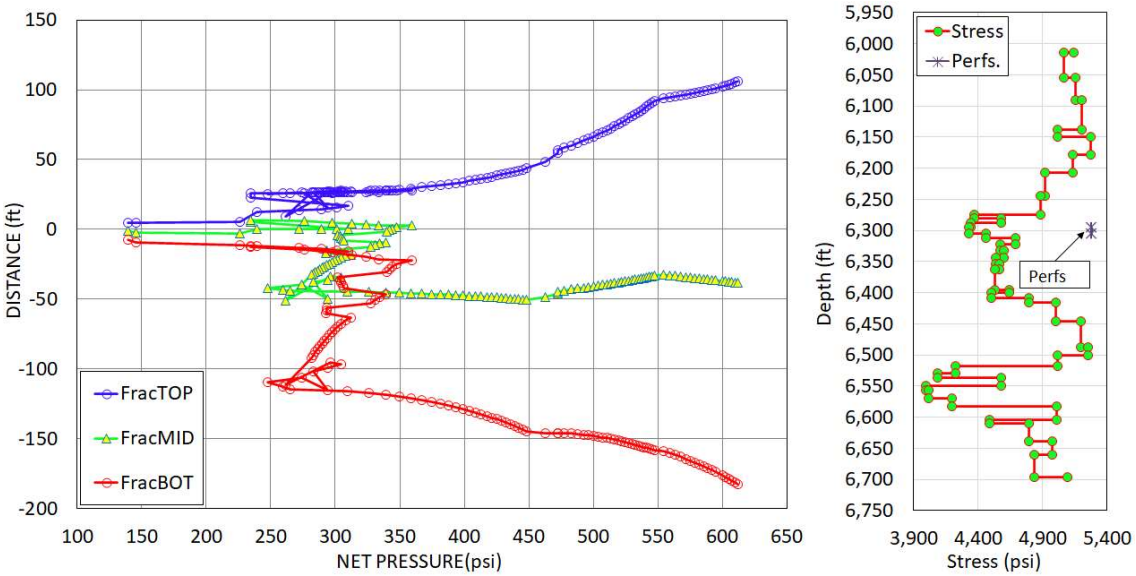

Fig. 5.9: Fracture height and location versus net pressure plot for Case 2.

The net pressure data from the treatment was history-matched till the onset of proppant in the formation. The effect of proppant "slug" injected in the middle of the pad, around 15 min as shown in **Fig. 5.11** on fracture growth containment or on net pressure evolution is ignored here. The fracture height continues to increase with the continuous increase of net pressure with the extent primarily dictated by the distance versus net pressure relationship established earlier in the modeling phase. At the end of 30 min of injection, a fracture vertical growth of nearly 195 ft (59.44 m) is simulated. There is minimal net pressure gain after this point indicating an onset of equilibrium conditions which can limit the fracture dimensions. In case the fracture toughness is set to zero, the fracture may understandably grow at a higher pace even for lower simulated net pressures. The simulated net pressure curve of K_{Ic} = 0 psi.in$^{0.5}$ is shown to depict the effect of fracture toughness in net pressure calculations; such inputs can lead to incorrect estimation of fracture heights and must be avoided during modeling process.

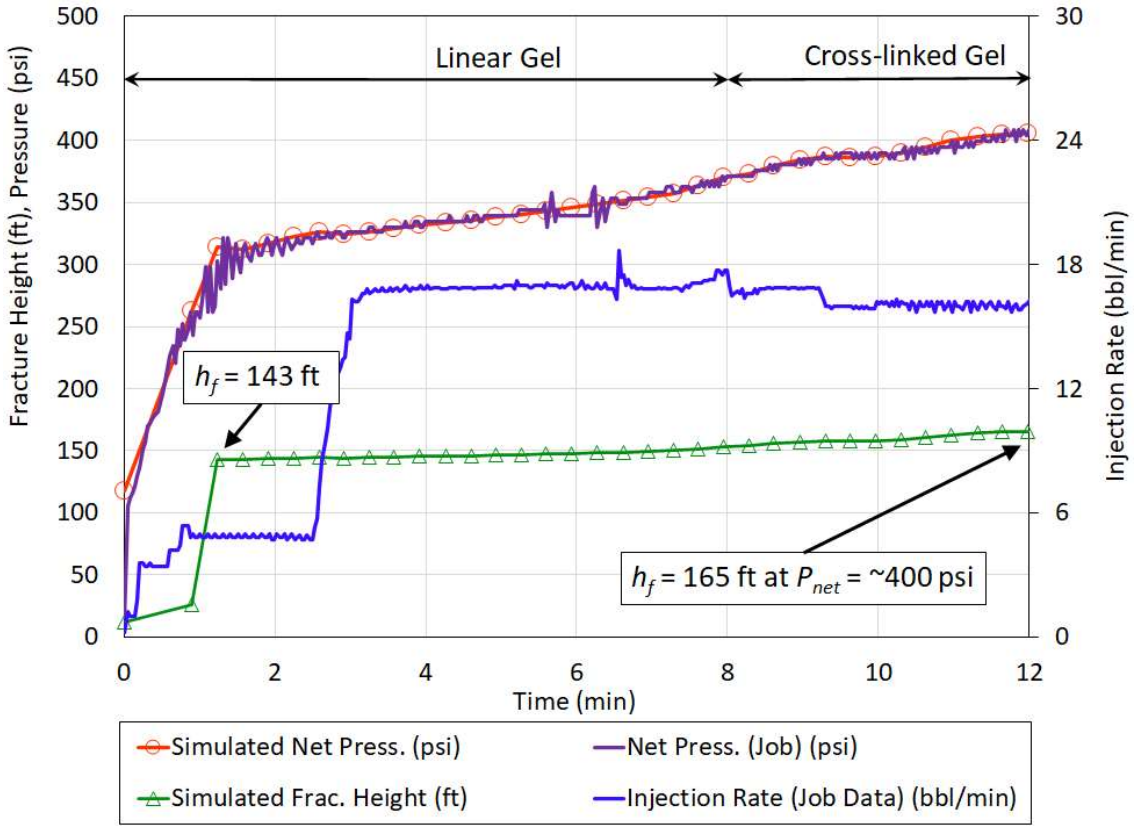

Fig. 5.10: Fracture height and location versus net pressure plot for Case 2.

The model enhancement in this phase of the study led to better characterization of how the fracture height evolves during the treatment. The uncertainty of fracture toughness was addressed by formulating a fracture tip velocity model that calculates apparent fracture

toughness and it is a useful tool in developing the relationship between fracture toughness and height even for non-Newtonian fluids.

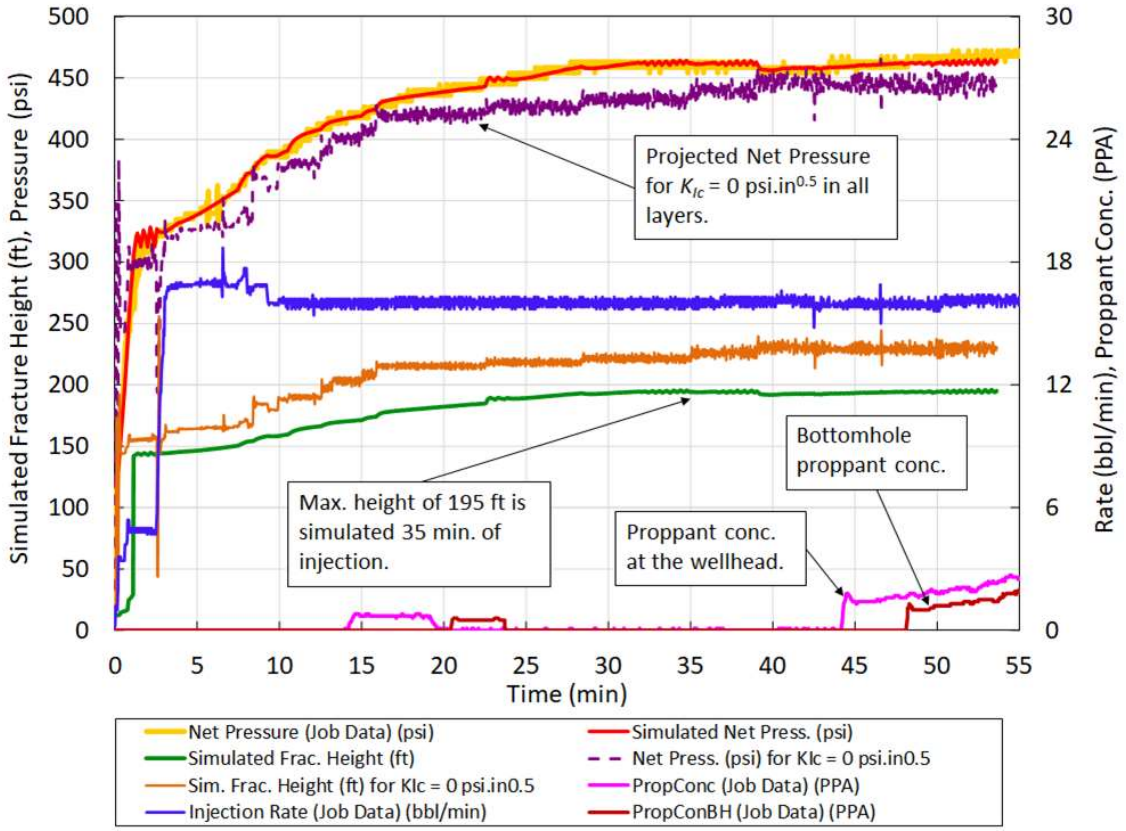

Fig. 5.11: Net pressure history match showing fracture height evolution for Case 2.

The predictive model was also used successfully in history matching process and clearly showed that nearly 65 % of fracture height growth occurred in the first few minutes of the treatment, an observation that is also supported by data such as microseismic survey gathered in the field. The increase in fracture height was occured even with a low viscosity fluid such as wellbore fluid and hence appears to be more dependent on injection rate. *If the fracture height must be controlled, the injection rates must be increased gradually in the beginning of the treatment*.

The analysis of simulation data also shows that tip effects tend to dominate only in the early treatment phase, especially in cases where highly viscous fluids are used for propagating the fracture. The gap between the viscous front and fracture tip is wide at the beginning but with time as the fracture dimensions increase with the increase in net pressure the viscous fluid front is seen to be in proximity of the fracture tip.

5.7. Nomenclature

a = radius of crack, crack half-length, fracture half-height, $M^0L^1t^0$, ft (m)

a_v = viscosity calibrating parameter, dimensionless

A = amplitude in Eq. (5.7), strength of singularity, $M^1L^{-0.5}t^{-2}$, psi-in.$^{0.5}$ (Pa.m$^{0.5}$)

c_F = fracture compliance, $M^{-1}L^2t^2$, ft/psi (m/Pa)

C_L = leakoff coefficient, $M^0L^1t^{-0.5}$, ft/min$^{0.5}$ [m/s$^{0.5}$]

$c_2(n)$ = constant, function of power law index, Eq. (5.17), dimensionless

d = characteristic length, $M^0L^1t^0$, ft (m)

$d\Delta p/dx$ = flowing pressure gradient along the fracture. Eq. (5.9), $M^1L^{-2}t^{-2}$, psi/ft (Pa/m)

D_h = hydraulic diameter, $M^0L^1t^0$, ft (m)

e = function of power law index, e = n+2, dimensionless

E' = plane strain modulus, $M^1L^{-1}t^{-2}$, psi (Pa)

h, h_f = fracture height, $M^1L^1t^0$, ft (m)

K_I = stress intensity factor, $M^1L^{-0.5}t^{-2}$, psi-in.$^{0.5}$ (Pa.m$^{0.5}$)

K_{Ic} = critical stress intensity factor or fracture toughness, $M^1L^{-0.5}t^{-2}$, psi-in.$^{0.5}$ (Pa.m$^{0.5}$)

ΔK_{Ic} = apparent fracture toughness, $M^1L^{-0.5}t^{-2}$, psi-in.$^{0.5}$ (Pa.m$^{0.5}$)

K = power law fluid consistency index, $M^1L^{-1}t^{n-2}$, lbf-sec^n/ft^2 (Pa.s^n)

L = crack half-length, $M^0L^1t^0$, ft (m)

L_h = characteristic length, $M^0L^1t^0$, ft (m)

m = variable – function of power law index shown in Eq. (5.11), unitless

n = power law fluid flow behavior index, dimensionless

p_F = viscous flow pressure, $M^1L^{-1}t^{-2}$, psi (Pa)

p_o = fracture tip pressure, $M^1L^{-1}t^{-2}$, psi (Pa)

p_T = influence of facture tip on fracture pressure, dimensionless

$p(x)$ = crack face traction (Fig. 3), $M^1L^{-1}t^{-2}$, psi (Pa)

P_f = fracture pressure, $M^1L^{-1}t^{-2}$, psi (Pa)

q = injection rate, $M^0L^3t^{-1}$, bbl/min (m^3/s)

q_w = volumetric flow rate per wing, $M^0L^3t^{-1}$, bbl/min (m^3/s)

R = constant describe in Eq. (5.10), $M^1L^{-1}t^{n-2}$, lbf-sec^n/ft^2 (Pa.s^n)

S = stiffness, $M^1L^{-2}t^{-2}$, psi/ft (Pa/m)

t_e = exposure time of fluid to a given formation, $M^0L^0t^1$, min (s)

t_p = injection time or pump time, $M^0L^0t^1$, min (s)

t^* = reduced time function, $M^0L^0t^1$, min (s)

u_1, u_2 = displacements in respective directions, $M^0L^1t^0$, in. (m)

v = average cross-sectional velocity, tip-velocity in y direction, $M^0L^1t^{-1}$, ft/sec (m/s)

V = vertical velocity of horizontal fracture, $M^0L^1t^{-1}$, ft/sec (m/s)

w, w_w = width of fracture, $M^0L^1t^0$, in. (mm)

$\bar{w}$ = average width of the fracture, $M^0L^1t^0$, in. (mm)

$w(x)$ = width along the crack in x direction, $M^0L^1t^0$, in. (mm)

x_1,x_2 = distances along crack axis in horizontal x-axis, $M^0L^1t^0$, ft (m)

x = distance from the tip at axis-crack, Eq. (5.7) to (5.9), and (5.12), $M^0L^1t^0$, ft (m)

x_f = fracture half-length, $M^0L^1t^0$, ft (m)

x^* = difference between arbitrary distance along x-axis & half-length, $M^0L^1t^0$, ft (m)

y = vertical displacement, $M^0L^1t^0$, in. (m)

z = any value in displacement along the axis of the crack, $M^0L^1t^0$, ft (m)

$\bar{z}$ = conjugate of complex variable z presented in Eq. (8).

Z = complex stress function Eq. (2), $M^1L^{-1}t^{-2}$, psi (Pa)

Z' = complementary of Z stress function Eq. (2), $M^1L^{-1}t^{-2}$, psi (Pa)

$\bar{Z}, \bar{\bar{Z}}$ = integrals with respect to arbitrary variable z.

α, $\alpha(n)$= exponent, function of n, dimensionless

β_p = net pressure ratio, dimensionless

$\Delta p(x)$ = pressure at any point x in the fracture measured from the tip, $M^1L^{-1}t^{-2}$, psi (Pa)

Δp_f = fracture net pressure, $M^1L^{-1}t^{-2}$, psi (Pa)

ΔP = fracture net pressure, $M^1L^{-1}t^{-2}$, psi (Pa)

$\phi(n)$ = dimensionless width over fracture cross-section, dimensionless

$\phi(z)$ = potential function resulting in stress, $M^1L^{-1}t^{-2}$, psi (Pa)

$\Phi(x,y)$ = Airy stress function in x and y plane, $M^1L^{-1}t^{-2}$, psi (Pa)

$\dot{\gamma}$ = shear rate, $M^0L^0t^{-1}$ (1/s)

η = fluid efficiency, fraction or percent

μ = fluid viscosity, $M^1L^{-1}t^{-1}$, cP (Pa.s)

σ = stress, $M^1L^{-1}t^{-2}$, psi (Pa)

σ_{xx}, σ_{yy} = normal stresses in x and y directions respectively, $M^1L^{-1}t^{-2}$, psi (Pa)

$\sigma_{\theta\theta}$ = stress in radial coordinates at angle θ, $M^1L^{-1}t^{-2}$, psi (Pa)

σ_o = far-field compressive stress acting on the fracture face, $M^1L^{-1}t^{-2}$, psi (Pa)

σ_3 = minimum in-situ stress in horizontal direction, $M^1L^{-1}t^{-2}$, psi (Pa)

τ_{xy} = shear stresses in *x*-*y* plane, $M^1L^{-1}t^{-2}$, psi (Pa)

ξ = distance from the fracture tip to the wellbore in near vicinity of tip, $M^0L^1t^0$, in. (m)

ξ' = dimensionless ratio of length, dimensionless

Chapter 6

Model Enhancements: Apparent Stresses

6.1. Net Stress Effects on Fracture Growth

The fracture height growth predicted with the help of the model developed in the study agrees reasonably well with the field observations. Most of the cases selected for the study were the ones that conform to equilibrium approach where the fracture advancement is at a slow pace. These treatments were intentionally pumped at low injection rates to limit the net pressure gain and prevent the fractures from rotating to a horizontal plane which is likely if the injection pressures exceed the overburden during the treatment. The formation of out-of-plane fractures can restrict fracture vertical growth propagation, but it is often difficult to predict the site where such an event will occur due to the uncertainties in characterizing rock properties in a fine scale. However, changes in the net compressive stresses generated in the plane normal to the main body of the vertical planar fracture can be used as a tool to determine if fracture tip extension in vertical direction will be restricted under the influence of cumulative increase of stresses. In this chapter such an approach is discussed where the influence of fracture width on resultant stresses is incorporated in the calculation process while solving for vertical growth of hydraulic fractures. The effects of viscous fluid movement in the fracture are also included in the calculation scheme.

It is clearly established in previous chapters that the vertical growth of the fracture is primarily controlled by the distribution of in-situ stresses in the various subterranean layers and their corresponding mechanical properties; the fracture height then ultimately depends on the available fracture net pressure. In case of layered formations however, the height growth prediction becomes a challenging task especially in presence of non-uniform formation properties which can introduce additional growth controlling mechanisms.

The hydraulic fracture's ability to cross or terminate at the layer-interface is dictated by existing conditions as noted by He and Hutchinson (1989). Possible outcomes range from delamination across the interface to kinked penetration or even bifurcation in case the fracture crosses the interface. Based on the field observations based on radio-active survey, Pandey and Agreda (2014), reported vertical fracture growth restrictions across the interfaces of a mix-layer composed of quartz, calcite and feldspar grains and fine-grained sandstones in shallow San Miguel sandstone formation. Pandey and Flottmann (2015) and Kirk-Burnnand et al. (2015) made similar observations when fracture stimulating shallow coal bed methane (CBM)

wells of the Surat basin, Australia. The heavily laminated and layered formations of Walloons coals are further compounded by the presence of strike-slip and reverse fault regimes (Flottmann et al. 2013) that often result in hydraulic fractures with a horizonal component and termination of the vertical growth across coal seams as evinced from several RA tracer and tiltmeter surveys. Based on experimental results, Daneshy (1978) noted that the obstacles to vertical growth of fracture were not imposed by the material properties alone, but also by the weak interfaces between the layers. At shallower depths, the influence of weak interfaces on fracture growth may dominate because the bonding between the various rock layers may not be very effective; based on the experiments it was suggested that strong interfaces would allow the fractures to grow through them. Similar observations of fractures propagating along the interface but not crossing them were also made by other researchers (Warpinksi et al. 1982; Teufel and Clark 1984). Reneshaw and Pollard (1995) proposed a crossing criterion for cohesionless surfaces which may be a reasonable assumption in cases where the layer interfaces are penetrated by the fracturing fluid. The experimentally derived criterion is shown to be a function of effective stresses in vertical (σ'_{yy}) and horizontal (σ'_{xx}) directions, rock tensile strength (T_o) and coefficient of friction μ.

$$\frac{\sigma'_{yy}}{T_o + \sigma'_{xx}} > \frac{0.35 + \frac{0.35}{\mu}}{1.06} \quad \text{.....(6.1)}$$

The vertical stress (overburden) acts normally on the interface thus applying the fracture-closing forces to any horizontal component. Since the tensile strength of the rock is generally small and can be neglected, the coefficient of friction is thus the only material property that is required for this criterion.

6.2. The Influence of fracture width in height growth calculations

The presence of a non-zero width fracture in the layered media will induce additional stress in the near vicinity of the body of the fracture. The magnitude of the stress will vary depending on the width profile along the fracture height. Thus, the presence of fracture width (w_p) can potentially alter the original stress state by an additional value that is equivalent to the net pressure in the layer. As per Palmer and Carroll (1983) the net (p_{net}) along the fracture can be defined for a propped fracture as follows for a non-uniform pressure field:

$$p_{net} = \frac{w_p E'}{4a} \quad \text{.....(6.2)}$$

where a is the fracture half-height and E' is the plane strain modulus. Tan et al. (2021) noted that the presence of tensile stresses in the near tip region facilitated fracture advancement, but

a compressive load normal to the plane of the fracture is also induced by the main body of the fracture in its surrounding. These forces are opposed by the insitu stresses which imposes limits on the total displacement. The net increase in stress due to this action can be considered as increased layered stress analogous to resistance by a compression spring under ever increasing loads.

The width-induced net stresses can be estimated with the help of local fracture compliance, and if added to the stress of the corresponding layers, will result in an "apparent" layered stress only for calculation purposes, but sufficient to investigate if this additional stress can limit vertical fracture growth. This is the approach discussed in this chapter. The factor β_p discussed in Ch. 5 which is applicable during the treatment pumping phase is the part of calculation process. Once the calculations for a given height-width combination are completed, the stress profile is reset to the original input prior to initiating the next set of calculations. To account for the history of stress modifications, the output arrays are stored in a virtual library during calculation and printed if needed.

The incremental stress around the fracture acting perpendicular to the plane of a vertical fracture can also be estimated with help of relationships proposed by Sneddon (1946) shown below:

$$\Delta\sigma_{xx} = \frac{E w_{max}}{4(1-\upsilon^2)a}\left\{1 - \left(\frac{x^2}{x^2+a^2}\right)^{3/2}\right\} \quad \text{.....(6.3)}$$

where, $\Delta\sigma_{xx}$ is the induced stresses away from the fracture face at distance x, E is the Young's Modulus, ν is the Poisson's ratio, a is the fracture half-height and w_{max} is the maximum fracture width. The stresses at any given distance away from fracture face are incrementally affected by the fracture height in addition to the existing principal stresses. Palmer (1993) proposed an approximate form derived from Eq. (6.3) by linearizing the behavior which suggests that the extent of fracture induced stresses or more commonly referred to as "stress shadow" can reach up to 1.5 times the fracture height. This can be obtained by setting stresses on left hand side of the Eq. (9) to zero.

$$\Delta\sigma_{xx} \approx \frac{w_{max}E'}{4a}\left\{1 - \frac{x}{3a}\right\} \quad \text{.....(6.4)}$$

where $E' = E/(1-\nu^2)$ is the plane strain modulus. Eq. (6.4) is of the same form as Eq. (6.3), though the traditional stress shadow calculations and studies have mainly focused on the propagation of fractures which may range from fracture coalescence, curving or restricted

growth (Olson 2004; Wu and Olson 2016) or increasing insitu stresses with successive stages in multi-stage hydraulic fracturing treatments (Yuan et al. 2003; Casero and Rylance 2020).

6.3. Workflow For Including Net Stress Calculations in Model

The solution to the contained fracture height growth problem was obtained in a three-step process. In the first step, the location of the fracture of a given height was obtained for a multilayered stress model by solving a set of non-linear equations presented in Ch. 2. The corresponding fracture pressure and width profile were obtained in the second step by solving Eq. (2.19) – here a provision was added to calculate fracture widths for non-uniform pressure distribution in the fracture. The third step consisted of calculation of width-induced apparent stresses that were used to temporarily modify the stress profile for the next iteration. Following steps outline the model modification to predict fracture growth in special cases:

1. Calculate local fracture compliance using the following relationship which is also described in Ch. 5 under Eq. (5.18):

$$c_F = \frac{\pi}{2}\frac{\beta_p}{E'} h_f \quad (6.5)$$

2. Calculate net stress in various layers using the local fracture compliance and fracture width distribution *w(y)* obtained from Eq. (2.21) as follows:

$$\Delta\sigma_{net} = w(y)/c_F \quad (6.6)$$

3. Add the net-stresses across the layers where the fracture of a given height penetrates (see Fig. 3.1), to the initial stress profile, which will influence the location of the next input fracture height because of the altered values of σ_i. If the net stresses are sufficiently high, the resultant stresses will prevent the fracture tip from crossing the high-stress layer (see Fig. 6.7).

The assumptions and features of the model developed in the study are listed below:

1. Height averaged fracture compliance sufficiently represents the corresponding influence of all the layers the fracture has contacted since plane strain moduli is adequately accounted for in the calculation process.
2. The net stress generated with the help of fracture width from the previous iteration step, e.g., i-1 is applied to the current step. This approach is valid provided the height increments are kept sufficiently small, e.g., 0.5 ft (0.15 m) or less, as is the case here.
3. During the calculation process, the stresses and the critical stress intensity factors at both fracture tips remain unaltered from original values input in the model, but the positioning of the fracture is affected due to superposition of stresses in other layers as

shown by Eq. (2.18).

4. Though *E'* does not influence fracture growth significantly, its effect on fracture width is considerable and hence eventually affects the incremental stress in Eq. (6.6).
5. For simplicity of calculations the width induced stresses as enforced only in the upper quarter of the fracture height simulated based on the observation that inclusion of all layers does not impact the overall model outcome which is demonstrated for one of the case histories.

6.4. Width Calculations for non-Uniform Fracture Pressures

The uneven width across the fracture height can result in non-linear pressure distributions induced by fluid flow during a fracturing treatment as noted by Weng (1992) and further addressed by Pandey and Rasouli (2021a, 2021c). This is also addressed in section 4.4.

6.4.1. Estimating fracture widths for various pressure distributions

The width solution proposed by Sneddon and Lowengrub (1969) requires the assumption that the fracture width has an arch arch-type fracture profile which limits its use. On the other hand, the solution method put forward by England and Green (1963) for determining crack width for a material exhibiting linearly elastic behavior offers the flexibility to include arbitrary pressure profiles in the calculations such as a quadratic pressure profile shown below.

$$p(y) = -p_{cp}[(y/a)^2 - c_1(y/a) - c_2] \quad \text{.....(6.7)}$$

Here $p(y)$ is pressure distribution along vertical y-axis, y/a is the ratio vertical displacement to the fracture half-height (a), and c_1 and c_2 are the coefficients of the polynomial. The width solution is obtained with the help of odd and even functions denoted by *g(y)* and *f(y)* respectively, such that the final pressure distribution *p(y)* satisfies the following condition:

$$p(y) = -f(y) - g(y) \quad \text{.....(6.8)}$$

where both the functions are also sectionally continuous between $0 \leq y \leq a$. The final width distribution in vertical y direction is obtained with the help of additional functions *G(t)* and *F(t)* described below (England and Green, 1963):

$$w(y) = \frac{-16(1-\nu^2)}{E} \int_{|y|}^{a} \frac{F(t)+yG(t)}{\sqrt{t^2-y^2}} dt \quad (|y| \leq a) \quad \text{.....(6.9)}$$

where, t is a placeholder variable, and a is the fracture half-height. The value of functions *F(t)* and *G(t)* are obtained from net pressure distribution (scalar quantity) described by Eq. (6.7). The value of function *G(t)* is given by:

$$G(t) = \frac{-1}{2\pi t} \int_0^t \frac{u\, g(u)}{\sqrt{t^2-u^2}} du \quad \text{.....(6.10)}$$

The above integral is solved by integrating from the center of the crack in either direction to reach the position of interest at distance *t*, with *u* being the other dummy variable. Thus, the width solution involves integration of two kernel components and yet another integration (Eq. 6.9) across the length of the crack. For Eq. (6.7), the even function can be defined as:

$$f(y) = p = -p_{cp}\left[\frac{1}{2}\left(\frac{y}{a}\right)^2 - c_1\frac{1}{2}\left(\frac{y}{a}\right) - \frac{1}{2}c_2\right] \quad \text{.....(6.11)}$$

where, *p* is the solution of the even function for any location *y* from the center of the crack at which the solution is desired. Similarly, the odd function *g(y)*, is given by:

$$g(y) = q = p_{cp}\left[\frac{3}{2}\left(\frac{y}{a}\right)^2 - c_1\frac{3}{2}\left(\frac{y}{a}\right) - \frac{3}{2}c_2\right] \quad \text{.....(6.12)}$$

with similar notations as Eq. (6.11) expect *q* denoting the final value of odd function.

Similarly, the value of function *F(t)* can be obtained by solving the following integral:

$$F(t) = \frac{-t}{2\pi}\int_0^t \frac{p}{\sqrt{t^2-u^2}}du \quad \text{.....(6.13)}$$

The integral is solved by accounting for all the layer interfaces *k*, that the fracture has crossed before reaching the point of interest *t*, starting from the middle of the fracture at 0, and likewise in the other direction to the point -*t*.

$$F(t) = \frac{-t}{2\pi}\int_0^t \frac{p}{\sqrt{t^2-u^2}}du = \frac{-t}{2\pi}\left[\sum_{n=1}^{k}(p_{n-1}-p_n)\sin^{-1}\left(\frac{d_n}{t}\right)\right] - \frac{p_k t}{4} \text{.....(6.14)}$$

Thus, when using the solution during the width estimation process, the fracture mid-point location must be continuously obtained. In Eq. (6.14), *n* denotes the various layer numbers and d_n represents the distance to the top of the interfaces starting from the center of the fracture and replaces the arbitrary integration variable *u* found in the original integral. The subscript *n* denotes the point of interest. The integration is carried out for both halves of the fracture to the point of interest *t* (and -*t*) located along the axis of the crack. To find the solution for *G(t)*, the rule $\int u\,du/\sqrt{t^2-u^2} = -\sqrt{t^2-u^2}$ is used and the results are summed up over the various layers as follows:

$$G(t) = \frac{-1}{2\pi t}\int_0^t \frac{u\,q}{\sqrt{t^2-u^2}}du = \frac{1}{2\pi t}\left[\sum_{n=1}^{k}(q_{n-1}-q_n)\sqrt{t^2-d_n^2}\right] \text{.....(6.15)}$$

To obtain the final width, the integration is carried out across the entire fracture height for odd and even functions for a specially defined grid generated with the help of a separate algorithm; this grid is over and above the layered data input in the model for height growth calculations. The reason for using a separate grid is because the center of the fracture and the fracture initiation point will not always coincide, thus making the problem a complex one. The subroutine to generate the fracture width vertical grid, first determines the number of stress-

layers that the fracture of a given height has crossed in either direction and, subsequently identifies the layer in which the mid-point of the fracture is located. While executing the code, the algorithm ensures that both y_t and y_b of the grids are greater than both, d_n and, the reference depth y at which the fracture width is to be determined. This segmentation process is the most difficult step in the model building process, especially when splitting the layer where the center of the fracture resides. Once the dynamic gridding is complete, the width distribution in vertical direction for a given fracture height input is obtained by combining the solutions of odd and even functions and multiplying the results with -16/E' as shown in Eq. (6.9) to obtain the final width solution. The process is then repeated for next set of input data and continues till the solution to the entire input array is completed.

Functions $F(t)$ and $G(t)$ in Eq. (6.9) can be evaluated separately, across end points y_t and y_b that denote equidistant points from the center of the fracture in the upper and lower sections respectively, which is a similar approach as the one adopted by Warpinski and Smith (1989). The depth positions represented by y_t and y_b are obtained from the algorithm-derived grid to serve as the points where the widths will be calculated.

The solution to the integral containing $F(t)$ and $G(t)$ are shown below:

$$-\int_{|y|}^{a}\frac{F(t)}{\sqrt{t^2-y^2}}dt=\frac{1}{2\pi}\sum_{n=1}^{k}(p_{n-1}-p_n)\left(A\sin^{-1}\left(\frac{d_n}{y_b}\right)-B\sin^{-1}\left(\frac{d_n}{y_t}\right)+ d_n\ln\left[\frac{A+C}{B+D}\right]+\frac{y}{2}\ln\left[\frac{d_nA+yC}{yC-d_nA}\times\frac{yD-d_nB}{yD+d_nB}\right]\right)-\frac{p_k}{4}\sqrt{a^2-y^2} \quad \text{.....(6.16)}$$

$$-\int_{|y|}^{a}\frac{yG(t)}{\sqrt{t^2-y^2}}dt=\frac{y}{2\pi}\sum_{n=1}^{k}(q_{i-1}-q_i)\left(ln\left[\frac{A+C}{B+D}\right]-\frac{d_n}{2y}ln\left[\frac{d_nA+yC}{d_nA-yC}\times\frac{d_nB-yD}{d_nB+yD}\right]\right) \quad \text{....(6.17)}$$

Where, $A=\sqrt{y_b^2-y^2}$, $B=\sqrt{y_t^2-y^2}$, $C=\sqrt{y_b^2-d_n^2}$, and $D=\sqrt{y_t^2-d_n^2}$.

6.5. Case Studies

The first two case histories (Pandey and Flottman 2015) pertain to the hydraulic fracturing treatments pumped in the shallow coal bed methane (CBM) wells drilled and completed in the Surat Basin, south-eastern Australia, which exhibit depth dependent stress regimes (Flottmann et al. 2013). As mentioned previously in Ch. 4, section 4.3, the sediments in the basin are dominated by siltstones and mudstones with minor sandstones that were all deposited in a fluvio-lacustrine depositional environment which was exposed to intermittent volcanic activity. The non-coal inter-burden (non-coal) rocks have low porosity and permeability which generally results in low fluid leak-off for typical polymer-based fracturing fluid systems in this heavily layered and laminated geologic setup. Multiple coal seams, with an average thickness of 0.4 m [1.3 ft] are a common occurrence in the field. The PR of 0.35 or higher and a low YM

of less than 1.0 MMpsi (6.9 GPa) in coal seams give them a ductile nature and results in lower in situ stress compared to interburden due to the compressive stress environment.

The stress state in the basin is depth dependent where a transition from reverse to strike slip regime occurs typically just below 400 m (1312.3 ft). The coal in the region is low strength with a YM around 0.65 to 1.0 MMpsi (4.5 to 6.9 GPa) and PR of more than 0.35 whereas the interburden has a YM that ranges from 1.39 to 2.5 MMpsi (9.6 to 14.5 GPa). These values reported by Pandey and Flottmann (2015) based on analytical calibration of injection test data and supported by triaxial test results. The region is characterized by intermediate differential stresses that fall in the range of 600 to 750 psi (0.41 to 0.52 MPa.

6.5.1. Case – 1: CBM Completion in Shallow/Laminated Formations

The stimulation treatment was pumped down a vertical well 7 in. (177. 8 mm) casing that set around 1,032 m (3,385.8 ft). During the stimulation, downhole microseismic survey was conducted to monitor the fracture geometry as it evolved with time. The monitoring was carried out using arrays lowered in two of the offset wells nearby.

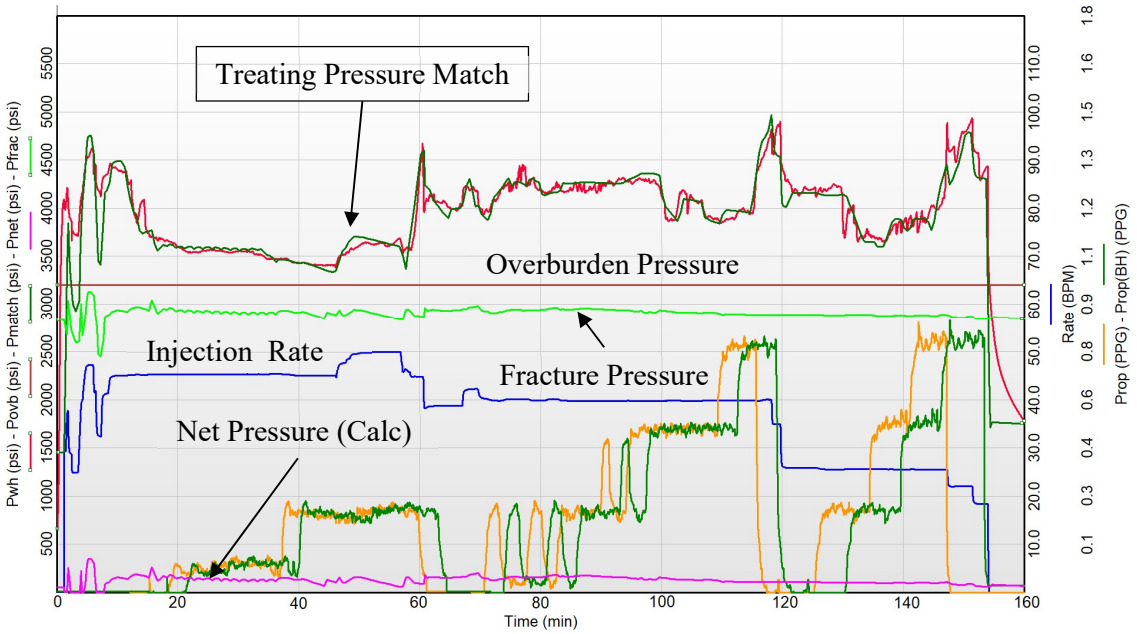

Fig. 6.1: Pressure, injection rate and proppant concentration plot for treatment of Case 1.

The first-stage treatment covered a gross interval of nearly 150.0 ft (45.9 m) with multiple perforation sets that targeted various coal seams with an average insitu stress gradient of 0.90 psi/ft (20.4 kPa/m). In the absence of a downhole pressure gauge the net pressure is calculated with the help of surface treating, frictional and hydrostatic pressures, and injection rates for

given fluid and proppant concentrations using average closure stresses. A small stage of 100 mesh sand was used for clearing up restrictions in near well region. The treatment net pressure shown in **Fig. 6.1** by "Pnet" curve is less than 150 psi (1,034.0 kPa) in the early part of the treatment but eventually increases to 160 psi (1,103 kPa) around 70 min into the treatment. This is followed by a small drop in pressure, before an upward trend is observed again, reaching nearly 165 psi (1,138 kPa) at 80 min. The fracture pressure (Pfrac) however remains below the overburden during the entire treatment which does not necessarily imply that horizontal components cannot form at these shallower depths, but just that vertical fracture orientation will dominate (Palmer and Carroll 1983; Daneshy 1978).

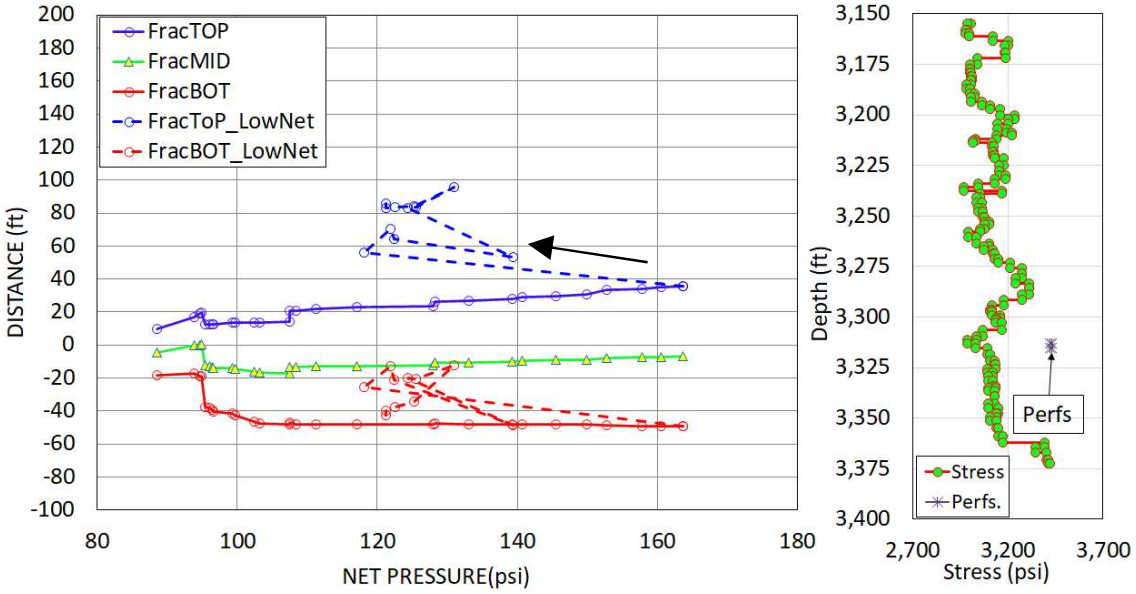

Fig. 6.2: Fracture height and location versus net pressure plot for Case 1.

The formation material properties input in the model are summarized below:

Number of layers in the stress model	100
Payzone Stress	3,038.3 psi (20.95 MPa)
Average Stress	3,122.7 psi (21.53 MPa)
Fracture initiation layer thickness	2.30 ft (0.70 m)
Average layer thickness	2.25 ft (0.69 m)
Average Young's Modulus (pay)	1.85×10^6 psi (12.8 GPa)
Average Poisson's Ratio (pay)	0.34
Average Fracture Toughness	727 psi.in$^{0.5}$ (2,767.3 kPa.m$^{0.5}$)
Payzone True Vertical Depths (TVD)	3,312 to 3,318 ft (6 ft thick)

TABLE 6.1: Formation properties used as input in Case 1.

As in the past cases, the fracture heights are obtained with the help of the distance versus net pressure relationship show in **Fig 6.2**, where distances of the top and bottom fracture tips are plotted as a function of net pressure. Unlike other cases, this plot is peculiar because it represents two distinct and probable trends of fracture growth. In the first instance, the fracture height tends to remain contained as long as the net pressures do not exceed 165 psi (1.14 Mpa) mostly because of the high stress layers of 3,280 psi (22.6 MPa) between 3,275 ft (998.2 m) and 3,283 ft (1,066.7 ft). However, as the net pressures exceed the threshold value, an upward fracture growth exceeding 80 ft (24.4 m) is possible even with lower net pressures. Possible vertical fracture growth after this point is predicted by the dashed curves that denote the upper (blue) and lower (red) fracture tip locations. As mentioned above, this condition is reached after 70 min into the treatment. The modeled evolution of fracture treatment with time is illustrated in **Fig. 6.3.** Fracture heights are represented by vertical bars and plotted according to their corresponding depth wise locations as determined by the model. The x-axis does not apply to vertical bars representing fracture heights. In the case of MS events shown by yellow triangles however, both the time and the depth axis are applicable. The model is thus able to accurately predict the vertical growth evolution of the fracture during the treatment

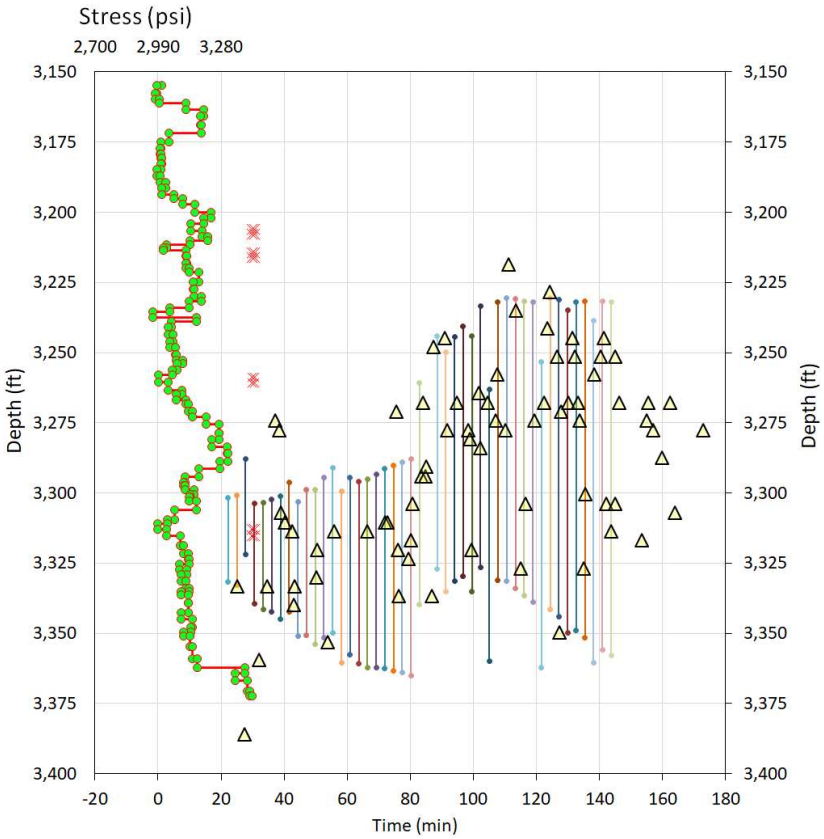

Fig. 6.3: Fracture height growth evolution; MS data is overlaid – Case 1.

The events from a microseismic survey have a spatial distribution which is commonly used in estimation of fracture geometry resulting from hydraulic fracturing treatments. In this case however, only a 2D plot of events is shown because the study primarily focuses on the modeling of vertical fracture growth which is mostly influenced by superimposed stresses of the layers that the fracture intersects and the critical stress intensity factors of layers where fracture tips reside. The fractures of various heights depicted by vertical bars in Fig. 10 are overlaid with MS data points to show that the modeled fracture location and height are reasonably close when compared to the observed events.

The MS data featured in Fig. 6.3 shows a downward growth of the fracture in the first 80 min of the treatment, which aligns reasonably with the fracture height and locations shown for net pressures that are limited to 160 psi in Fig. 6.2. Once the treatment net pressures exceed this value, the upper barrier at 3,285 ft (1,001.3 m) is breached and the fracture grows upwards; a drop in calculated net pressure is observed at this point which now reduces to 125 psi (0.862 MPa psi) as seen in Fig. 6.1. A maximum height of 121 ft (39.0 m) inferred from MS events observed after nearly 2 hours of pumping is matched by model output with lower net pressure of 130 psi (0.896 MPa).

The successful match of MS based fracture height estimates with that from the fracture height growth model validates its application in layered formations such as these and was found to adequately describe the field observations without the need of using the features developed during model modification.

6.5.2. Case – 2: CBM Completion in Shallow/Laminated Formations

The second case study (Pandey and Flottmann, 2015) discusses a shallow CBM well treated with 20 lbm/Mgal (2.4 kg/m^3) borate cross-linked fluid and 16/30 U.S. mesh size (1.194 – 0.584 mm) sand. The treatment was injected down a 5-½ inch (139.7 mm) N-80 casing set at 758.0 m (2,486.9 ft) with the mid-perforations located at 1,401.0 ft (427.0 m). Stress and mechanical properties were calculated with the help of dipole sonic log data and calibrated with injection tests.

Pre-treatment diagnostics indicated a fracture gradient of nearly 0.97 psi/ft (21.94 kPa/m) implying that fracture pressures could conceivably exceed the overburden during the treatment and rotate to a horizontal plane which can limit fracture vertical growth. Furthermore, a few of the shallower coal seams situated above the above the targeted coal package, e.g., at depth of 1,296 ft (395.0 m), showed a low YM 0.08 to 1.0 MMpsi (551.6 to 689.5 MPa) and PR of nearly 0.39, that could result in higher widths if the fracture penetrated that layer. The

combination of these two factors could lead to formation of a horizontal component that can limit the fracture height growth. The pressure match of surface pressure is shown in **Fig. 6.4**. The presence of near wellbore restrictions that result in higher treating pressures initially is evident. However, with the onset of proppant in the formation and ensuing erosion, there is significant drop in the treating pressures owing to the removal of those restrictions and possible erosion of perforations shot in N-80 casing. As is obvious, with the gain of only 0.03 psi/ft or mere 40 psi (275.8 kPa), the fracture pressures will equal the overburden. This condition is reached approximately 14 minutes into the treatment coinciding with the time when the injection rates of 35.0 bbl/min (0.093 m^3/s) are achieved. Table 6.2 summarizes model input.

Number of layers in the stress model	100
Payzone Stress	1,323.7 psi (9.13 MPa)
Average Stress	1,365.2 psi (9.41 MPa)
Fracture initiation layer thickness	3.70 ft (1.13 m)
Average layer thickness	3.98 ft (1.21 m)
Average Young's Modulus (pay)	1.04×10^6 psi (7.2 GPa)
Average Poisson's Ratio (pay)	0.37
Average Fracture Toughness	977 $psi.in^{0.5}$ (3,719.0 $kPa.m^{0.5}$)
Payzone True Vertical Depths (TVD)	1,354 to 1,360 ft (6 ft thick)

TABLE 6.2: Formation properties used as input in Case 2.

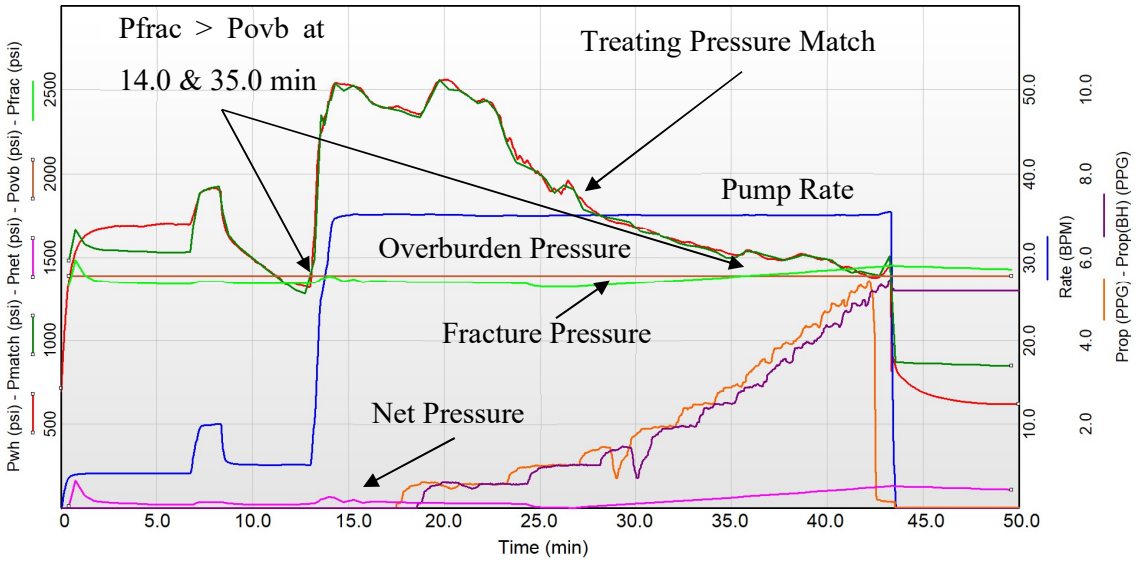

Fig. 6.4: Pressure, injection rate and proppant concentration plot for treatment of Case 2.

The MS activity recorded around 14 min shows majority of events occurring at shallow depths ranging from 1,294.4 to 1,296.6 ft (394.5 to 395.2 m) in the left-hand side plot of **Fig. 6.5**. Most of the events occur below these depths as the treatment continues, indicating a possible limit to upward growth after this point in time. The base model was unable to replicate this growth pattern; however, with the width induced net stress calculation mode, the real-world observations could be reasonably replicated as shown in the right-hand side plot of **Fig. 6.6**.

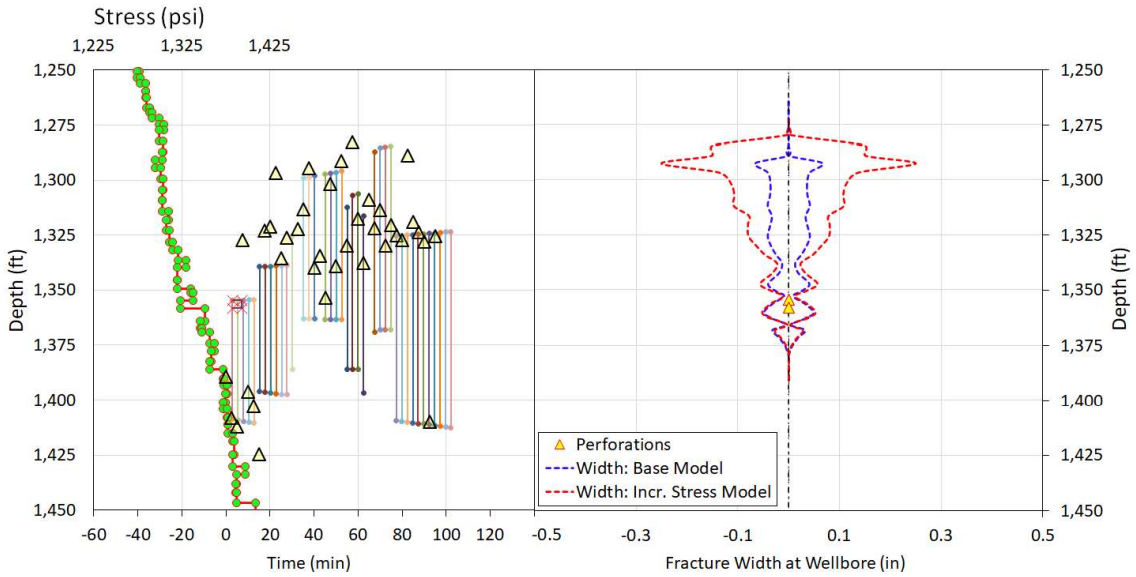

Fig. 6.5: Fracture heights and MS data (Left) and widths at corresponding depths (Right).

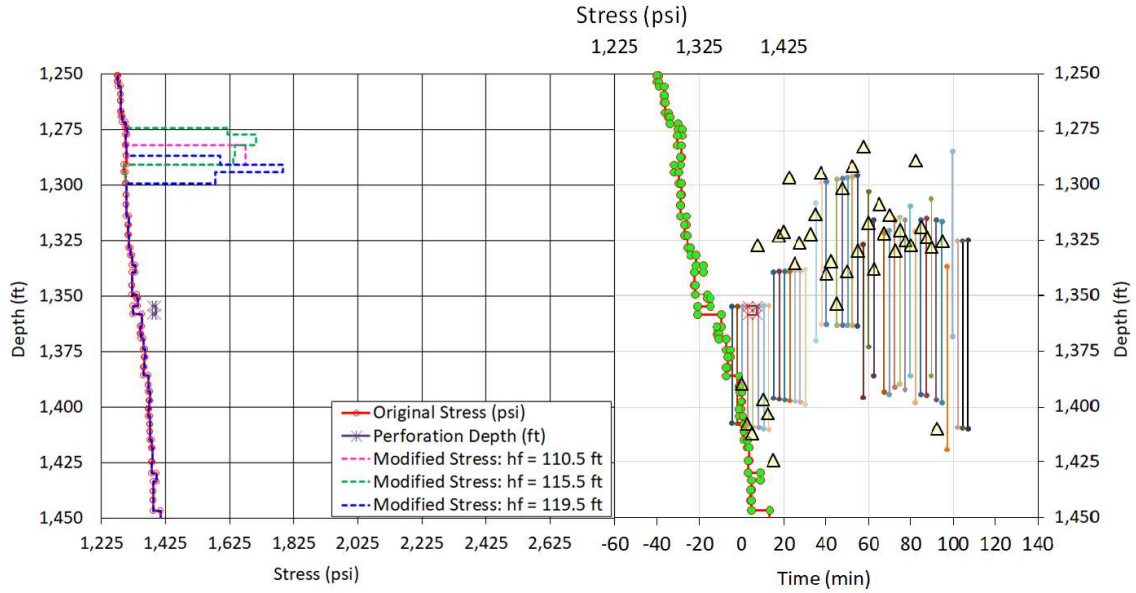

Fig. 6.6: Stress modification (Left) and revised heights (Right) for same depth scale.

The simulations carried out with the modified model generated higher widths (though apparent and not real), that are shown in the right-hand side plot of Fig. 6.5 by red curve, along with the width profile (blue curve – base model) generated using Eq. (2.21) that does not consider the effects of incremental net stress. The corresponding induced net-stresses are displayed in the left-hand side plot of Fig. 6.6, around the depth of 1,296 ft (395.0 m) where a 3.3 ft (1.0 m) thick coal seam with low YM value of 0.81 MMpsi (5.6×10^4 MPa) is known to exist. The incremental net stresses (simulated *only* – not real) are nearly 500 to 600 psi (3.45 to 4.14 MPa) higher than the base model and play a dominant role in restricting the fracture vertical growth.

The change in compliance with increase in height translates to a corresponding change in net stresses (Eqs. 6.5 and 6.7), which when added to the original stress is coined as "Modified Stress" for the given height case and plotted versus depth as shown in the left plot of Fig. 6.6. The final output of this simulation is presented in the right-hand side plot of Fig. 6.6 where the fracture heights and locations for the period after 45 min appear to match reasonably well with the MS events recorded during the treatment. Not many events are recorded at deeper depths, especially after a possible initiation of a horizontal component around 1,300 to 1,325 ft (396.2 to 40.3.9 ft) where most of the late time events are confined.

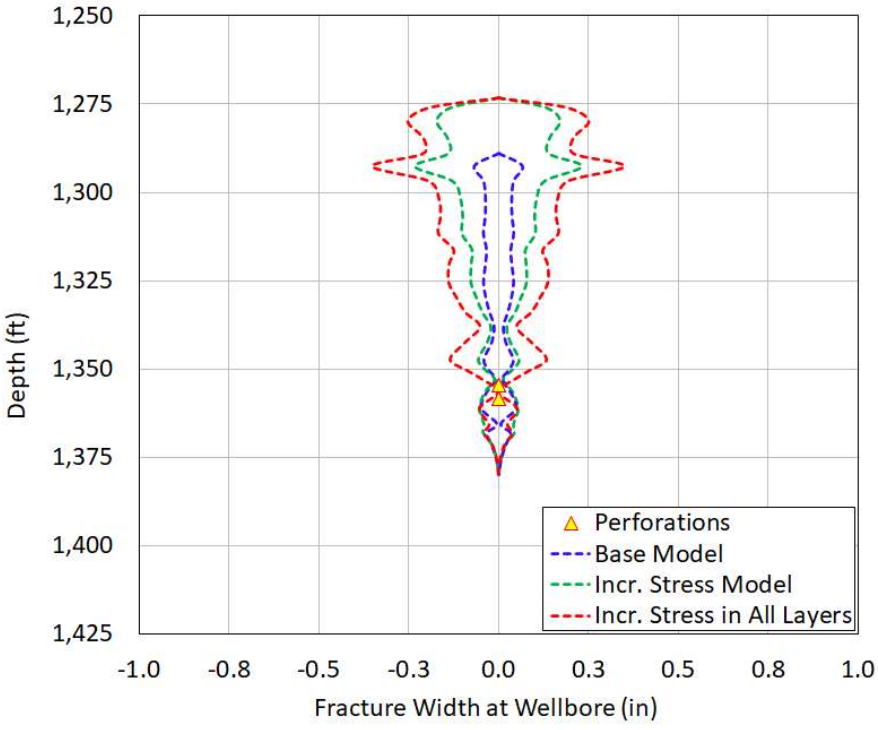

Fig. 6.7: Comparison of fracture width distribution from base and modified model.

For computational efficiency, the net stress calculations are sectionally carried out in the upper half of the perforation depth. The outcome for cases where such a constraint is not enforced, is however not significantly different from what is shown in Fig. 6.7 because the stress profile is reset to original stress profile prior to carrying out calculations for every input data set. Despite this however, the width projection will differ because the net stresses will be influenced by contributions from several layers instead of the few, especially in the case where only the layers in upper section of the fracture are included in the calculations. The simulated vertical width distributions shown in **Fig. 6.7** illustrate this behavior where the profiles for incremented stress for limited number of layers (dashed green curve) or all layers (dashed red curve) bear similar profile and vary only in magnitude.

The net stress values for various fracture heights as they increase are shown in the depth versus stress curve of **Fig. 6.8** which is plotted in the same depth scale as Fig. 6.7. Note that for a given fracture height, only a few layers are influenced by apparent stresses (also see Fig. 6.6). The simulated net stresses in this mode of calculation range from 50 to 625 psi (0.35 to 4.31 MPa) with the maximum value closely matching with what was obtained with fewer layers. Overall, the width induced net stresses tend to limit the simulated vertical growth of fracture as shown in the right-hand side plot of Fig. 6.6.

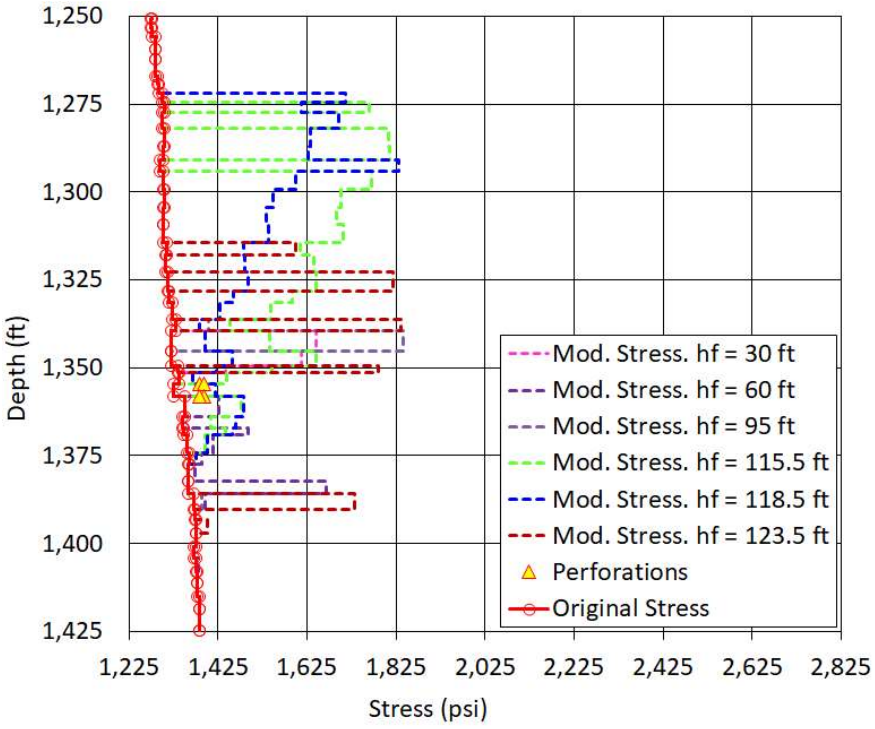

Fig. 6.8: Corresponding temporary net stress calculated for various fracture heights.

6.5.3. Case – 3: Horizontal Well Shale Oil Completion

This example represents one of the fracture-stimulated zones on a horizontal well completed in a shale play. The formation under consideration is typically highly laminated, organic-rich, ultra-low permeability calcareous shale. The deposition is believed to have occurred in low-energy marine waters farther away from the shore and at deeper depths that helped in avoiding effects of wave disturbance. The shales are relatively brittle with moderate modulus, but the low Poisson's ratio (brittle rocks) helps in creating fracture complexity during the hydraulic fracturing treatments resulting in favorable well performance.

Number of layers in the stress model	97
Payzone Stress	12,035.4 psi (83.0 MPa)
Average Stress	12,491.3 psi (86.1 MPa)
Fracture initiation layer thickness	3.40 ft (1.13 m)
Average layer thickness	3.48 ft (1.21 m)
Average Young's Modulus (pay)	4.04×10^6 psi (27.9 GPa)
Average Poisson's Ratio (pay)	0.26
Average Fracture Toughness	1,756 psi.in$^{0.5}$ (6,684.0 kPa.m$^{0.5}$)
Payzone True Vertical Depths (TVD)	12,125 to 12,325 ft (200 ft thick)

TABLE 6.3: Formation properties used as input in Case 3.

The treatment consisting of 30 lbm/Mgal (3.6 kg/m^3) cross-linked fluid and intermediate strength proppant with maximum concentration of 3.5 PPA (419.4 kg/m^3) was pumped down a 5 ½ in. (139.7 mm) casing at 70 bbl/min (0.185 m^3/s) with 8 perforation sets spread across 200 ft (60.1 m) laterally in a horizontal well completion. The fluid leakoff calibrated from treatment injection pressure match obtained with the help of a commercial numerical simulator is around 0.00011 ft/min$^{0.5}$ (4.3×10^{-6} m/s$^{0.5}$). The treatment data and pressure match curves are shown in **Fig. 6.9**. The stress and mechanical properties were determined from sonic logs and calibrated with injection data. The effective formation face pressures (Pandey et al., 2020) were calculated with the help of data obtained from downhole memory pressure gauge and found to be exceeding the overburden at 12,800 psi (88.3 MPa) during the treatment. Despite high bottomhole injection pressures of nearly 13,500 psi (93.1 MPa) which is inclusive of perforation friction, the net pressures were calculated in the range of around 450 psi (3.1 MPa).

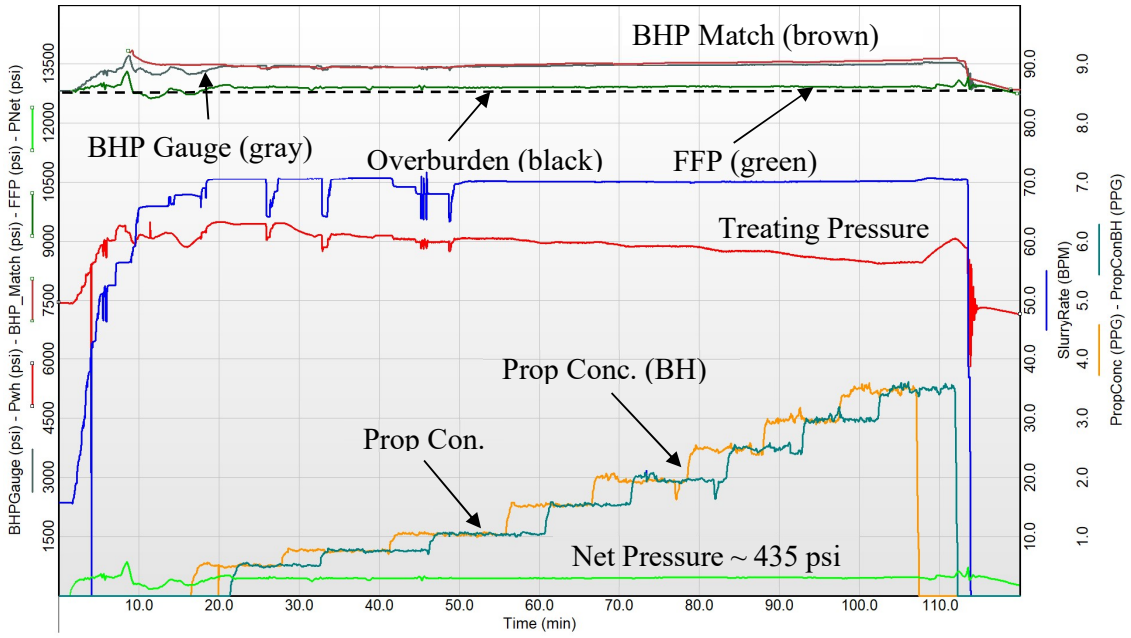

Fig. 6.9: Pressure, injection rate and proppant concentration plot for treatment of Case 3.

The fracture height generated from the pressure history match using a commercial software is shown in **Fig. 6.10**, which shows an over-estimation when compared to the MS events that overlaid in the plot. After observing this mismatch between predicted and MS data, the height growth model was employed to compare its output for the given conditions.

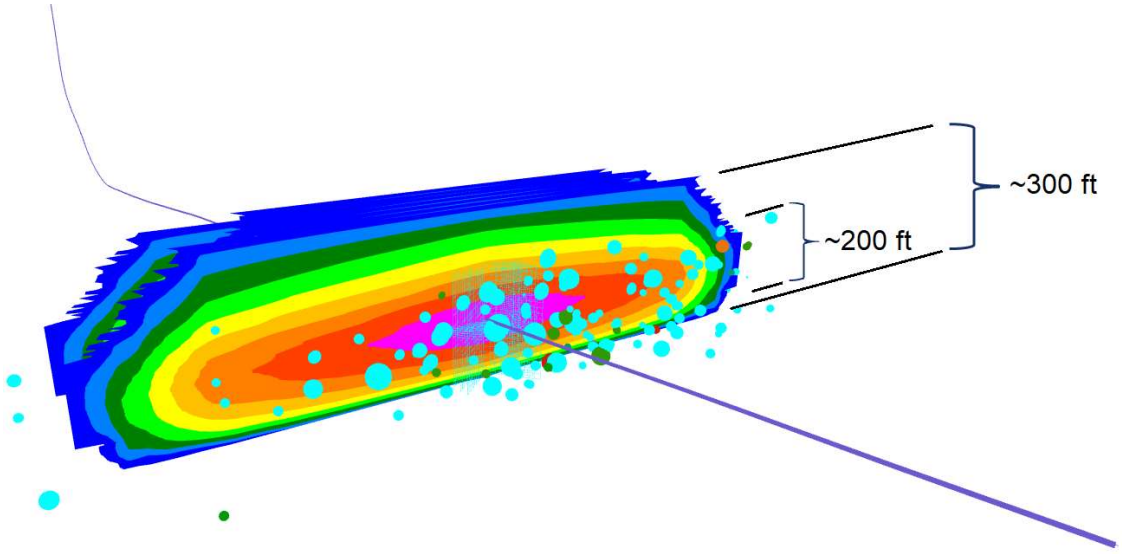

Fig. 6.10: Fracture geometry derived from commercial simulator for Case 3.

The distance versus net pressure plot shown in **Fig. 6.11** indicates that for the given vertical stress distribution, a fracture growth of 200 ft (61.0 m) is possible if a net pressure of 435 psi (3.0 MPa) is available during the treatment. However, when various fracture heights are

overlaid on the MS data points, it is apparent that except for early time, when fracture growth occurs rapidly, the predicted fracture locations and height do not match the MS survey data.

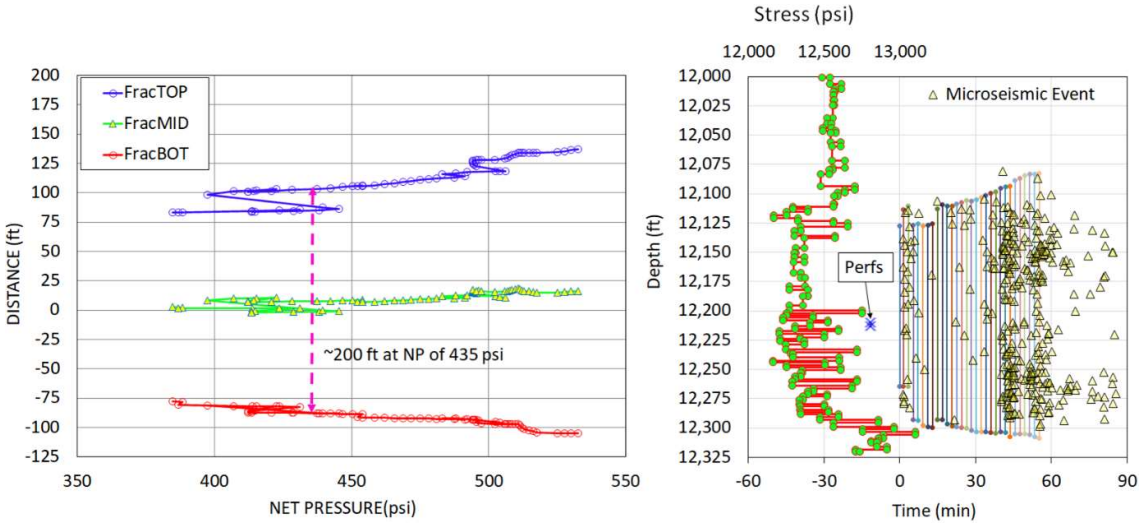

Fig. 6.11: Fracture height growth potential and comparison with MS data for Case 3.

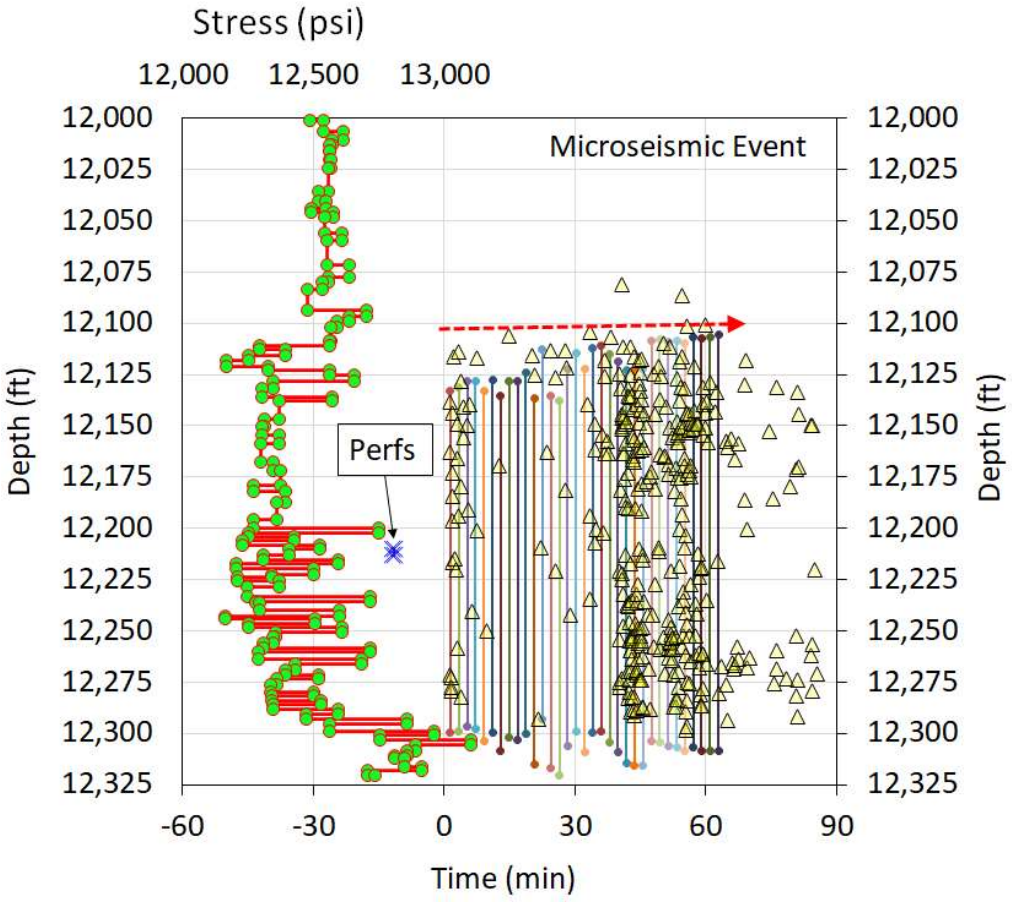

Fig. 6.12: Fracture placement prediction – width induced stress modification for Case 3.

The normal simulation yields to a prediction of upward fracture growth with the bottom of the fracture nearly static. This however does not align with the MS data shown by yellow triangles on the right plot that clearly show that most of the late time events are below the depth of 12,100 ft (3688.1 m) as though the fracture is contained at that depth.

Using width induced net stress feature, more accurate prediction of fracture height that compares well with the MS events was obtained. This is shown in **Fig. 6.12**. With the increased apparent stresses applied in the shallower section around the depths of 12,110 ft (3,691.1 m), the model predicts that the upward fracture growth will be constrained, causing the fracture to be bound between the lower higher stress member at 12,300 ft (3,749.0 m) and 12,100 ft (3,688.1 m) which closely matches the real time observations. Because the net pressure in the fracture does not evolve much beyond 435 psi, with passage of time, the fracture growth will stabilize. The plot in **Fig. 6.15** shows the fracture pressure distribution generated from even and odd functions in Eq. (6.11) and (6.12), respectively, for a quadratic pressure distribution of the form expressed in these equations.

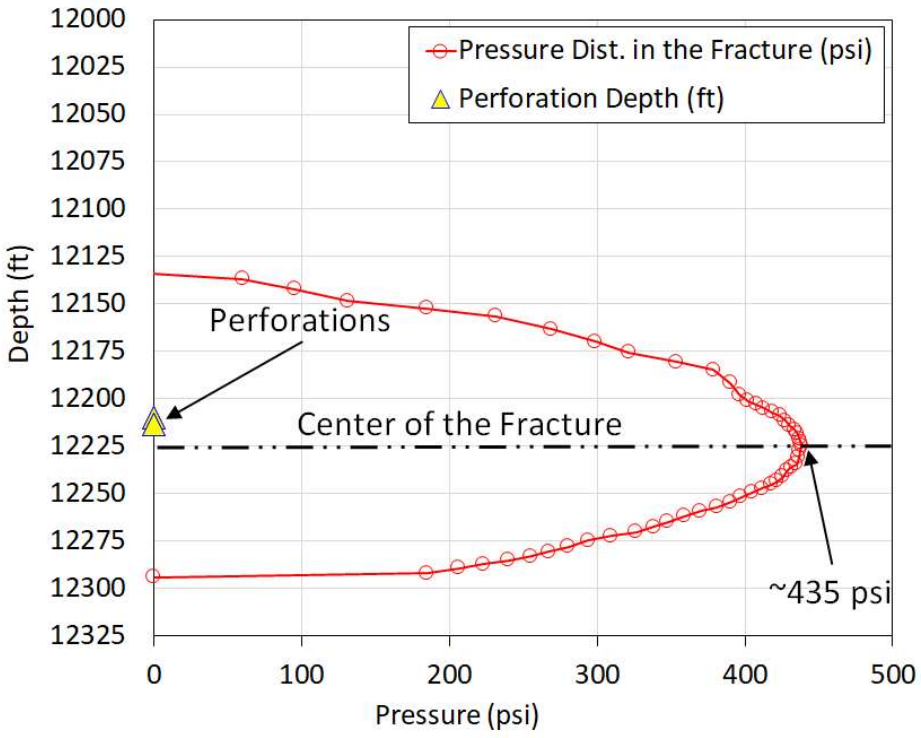

Fig. 6.12: Quadratic Pressure distribution in the fracture – Case 3.

The vertical growth of a hydraulic fracture is dictated by several variables, some of which were discussed in this chapter. In laminated or heavily layered formations of varying material

properties such as toughness and elastic modulus, the modeling of fracture height growth, especially early termination can be challenging. A mathematical model capable of computing incremental stress in the presence of a finite width, and normal to the plane of fracture was developed in this phase of the study. The additional stresses, denoted as net stresses, were then added to the input array of depth-dependent stress profile in a dynamic mode to calculate the fracture position in the modified stress profile for a given height while the fracture height versus net pressure mapping were being generated.

Results from the model showed that for cases where larger fracture widths were simulated, e.g., layers with low elastic modulus that were reasonably stressed, the level of fracture truncation was higher which is also observed in real world cases that were studied. In the cases presented, the fracture entry pressures exceeded the overburden and the possible horizontal or pancake fractures resulting from such an action, apparently acted to contain the fracture vertical growth. The model was able to accurately replicate the fracture height and its relative position with respect to the initiation point observed in field with the help of MS survey.

6.6. Nomenclature

a = fracture half-height, $M^0L^1t^0$, ft (m)

a_v = fluid viscosity behavior coefficient, unitless

c = constant of integration, various units

c_F = fracture compliance, $M^0L^1t^2$, ft/psi (m/Pa)

c_1, c_2, c_3 = calibration constants, unitless

d_n = elevation or distance of the n^{th} layer from the middle of the facture, $M^0L^1t^0$, ft (m)

E = Young's modulus, $M^1L^{-1}t^{-2}$, psi (Pa)

E' = plane strain modulus, $M^1L^{-1}t^{-2}$, psi (Pa)

$f(y)$ = even function Eq. (6.11), $M^1L^{-1}t^{-2}$, psi (Pa)

$g(y)$ = odd function Eq. (6.12), $M^1L^{-1}t^{-2}$, psi (Pa)

$F(t)$ = width function Eq. (6.13), $M^1L^{-1}t^{-2}$, psi (Pa)

$G(t)$ = width function Eq. (6.10), $M^1L^{-1}t^{-2}$, psi (Pa)

h_f = fracture height, $M^1L^1t^0$, ft (m)

k = count of the interface the fracture has crossed, unitless

n = layer count, unitless

p = solution to even function Eq.(6.11), $M^1L^{-1}t^{-2}$, psi (Pa)

p_n = solution to even function from $n = 1$ to k, $M^1L^{-1}t^{-2}$, psi (Pa)

p_{cp} = pressure at the center of the perforations, $M^1L^{-1}t^{-2}$, psi (Pa)

$p(y)$ = pressure in the crack in vertical direction, $M^1L^{-1}t^{-2}$, psi (Pa)

P_{net} = net pressure, $M^1L^{-1}t^{-2}$, psi (Pa)

q_n = solution to odd function from $n = 1$ to k, $M^1L^{-1}t^{-2}$, psi (Pa)

t = placeholder variable, $M^1L^1t^0$, ft (m)

T_o = rock tensile strength, $M^1L^{-1}t^{-2}$, psi (Pa)

u = placeholder variable, $M^1L^1t^0$, ft (m)

w_{max} = maximum fracture width, $M^0L^1t^0$, in. (mm)

w_p = propped fracture width, $M^0L^1t^0$, in. (mm)

$w(y)$ = width in vertical direction y, $M^0L^1t^0$, in. (mm)

x = any value of distance in horizontal x-axis, $M^0L^1t^0$, ft (m)

y = elevation in vertical distance, $M^0L^1t^0$, in. (m)

y_b = depth from the center of fracture to the lowermost point of interest, $M^0L^1t^0$, in. (m)

y_t = elevation from center of the fracture to uppermost point of interest, $M^0L^1t^0$, in. (m)

β_p = net pressure ratio in Eq. (6.5), dimensionless

μ = coefficient of friction, unitless

ν = Poisson's ratio, unitless

σ'_{xx} = effective minimum insitu stress, $M^1L^{-1}t^{-2}$, psi (Pa)

σ'_{yy} = effective overburden, $M^1L^{-1}t^{-2}$, psi (Pa)

$\Delta\sigma_{net}$ = net stress, $M^1L^{-1}t^{-2}$, psi (Pa)

$\Delta\sigma_{xx}$ = net stress in x-direction along horizontal direction, $M^1L^{-1}t^{-2}$, psi (Pa)

Chapter 7

Predicting Fracture Complexity During Treatment

7.1. Fracture Growth in Presence of Fracture Complexity

The modeling of hydraulic fractures using the traditional pseudo-3D (P3D) numerical simulators results in planar fracture that vary in widths across the height of the fracture. The variation depends on the stresses and mechanical property of the layers that the fracture crosses. The laboratory experiments, that are discussed in some of the sections below, show that the propagating cracks may have a three-dimensional (3D) characteristic given the observed combination of deviation (kinking) and out-of-plane displacements that can hinder the vertical growth. In a test specimen with prefabricated multiple flaws, a 3-dimension failure patterns and crack propagation are seen which can be approximated as a two-dimensional (2D) model by considering it as a mixed boundary value, triple-crack problem where the crack is internally pressurized. The stress intensity factors (SIF) at the tip of such discrete (or mildly continuous via fine ligament like cracks) may be determined first and then their effects can be superimposed on to the primary crack propagation solution to include the influence of real-world 3D cracks on vertical growth estimation.

Incorporating the effects of fracture complexity in the traditional models that predict height growth, allows for the prediction of out-of-plane fracture such as a horizontal component of the fracture across certain layers. These, generally unwanted features, can often result in early truncation of fracture height or in some cases even lead to undesirable case of casing shear or failure. The predictive model can be developed by constructing a mathematical algorithm that is continuously investigating for criteria or conditions that favor fracture complexity, during the height growth simulation process. Once these conditions are detected, the model can predict the liable depths and the interfaces where complexity will be enhanced, with a high degree of confidence, especially if the injection parameters such as fracture pressures also favor such an event. The predictions can then be verified in real world cases where height growth measurements were carried out during the treatment combined with well history that corroborates the model forecast.

7.2. Crack growth under compressive loads

The vertical growth of fractures (or cracks) in a layered formation depends on the in-situ stresses variations amongst the various geologic layers, their corresponding stress intensity

factors, and the internal pressure of the crack. Fairhurst and Cook (1966) explained that the rocks tend to split along the direction of maximum compression in the presence of an existing flaw. In a vertically held specimen show in left-hand side plot of **Fig. 7.1**, that is subjected to horizontal confining stress (σ_3) and loaded along the vertical axis, as the vertical compressive stress (σ_1) exceeds a certain critical Griffith criterion (G_c), the associated shear stress (τ) along any pre-existing crack of length $2a$, will cause its extension across the sliding surfaces of the crack $\overline{ab}$, which will result in reduction of both, the compressive stress (σ_f), and shear stress across the crack $\overline{aa}$. This crack propagation will continue till the energy from compression is no longer sufficient to generate requisite tensile stresses at the tip region (b) to overcome the resistive forces offered by the confining stresses and material properties. Because the crack growth originates due to tensile stress concentrations at its tips, a mode-I propagation is assumed. This assumption is sufficient to only account for the forces in horizontal direction ($p - \sigma_3$) that produce normal opening of the crack (Germanovich et al. 1994) as seen in the right-hand side sketch of Fig. 7.1 which is an important conclusion that enables crack-modeling.

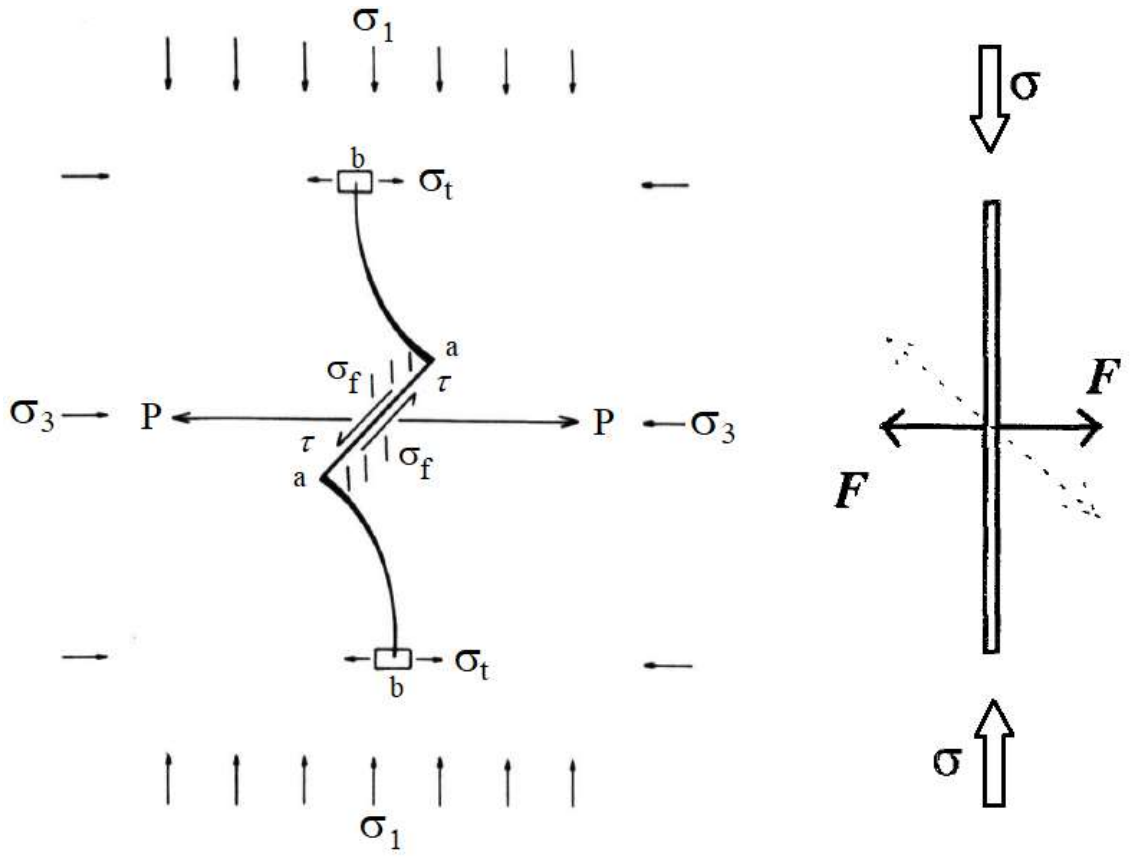

Fig. 7.1: Crack-extension: Fairhurst & Cook (Left). 2D Crack: Germanovich et al. (Right)

7.3. Vertical and Horizontal Fracture Components

As is known and also mentioned in the introductory text, that apart from insitu stress distribution, the vertical propagation of a hydraulic fracture is also influenced by the presence of formation layers of various rock types and their corresponding material properties. Daneshy (1978), Warpinksi et al. (1982) and, Teufel and Clark (1984) all noted that the weak interfaces between the layers can also resist vertical propagation. The effects of rock layering are more dominant at shallower depths where the interlayer bonding may be weak, though the fracture growth truncation can also occur in deeper formations if the conditions favor such an event. The failure of bonding between weak interfaces can result in the possible forming of horizontal components of a hydraulic fracture along the bedding planes if there is sufficient pressure energy available to overcome the overburden. The presence of such an out-of-plane fracture adds yet another dimension to the existing 2D fracture plane which is generally assumed to be in vertical direction for normal stressed extensional environments (Anderson 1951).

Occurrences of horizontal fracture components in shallow well completions have been noted and documented by various researchers (Warpinsiki et al. 1982, Pandey and Agreda 2014; Pandey and Flottmann 2015; Kirk-Burnnand et al. 2015) though the existence of horizontal fracture components when stimulating deeper formations are mostly inferred from downhole treating pressures and with the aid of measurement devices such as tiltmeters (Wright et al. 1997; Wright et al. 1998). With the help of tiltmeter survey conducted on a horizontal well stimulation in the Bakken formation at depths of nearly 10,858 ft (3,309.50 m) a total of 20% horizontal fracture component with tilt ranging from 1,000 to 2,500 μin (0.0254 to 0.0635 mm) was observed on average for the 2 stages that were pumped (*North Dakota Govt. Report*, 2007). The treatment data shows that the fracture pressures exceeded the overburden of 10,860 psi at nearly 1.0 psi/ft (22.62 kPa/m) in the final stages of the treatment, which could explain the presence of a horizontal fracture component in some of the portions of the horizontal lateral.

In the modern multi-stage completions of long horizontal laterals, the increase in bottomhole injection pressures and instantaneous shut-in pressures (ISIP) after successive zone-wise stimulation stages is a well-known phenomenon and has been routinely reported (Yuan et al. 2003; Casero and Rylance 2020). Some of these values are often higher than overburden, especially in cases where the initial conditions indicated higher than routinely observed fracture gradients (high pressured or tectonically charged formations). It may also be noted that the presence of a horizontal fracture component does not unconditionally imply its immediate dominance on the fracture propagation trend, but as suggested by downhole

microseismic data, if such a component develops around a certain weak interface, the hydraulic fractures cease to grow vertically. The untimely growth arrest can lead to suboptimal treatment outcome, and in some cases, even lead to damage to tubular goods if the existence of the horizontal fracture component is associated with layer-movement or slippage around the bedding plane.

7.3.1. 2D and 3D Crack Growth

The uniaxial crack propagation along the vertical axis of the specimen and associated mode-I opening is represented as a 2D crack problem in Fig. 7.1 (rightmost sketch). Propagation of such cracks is generally smooth because there are no constraints other than internal resistance due to possible branching or friction. The real-world scenarios may however be far more complex, although it is recognized that the mathematical modeling of a 3D crack is not simple either because there is a lack of consistent theory to predict such occurrences.

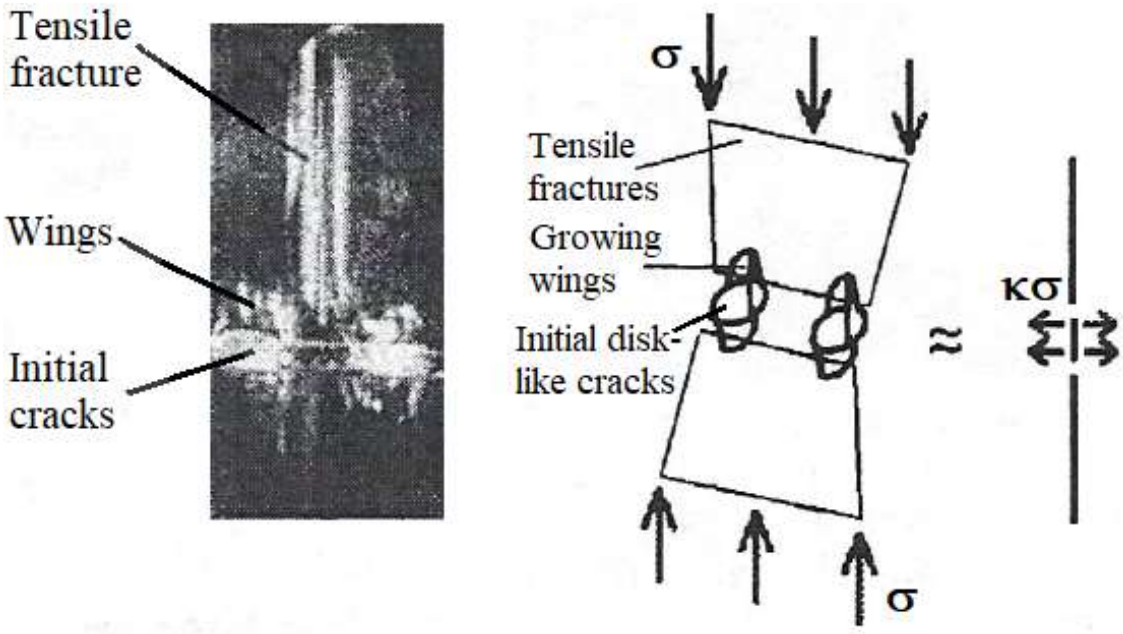

Fig. 7.2: Splitting crack (Dyskin et al.) and 2D model of 3D crack (Germanovich et al).

The probability of a 3D crack condition arises in an equiaxial scenario when there is a significant body of the fracture in both the axes. Such a condition induces additional complexity merely because of the resistance met during the fracture propagation while trying to fail the material along both the axes. As observed by Dyskin et al. (1994) and Germanovich et al. (1996), these additional constraints obstruct the crack growth that result from a split-opening

fracture shown in the right-hand side sketch of Fig. 7.2 to mix-mode fractures shown in **Fig. 7.2** obtained from the experiments conducted on transparent casting polyester resin that was pre-notched with a laser. The material behaved plastically under ambient conditions but becomes sufficiently brittle if frozen to -20°C (-4°F) and exhibits near linear stress-strain relationship with a Young's Modulus of 0.58×10^6 psi (4 GPa) and K_{Ic} of 546 psi.in^{05} (0.6 MPa.m$^{0.5}$).

The experimental study shows wing like fractures growing from initial cracks and ultimately resulting in large tensile fractures that are independent of how the crack was initialized. One important observation made from the experiments (Dyskin et. al 1994) was that the mere presence of complex fractures may be sufficient for a horizonal fracture component to develop and propagate. Thus technically, the presence of an extended crack along the initial direction, and associated wing like and/or tensile fractures are sufficient to represent the complexity of a 3D crack growth. The 2D equivalent of such a complex crack setup is in the extreme right sketch shown in Fig. 7.2, represented as a case of three collinear cracks of mixed mode, where the middle crack in the center acts as the driver to the wing cracks with energy provided by compressive load σ. The coefficient κ represents the crack density.

7.3.2. Modeling of 3D Cracks: Oblique and/or Elliptical Fractures

For a 3D elliptical crack, the fracture propagation criteria proposed by Key (1969) in terms of average strain energy release rate (G) along the crack boundary is as follows:

$$G = \frac{4\pi}{3E'}\sigma^2 \frac{\partial}{\partial A_c}\left(\frac{x^2 c}{E(k)}\right) \quad \text{..... (7.1)}$$

where, x and c are the minor and major axes of the elliptical crack, respectively, A_c is the area of elliptical crack given as πxc, σ is the uniaxial stress normal to the crack that has developed into an ellipsoidal cavity in three dimensions, and $E(k)$ is the complete elliptical integral of the second kind, and $k = [1 - (x/c)^2]^{½}$. The solution to the above equation was presented by Daneshy (1978) after taking effective stress as the difference between crack internal pressure and closure stresses ($p - \sigma$). The solution shown below was obtained after using the relation for G (or G_f) from Eq. (2.1) in terms of critical stress intensity factor or *fracture toughness*, K_{Ic}.

$$K_{Ic} = \frac{(p-\sigma)}{E(k)}\sqrt{\frac{2}{3}\frac{x[2(x^2+c^2)E(k)-x^2K(k)]}{(x^2+c^2)}} \quad \text{..... (7.2)}$$

where, *K(k)* is the complete elliptical integral of the first kind. For a penny-shaped fracture with a large value of minor axis such that $x \rightarrow c$, Eq. (7.2) reduces to the criterion proposed by Sneddon (1946) for penny shaped fractures, as both $E(k)$ and $K(k)$ are reduced to a value of $\pi/2$ for $k = 0$ (since $x = c$).

7.4. Collinear Cracks and Their Coalescence

For a system of two coplanar cracks where the end members are yet to coalesce the stress intensity factor K_I^{tip} at the outer tips of the cracks can be given as follows (Cherepanov 1979):

$$K_I^{tip} = \frac{2F}{\sqrt{\pi w(w^2-y^2)}}\left[L\sqrt{\frac{L^2-y^2}{w^2-y^2}} - \frac{ln(y)}{wL} \times \frac{w\sqrt{(w^2-L^2)(w^2-y^2)}}{K(k)}\right] \quad \text{..... (7.3)}$$

where, w is crack half-length, F is the average force equal to the horizontal projection $2w\sigma\beta(\alpha_a)$ with α_a being the angle representing the direction of stress compression (σ). The variable $\beta(\alpha_a)$ depends on the angle α_a and the friction angle μ of the material. The variable y represents the distance from the middle of the gap between the two coplanar fractures, e.g., half the distance between the points -*b* and -*c* in **Fig. 7.4**, and w is the distance from midpoint of the gap to the tip of the fracture on either side. L is the distance from the midpoint to the loading point along the axis of the crack where the force F is acting normal to the crack (see Fig. 7.1 right plot). If the gap $2y$ between the cracks vanishes and the cracks coalesce, a more simplified form of SIF, as shown below, emerges:

$$K_I^{tip} = \frac{2\sqrt{w}F}{\sqrt{\pi(w^2-L^2)}} \quad \text{..... (7.4)}$$

where, the system is still pressurized at two locations consistent with the conditions prior to coalescing. If after coalescing, the force is assumed to be uniform throughout the crack and acting at $L = 0$ which is the center of the total crack length now $2w$, Eq. (7.4) assumes a similar form as that of the stress intensity factor for a crack in an infinite elastic medium.

7.5. Crack Propagation in 3D Under Compression

The 3D mode of crack propagation illustrated in the middle schematic of Fig. 7.3 were also observed and modeled by other researchers (Adams and Sines 1978; Scholz 1990) with remarkable similarity in observations. The main body of the crack lies in the horizontal direction; its propagation was assisted by the starter flaws that bore elliptical or penny shapes that were planted to help initiate complex 3D fracturing. Under the compressive loads, several

vertical tensile fractures developed around the boundary of the primary crack, assisted by secondary wing or petal-shaped fractures, even under triaxial loading conditions as seen in **Fig. 7.3**. The 3D pattern of fracture growth is simplified to a 2D problem by adopting the approach shown in the right-most sketch of Fig. 7.2 where the complexity is now represented as a collection to three discrete collinear cracks.

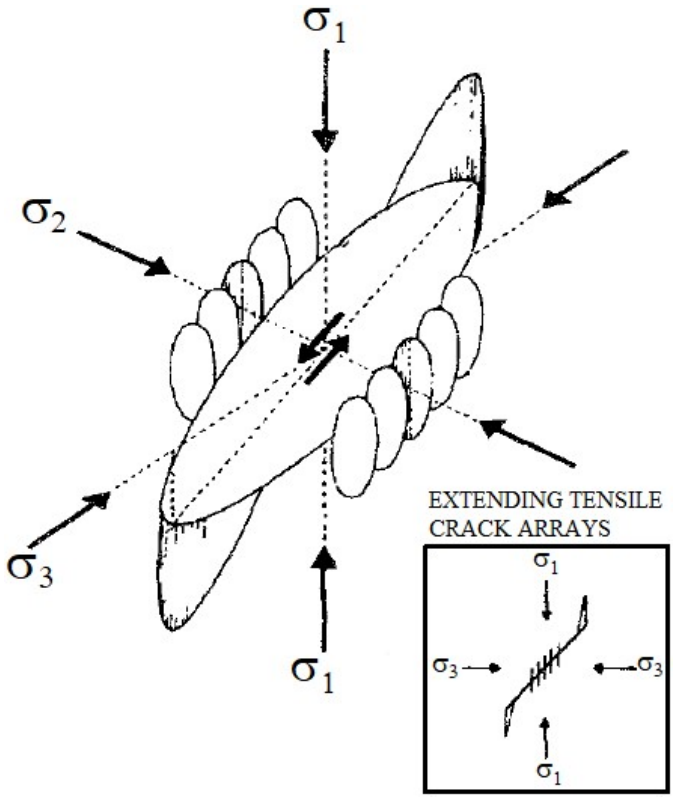

Fig. 7.3: Crack propagation under 3D compression loads. (*Adapted from* Scholz 1990)

The collinear cracks can be configured in 2 different modes illustrated in **Fig. 7.4** . In case (a), the fractures mirror across an imaginary midpoint of the center fracture with distances $c < b < l$ along the crack x axis. The crack in the middle is held open by pressure p and is equivalent to the influence that wing cracks have on the growth of large fractures in the middle schematic of Fig. 7.2. The pressure p is in fact the effective stress that will result in the same opening of the middle crack as that of the simulated wing crack. Because of this arrangement, stress singularities are expected at the points $x \pm c$, $x \pm b$ and $x \pm l$, and in the region $c < |x| < b$ shown in (b) where the condition of non-zero displacement distribution $u_y(x) \neq 0$ exists. Because of the symmetry in the layout of the problem, the solution is only required for positions of x at c, b,

and *l*. It may be noted that in the solution provided by Germanovich et al. (1996), the displacement is set to a zero value which will result in a different SIF value.

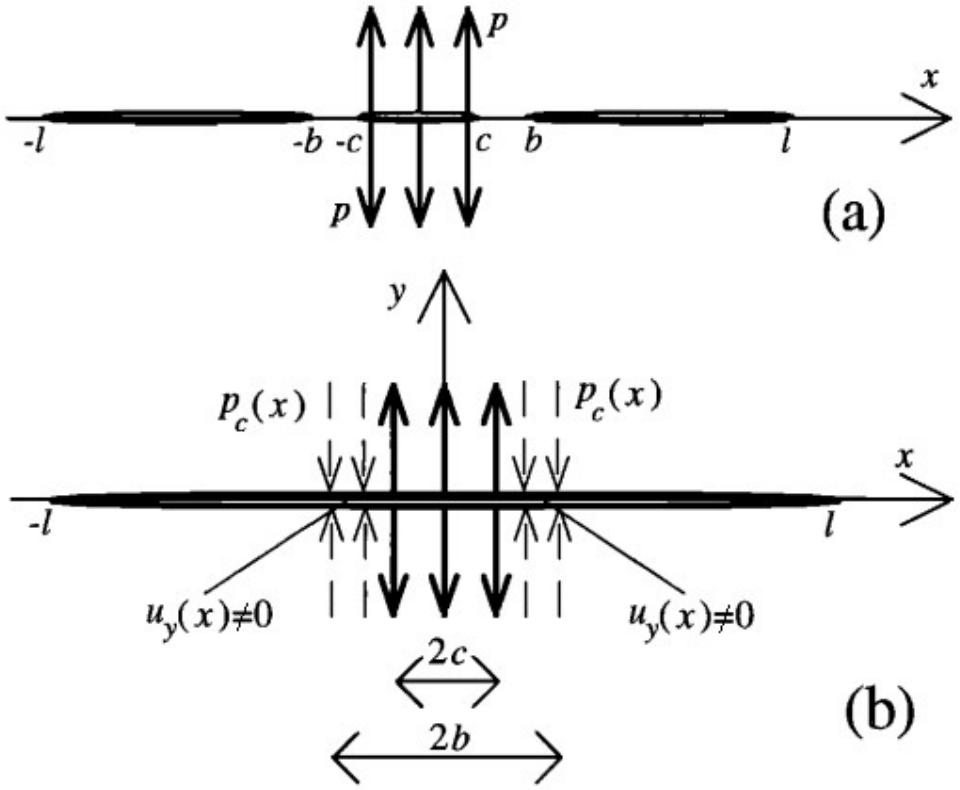

Fig. 7.4: Collinear Cracks (a); mixed boundary conditions (b). (Germanovich et al. 1996)

7.6. Modeling Approach

Though the modeling of 3D fractures is complex, its inclusion in some form or other is important to ensure predictions that match the field occurrences, especially those related with formation of horizontal components and fallouts from that. To accomplish this, the model can be improved by adopting a more simplified mathematical representation of a 3D fracture with active horizontal component, as discussed above, and elaborated in Pandey and Rasouli (2022a). While taking this approach, it can be hypothesized that in the presence of at least three discrete collinear fractures, if infinitesimally small displacements can be detected during the simulation process, then there exists a possibility of horizontal component forming across the plane where such a behavior was detected. For the fractures to orient in a horizontal plane however the effective fracture pressures must exceed overburden, which is not unusual in hydraulic fracturing treatments where the initial stresses are high.

The simulation of width profile from an example case that emulates the presence of 3 collinear cracks is shown in **Fig. 7.5.** The changes in width as the net pressure increases are simulated for three instances: early, middle, and late time. The fracture appears to be sufficiently held open in early stages of the treatment but offers little hint that ultimately it will progress to a scenario that will support development of any horizontal component.

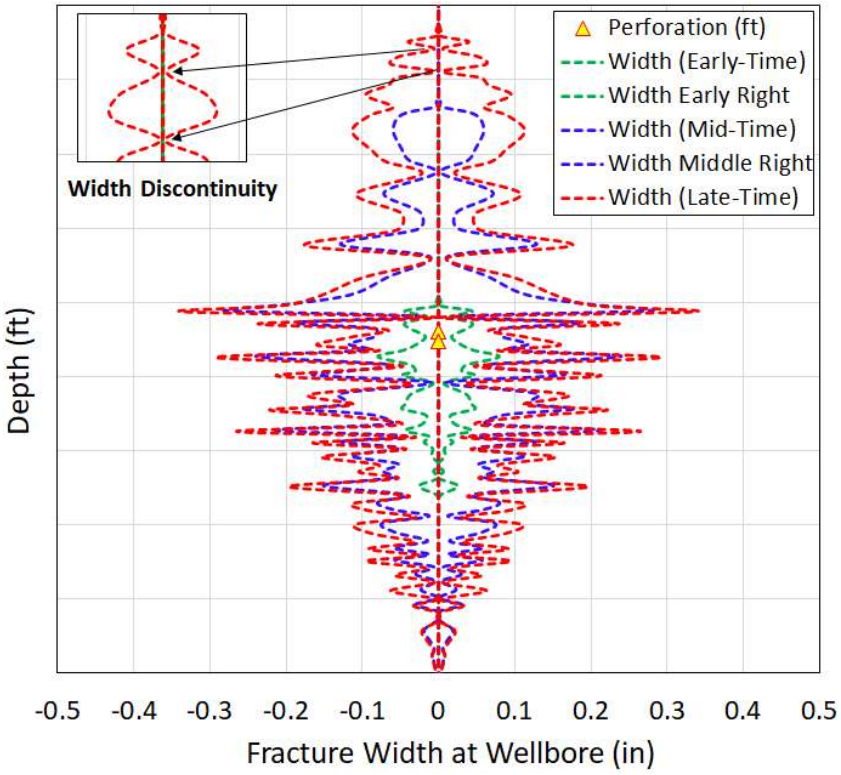

Fig. 7.5: Evolution of fracture width and existence of collinear cracks in late time.

The fracture height increases with the net pressure and as the late-time width profile beings to take shape, it is evident that the criteria of discrete collinear fractures will be eventually met. Thus, for the purposes of prediction for fracture complexity, the simulator was programmed to detect these possible discontinuities and if other conditions are met, flag the corresponding depths as possible sites where the horizontal fracture components can initiate and propagate from. For accuracy of calculations and to incorporate the mechanics of the problem, the effects of modified stress intensity factors must be superimposed to the original calculations to account for anomalies in fracture vertical growth.

7.7. Stress Intensity Factors (SIF) for Specific Cases

The solution to the triple crack problem with mixed boundary conditions (discussed in section 7.5) was explicitly derived and presented by McCartney (1983). The solution process involves several mathematical sub-steps that operate around the assumed boundary conditions and a set of transforms for appropriate coordinate system. As the problem is set up for a symmetric case, only the positive values of displacement from *c* to *l* are evaluated. For triple collinear cracks of Fig. 7.5, the transformation parameter *t* is given as follows:

$$t = \frac{2\xi^2 - b^2 - c^2}{b^2 - c^2} \quad \text{.....(7.5)}$$

where, ξ is the elemental length advancing from midpoint of middle fracture to *l*. For positions of ξ ranging from 0, *c*, *b* and *l*, *t* assumes various values that are denoted by $t = -t_0$, t = -1, $t = 1$, and $t = t_l$, which are used in the principal solution equation being given by Eq. (21) in McCartney (1983).

7.7.1. SIF for Triple Collinear Crack Conditions

When expanding the height prediction model to include fracture complexity from 3D fractures, the effects of SIF in the presence of both zero and non-zero displacements along the crack axes for regions lying between the two collinear cracks shown as $u(x)$ in Fig. 7.4(a), were comprehensively accounted for in the calculation routines. The stress intensity factors at the tips of a pressurized crack of length $2l$ such as shown in Fig. 7.4(b) was proposed by Sneddon and Lowengrub (1969) as follows:

$$K_I = 2\sqrt{\frac{l}{\pi}} \int_0^l \frac{p(\xi)d\xi}{\sqrt{(l^2 - \xi^2)}} \quad \text{..... (7.6)}$$

for a symmetric pressure distribution of $p(\xi) = p(-\xi)$. If Eq. (7.6) is expanded for mixed boundary conditions, the following expression that superposes various SIFs for regions of the crack from the midpoint of the central crack (0) to the tip of the extreme crack (l) is obtained:

$$K_I = 2\sqrt{\frac{l}{\pi}} \left[\int_0^c \frac{p_o(\xi)d\xi}{\sqrt{(l^2 - \xi^2)}} + \int_c^b \frac{p(\xi)d\xi}{\sqrt{(l^2 - \xi^2)}} + \int_b^l \frac{p_1(\xi)d\xi}{\sqrt{(l^2 - \xi^2)}} \right] \quad \text{..... (7.7)}$$

where, p_o and p_1 represent effective pressures in the sections 0 to c and b to l, respectively. On transforming to variable t defined in Eq. (7.5), the expression transforms to:

$$K_I = \sqrt{\frac{l}{\pi}}\left[\int_{-t_0}^{-1} \frac{P_o(t)dt}{\sqrt{(t_1-t)}\sqrt{(t_0+t)}} + \int_{1}^{t_1} \frac{P_1(t)dt}{\sqrt{(t_1-t)}\sqrt{(t_0+t)}} + 2\bar{q}(1) - \int_{-1}^{1} \frac{\bar{q}(t)dt}{t_1-t}\right] \quad \text{..... (7.8)}$$

Here, $P_0(t) \equiv p_0(\xi)$, $P_1(t) \equiv p_1(\xi)$, and $\bar{q}(t) = \int_c^{\xi} p(y)dy/\sqrt{(l^2-\xi^2)}$ describes the pressure distribution of the crack in the region between c and b for appropriate values of t. It may be noted that during height growth simulation if the internal pressure distribution in the crack is known (which is usually the case), the solution to the problem is greatly simplified. If the displacement in the region $c < |x| < b$ is assumed to be zero, the solution reduces to the triple crack problem for which an exact solution was developed using Muskhelishvili's (1953) method (Tada et al. 1973). The mode–I SIFs at locations, c, b, and l are presented below.

$$K_I^c = p\sqrt{\pi c}\sqrt{\frac{(l^2-c^2)}{(b^2-c^2)}}\frac{E(k)}{K(k)} \quad \text{..... (7.9)}$$

$$K_I^b = p\sqrt{\pi b}\sqrt{\frac{(b^2-c^2)}{(l^2-b^2)}}\left\{\frac{l^2-c^2}{b^2-c^2}\frac{E(k)}{K(k)} - 1\right\} \quad \text{..... (7.10)}$$

$$K_I^l = p\sqrt{\pi l}\sqrt{\frac{(l^2-c^2)}{(l^2-b^2)}}\left\{1 - \frac{E(k)}{K(k)}\right\} \quad \text{..... (7.11)}$$

where, p is the crack opening pressure, K_I^c, K_I^b and K_I^l are the stress intensity factors at the locations c, b and l described in Fig. 7.4, and k is obtained as $k = (l^2 - b^2)/(l^2 - c^2)$ for $c < b < l$. When solving for SIFs, the values of complete elliptical integrals of the first and second kinds, given by $K(k)$ and $E(k)$ respectively, were obtained from tables provided in Appendix L of Tada et al. (1973). The solution to SIFs for the triple crack problem was also obtained by Goyal (1974) but should be corrected by proper substitution of constants C_1 and C_2 described in the study which leads to final form that resembles Eq. (7.9) to (7.11).

7.7.2. SIF for Triple Collinear Cracks with non-Zero Displacements

The problem defined in Fig. 7.4(b) shows a condition where the 3D crack is transformed to a 2D crack while maintaining non-zero widths in the regions of $c < |x| < b$ which is more appropriate representation of real-world conditions where collinear cracks of varying widths may exist and maybe connected via hairline fractures. For these conditions the solution offered by McCartney (1981) for a main crack linked with micro-void via a ligament is suitable; in terms of current problem set up the one-half of middle crack shown in Fig. 7.4(a) acts as the main crack, the gap between locations c and b where $c < b$ denotes the ligament with non-zero widths and the location $b < x < l$ represents the void, with all the cracks being coplanar. The SIF at position l is given by

$$K_I^l = \sqrt{\left(\frac{l}{\pi}\right)}\left[\sum_{r=1}^{\infty}\alpha_r\left\{t_1-\sqrt{t_1^2-1}\right\}^r+(\alpha_0-\pi\sigma)\left\{1-\frac{1}{k}\left(1-\frac{E(k)}{K(k)}\right)\right\}\right] \quad .. (7.12)$$

where, α_r and α_0 are coefficients to Chebyshev polynomials bearing the units of stress that can be obtained using standard procedures. Here it is assumed that $\alpha_0 = \pi p$, σ is the external stress acting normal to the plane of the crack, and r is the number of degrees of the Chebyshev polynomials. Also, based on Eq. (7.5) the value of $t_1 = (2l^2\text{-}b^2\text{-}c^2)/(b^2\text{-}c^2)$ for $\xi = l$.

The expressions for stress intensity factors at crack tips at c and b are given by the following relations that are modified from the original text that presented these in the terms of transform variable t.

$$K_I^c = 2\sqrt{\frac{c}{\pi}}\sqrt{\frac{l^2-c^2}{b^2-c^2}}\left[\sum_{r=1}^{\infty}(-1)^{r+1}\alpha_r-\frac{(\alpha_0-\pi\ )}{2}\frac{E(k)}{K(k)}\right] \quad ..... (7.13)$$

$$K_I^b = 2\sqrt{\frac{b}{\pi}}\sqrt{\frac{l^2-b^2}{b^2-c^2}}\left[-\sum_{r=1}^{\infty}r\,\alpha_r-\frac{(\alpha_0-\pi\sigma)}{2k^2}\left\{\frac{E(k)-\left(1-k^2\right)K(k)}{K(k)}\right\}\right] \quad ..... (7.14)$$

For zero displacement in the region between c and b, and uniform pressure in the crack p, Equations (7.12) to (7.14) will reduce to corresponding solutions shown for discrete triple crack case as the term α_r will be reduced to zero.

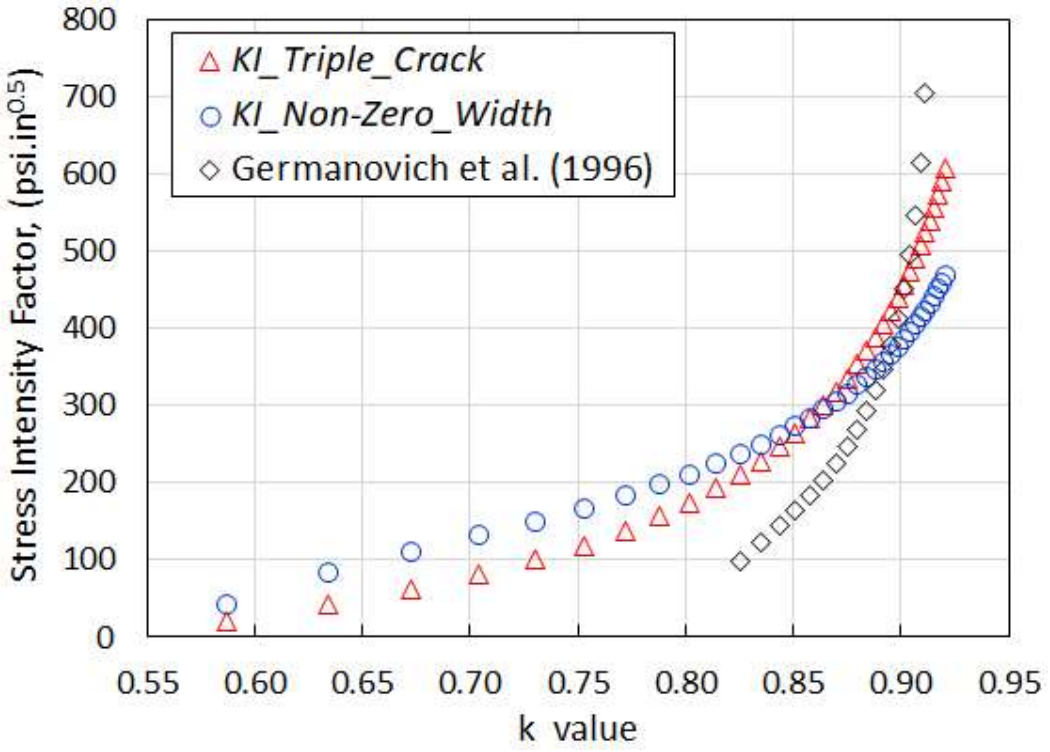

Fig. 7.6: Plot of SIF versus k values generated with random inputs of *c*, *b* and *l*.

Assuming a case where total force $F = pc$ opens the crack shown in Fig. 7.4(b), Germanovich et al. (1996) also presented a solution based on the work by McCartney (1983) for mixed boundary conditions. The final equation from the study is shown below with a correction in the term originally reported as $\sqrt{b^2 - l^2}$ which will lead to errors if the assumed precondition of $l >> b > c$ is applied.

$$K_I^l = \frac{F}{\sqrt{\pi l}} \frac{b[K(c/b) - E(c/b)]}{c l n\left(4l/\sqrt{l^2 - b^2}\right)} \quad \text{..... (7.15)}$$

A plot of SIF at the outer tip of the fracture (l) versus k was generated for plotting purposes using random values of *c*, *b,* and *l* such that the resultant k was observed as increasing function. The behavior of k clearly depicts a singularity, as shown in **Fig. 7.6** for both cases of triple cracks discussed above along with the values of SIF obtained from Eq. (7.15). The initial calculated data points show higher SIF values for case where $u_y(y) \neq 0$ that represents non-zero width, analogous to a thin ligament connecting the main cracks. In laboratory experiments this ligament represents the initial horizontal crack that assists in development of both wing cracks

and vertical tensile cracks under compression (Fig. 7.2), and in the real world its presence may provide a site for initiating a horizontal component of fracture. Although the data set was generated using random values, increases in SIF values of the triple crack case (3 discrete cracks) with that of *k* values, cannot be ruled out. The calculated data points from Eq. (7.15) increase at a rapider pace than the data sets representing other cases. The method does not offer solutions for smaller *k* values, hence was found unreliable during the simulation process.

7.8. Calculation Sequence of the Model

The height growth model carries out the following operations sequentially to predict complex fracture induced height growth restrictions:

1. The model generates a "count" of zero-width features interspersed within the non-zero width fractures around the tip, where it attempts to identify an "island" like crack with a lower continuous crack and an isolated crack in upper flank, as depicted by Fig. 7.4(a). The variable *l* designates the upper tip of the fracture.
2. The calculations continue to determine corresponding SIFs if the crack count suggests that at least 3 non-zero widths are available (though a count of two theoretically sufficient, the programming logic creates mathematical instability) which allows obtaining the value of crack lengths *a*, *b* and *l*.
3. The value of *k* is then calculated and eventually SIFs for various conditions are obtained.
4. For record-keeping purposes, the model retains all solutions of each height increment for both zero and non-zero crack widths calculated during the simulations.

7.9. Model Application to Field Cases

The model was applied to field cases to predict the possible occurrence of horizontal fracture components, especially in the presence of fracture pressures that exceeded the overburden at the depth of application. The model construction and simulation for a given case is a 3-step process that can be stated as below:

1. Gathering model input data which includes layered input of formation true vertical depths, layer thicknesses, stresses, fracture toughness, layered moduli, Poisson's ratio, expected layer leakoffs, fluid rheology and others. Uncertainties in the fracture toughness values can be handled by the model while generating the stress and fracture toughness matrix prior to history matching process elaborated in Chapter 5 and 6.

2. The second step in the process consists of determining the location of the fracture, corresponding net pressure and fracture width for a given input value of fracture height – the height increments are very small, simulating a slowly advancing fracture. The pressure distribution inside the fracture is allowed to vary based on the assumptions made – linear, power law, or following a quadratic behavior. These influence the fracture width calculations. During this second step itself the simulator identifies the presence of three collinear cracks for each height input starting from the upper tip of the fracture to the middle of the fracture (see Fig. 7.5) and applies the necessary correction to the fracture toughness that was either calculated based on fluid velocity or input as a layered property. The effect of solid mechanics-based width estimation and the ensuing effect on dependent calculations, is thus incorporated simultaneously as discussed in Pandey and Rasouli (2022a).

3. In the third step, the fracture top and bottom tip distance from midpoint versus net pressure mapping generated at the end of the second step is then used in carrying out a pressure history match of actual field data using the rate, fluid rheology data, and formation leakoff.

7.9.1. Case – I: Fracturing in Highly Laminated Formation

This case history pertains to the fracture stimulation treatment pumped as the last stage in a multi-stage horizontal well completion of a deep and highly laminated limestone and shale formation consisting of alternate sequences of shales, siltstones, mudstones, and limestones with significant variations in Young's Modulus ranging from 2.25 MMpsi (1.55×10^4 MPa) for shaly layers to nearly 5.88 MMpsi (4.054×10^4 MPa) for limestones. The primary target was oil reserves trapped in limestone with low porosity of 9% and permeability of less than 0.1 md which results in a calculated fluid leakoff of 0.00011 ft/min$^{0.5}$ (4.3×10^{-6} m/s$^{0.5}$) that was determined from the falloff during pre-treatment diagnostic tests. The treatment plot is shown in **Fig. 7.7** that displays various data related to fracturing treatment including the simulated net pressure and the match of the surface pressure data.

The initial fracture gradient (F.G.) of 0.946 psi/ft (21.40 kPa/m) probably resulting from stress accumulation after the fracture stimulation of previous stages, was observed. Considering the true vertical depth (TVD) of 9,942 ft (3,030.3 m), this meant that a net pressure gain of approximately 525 psi (3.62 MPa) will result in fracture pressures reaching the overburden gradient of 1.0 psi/ft (22.62 kPa/m). In the treatment plot presented, the end-of-the-treatment F.G. is 0.99 psi/ft indicating that during the pumping, the pressures were higher than

overburden. The treatment was pumped down 4 ½ in. (114.3 mm) casing at 22.0 bbl/min (0.06 m^3/s) using a 20 lbm/Mgal (2.4 kg/m^3) cross-linked fluid with a maximum proppant concentration of 1.5 PPA (179.74 kg/m^3).

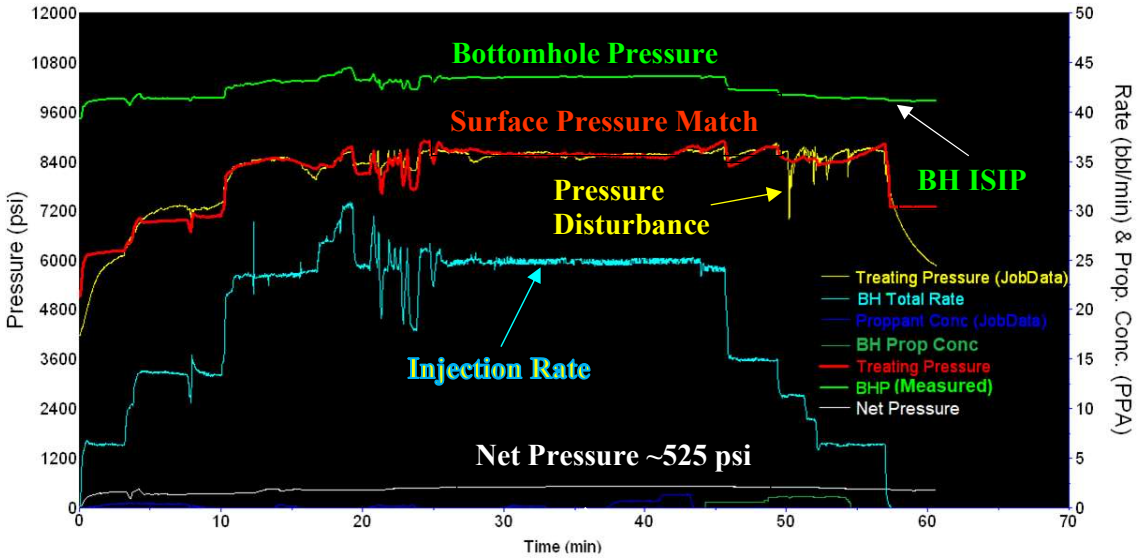

Fig. 7.7: Fracturing treatment and surface pressure history match – Case 1.

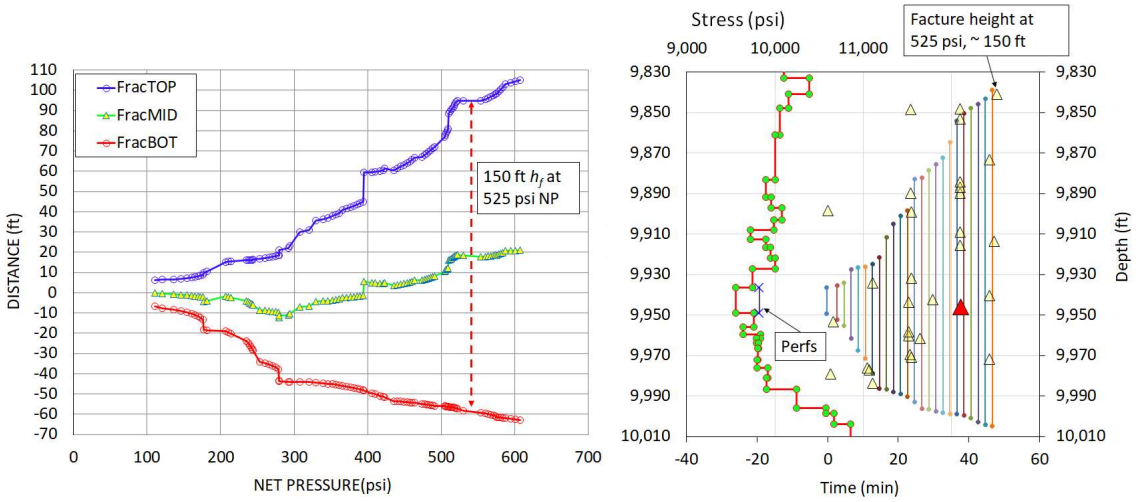

Fig. 7.8: Height growth vs. net pressure (left) and comparison with MS Data – Case 1.

The fracture distance versus the net pressure plot shown in the left of **Fig. 7.8** suggests that with the net pressure of 525 psi (3.62 MPa) that was observed during the treatment (see Fig. 7.7), the fracture height can increase up to 150 ft which closely matches the field measurements based on the microseismic (MS) survey shown in right hand side plot of Fig. 7.8. The upper and lower fracture-tips are denoted as FracTOP and FracBOT respectively, and FracMID shows the mid-depth of the fracture that may not always coincide with perforation depth at 0

distance. The corresponding layered stress model is shown on the right plot along with fracture height and locations represented by vertical bars for various net pressures. The yellow triangles represent the MS events with respect to time that that is shown in x-axis; the event depth can be obtained from either of the y-axes. The red triangle designates the event that was measured around 900 ft (274.3 m) south of the wellbore heel.

The simulated fracture width profiles along the fracture for some of the fracture heights depicting early to late time hydraulic width evolution are shown in **Fig. 7.9**. Mathematically, the profile suggests a probability of three-dimensional (3D) fractures to take form because of the presence of near zero width collinear cracks at the fracture tip that develop at late time and the fact that the injection pressures exceeded the overburden during the treatment.

The low YM shales contribute to larger simulated widths near the perforation depth shown by the yellow triangle in Fig. 7.10, supported by availability of maximum net pressure at that depth. The width constrictions seen at 9,900 ft (3,017.5 m) and 9,914.7 ft (3,022 m) can act as a potential site for horizontal fracture component if the effective fracture pressures were to exceed the overburden.

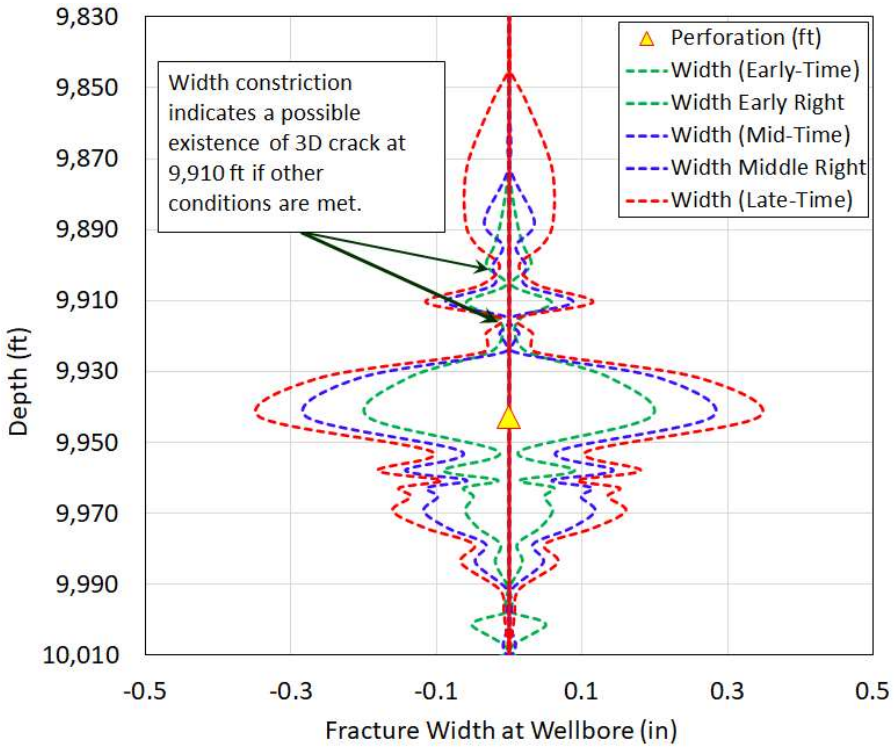

Fig. 7.9: Fracture width profile and prediction of site of fracture complexity – Case 1

The fractures were initiated from the base of the limestone member, primarily in laminated shales, mudstones, and brittle siltstones which is shown by the wellbore schematic in **Fig. 7.10**. The laminated nature of the formation can act as a catalyst in creating fracture complexity as layers with relatively weak bonding such as the one with highly contrasting moduli may not only facilitate formation of horizontal component but also promote slippage along a dipped formation bed as was the case here.

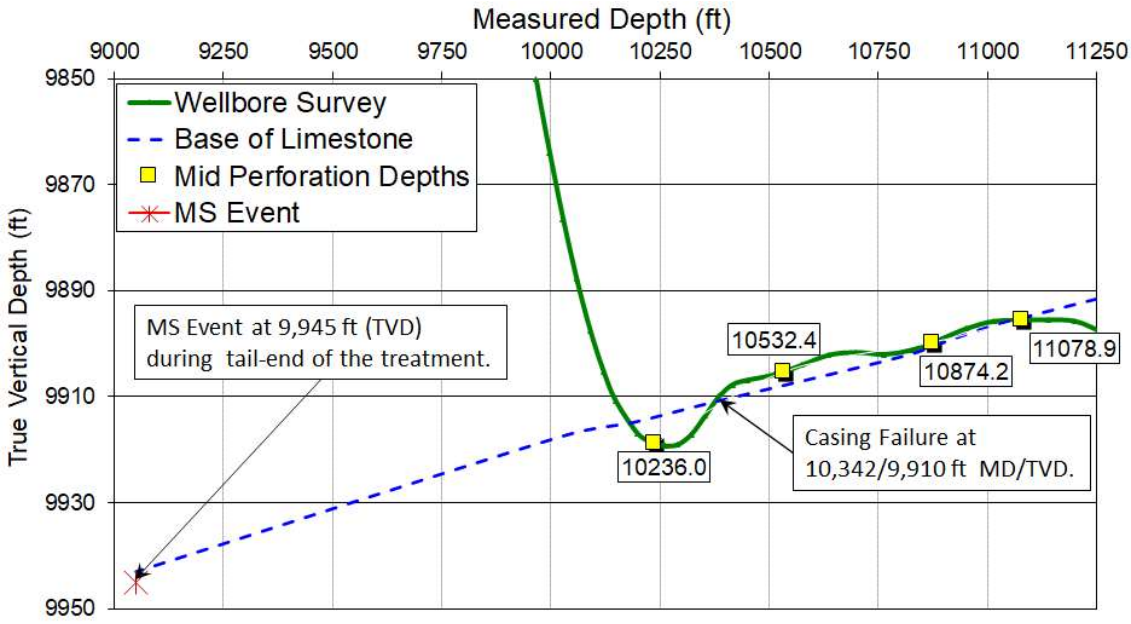

Fig. 7.10: Wellbore trajectory, along with MS event and casing failure depth – Case 1.

The wellbore survey sketch in Fig. 7.10 shows the undulating well (in a laterally compressed scale) and marks the measured perforation depth for the final stage at 10,236 ft (3,119.9 m) (9,942 ft TVD) as below the base of the limestone formation and into the underlying shale layer. The TVD of the base of limestone at this point in the wellbore is 9,915 ft (3,022.1 m). A high intensity mircoseismic signal was recorded at a location nearly 900 ft (274.3 m) south of the wellbore heel and at a TVD of 9,945 ft (3,031.2 m) around 37 minutes into the treatment. This depth is in the vicinity of the projected limestone/shale bed boundary at that location as illustrated on the bottom left of Fig. 7.10 with a red cross-shaped marker. Given the prevalent conditions of higher than overburden injection pressures, possible weak cohesion between materials of high YM contrast and varying material properties, and a potential to form complex fractures in presence of discrete collinear cracks as simulated by the model, a physical event of

slippage along bedding plane cannot be ruled out and may explain the casing shear failure at the depth that coincided with the limestone and shale bed boundary.

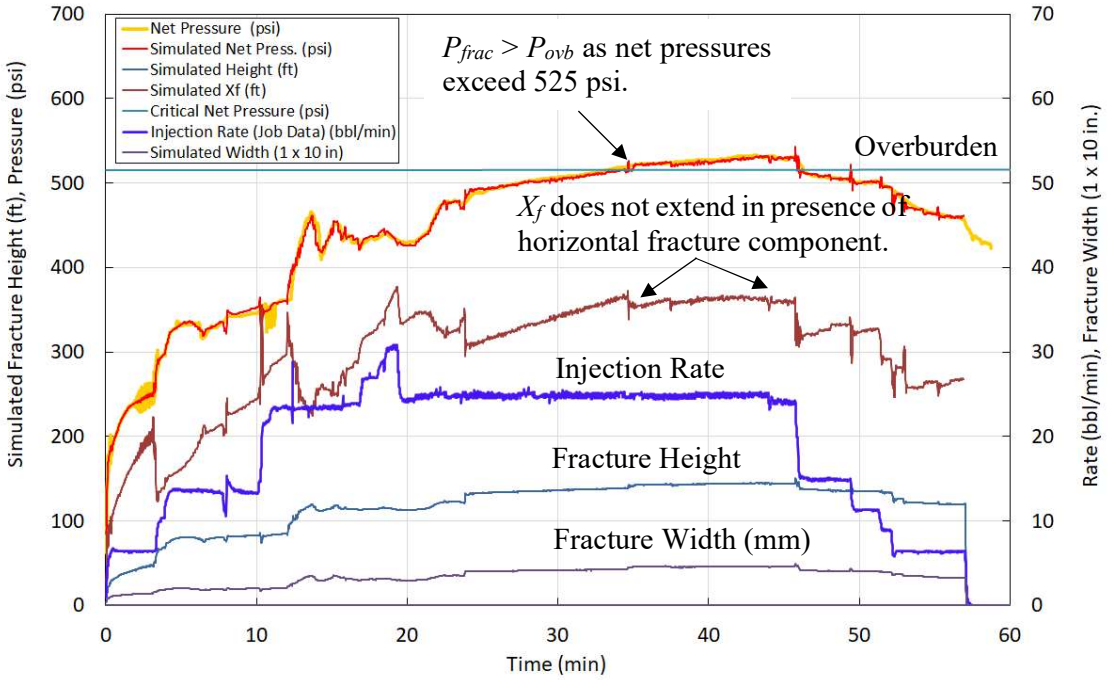

Fig. 7.11: History match of net pressure and explanation of fracture extension – Case 1.

The net pressure from the treatment was history matched with the help of the model (Pandey and Rasouli 2022a) and the results are shown in **Fig. 7.11.** The match predicts a fracture height of nearly 150 ft (45.72 m) during the treatment which agrees with the MS data. The fracture half-length is restricted to 375 ft (117.3 m) once the fracture pressures exceed the overburden; the half-length is nearly the same as that inferred from MS survey (not shown here). The possibility of a horizontal component at this point which also manifests in a "flat" net pressure response (Nolte 1979) due to enhanced fluid leakoff cannot be ruled out. The event of high seismicity occurs around the same time when the critical net pressures are reached. The actual damage to the casing coincided with another event triggered after the rate drop at 49 minutes which was followed by a sudden perturbation in surface pressure (see Fig. 7.7). With the rate drops and as the net pressure recedes, an increasing trend in simulated fracture half-length is observed. This combined solid mechanics and fluid dependent lubrication model (Pandey and Rasouli 2021b) predicts a maximum width of 0.466 inch (12.0 mm) compared to a higher value of 0.6 inch (15.2 mm) obtained from stress and mechanical property model alone (Fig. 7.11).

7.9.2. Case – II: Exceeding Overburden Pressure in Deeper Wells

As evinced from pressure data of several fracturing treatments pumped in deep ultra-low permeability unconventional reservoirs, the bottom hole injection pressures at the inlet of the fracture often exceeds the overburden during the treatment. This case history relates to a horizontal well completion in a source rock reservoir characterized as highly laminated, organic-rich, ultra-low permeability calcareous shale where higher than overburden pressures were interpreted from the recorded bottomhole pressures. For the treatment, a 30 lbm/Mgal (3.6 kg/m^3) cross-linked fluid was used to pump intermediate strength proppant with maximum concentration of 3.5 PPA (419.4 kg/m^3) down a 5 ½ casing at 70 bbl/min (0.185 m^3/s) with 8 perforation sets spread across 200 ft (60.1 m) laterally. The mechanical properties of the formation that included Young's Modulus and Poisson's ratio were generated with the help of sonic logs and later calibrated with the field data. On average, the YM was determined to be 3.0 MMpsi (2.1 × 10^4 MPa) whereas the Poisson's ratio was nearly 0.24. Given the low permeability formation the effective fluid leakoff was nearly 0.00011 ft/min$^{0.5}$ (4.3 × 10^{-6} m/s$^{0.5}$) from data analysis. The effective formation face pressures were calculated with the help of data obtained from downhole memory pressure gauge following the procedures outlines by Pandey et al. (2020) and were found to be exceeding the overburden of 12,800 psi (88.3 MPa) during the treatment. Despite high bottomhole injection pressures of nearly 13,500 psi (93.1 MPa) which is inclusive of perforation friction, the net pressures were calculated in the range of around 450 psi (3.1 MPa).

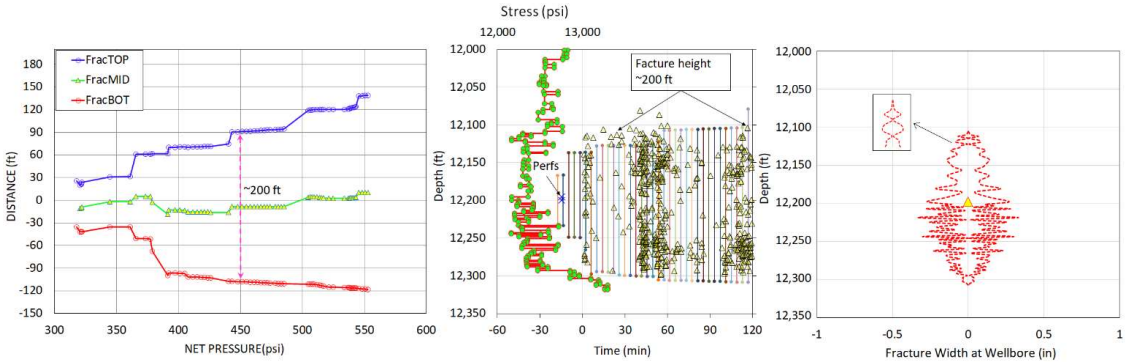

Fig. 7.12: Predicted growth and complexity compared with measured data – Case 2.

The spread of initial MS events recorded during the treatment is shown in the middle plot of **Fig. 7.12**. It can be inferred from the event log that a rapid fracture height growth occurs in the first few minutes of the treatment. This behavior is also noted in some of previous case histories discussed in earlier chapters, where the height growth rate appeared to be resulting from the

steep increase in injection rates at the start of the treatment shown in the treatment plot of Fig. 7.12. The modeled fracture heights shown by vertical bars align well with MS data. A fracture height growth of 200 ft (61.0 m) is observed which is per expectations from the distance versus net pressure plot illustrated in the left.

Although the solid mechanics based net pressure mapping (extreme left sketch in Fig. 7.12) suggests that it is possible to vertically grow the fractures even beyond 200 ft if additional net pressures were available, in real world if horizontal fracture components form, then the further vertical propagation of the fracture will be limited or not occur at all. The width profile in the extreme right shows that in the late time as the fracture growth reaches nearly 200 ft, the possibility of generating collinear fractures that are connected or remain discrete is high and can lead to complexity like giving rise to a horizontal component that can limit the vertical growth of the fracture around the depths shown and supported by MS data in the middle plot. The vertical bars in the middle plot designate various fracture heights for the modeling run.

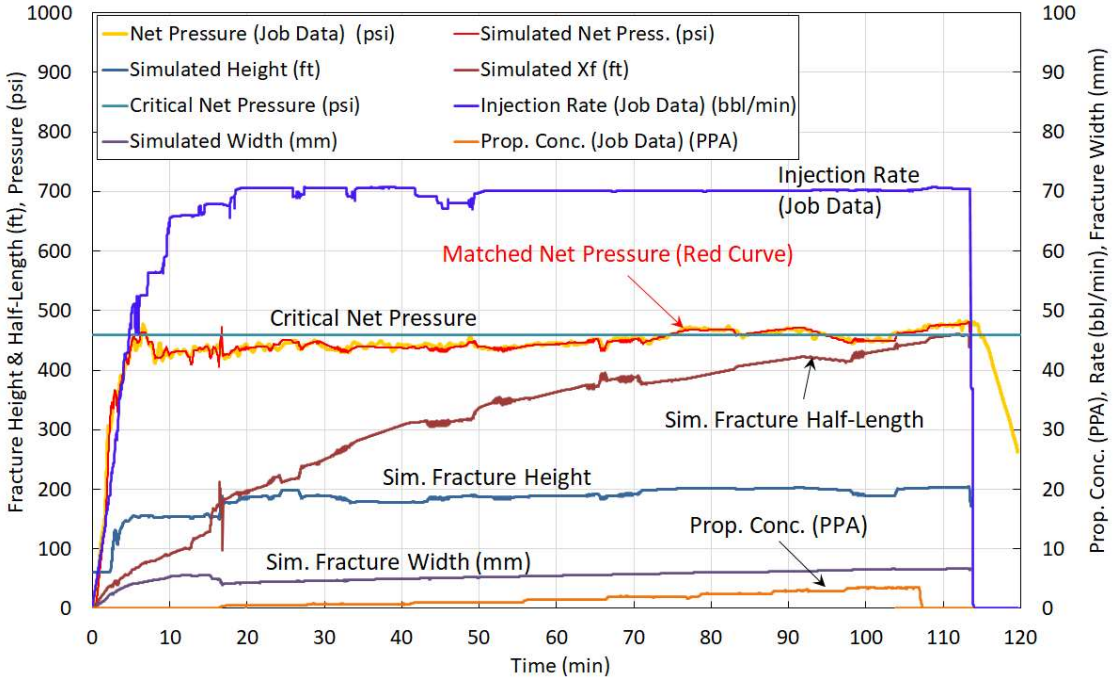

Fig. 7.13: History match of net pressure and other simulated fracture parameters – Case 2.

The bottomhole injection pressures exceeds the overburden pressure as the net pressure increases to 460 psi (3.2 MPa) around 75 min. into the treatment; the pressure history plot of **Fig. 7.13** shows the fracture height reaching nearly 200 ft, whereas the fracture half-length extension rate slows down due to possible increase in fracturing fluid leakoff. There is little

gain in fracture height during the remainder of the treatment. The rightmost width plot in Fig. 7.12 shows multiple sites where conditions favorable to formation of horizontal components exists, especially at a depth of 12,110 ft. The bottom of the fracture is contained by high stress layers starting at 12,300 ft (3,749.0 m) shown in the stress profile in the middle plot.

7.10. Predicting Fracture Complexity During the Treatment

Some of the interesting observations made during the model application on case histories include the simulated data analysis using specialized diagnostic plots. These plots can be used in predicting the likelihood and timing where the fracture complexity can peak. These plots are shown in **Fig. 7.14** and **Fig. 7.15** where the frequency of number of counts of non-zero and zero widths are shown along with the corresponding modified stress intensity factors that were superposed on the basic solution. The superposition process tends to influence the outcome of the simulator that favors fracture truncation if suitable conditions are met. The model identifies the occurrences when fracture width profiles are generated for a given height input and incrementation of the overall SIFs only if at least three non-zero widths are identified, prior to resetting the input matrix to the original values input.

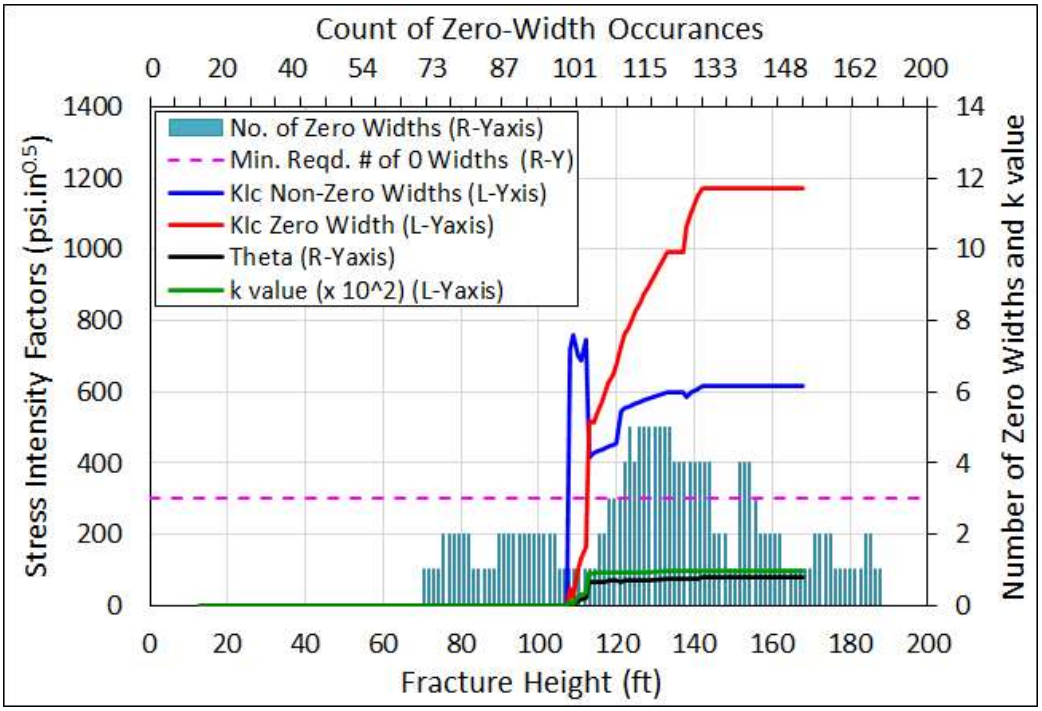

Fig. 7.14: Count of zero width occurrences during height growth simulations – Case 1.

The simulator behavior is noteworthy and varies from case-to-case basis mostly because of the input parameters that can dictate the outcome especially when the additional SIFs are to be applied selectively only when the preset criteria is met.

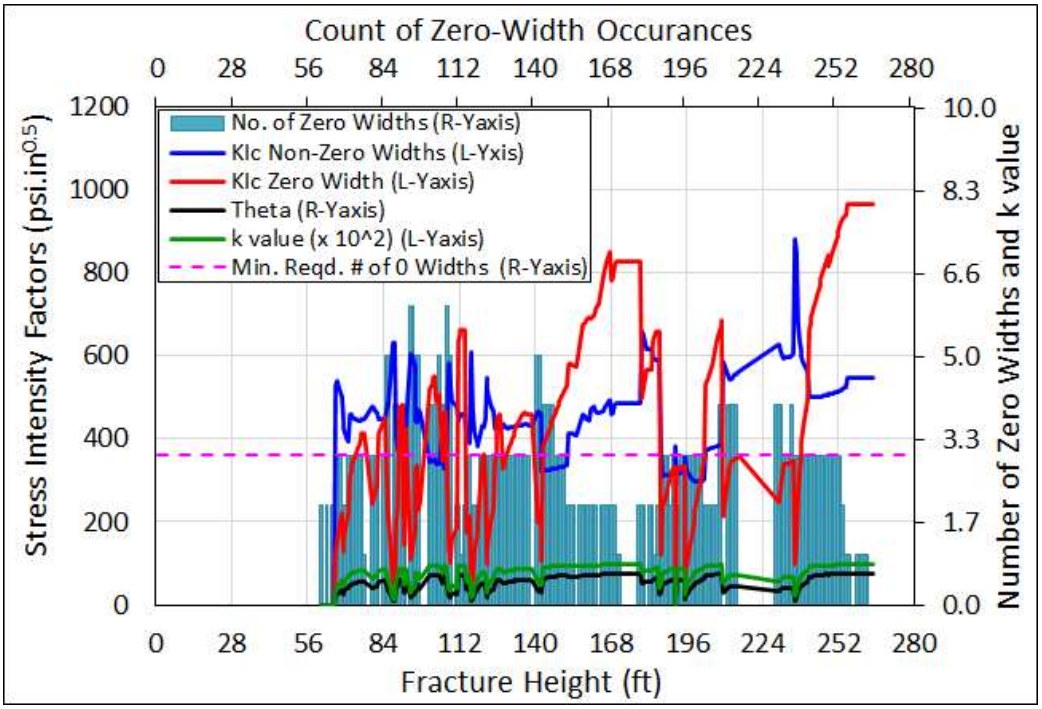

Fig. 7.15: Count of zero width occurrences during height growth simulations – Case 2.

There are fewer occurrences of zero-width for smaller facture heights in the first case shown by Fig. 7.14 in comparison to the second case history represented by Fig. 7.15. In both cases, the initial fracture gradient is greater than or equal to 0.94 psi/ft (21.3 kPa/m) and changes in net pressure can tilt the balance in favor of generating horizontal component or enhancing fracture complexity.

As seen in Fig. 7.14, representing the first case history, once the fracture height exceeds a threshold value, e.g., 110 ft (33.53 m) there is large increase in the number of such occurrences as depicted by the blue vertical bars. For the second case this occurs around 55 ft (16.80 m) presented in Fig. 7.15. Hence, with increasing net pressures, which lead to increased fracture heights (see Fig. 7.11 and Fig. 7.13), the 3D crack scenario begins to emerge which can lead to complex fracturing and only a little additional gain from fracture geometry can be extracted, because X_f, h_f and $\bar{w}$ are nearly constant. The increased forecasted occurrences of zero width thus are an indication of higher probability of fracture complexity and the corresponding

fracture heights can then be related to the net pressure to predict the critical pumping parameters that could cause such an event to occur.

Attempts to close the horizontal components by reducing the rates may not be practical in the actual treatment (especially in proppant stages) and hence it is more advantageous to prevent them from forming during the treatment by redesigning the treatment sizes. If the diagnostics are done in real-time, early termination of the treatment may be advised.

7.11. Nomenclature

A_c = area of an elliptical crack, $M^0L^2t^0$, ft^2 (m^2)

b = distance to crack tip in Fig. 7.5, $M^0L^1t^0$, ft (m)

c = major axis - elliptical crack in Eq. (7.1); crack tip distance (Fig. 7.5), $M^0L^1t^0$, ft (m)

E' = plane strain modulus, $M^1L^{-1}t^{-2}$, psi (Pa)

$E(k)$ = elliptical integral of the second kind, mathematical operator

F = average force, $M^1L^1t^{-2}$, lbf (N)

$K(k)$ = elliptical integral of the first kind, mathematical operator

G = average strain energy release rate, $M^1L^0t^{-2}$, J/m^2

k = geometric factor used in Elliptical Integral, dimensionless

K_I = stress intensity factor, $M^1L^{-0.5}t^{-2}$, psi-$in.^{0.5}$ (Pa.$m^{0.5}$)

K_I^s = SIFs at $s = c$, b and l, *various Equations*, $M^1L^{-0.5}t^{-2}$, psi-$in.^{0.5}$ (Pa.$m^{0.5}$)

K_{Ic} = critical stress intensity factor (fracture toughness), $M^1L^{-0.5}t^{-2}$, psi-$in.^{0.5}$ (Pa.$m^{0.5}$)

K_I^{tip} = stress intensity factor at the tip, $M^1L^{-0.5}t^{-2}$, psi-$in.^{0.5}$ (Pa.$m^{0.5}$)

l = distance to the tip of the crack in Fig. 7.5, $M^0L^1t^0$, ft (m)

L = distance in Eq. (7.3), $M^0L^1t^0$, ft (m)

p = pressure in the crack, $M^1L^{-1}t^{-2}$, psi (Pa)

$p(y)$ = pressure in the crack in vertical direction, $M^1L^{-1}t^{-2}$, psi (Pa)

$p(\xi)$ = pressure in the crack at elemental distance, $M^1L^{-1}t^{-2}$, psi (Pa)

$p(_{0,1})$ = pressure distribution in the crack along transformed distance, $M^1L^{-1}t^{-2}$, psi (Pa)

r = number of degrees in Chebyshev polynomials, unitless

t = transformation parameter in Eq. (7.5), dimensionless

t_0, t_1 = values of t for given elemental displacements, dimensionless

$u_y(x)$ = displacement distance (width) along crack-axis x, , $M^0L^1t^0$, inch (mm)

w = crack half-length, distance in Eq. (7.3), $M^0L^1t^0$, ft (m)

y = half-gap between two fractures in Eq. (7.3), $M^0L^1t^0$, in. (m)

α_0, α_r = coefficients of Chebyshev polynomials, $M^1L^{-1}t^{-2}$, psi (Pa)

σ = uniaxial stress normal to the elliptical crack, $M^1L^{-1}t^{-2}$, psi (Pa)

$\sigma_{1,2,3}$ = tri-axial stresses, Fig. 7.4, $M^1L^{-1}t^{-2}$, psi (Pa)

ξ = elemental distance in Eq. (7.5), $M^1L^1t^0$, ft (m)

Chapter 8

Summary and Conclusions

The performance from a fracturing treatment can be maximized if the treatment results in a desired geometry, i.e., where the effective fracture half-length reaches the designed value and the conductive fracture adequately covers but remains bound within the payzone. To accomplish this goal, the height growth is often modeled based on various numerical schemes that account for various critical parameters such as stress distribution in the formation and rock mechanical properties. The accuracy of prediction however depends on the workings of the model, and it is not uncommon to see variation in outcomes from various simulators and an overall mismatch of predicted and observed data. This shortcoming often results in unfavorable treatment outcomes which negatively effects the well performance.

A new model to accurately predict the fracture height growth in various cases was developed in this study. The model was then extended to incorporate additional features to expand its application to cases that are difficult to model with typical simulators. The key highlights and conclusions from the study are provided in the text below where the new height growth prediction model is referred to as “model”.

8.1. Base Model Construction and Application

1) The underlying theory related to fracture height growth modeling is presented in Chapter 2 which also provides an insight into the existing body of literature.
2) The height growth model construction steps are provided in Chapter 3. The mathematical semi-analytical model developed using Excel VBA coding script, employs new and unique approach to develop a fracture height and location versus net pressure map to assist in fracture growth predictions.

8.1.1. Base Model Development Steps

a. Developed a layered mathematical model set up that uses array tables to store input formation depths, layer thicknesses, layered stresses and formation mechanical properties, and formation layer leakoff characteristics as inputs.
b. Develop codes to solves non-linear equations for multiple layers of input data by employing Bisection, Newton-Raphson (NR), or a combination to determine the location of input height for given stress and mechanical property distribution.

c. Calculate net pressures and fracture width for every fracture height where the solution could be obtained.

8.1.2. Base Model Features

a. In default calculations, the fracture location is not force fed into the simulator as is the case in some of the current simulators, though the simulator does provide such an option if so desired. Instead, the model determines the best location for a given input height which makes it more realistic and often moves the center of the fracture away from the point where the fracture initiates.
b. To speed up the calculations, the calculation engine employs a unique algorithm to arrive at the root in minimum number of steps.
c. Solutions for a 100-layered model can be obtained within 3 minutes. The error for NR method is around 10^{-7} % and that from Bisection is 10^{-5} %.
d. Fracture height versus net pressure mapping can be developed for two modes:
    i. for cases where the height increases proportionally to the net pressure owing the defined stress profile and,
    ii. for cases where an alternate height-net-pressure pair solution is possible where a taller fracture may be obtained for lower net pressure. This condition will arise if a certain stress barrier is overcome and the stresses above the barrier are significantly lower.

8.1.3. Base Model Testing

a. The model was successfully tested and benchmarked with industry data prior to applying on real world cases. During the development phase other models such as those described in Chapter 2, were also constructed, and tested to ensure that the current model can satisfactorily repeat the published data.
b. The model was accurately able to replicate the published data in both solution modes mentioned in item 2.d above as is shown in Chapter 3.

8.1.4. Application of Base Model to Case Histories

a. The model was employed to evaluate height growth in several real-world cases that conformed to equilibrium model approach where the fracture advancement was at a slower pace and fluid leakoff could be ignored. Also, in these cases, the fracture pressure was near uniform due to slow injection rates ranging from

8 to 12.0 bbl/min in fracture heights that were reasonably contained.

i. In majority of cases, the model predicted results were within 5% of the field observed fracture height obtained from Radioactive (RA) survey conducted on vertical wells.
ii. The model was able to accurately forecast fracture height growth in case of offshore frac pack application where the treatment was pumped at 30.0 bbl/min.

b. Apart from accurately predicting the total extent of fracture height growth as a function of net pressure, the model was also able to accurately predict the migration of the center of the fracture with respect to vertical depth, which was based on the distribution of stress in the formation and the associated mechanical properties such as fracture toughness and elastic moduli.

8.2. Model Enhancements

8.2.1. Modification: Non-Uniform Fracture Pressures

8.2.1.1. Enhancement

The model predicted height did not match with the ones observed in the field for cases that were pumped with foamed fluid where higher net pressures than those predicted by solid mechanics solution were observed which led to mismatch of up to 30% from the predicted versus observed data. The model was modified by adding possible effects of non-uniform pressure distribution to match the observed results.

8.2.1.2. Application

The enhancement was successfully tested by using a calibration constant which is simple to determine using initial boundary conditions. A double nested loop was also introduced to allow for model carrying out simultaneous calculations for height for a given net pressure. The results are shared in Chapter 4.

8.2.2. Modification: New Method of Fracture Toughness Calculations

8.2.2.1. Enhancement

Fracture height growth model was improved to allow generation of fracture toughness values with the help of a fracture tip velocity-based relationship developed in the study by combining the lubrication equation with solids mechanics solution. The new relation accounts for power law fluid indices and addresses the concerns of dependence of fracture toughness on fracture geometry and other rock mechanical properties.

8.2.2.2. Features

The model develops a dynamic library of fracture toughness for several inputs of fracture tip or fluid velocity ranging from 0.1 to 1125 ft/s for input apparent viscosity and power law fluid indices and subsequently generates net pressures for each case. These are stored in virtual memory to assist in pressure history matching.

8.2.2.3. Application

The new feature was routinely used in most of the simulations or wherever there the input fracture toughness values were not reliable. The results of some of the simulations are provided in Chapter 5.

8.2.3. Modification: Pressure History Matching

8.2.3.1. Enhancement

To evaluate the fracture height growth evaluation based on pressure data, the model was enhanced to carry out net pressure history matching of rate and pressure data recorded during a hydraulic fracturing treatment. The simulator uses fluid rheology values such as n and K, and fluid leakoff for the purpose of history matching and in essence, combines the equilibrium model with non-equilibrium approach where fracture tip velocity is an important parameter.

8.2.3.2. Features

The pressure history match features allow input of per second data that describes injection rate, wellhead density and net pressure data. The time stamped data output includes net pressure, fracture height, fracture half-length, fracture width, fluid efficiency, fluid shear rate, fracture velocity, fracture tip pressures, calibration values, fracture compliance, viscous component of net pressure, and several such parameters.

8.2.3.3. Application

The pressure history match feature was applied on several treatments and the results are provided in Chapters 5 to 7.

8.2.4. Modification: Width Induced Net Stresses

8.2.4.1. Enhancement

Using the principles of induced stresses normal to the body of the main fracture with width generation, a method that employs local fracture compliance was used to temporarily increase layered stresses for mathematical modeling purposes to predict fracture height growth truncation across layers that facilitated larger widths. The increase in stresses was confined to a local site where higher widths were calculated and were treated as an apparent value for

calculation purposes only. The induced stresses however showed an ability to limit fracture growth across susceptible layers of low strength, both moduli and stress wise.

8.2.4.2. Features

With this enhancement, a library of enhances stresses was generated for every fracture input height. The arrays were stored in virtual memory and published as desired, thus providing the history of evolution of apparent net stresses. The result of this feature is shown Chapter 6.

8.2.4.3. Application

The width induced net-stress feature was used on three case studies that included shallow vertical wells completed in coals and a deep horizontal well completed in shales. In all cases an abrupt fracture growth truncation was observed, which was successfully replicated by the model as detailed in Chapter 6.

8.2.5. Modification: Fracture Complexity as Height Growth Constraint

8.2.5.1. Enhancement

Using a 2D approximation of 3D fracture growth, the height growth model was enhanced to detect the presence of non-continuous discrete collinear fractures at the fracture tips which allowed determining the layer interfaces where a horizontal fracture can develop. The presence of horizontal fractures can deter or slow down fracture vertical growth and explain some of the fracture truncation observed in the field measurements likes MS surveys or RA tracer surveys.

8.2.5.2. Features

Similar to other enhancements, if the model detects the presence of discrete triple collinear cracks or presence of fine hairline fracture widths between seemingly disconnected fracture it revaluates the SIF and applies them to next iteration which is reasonable for a slowly advancing fracture. The output string of data is stored in virtual arrays that are used as necessary to compute fracture height growth. The library can be printed to spreadsheet if necessary.

8.2.5.3. Application

The new enhancement and features were applied to the cases histories including the one where casing shear was observed. The model was able to predict the probable depth where the incident occurred. In other examples there was good agreement between the observed and predicted total fracture heights.

8.3. Summary of General Observations

1) A good agreement between the modeled and observed fracture height was seen in all the cases where the treatments were placed at low rates limited to 12.0 bbl/min (1.91

m^3/s) that promote a contained fracture.

2) There could be high mismatch of up to 30% in cases where fluid friction in the fracture dominates the pressure behavior. However, if properly accounted for, accurate predictions of height growth can be made.
3) The uncertainty in fracture toughness can results in inaccurate prediction of fracture height and hence other more accurate semi-analytical methods proposed in this study are recommended.
4) Observations and Recommendations from Pressure History Matching
    a. The pressure history match of several field case studies shows that in most cases, nearly 65% of fracture height is generated in the first few minutes of the treatment and is influenced by the injection rate and net pressure rate.
    b. The output from this model was successfully compared to that from a well-known commercial stimulator for majority of the treatment, though the current model outperformed the numerical simulator when evaluating early time fracture growth.
    c. To limit fracture height growth a gradual increase in injection rates at the start of fracturing treatment is recommended.
    d. The pressure history match shows that with increase in fluid viscosity the simulated net pressure increases and could lead to higher vertical growth if other factors allow, whereas the fracture half-length tends to stay the same or even recede if there is high leakoff.
    e. Increased leakoff results in limited fracture geometry (height and length).
    f. With a drop in apparent fluid viscosity, the fracture growth may recede, but the fracture length will increase unless the drop in fluid viscosity also results in enhanced fluid leakoff.
    g. In general, high viscosity and low leakoff tend to stabilize the numerical simulations and helps in better convergence as compared to low viscosity fluids with higher leakoff values.
5) The inclusion of width induced net stress in the height growth calculation procedure constraints the fracture growth; the simulator may limit the number of fracture height inputs for which the solutions would be available and in doing so may position them differently in the vertical stress field when compared to the simulation when the net stress feature is not used.
6) Fracture containment can be predicted with reasonable accuracy for cases where the

fracture complexity is suspected owing to the prevalent stresses in the layered formations of contrasting material properties.

7) The diagnostic plot comprising the count and frequency of non-zero widths occurrences can help in prediction of likelihood of horizontal fracture components in real time.

The problem of modeling fracture height is a complex one given the uncertainties in the process and several variables that are at play. However, this study shows that with a concerted effort, and adopting models developed in the study, the wide gap between the predicted and observed results can be narrowed. The evaluation of several case studies shows that the model after accounting for all critical inputs can predict the fracture growth accurately.

REFERENCES

Adams, M. and Sines, G. 1978. Crack Extensions from Flaws in a Brittle Material Subjected to Compression. *Techtonophys.* **49,** 97-118.

Anderson, E.M., 1951. *The Dynamics of Faulting and Dyke Formation with Application to Britain,* second edition, Edinburgh, Scotland, Oliver and Boyd (1951).

Anderson, T. L. 2005. *Fracture Mechanics: Fundamentals and Applications,* third edition. CRC Press, Taylor & Francis Group, Boca Raton, FL. 58.

Barenblatt, G. I. 1962. "Mathematical Theory of Equilibrium Cracks," *Advances in Applied Mech.*(1962) 7, 56–131.

Biot, M.A. 1941. General Theory of Three-Dimensional Consolidation. *Journal of Applied Physics* **12**.155-164.

Biot, M.A. 1956. General Solutions of the Equations of Elasticity and Consolidation for a Porous Material. *Journal of Applied Mechanics* **23** (01). 91-96.

Britt, L. K., Smith, M. B., Haddad, Z. A. et al. 2006. Waterfracs: We Do Need Proppant After All. Presented at the SPE Annual Technical Conference and Exhibition, San Antonio, Texas, 24–27 September. SPE-102227-MS. http://dx.doi.org/10.2118/102227-MS.

Casero, A. and Rylance, M. 2020. The Unconventional Unconventionals: Tectonically Influenced Regions, Stress, States and Casing Failures. SPE-199710-MS. Presented at the Hydraulic Fracture Technical Conference and Exhibition, The Woodlands, Texas, USA. Feb 4 -6. http://dx.doi.org/10.2118/199710-MS.

Cherepanov, G. P. 1979. *Mechanics of Brittle Fracture* .McGraw-Hill, New York. 1979.

Cohen, C. E., Kresse, O., and Weng, X. 2015. A New Stacked Height Growth Model for Hydraulic Fracturing Simulation. Presented at the 49th U.S. Rock Mechanics/Geomechanics Symposium,28 June-1 July, San Francisco, California. *American Rock Mechanics Association.* ARMA-2015-073.

Cook, A. G. and Draper, J. J. 2013. Jell, P. A Geology of Queensland, Geological Survey of Queensland, Australia.

Daneshy, A. A. 2003. Off-Balance Growth: A New Concept in Hydraulic Fracturing. *J. Pet Technol* ***55*****(04)**, 78 – 85. SPE-80992-JPT. http://dx.doi.org/10.2118/80992-JPT.

Darcy, H.: *Les Fontaines Publiques de la Ville de Dijon,* Paris, France, Victor Dalmont (1856).

Desroches, J., Detournay, E., Lenoach, B., Papanastasiou, P., Pearson, J. R. A., Thiercelin, M. and ,Cheng, A. 1994. The crack tip region in hydraulic fracturing. *Proc. R. Soc. Lond.* A (1994). **447**. 39-48.

Detournay, E., Cheng, A.H.-D., 1993. Fundamentals of poroelasticity. In: Fairhurst, C. (Ed.), Comprehensive Rock Engineering: Principles, Practice and Projects, Analysis and Design Method, vol. II. Pergamon Press, **Ch**. 5. 113 – 171.

Dietz, D. N., 1965. Determination of Average Reservoir Pressure from Build-Up Surveys. *J. Pet. Tech.,* Aug: 955-959.

Dontsov, E. V. and Peirce, A. P. 2015. An enhanced pseudo-3D model for hydraulic fracturing accounting for viscous height growth, non-local elasticity, and lateral toughness. *Engineering Fracture Mechanics.* **142** (2015). 116-139. http://dx.doi.org/10.1016/j.engfracmech.2015.05.043.

Dyskin, A. V., Jewell, R. J., Joer, H., Sahouryeh, E. and Ustinov, K. B. 1994. Experiments on 3-d crack growth in uniaxial compression. *Intern. J. Fracture.* **65:** R77– R83.

Elbel, J. L. 1993. A Method to Estimate Multizone Injection Profiles During Hydraulic Fracturing. The Rocky Mountain Regional Meeting and Low-Permeability Reservoirs Symposium, Denver, Colorado, USA. 15-17 April. SPE-21869-MS. http://dx.doi.org/10.2118/21869-MS.

England, A. H. and Green, A. E., 1963. Some Two-Dimensional Punch and Crack Problems

in Classical Elasticity. *Proc. Camb. Phil. Soc.,* Great Britain, **59**, 489-500.
Erdogan, F. 1962. On the Stress Distribution Of Plates with Collinear Cuts under Arbitrary Loads. *Proc*., Fourth U. S. Nat. Cong. of Appl. Mech. (1962) 547.
Fairhurst, C. and Cook, N. G. W. 1966. The phenomenon of rock splitting parallel to the direction of maximum compression in the neighborhood of a surface. *Proc. First Congress International Society for Rock Mechanics,* Lisbon. **3.75.** 687-692.
Fisher, K. M. and Warpinski, N. R. 2012. Hydraulic-Fracture-Height Growth: Real Data. *SPE Prod. & Ops*. **27** (01). 8-19. SPE-145949-PA. http://dx.doi.org/10.2118/145949-PA.
Flottmann, T., Brooke-Barnett, S., Trubshaw, R. et al. 2013. Influence of In-Situ Stresses on Fracture Stimulations in the Surat Basin, Southeast Queensland. Presented at the Unconventional Resources Conference and Exhibition-Asia Pacific, Brisbane, Australia. 11-13 November, SPE-167064-MS. http://dx.doi.org/10.2118/167064-MS.
Fung, R.L., Vijaykumar, S., and Cormack, D.E. 1987. Calculation of Vertical Fracture Containment in Layered Formation. *SPE Formation Evaluation **2*** (04): 518 – 522. SPE-14707-PA. http://dx.doi.org/10.2118/14707-PA**.**
Germanovich, L. N., Salganik, R. L., Dyskin, A. V. and Lee, K. K. 1994. Mechanisms of brittle fracture of rock with multiple pre-existing cracks in compression. *Pure and Applied Geophysics.* **143:** 117 – 149**.**
Germanovich, L. N., Carter, B. J., Ingraffea, A. R., Dyskin, A. V., and Lee, K. K. 1996. Mechanics of 3-D crack growth under compressive loads. *Rock Mechanics,* Hassani & Mitri (eds). 1996. Balkema, Rotterdam.
Goyal, D. P. 1974. On three coplanar Griffith cracks in an infinite elastic medium. *Indian J. Pure and Appl. Math.* **5:** 556-567.
Griffith, A. A., & Taylor, G. I. (1921). VI. The phenomena of rupture and flow in solids. *Philosophical Transactions of the Royal Society of London. Series A, Containing Papers of a Mathematical or Physical Character, 221*(582-593), 163-198. doi:doi:10.1098/rsta.1921.0006.
Griffith, A. A. (1924). *The theory of rupture*. Paper presented at the Proceedings of the 1st International Congress for Applied Mechancis, Delft, Netherlands.
Gulrajani, S., & Nolte, K. G. (2000). Fracture Evaluation Using Pressure Diagnostics. In M. J. Economides & K. G. Nolte (Eds.), *Reservoir Stimulation* (3rd ed.). Chichester, England: John Wiley & Sons.
Haddad, Z., Smith, M. B., and De Moraes, F. D. 2012. Designing Multistage Frac Packs in the Lower Tertiary Formation—Cascade and Chinook Project. *SPE Drill & Compl* **27** (1): 50–64. SPE-140498-PA. http://dx.doi.org/10.2118/140498-PA.
He, M. Y. and Hutchinson, J. W. 1989. Crack Deflection at an Interface Between Dissimilar Elastic Materials. *Int. J. Solids Structures*, **25**. 1053.
Hooke, Robert (1678). *De Potentia Restitutiva, or of Spring. Explaining the Power of Springing Bodies*,London, 1678.
Irwin, G.R. 1957. Analysis of Stresses and Strains Near the End of a Crack Traversing a Plate, *J. App. Mech.* (1957). **24**, 361.
Irwin, G. R. (1960). Structural Mechanics: Proceedings of the 1st Symposium on Naval Structural Mechanics, 1958. (Goodier, J. N. and Hoff, N. J. eds.), pp. 557-591. Pergamon, New York.
Kirk-Burnnand, E., Pandey, V. J., Flottmann, T. and Trubshaw, R. L. 2015. Hydraulic Fracture Design Optimization in Low Permeability Coals, Surat Basin, Australia. Presented at The SPE Asia Pacific Unconventional Resources Conference and Exhibition, Brisbane, Queensland, Australia. 9-11 November. SPE-176895-MS. http://dx.doi.org/10.2118/176895-MS.
Lenoach, B. 1994. Hydraulic Fracture Model Based on Analytical Near-Tip Solutions.

Computer Methods and Advances in Geomechanics. 1597-1602.
Lenoach, B. 1995. The Crack Tip Solution for Hydraulic Fracturing in a Permeable Solid. *J. Mech. Phys. Solids*. **43** (7), 1025.
Liu, S. and Valko, P.P. 2015. An Improved Equilibrium-Height Model for Predicting Hydraulic Fracture Height Migration in Multi-Layered Formations. Presented at The SPE Hydraulic Fracturing Technology Conference, The Woodlands, Texas, USA. 3-5 February. SPE-173335-MS. http://dx.doi.org/10.2118/173335-MS.
Mack, M.G, Elbel, J.L and Piggott, A.R, 1992: Numerical representation of multilayer hydraulic fracturing. The 33rd U.S. Symposium on Rock Mechanics (USRMS), Santa Fe, New Mexico, USA. 3-5 June. American Rock Mechanics Association, ARMA-92-0335.
McCartney, L. N. *1981*. On The Interaction of a Micro-void and a Crack. *Res Mechanica* **3**, 241 -244.
McCartney, L. N. 1983. General solution of a certain mixed boundary value crack problem, *Int. J. Engng. Sci.* 21 No. 2: 131-142.
Montgomery, C. T. and Smith, M. B. 2010. Hydraulic Fracturing: History of an Enduring Technology. *J. Pet. Technol.* **62** (12): 26-32. (Special Section – Hydraulic Fracturing: The Past, Present, and Future).
Muskhelishvili, N. I. 1953a. "Singular Integral Equations" (J. R M. Radok, trans.). Noordhoff, Groningen, Holland.
Muskhelishvili, N. I. (1953b). "Some Basic Problems in the Mathematical Theory of Elasticity" (J. R M. Radok, trans.). Noordhoff, Groningen, Holland.
Nolte, K. G. 1979. Determination of Fracture Parameters from Fracturing Pressure Decline. Presented at The Annual Technical Conference and Exhibition, Las Vegas, Nevada. 23-26 September. SPE-8341-MS. http://dx.doi.org/10.2118/8341-MS.
Nolte, K. G. 1986. A General Analysis of Fracturing Pressure Decline With Application to Three Models. *SPE Form Eval* **1** (6): 571–583. SPE-12941-PA. http://dx.doi.org/10.2118/12941-PA.
Nolte, K. G. 1991. Fracturing-Pressure Analysis for Nonideal Behavior. *J Pet Technol* **43** (2): 210–218. SPE-20704-PA. http://dx.doi.org/10.2118/20704-PA
North Dakota Govt. Report. 2007. *Surface Tiltmeter Fracture Mapping Results for the Klatt No. 31-14H.* Govt. of North Dakota. Report. http://www.nd.gov/ndic/ogrp/info/g-007-020pin.pdf.
Olson, J. E. 2004. Predicting fracture swarms – the influence of subcritical crack growth and the crack-tip process zone on joint spacing in rock. *Geological Society, London, Special Publications.* V. 231. 73-88.
Palmer, Ian D., Carroll, H. B. 1983. Three-Dimensional Hydraulic Fracture Propagation in the Presence of Stress Variations. *SPE J.* **23** (1983): 870–878. doi: https://doi.org/10.2118/10849-PA.
Palmer, I. D. 1993. Induced Stresses Due to Propped Hydraulic Fracture in Coalbed Methane Wells. Presented at The Low Permeability Reservoirs Symposium, Denver, Colorado, USA. 26-28 April. SPE-25861-MS. http://dx.doi.org/10.2118/25861-MS.
Pandey, V. J. and Cramer, D. D. 2019. Jennifer Miskimins, Editor-in-Chief. 2019. *Hydraulic Fracturing: Fundamentals and Advancements.* ISBN: 978-1-61399-719-2. *SPE*. **Ch.** 10. 291-344.
Pandey, V. J. and Agreda, A. J. 2014. New Fracture-Stimulation Designs and Completion Techniques Result in Better Performance of Shallow Chittim Ranch Wells. *SPE Prod & Oper* **29** (4): 288–309. SPE-147389-PA. http://dx.doi.org/10.2118/147389-PA.
Pandey, V. J. and Flottmann, T. 2015. Applications of Geomechanics to Hydraulic Fracturing:

Case Studies From Coal Stimulations. Presented at the SPE Hydraulic Fracturing Technology Conference, The Woodlands, Texas, 3–5 February. SPE-173378-MS. http://dx.doi.org/10.2118/173378-MS.

Pandey, V. J., Burton, R. C. and Capps, K. 2020. Real-Time Analysis of Formation-Face Pressures in Acid-Fracturing Treatments. SPE Production & Operations. Preprint. May 2020. SPE-194351-PA. https://doi.org/10.2118/194351-PA.

Pandey, V. J. and Rasouli, V., 2021a. Vertical Growth of Hydraulic Fractures in Layered Formations. Presented at The Virtual SPE Hydraulic Fracturing Technology Conference, The Woodlands, TX, USA, 4–6 May. SPE-204155-MS. http://dx.doi.org/10.2118/204155-MS.

Pandey, V.J. and Rasouli, V., 2021b Fracture Height Growth Prediction Using Fluid Velocity Based Apparent Fracture Toughness Model. *Rock Mech. Rock Engg. J.* May 2021. **54:** 4059-4078. https://doi.org/10.1007/s00603-021-02489-w

Pandey, V.J. and Rasouli, V., 2021c. A semi-analytical model for estimation of hydraulic fracture height growth calibrated with field data. *J. Pet. Sci. and Eng*. **202**, July 2021, 108503. https://doi.org/10.1016/j.petrol.2021.108503.

Pandey, V.J. and Rasouli, V., 2022a. Estimating Fracture Containment in Layered Formations Using 3D Fracture Growth Assumptions. Presented in the SPE Hydraulic Fracturing Technology Conference and Exhibition, The Woodlands, Texas, USA, 3-5 February. SPE-209151-MS.doi: https://doi.org/10.2118/209151-MS.

Pandey, V.J. and Rasouli, V. 2022b Pandey, V.J. and Rasouli, V., 2022. Development of a Fracture Width Induced Net Stress Model to Predict Constraints to Fracture Height Growth. *J. of Pet. Sci. & Eng.* **213**. June. 2022. 110429, https://doi.org/10.1016/j.petrol.2022.110429.

Poisson, S.D., 1829. Mémoire sur l'équilibre et le movement des corps élastiques. Mém. De l'Acad. Sci.8, 357.

Raghavan, R. and Hadinoto, N. 1978. Analysis of Pressure Data for Fractured Wells: The Constant-Pressure Outer Boundary. *SPE J.* **18** (02): 139–150.SPE-6015-PA. https://doi.org/10.2118/6015-PA.

Renshaw, C. E. and Pollard, D. D. 1995. An Experimentally Verified Criterion for Propagation across Unbounded Frictional Interfaces in Brittle, Linear Elastic Materials. *Int. J. Rock Mech. Min. Sci. & Geomech. Abstr.* **32**, 237-249.

Rice, J.R. 1968. Mathematical Analysis in the Mechanics of Fracture. *Treatise on Fracture,* Academic Press Inc., New York City (1968). **Ch**. 3, 2, 191.

Rummel, F. and Winter, R. B. (1982). Application of laboratory fracture mechanics data hydraulic fracturing field test, Proc. *1st Japan-USA Symp on Fracture Mechanics Approach, Hydraulic Fracture and Geothermal Energy*, Sendai, Japan, 495 – 501.

Sadd, Martin H. 2005. Elasticity: Theory, Applications and Numerics. 123-259. Burlington, MA.: Elsevier Academic Press.

Scholz, C. H. 1990. *The Mechanics of Earthquakes and Faulting.* Cambridge University Press, Cambridge, New York, Sydney.

SCR Geomechanics Group. 1993. On the Modeling of Near Tip Processes in Hydraulic Fractures. *International Journal of Rock Mechanics and Mining Sciences & Geomechanics Abstracts.* **30**, No. 7, 1127-1134.

Sharma, M. M. and Manchanda, R. 2015. The Role of Induced Un-Propped (IU) Fractures in Unconventional Oil and Gas Wells. Presented at the SPE Annual Technical Conference and Exhibition, Houston, 28–30 September. SPE-174946-MS. http://dx.doi.org/10.2118/174946-MS.

Shlyapobersky, J. 1985. Energy Analysis of Hydraulic Fracturing. *Proc*., 26th U.S. Symposium on Rock Mechanics, Rapid City, South Dakota, 26–28 June, 539–546.

Simonson, E. R., Abou-Sayed, A. S., & Clifton, R. J. 1978. Containment of Massive Hydraulic Fractures. *J. Pet Technol.* **18** (1): 27–32. SPE-6089-PA. http://dx.doi.org/10.2118/6089-PA.

Smith, M. B. 1985. Stimulation Design for Short, Precise Hydraulic Fractures. *SPE J.* **25** (3): 371–379. SPE-10313-PA. http://dx.doi.org/10.2118/10313-PA.

Smith, M. B., Miller II, W. K., and Haga, J. 1987. Tip Screenout Fracturing: A Technique for Soft, Unstable Formations. *SPE Prod Eng* **2** (2): 95–103. SPE-13273-PA. http://dx.doi.org/10.2118/13273-PA.

Smith, M. B. and Hannah, R. R. 1996. High-Permeability Fracturing: The Evolution of a Technology. *J Pet Technol* **48** (7): 628–633. SPE-27984-JPT. http://dx.doi.org/10.2118/27984-JPT.

Sneddon, I. N. 1946. The Distribution of Stress in the Neighbourhood of a Crack in an Elastic Solid. *Proceedings of the Royal Society A* **187** (1009): 229–260. https://doi.org/10.1098/rspa.1946.0077.

Sneddon, I. N. and Lowengrub, M. 1969. *Crack Problems in the Classical Theory of Elasticity,* **77-81**. New York City: John Wiley and Sons.

Stegent, N., Dusterhoft, R. , and Hari M. 2019. Insight into Hydraulic Fracture Geometries Using Fracture Modeling Honoring Field Data Measurements and Post-Fracture Production. Presented at the SPE Europec featured at 81st EAGE Conference and Exhibition, London, England, UK, June 2019. https://doi.org/10.2118/195524-MS.

Tada, H., Paris, P. and Irwin, G. 1973. *The Stress Analysis of Crack Handbook.* Del Research Corp., Hellertown, PA. (1973).

Tan, Y., Wang, S. , Rijken, M. et al. 2021. Geomechanical Template for Distributed Acoustic Sensing Strain Patterns during Hydraulic Fracturing. *SPE J.* (2021)1-12: doi: https://doi.org/10.2118/201627-PA.

Teufel, L. W., and Clark, J. A. 1984. "Hydraulic Fracture Propagation in Layered Rock: Experimental Studies of Fracture Containment." *SPE J.* 24 (1984): 19–32. https://doi.org/10.2118/9878-PA

Thiercelin, M. 1987: Fracture Toughness and Hydraulic Fracturing. *Proc*., 20th U.S. Symposium on Rock Mechanics. 149–156.

Thiercelin, M. J. and Plumb, R. A. 1994. A Core-Based Prediction of Lithologic Stress Contrasts in East Texas Formations. *SPE Form Eval* **9** (4): 251–258. SPE-21847-PA. http://dx.doi.org/10.2118/21847-PA.

Warpinski, N. R., Schmidt, R. A., and Northrop. D. A. 1982. "In-Situ Stresses: The Predominant Influence on Hydraulic Fracture Containment." *J Pet Technol* 34 (1982): 653–664. https://doi.org/10.2118/8932-PA.

Warpinski, N. R. and Smith, M. B. 1989. Rock Mechanics and Fracture Geometry. *Recent Advances in Hydraulic Fracturing*, Vol. 12, ed. Gidley, J. L., Holditch, S. A., Nierode, D. E., and Veatch, R. W., Jr., Ch. **3**, 57–80. Richardson, Texas: Monograph Series, SPE.

Warpinski, N. R. 2010. Stress Amplification and Arch Dimensions in Proppant Beds Deposited by Waterfracs. *SPE Production & Operations.* **25** (04). 461–471. SPE-119350-PA. http://dx.doi.org/10.2118/119350-PA.

Weng X. 1992. Incorporation of 2D Fluid Flow Into a Pseudo-3D Hydraulic Fracturing Simulator. *SPE Prod. & Oper* **7** (04): 331–337. SPE-21849-PA. https://doi.org/10.2118/21849-PA.

Weng, X., Kresse, O., Cohen, C. et al. 2011. Modeling of Hydraulic-Fracture-Network Propagation in a Naturally Fractured Formation. *SPE Prod & Oper* **26** (4): 368–380 SPE-140253-PA. http://dx.doi.org/10.2118/140253-PA.

Westergaard, H.M. 1939; Bearing Pressures and Cracks. *Journal of Applied Mechanics,* Vol. 6, pp. A49-53, 939.

Wright, C.A., Davis, E.J., Weijers, L., Minner, W.A., Hennigan, C.M. and Golich, G.M. 1997. Horizontal Hydraulic Fractures: Oddball Occurrences or Practical Engineering Concern? SPE-SPE-38324 -MS. Presented at the 1997 Western Regional Meeting, Long Beach, June 25-27.

Wright, C. A, Davis, E. J., Weijers L., Golich, G. M., Ward, J. F., Demetrius, S. L., & Minner, W. A. 1998. Downhole tiltmeter fracture mapping: A new tool for directly measuring Hydraulic fracture Dimensions. SPE-49193-MS. Presented at the SPE Annual Technical Conference and Exhibition, New Orleans, Louisiana, September 27 -30. http://dx.doi.org/10.2118/49193-MS.

Wu, K. and Olson, J. E. 2016. Mechanisms of Simultaneous Hydraulic-Fracture Propagation From Multiple Perforation Clusters in Horizontal Wells. *SPE J* **21** (21). 1,000 – 1,008. SPE-178925-PA. http://dx.doi.org/10.2118/178925-PA.

Xu, W., Prioul, R., Beard, T., Weng, X. and Kresse, O. 2019. Barriers to Hydraulic Fracture Height Growth: A New Model for Sliding Interface. Presented at The SPE Hydraulic Fracturing Technology Conference and Exhibition, The Woodlands, Texas, USA. 5-7 February. SPE-194327-MS. http://dx.doi.org/10.2118/194327-MS.

Yuan, R., Jin, L., Zhu, C., Vitthal, S. and Xu, B. 2003. High Pressure Stimulation – Impact of Hydraulic Fracture Geometry to Unconventional Gas Appraisal and Development in Compressional Settings. SPE-166348-MS. Presented at The SPE Annual Technical Conference and Exhibtion held in New Orleans, Louisiana, USA, Sept. 30 – Oct. 2. http://dx.doi.org/10.2118/166348-MS.

APPENDIX A

Solution to Simonson et al. (1978) 3-layered asymmetric stress model is presented here. The stress intensity factor at the upper tip of the fracture, is given as follows (Rice 1968):

$$K_I^{top} = \frac{1}{\sqrt{\pi l}} \int_{-l}^{+l} p(y) \sqrt{\frac{l+y}{l-y}}\, dy = I \quad \text{.....(A1)}$$

To obtain stress intensity factor at the bottom tip of the fracture, the term under the square root is expressed as $\sqrt{(l-y)/(l+y)}$. Furthermore, following boundary conditions are applicable for a 3-layered system shown in Fig. 4.

$$p(y) = (p - \sigma_c) \text{ for } -l < y < -L \quad \text{.....(A2a)}$$

$$p(y) = (p - \sigma_a) \text{ for } -L < y < L \quad \text{.....(A2b)}$$

$$p(y) = (p - \sigma_b) \text{ for } \quad L < y < l \quad \text{.....(A2c)}$$

Thus,

$$\mathrm{I} = \frac{1}{\sqrt{\pi l}} \left(\int_{-l}^{-L} p(y) \sqrt{\frac{l+y}{l-y}}\, dy \; + \int_{-L}^{L} p(y) \sqrt{\frac{l+y}{l-y}}\, dy + \int_{L}^{l} p(y) \sqrt{\frac{l+y}{l-y}}\, dy \right) \text{.....(A3)}$$

where, each of the integral on can be denoted as I_1, I_2 and I_3. Multiplying the integral by $\sqrt{l+y}/\sqrt{l+y}$, the following form is obtained:

$$\mathrm{I}\sqrt{\pi l} = \int_{-l}^{-L} p(y) \frac{l+y}{\sqrt{l^2-y^2}}\, dy \; + \int_{-L}^{L} p(y) \; \frac{l+y}{\sqrt{l^2-y^2}}\, dy + \int_{L}^{l} p(y) \frac{l+y}{\sqrt{l^2-y^2}}\, dy \quad \text{.....(A4a)}$$

Or,

$$\mathrm{I}\sqrt{\pi l} = I_1 + I_2 + I_3 \quad \text{.....(A4b)}$$

By using the integration rules,

$$\int \frac{l}{\sqrt{l^2-y^2}}\, dy = l \; \sin^{-1}\left(\frac{y}{l}\right) \text{ and } \int \frac{y}{\sqrt{l^2-y^2}}\, dy = \; -\sqrt{l^2 - y^2} \quad \text{.....(A5)}$$

the individual definite integral components of (A4) can be expanded and solved as follows:

$$\mathrm{I}_1 = (p - \sigma_c) \left[-l \sin^{-1}\left(\frac{L}{l}\right) - \sqrt{l^2 - L^2} + l \sin^{-1}(1) + \sqrt{l^2 - l^2} \right] \text{.....(A6a)}$$

which results in the following form after simplification:

$$\mathrm{I}_1 = (p - \sigma_c) \left[\frac{\pi}{2} l - l \sin^{-1}\left(\frac{L}{l}\right) - \sqrt{l^2 - l^2} \right] \text{.....(A6b)}$$

Similarly, I_2 and I_3 can be solved to obtain the following:

$$\mathrm{I}_2 = 2(p - \sigma_a) l \sin^{-1}\left(\frac{L}{l}\right) \quad \text{.....(A7)}$$

$$\mathrm{I}_3 = (p - \sigma_b) \left[\frac{\pi}{2} l - l \sin^{-1}\left(\frac{L}{l}\right) - \sqrt{l^2 - l^2} \right] \quad \text{.....(A8)}$$

For final solution, I_1, I_2 and I_3 are added, and the various terms are grouped after rearrangement. The final solution is shown in Eq. (A9) below and in Eq. (2.11) in the main text.

$$K_I^{top} = \frac{\sqrt{\pi l}}{2}(2p - \sigma_b - \sigma_c) + \frac{1}{\sqrt{\pi l}}(\sigma_c - \sigma_b)\sqrt{l^2 - L^2} + \sqrt{\frac{l}{\pi}} \sin^{-1}\left(\frac{L}{l}\right)(\sigma_c + \sigma_b - 2\sigma_a) \quad \text{(A9)}$$

The stress intensity factor near the bottom tip of the fracture can be derived using a similar procedure. If the barrier strengths are identical ($\sigma_c = \sigma_b$), the stress intensity factor can be obtained with the following equation:

$$K_I = (\sigma_b - \sigma_a) \sqrt{\frac{l}{\pi}} \left\{ 2 \sin^{-1}\left(\frac{L}{l}\right) \right\} + (p - \sigma_b)\sqrt{\pi l} \quad \text{.....(A10)}$$

APPENDIX B

The solution to the Mack et al. (1992) model that takes after Fung et al. (1987) model, for stress intensity factor at the bottom tip of the fracture is presented below because of its relevance to the approach adopted in this study. The stress intensity factor at the bottom tip of the fracture is defined as follows by Rice (1968):

$$K_I^{bot} = \frac{1}{\sqrt{\pi a}} \int_{-a}^{a} [p - \sigma(z)] \sqrt{\frac{a-z}{a+z}}\, dz \quad \text{.....(B1)}$$

Substituting p with $p_{cp} + \rho_f g(h_{cp} - z)$ to account for gravity, and rearranging results in:

$$K_I^{bot} = \frac{1}{\sqrt{\pi a}} \int_{-a}^{a} \left\{ \left[p_{cp} + \rho_f g h_{cp} - \sigma(z) \right] - \rho_f g z \right\} \sqrt{\frac{a-z}{a+z}}\, dz \quad \text{.....(B2)}$$

For a multi-layered set up of $-a$ to a comprising 5 layers such as Fig. 2.3 and Fig. 2.4, (B2) can be expanded as:

$$K_I^{bot}\sqrt{\pi a} = \int_{-a}^{h_1-a} [X - S_1] \sqrt{\frac{a-z}{a+z}}\, dz - \int_{-a}^{h_1-a} Yz \sqrt{\frac{a-z}{a+z}}\, dz + \int_{h_1-a}^{h_2-a} [X - S_2] \sqrt{\frac{a-z}{a+z}}\, dz$$

$$- \int_{h_1-a}^{h_2-a} Yz \sqrt{\frac{a-z}{a+z}}\, dz + \int_{h_2-a}^{h_3-a} [X - S_3] \sqrt{\frac{a-z}{a+z}}\, dz - \int_{h_2-a}^{h_3-a} Yz \sqrt{\frac{a-z}{a+z}}\, dz$$

$$+ \int_{h_3-a}^{h_4-a} [X - S_4] \sqrt{\frac{a-z}{a+z}}\, dz$$

$$- \int_{h_3-a}^{h_4-a} Yz \sqrt{\frac{a-z}{a+z}}\, dz + \int_{h_4-a}^{a} [X - S_5] \sqrt{\frac{a-z}{a+z}}\, dz - \int_{h_4-a}^{a} Yz \sqrt{\frac{a-z}{a+z}}\, dz \quad \text{.....(B3)}$$

where, $X = p_{cp} + \rho_f g h_{cp}$, $Y = \rho_f g$ and S_i denotes the corresponding stresses in layers 1 to n. Also, for sake of convenience the expression defining the stress intensity factor for a 5-layered problem may be expressed as a sum of integrals I_1 to I_5, where each integral is a part of Eq. (B3), with I_1 described in Eq. (B5).

$$K_I^{bot} = \mathrm{I} = \mathrm{I}_1 + \mathrm{I}_2 + \mathrm{I}_3 + \mathrm{I}_4 + \mathrm{I}_5 \quad \text{.....(B4)}$$

In the solution process, the integrals are first multiplied by $\sqrt{a-z}/\sqrt{a+z}$ which results in the following format, shown for the first pair of integrals on the RHS of (B3) with limits from -a to h_1-a.

$$\mathrm{I}_1 = \int_{-a}^{h_1-a} [X - S_1] \frac{a-z}{\sqrt{a^2-z^2}}\, dz - \int_{-a}^{h_1-a} Yz \frac{a-z}{\sqrt{a^2-z^2}}\, dz \quad \text{.....(B5)}$$

Applying the rules of integration as shown in Eq. (A5) and substituting $\sin^{-1}(z/a)$ with $\cos^{-1}(-z/a)$, the integral I_1 is expanded as follows:

$$I_{-a}^{h_1-a} = (X - S_1)\left[a\cos^{-1}\left(\frac{-z}{a}\right) + \sqrt{a^2 - z^2} + \frac{1}{2}z\sqrt{a^2 - z^2} - a\sqrt{a^2 - z^2} - \frac{a^2}{2}\cos^{-1}\left(\frac{-z}{a}\right)\right] \quad \text{(B6)}$$

Now substituting $z = -a$ and $z = h_1 - a$ for the limits of I_1 and solving this first pair, the following expression is obtained after simplification:

$$A = aX\cos^{-1}\left(\frac{h-2h_1}{h}\right) + X\sqrt{h_1(h-h_1)} - aS_1\cos^{-1}\left(\frac{h-2h_1}{h}\right) - S_1\sqrt{h_1(h-h_1)} \ldots$$

$$-aY\sqrt{h_1(h-h_1)} - \frac{a^2}{2}Y\cos^{-1}\left(\frac{h-2h_1}{h}\right) + \frac{Y}{2}(h_1 - a)\sqrt{h_1(h-h_1)} \quad \text{(B7)}$$

where is A is the interim solution to I_1. Similarly, the solutions to the remainder of integration terms of Eq. (B3) are shown below, where *B, C, D* and *E* represent the solution to every pair of Eq. (B3).

$$B = aX\cos^{-1}\left(\frac{h-2h_2}{h}\right) + X\sqrt{h_2(h-h_2)} - aX\cos^{-1}\left(\frac{h-2h_1}{h}\right) - X\sqrt{h_1(h-h_1)}$$

$$-aS_2\cos^{-1}\left(\frac{h-2h_2}{h}\right) - S_2\sqrt{h_2(h-h_2)} + aS_2\cos^{-1}\left(\frac{h-2h_1}{h}\right) + S_2\sqrt{h_1(h-h_1)}$$

$$-aY\sqrt{h_2(h-h_2)} - \frac{a^2}{2}Y\cos^{-1}\left(\frac{h-2h_2}{h}\right) + \frac{Y}{2}(h_2 - a)\sqrt{h_2(h-h_2)} + aY\sqrt{h_1(h-h_1)}$$

$$+\frac{a^2}{2}Y\cos^{-1}\left(\frac{h-2h_1}{h}\right) - \frac{Y}{2}(h_1 - a)\sqrt{h_1(h-h_1)} \quad \text{(B8)}$$

$$C = aX\cos^{-1}\left(\frac{h-2h_3}{h}\right) + X\sqrt{h_3(h-h_3)} - aX\cos^{-1}\left(\frac{h-2h_2}{h}\right) - X\sqrt{h_2(h-h_2)}$$

$$-aS_3\cos^{-1}\left(\frac{h-2h_3}{h}\right)-S_3\sqrt{h_3(h-h_3)}+aS_3\cos^{-1}\left(\frac{h-2h_2}{h}\right)$$
$$+S_3\sqrt{h_2(h-h_2)}$$
$$-aY\sqrt{h_3(h-h_3)}-\frac{a^2}{2}Y\cos^{-1}\left(\frac{h-2h_3}{h}\right)+\frac{Y}{2}(h_3-a)\sqrt{h_3(h-h_3)}$$
$$+aY\sqrt{h_2(h-h_2)}$$
$$+\frac{a^2}{2}Y\cos^{-1}\left(\frac{h-2h_2}{h}\right)-\frac{Y}{2}(h_2-a)\sqrt{h_2(h-h_2)} \quad \text{(B9)}$$

$$D=aX\cos^{-1}\left(\frac{h-2h_4}{h}\right)+X\sqrt{h_4(h-h_4)}$$
$$-aX\cos^{-1}\left(\frac{h-2h_3}{h}\right)-X\sqrt{h_3(h-h_3)}$$
$$-aS_4\cos^{-1}\left(\frac{h-2h_4}{h}\right)-S_4\sqrt{h_4(h-h_4)}+aS_4\cos^{-1}\left(\frac{h-2h_3}{h}\right)$$
$$+S_4\sqrt{h_3(h-h_3)}$$
$$-aY\sqrt{h_4(h-h_4)}-\frac{a^2}{2}Y\cos^{-1}\left(\frac{h-2h_4}{h}\right)+\frac{Y}{2}(h_4-a)\sqrt{h_4(h-h_4)}$$
$$+aY\sqrt{h_3(h-h_3)}$$
$$+\frac{a^2}{2}Y\cos^{-1}\left(\frac{h-2h_3}{h}\right)-\frac{Y}{2}(h_3-a)\sqrt{h_3(h-h_3)} \quad \text{(B10)}$$

$$E=aX\cos^{-1}(-1)+X\sqrt{a^2-a^2}-aX\cos^{-1}\left(\frac{h-2h_4}{h}\right)-X\sqrt{h_4(h-h_4)}$$
$$-aS_5\cos^{-1}(-1)-S_5\sqrt{a^2-a^2}-aS_5\cos^{-1}\left(\frac{h-2h_4}{h}\right)+S_5\sqrt{h_4(h-h_4)}$$
$$-aY\sqrt{a^2-a^2}-\frac{a^2}{2}Y\cos^{-1}(-1)+\frac{Y}{2}(a)\sqrt{a^2-a^2}+aY\sqrt{a^2-a^2}$$
$$+\frac{a^2}{2}Y\cos^{-1}\left(\frac{h-2h_4}{h}\right)-\frac{Y}{2}(h_4-a)\sqrt{h_4(h-h_4)} \quad \text{(B11)}$$

The final solution to stress intensity factor at the lower tip of the fracture is obtained after summing the individual solutions presented in equations (B7) to (B11) and substituting the values of *X*, *Y* and *a*. After simplification and rearrangement of the terms, the solution can be expressed as follows, which is the same as Eq. (2.18) in the main text:

$$K_I^{bot} = \sqrt{\frac{\pi h}{2}}\left[p_{cp} - \sigma_n + \rho_f g\left\{h_{cp} - \frac{h}{4}\right\}\right] + \sqrt{\frac{2}{\pi h}}\sum_{i=1}^{n-1}(\sigma_{i+1} - \sigma_i)\left[\frac{h}{2}\cos^{-1}\left(\frac{h-2h_i}{h}\right) + \sqrt{h_i(h-h_i)}\right] \quad \text{.....(B12)}$$

where, the term S_i in solution is substituted by σ_i. The solution to the stress intensity factor at the upper tip of the fracture can be obtained similarly.

APPENDIX C

Solution to functions *F(t)* and *G(t)*:

Example solution to the function *F(t)* for a 4-layer case is provided below:

$$F(t) = \frac{-t}{2\pi}\left[\int_0^{d_1} \frac{p_1}{\sqrt{t^2-u^2}}\,du + \int_{d_1}^{d_2} \frac{p_2}{\sqrt{t^2-u^2}}\,du + \int_{d_2}^{d_3} \frac{p_3}{\sqrt{t^2-u^2}}\,du + \int_{d_3}^{t} \frac{p_4}{\sqrt{t^2-u^2}}\,du\right] \text{.....(C1)}$$

where p_1 to p_k are solutions to even function *f(y)* that can be obtained from Eq. (6.11) and d_1 to d_2 denote elevation to the interfaces that the fracture crosses to reach point the tip *t*. Now using the rule $\int du/\sqrt{t^2-u^2} = \sin^{-1}(u/t)$, each term can be solved and regrouped after expansion as follows:

$$F(t) = \frac{-t}{2\pi}\left[(p_1-p_2)\sin^{-1}\left(\frac{d_1}{t}\right) + (p_2-p_3)\sin^{-1}\left(\frac{d_2}{t}\right) + (p_3-p_4)\sin^{-1}\left(\frac{d_3}{t}\right)\right] - \frac{p_4 t}{4} \text{.....(C2)}$$

which can be further simplified to the form shown below which is same as Eq. (19).

$$F(t) = \frac{-t}{2\pi}\int_0^t \frac{p}{\sqrt{t^2-u^2}}\,du = \frac{-t}{2\pi}\left[\sum_{n=1}^{k}(p_{n-1}-p_n)\sin^{-1}\left(\frac{d_n}{t}\right)\right] - \frac{p_k t}{4} \text{.....(C3)}$$

The solution for *G(t)*, can be obtained by first expanding the integral shown in Eq. (6.10) as follows:

$$G(t) = \frac{-1}{2\pi t}\left[\int_0^{d_1} \frac{u\,q_1}{\sqrt{t^2-u^2}}\,du + \int_{d_1}^{d_2} \frac{u\,q_2}{\sqrt{t^2-u^2}}\,du + \int_{d_2}^{d_3} \frac{u\,q_3}{\sqrt{t^2-u^2}}\,du + \int_{d_3}^{t} \frac{u\,q_4}{\sqrt{t^2-u^2}}\,du\right] \text{.....(C4)}$$

Now, and employing the rule $\int u\,du/\sqrt{t^2-u^2} = -\sqrt{t^2-u^2}$ on Eq. (A4) the following expression is obtained after expanding and grouping the common terms:

$$G(t) = \frac{-1}{2\pi t}\left[(q_2-q_1)\sqrt{t^2-d_1^2} + (q_3-q_2)\sqrt{t^2-d_2^2} + (q_4-q_3)\sqrt{t^2-d_3^2}\right] \text{.....(C5)}$$

After summing up the terms and applying the appropriate signage, the following final expression is obtained which is same as Eq. (6.15).

$$G(t) = \frac{-1}{2\pi t}\int_0^t \frac{u\,q}{\sqrt{t^2-u^2}}\,du = \frac{1}{2\pi}\left[\sum_{n=1}^{k}(q_{n-1}-q_n)\sqrt{t^2-d_n^2}\right] \text{.....(C6)}$$

Solution to England and Green width Equation:

The general solution for *F(t)* in Eq. (6.9) can be expressed as the sum of two integrals as shown below:

$$\int_{|y|}^{a} \frac{F(t)}{\sqrt{t^2-y^2}}\,dt = I = \frac{-1}{2\pi}\int_{|y|}^{a} \frac{pt\sin^{-1}\left(\frac{d_n}{t}\right)}{\sqrt{t^2-y^2}}\,dt - \frac{1}{4}\int_{|y|}^{a} \frac{pt}{\sqrt{t^2-y^2}}\,dt \text{.....(C7)}$$

where *p* is the solution to even function, and p_k is the value of even function at the last interface that the fracture has crossed. This integral is of the form $I = -I_1 - I_2$ where for Eq. (C7), *I* is the integral on left-hand side (LHS) , I_1 is the first term on the RHS, and I_2 represents the second. The solution is given as:

$$-I_1 = \frac{1}{2\pi}\left\{p\sqrt{t^2-d^2}\left(d\sqrt{t^2-y^2}\sinh^{-1}\left(\frac{\sqrt{t^2-d^2}}{\sqrt{d^2-y^2}}\right) - y\sqrt{t^2-y^2}\tanh^{-1}\left(\frac{y}{b}\frac{\sqrt{t^2-d^2}}{\sqrt{t^2-y^2}}\right)\right)\right\} \div$$

$$\sqrt{t^2-d^2}\sqrt{t^2-y^2} + p\sqrt{t^2-y^2}\sin^{-1}\left(\frac{d}{t}\right) + c \quad \text{.....(C8)}$$

where c is the constant of integration. The solution to integral I_2 can be expressed as follows:

$$-I_2 = \frac{1}{4}\int_{|y|}^{a}\frac{pt}{\sqrt{t^2-y^2}}dt = \frac{p}{4}\sqrt{a^2-y^2} \quad \text{.....(C9)}$$

Using the known relationships:

$$\sinh^{-1}(x) = \ln\left(1+\sqrt{x^2+1}\right) \; and \; \tanh^{-1}(x) = \frac{1}{2}\ln\left(\frac{1+x}{1-x}\right) \quad \text{.....(C10)}$$

Eq. (C8) can be simplified further to result in the following form:

$$-I_1 = \frac{1}{2\pi}\left\{p\left(d\ln\left(\frac{\sqrt{t^2-d^2}+\sqrt{t^2-y^2}}{\sqrt{d^2-y^2}}\right) - \frac{y}{2}\ln\left(\frac{d\sqrt{t^2-y^2}+y\sqrt{t^2-d^2}}{d\sqrt{t^2-y^2}-y\sqrt{t^2-d^2}}\right)\right) + \sqrt{t^2-y^2}\sin^{-1}\left(\frac{d}{t}\right)\right\} + c \quad \text{..(C11)}$$

Applying the definite integral when incrementally integrating from points y_b to y_t, the generic solution shown below where the placeholder variable t and integration constant c vanish:

$$-I_1\Big|_{y_b}^{y_t} = \frac{1}{2\pi}\left\{p\left(d\ln\left(\frac{\sqrt{y_t^2-d^2}+\sqrt{y_t^2-y^2}}{\sqrt{d^2-y^2}}\right) - \frac{y}{2}\ln\left(\frac{d\sqrt{y_t^2-y^2}+y\sqrt{y_t^2-d^2}}{d\sqrt{y_t^2-y^2}-y\sqrt{y_t^2-d^2}}\right) + \right.\right.$$

$$\left.\left.\sqrt{y_t^2-y^2}\sin^{-1}\left(\frac{d}{y_t}\right)\right)\right\} - \frac{1}{2\pi}\left\{p\left(d\ln\left(\frac{\sqrt{y_b^2-d^2}+\sqrt{y_b^2-y^2}}{\sqrt{d^2-y^2}}\right) - \frac{y}{2}\ln\left(\frac{d\sqrt{y_b^2-y^2}+y\sqrt{y_b^2-d^2}}{d\sqrt{y_b^2-y^2}-y\sqrt{y_b^2-d^2}}\right) + \right.\right.$$

$$\left.\left.\sqrt{y_b^2-y^2}\sin^{-1}\left(\frac{d}{y_b}\right)\right)\right\} \quad \text{.....(C12)}$$

Further simplification with the help of known relation $\ln(x)$-$\ln(y) = \ln(x/y)$ leads to:

$$-I_1 - I_2 = \frac{1}{2\pi}\left\{p\left(d\ln\left(\frac{\sqrt{y_t^2-d^2}+\sqrt{y_t^2-y^2}}{\sqrt{y_b^2-d^2}+\sqrt{y_b^2-y^2}}\right) - \frac{y}{2}\ln\left(\frac{d\sqrt{y_t^2-y^2}+y\sqrt{y_t^2-d^2}}{d\sqrt{y_t^2-y^2}-y\sqrt{y_t^2-d^2}} \times \frac{d\sqrt{y_b^2-y^2}-y\sqrt{y_b^2-d^2}}{d\sqrt{y_b^2-y^2}+y\sqrt{y_b^2-d^2}}\right) + \right.\right.$$

$$\left.\left.\left[\sqrt{y_t^2-y^2}\sin^{-1}\left(\frac{d}{y_t}\right) - \sqrt{y_b^2-y^2}\sin^{-1}\left(\frac{d}{y_b}\right)\right]\right)\right\} + \frac{p}{4}\sqrt{a^2-y^2} \quad \text{.....(C13)}$$

Equation (C13) can be used to obtain the value of *F(t)* for the crack between the incremental points y_t and y_b, across the various interfaces that the fracture has crossed, for the points of interest y in vertical direction, and elevations of the interfaces d from the mid-points of the fracture. In a similar manner, the solution to the *G(t)* term in Eq. (6.9) can also be obtained as shown below.

$$\int_{|y|}^{a}\frac{y\,G(t)}{\sqrt{t^2-y^2}}dt = I = \frac{1}{2\pi}\int_0^t\frac{yq\sqrt{t^2-d^2}}{t\sqrt{t^2-y^2}}dt \quad \text{.....(C14)}$$

The general solution to the above integral is as follows, where q is the solution to the odd function:

$$I = -\frac{q}{2\pi}\left\{d\ln\left(\frac{\sqrt{t^2-y^2}-\sqrt{t^2-d^2}}{\sqrt{t^2-d^2}}\right) - ln\left(\frac{\sqrt{t^2-y^2}+\sqrt{t^2-d^2}}{\sqrt{t^2-d^2}}\right) + y\ln\left(\frac{\sqrt{t^2-y^2}-\sqrt{t^2-d^2}}{\sqrt{t^2-y^2}+\sqrt{t^2-d^2}}\right)\right\} \text{.....(C15)}$$

As in Eq. (C13) above is the integration is carried across point y_b and y_t, then we get the following form after simplification and using the relation ln(x)-ln(y) = ln(x/y) :

$$-I|_{y_b}^{y_t} = -\frac{q}{2\pi}\left\{d\ln\left(\frac{d\sqrt{y_t^2-y^2}+y\sqrt{y_t^2-d^2}}{d\sqrt{y_t^2-y^2}-y\sqrt{y_t^2-d^2}} \times \frac{d\sqrt{y_b^2-y^2}-y\sqrt{y_b^2-d^2}}{d\sqrt{y_b^2-y^2}+y\sqrt{y_b^2-d^2}}\right) + y\ln\left(\frac{\sqrt{y_t^2-y^2}-\sqrt{y_t^2-d^2}}{\sqrt{y_t^2-y^2}+\sqrt{y_t^2-d^2}} \times \right.\right.$$

$$\left.\left.\frac{\sqrt{y_b^2-y^2}+\sqrt{y_b^2-d^2}}{\sqrt{y_b^2-y^2}-\sqrt{y_b^2-d^2}}\right)\right\} \text{.....(C16)}$$

Since y_t = -y_b because the points are equidistant from the center of the fracture, the expression can be simplified further after substitution to result in the following expression for *G(t)*:

$$-I|_{y_b}^{y_t} = -\frac{q}{2\pi}\left\{d\ln\left(\frac{d\sqrt{y_t^2-y^2}+y\sqrt{y_t^2-d^2}}{d\sqrt{y_t^2-y^2}-y\sqrt{y_t^2-d^2}} \times \frac{d\sqrt{y_b^2-y^2}-y\sqrt{y_b^2-d^2}}{d\sqrt{y_b^2-y^2}+y\sqrt{y_b^2-d^2}}\right) + y\ln\left(\frac{\sqrt{y_b^2-y^2}+\sqrt{y_b^2-d^2}}{\sqrt{y_t^2-y^2}+\sqrt{y_t^2-d^2}}\right)\right\} \text{.....(C17)}$$

On integration across the entire fracture height and accounting for various interfaces and layers, the solution to Eq.(C17) yields to Eq. (6.17).

APPENDIX D

(A) Input Screen: Example Height Growth Model Input

43 Layer Model. Perforation Depth at Layer No. 22.

LayerNo.	Depth (ft)	Thick (ft)	Stress (psi)	K1c	YM	PR	Leakoff
	(ft)	(ft)	(psi)	(ft.min0.5)	(psi)	Unitless	(ft/min0.5)
1	5380.0	8.6	4494.6	1379	2159574	0.34	0.003861
2	5388.6	9.3	4476.6	1327	1831915	0.35	0.003897
3	5397.9	10.2	4469.5	1373	2634370	0.29	0.003822
4	5408.1	10.1	4444.3	1322	2490000	0.27	0.003867
5	5418.2	12.7	4433.2	1379	2520000	0.23	0.003771
6	5430.9	11.2	4402.5	1252	2490000	0.28	0.003621
7	5442.1	12.4	4384.4	1302	1846809	0.33	0.003759
8	5454.5	7.9	4354.8	1262	1519149	0.34	0.003834
9	5462.4	4.3	4317.1	1200	2794120	0.31	0.003879
10	5466.7	7.5	4298.2	1129	2070210	0.29	0.003687
11	5474.2	5.9	4256.8	1200	2415970	0.25	0.004089
12	5480.1	5.7	4186.2	1302	2689080	0.27	0.004008
13	5485.8	6.8	4135.9	1122	2331930	0.27	0.003966
14	5492.6	7.4	4097.9	1357	2521010	0.23	0.00405
15	5500.0	4.1	4030	1451	2821870	0.27	0.003897
16	5504.1	4.8	3999.1	1326	2457980	0.28	0.004047
17	5508.9	8.1	3962.9	1208	3235290	0.23	0.004074
18	5517.0	7.0	3926.3	1404	2709380	0.27	0.003972
19	5524.0	5.4	3908.4	1200	2310920	0.25	0.00396
20	5529.4	6.8	3887.4	1341	2906250	0.28	0.004014
21	5536.2	6.6	3865.9	1169	2184870	0.22	0.004107
22	5542.8	5.3	3848.5	1302	2617020	0.24	0.004116
23	5548.1	5.4	3859.3	1559	1957450	0.25	0.004089
24	5553.5	5.3	3876.6	1343	3187500	0.29	0.004017
25	5558.8	5.7	3893.4	1458	2042550	0.32	0.003906
26	5564.5	4.5	3912.6	1226	3063830	0.33	0.003996
27	5569.0	4.2	3929.3	1529	1906380	0.35	0.003975
28	5573.2	4.6	3941.1	1129	2468080	0.32	0.004011
29	5577.8	5.3	3970	1200	2689360	0.23	0.004077
30	5583.1	4.4	4010	1200	2331920	0.25	0.004044
31	5587.5	7.3	4060	1235	1702130	0.33	0.003876
32	5594.8	7.2	4097.9	1088	2110640	0.35	0.004008
33	5602.0	4.3	4153.9	1200	2808510	0.22	0.004053
34	5606.3	5.8	4239.1	1353	2368090	0.31	0.003933
35	5612.1	5.5	4301.9	1245	2502130	0.32	0.003912
36	5617.6	4.8	4368.5	1314	2248940	0.33	0.003969
37	5622.4	6.8	4450.9	1245	2070210	0.35	0.003969
38	5629.2	6.2	4486.2	1333	2636170	0.29	0.003939
39	5635.4	4.8	4505.7	1298	2427660	0.28	0.003933
40	5640.2	5.8	4521.9	1329	2725530	0.30	0.003924

(B) Input Screen: Simulator Control Screen

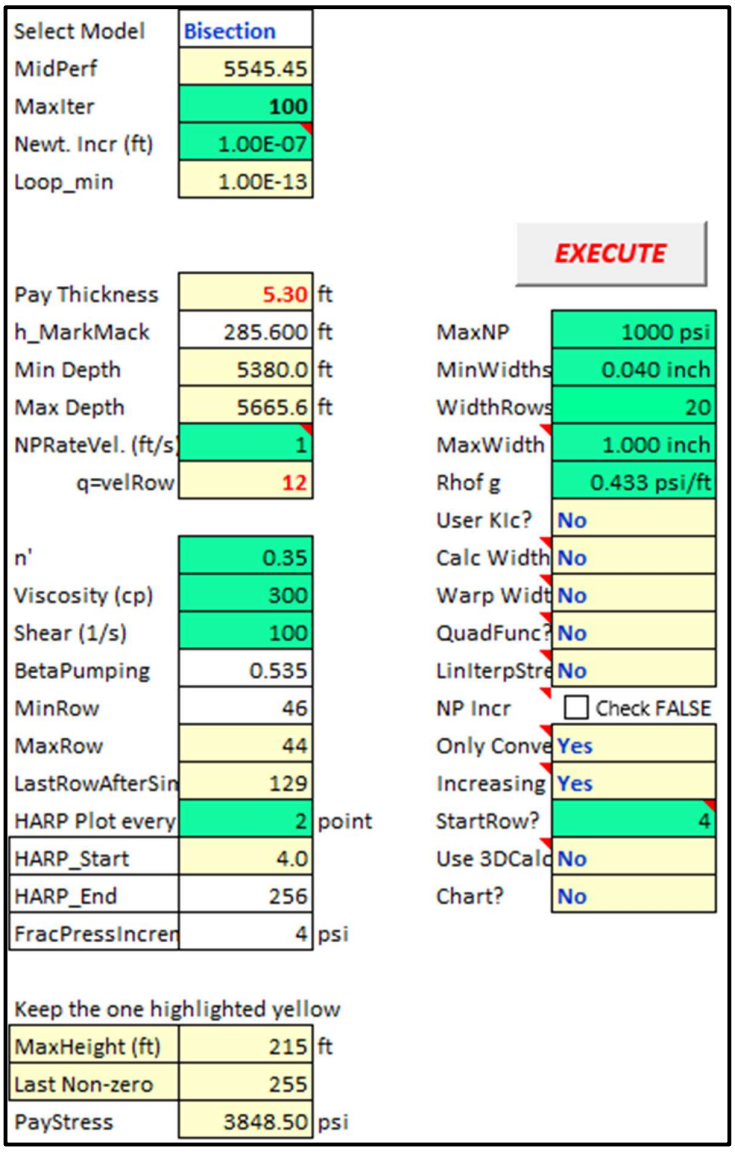

Select Model	Bisection				
MidPerf	5545.45				
MaxIter	100				
Newt. Incr (ft)	1.00E-07				
Loop_min	1.00E-13				
			EXECUTE		
Pay Thickness	5.30	ft			
h_MarkMack	285.600	ft	MaxNP	1000 psi	
Min Depth	5380.0	ft	MinWidths	0.040 inch	
Max Depth	5665.6	ft	WidthRows	20	
NPRateVel. (ft/s)	1		MaxWidth	1.000 inch	
q=velRow	12		Rhof g	0.433 psi/ft	
			User KIc?	No	
n'	0.35		Calc Width	No	
Viscosity (cp)	300		Warp Widt	No	
Shear (1/s)	100		QuadFunc?	No	
BetaPumping	0.535		LinInterpStre	No	
MinRow	46		NP Incr	Check FALSE	
MaxRow	44		Only Conve	Yes	
LastRowAfterSin	129		Increasing	Yes	
HARP Plot every	2	point	StartRow?	4	
HARP_Start	4.0		Use 3DCalc	No	
HARP_End	256		Chart?	No	
FracPressIncren	4	psi			
Keep the one highlighted yellow					
MaxHeight (ft)	215	ft			
Last Non-zero	255				
PayStress	3848.50	psi			